



UNIVERSIDAD DE LAS PALMAS DE GRAN CANARIA
Departamento de Física

PROGRAMA DE DOCTORADO: Oceanografía 2004-2006

Título de la Tesis

Multiscale variability in the North Atlantic Ocean

(Variabilidad multiescalar en el océano Noratlántico)

Tesis doctoral presentada por Verónica María BENÍTEZ BARRIOS

Dirigida por : Dr. Alonso HERNÁNDEZ GUERRA - ULPGC
Dr. Jose Luis PELEGRÍ LLOPART - ICM-CSIC

Dr. Alonso Hernández Guerra Dr. Jose L. Pelegrí Llopard D^a. Verónica M. Benítez Barrios

LAS PALMAS DE GRAN CANARIA A 27 DE MAYO DE 2011

A mis padres e Iván

Agradecimientos

Hace más de cinco años que inicié el camino de la tesis doctoral. Sin pensar muy bien lo que suponía doctorarse, y a pesar de los muchos avisos de que no sería fácil, decidir dar este paso. Ahora que estoy llegando al final del camino quisiera agradecer a todas aquellas personas que me han acompañado.

En primer lugar quisiera expresar mi más profundo agradecimiento a mis padres, Pedro y Josefa. Ellos han sido para mí un ejemplo de respeto, perseverancia, sacrificio y generosidad, acompañado de un largo etcétera. Les agradezco su apoyo incondicional y todos los cuidados, consejos y cariño que me han dado ... incluyendo tus comiditas mamá y las veces que hiciste de mi agenda personal papá. Extiendo mis agradecimientos a mis hermanos, Carmelo, Germán, Domingo y Pedro, porque además de todo lo que un buen hermano te puede dar, han mostrado un gran interés por mi trabajo y compatido mis alegrías y tristezas en él. También agradezco a mis cuñadas, Carmen, Tina, Ana y Natalia, su interés por mi bienestar.

A tí Iván , por estar a mi lado en todo momento, apoyándome y cuidándome; soportando toda la tensión de hacer una tesis. He aprendido muchas cosas contigo. Entre ellas admiro ese temple que tienes para afrontar cualquier situación, haciendo que todo parezca más fácil.

A mi "otra familia", a Antonio y Ángela, por cuidarme como si fuera una más, y a mis cuñados Sandra, Raúl, Toño, Nely y, muy especialmente, a Ayoze, por estar ahí para lo que hiciera falta.

A todos los "peques", Airam, Andrea, Daniel, Cynthia, Pedro, Carla, Diego, Daniel, Adrián y Jordan, por inundar todo de alegría .. y de inocentes preguntas que te hacen pensar.

Un GRACIAS muy grande va para mis directores de tesis, Alonso Hernández Guerra y José Luis Pelegrí Llopert, por su enorme paciencia y los sabios consejos que me brindaron y me han guiado hasta aquí. Alonso, te agradezco el haberme dado la oportunidad de hacer una tesis y ponerme todos los medios necesarios para la misma, enseñarme los pasos fundamentales en el tratamiento de datos y hacerme pensar. A tí Jose Luis te agradezco el inmesurable entusiasmo con que siempre transmites todos tus conocimientos, induciendo de una forma natural a la reflexión; así como tu comprensión, ánimos y la cercanía con la que me has tratado. Gracias por ayudarme tanto en esta recta final!

También doy gracias a los supervisores de mis estancias en Estados Unidos y Francia. Thanks to Kamazima Lwiza (School of Marine and Atmospheric sciences, NY), the tireless man, no matter how many questions I have got or how far I am, I always get an answer from you. I also appreciate the stories you told me, as for example "The old shy woman was buried alive". A Fabrice Hernández y Romain Bourdallé, por acogerme en Mercator Ocean, introducirme en el mundo de los modelos y dejar la puerta abierta a numerosas colaboraciones. Merci beaucoup Bruno Levier, pour faire ma séjour très agréable!

Muchísimas gracias a mis compañeros de batalla, oyentes de mis problemas y preocupaciones .. y buscadores de soluciones de muchos de ellos, Isis, Evan, David y Lola, y muy especialmente a Francisco Machín y Eugenio Fraile por enseñarme a dar mis primeros pasos y siempre contar conmigo.

Debo agradecer las respuestas tan rápidas y elaboradas que me ofreció Manuel Vargas acerca del método de Bindoff and McDougall, a Ángelo Santana por las tantas horas que me dedicó aclarándome dudas estadísticas y a Pedro Vélez y Damiá Gomis por sus concienzudas explicaciones sobre el análisis espacial objetivo.

Agradezco a la UTM su asistencia en la mar, y de manera especial a Javier Vallo y Andrés Giraldez por hacer más amenas las largas noches que compartimos de turno y tener paciencia para responder a todas mis curiosidades.

Doy gracias al Gobierno de Canarias, por concederme la financiación necesaria para la realización de esta tesis doctoral.

.. y como no, a todas aquellas personas con las que he tenido el placer de compartir este camino .. y alguna que otra fiesta ... y que agrupo por laboratorios para no dejarme a nadie atrás; la gente de los laboratorios de biología B201 y de química de la ULPGC, muy especialmente a Jacob Cardona y Minerva Espino, por estar pendientes de mí, y a la gente del ICM, principalmente a María Pastor y Mariona Claret.

La imagen de la portada y contraportada refleja una de las numerosas explicaciones con las que me ilustró el Dr. José Luis Pelegrí durante la elaboración de mi tesis doctoral.

Abstract

The world ocean heat content has increased between mid 1950's and mid 1990's, highlighting the key role of the ocean in the climate system. A set of ship-based observations have evidenced substantial temperature and salinity changes in the Atlantic thermocline, although they are neither uniform nor monotonic. In this thesis we evaluate the recent variability of the tropical and subtropical North Atlantic Ocean over different spatial scales, and explore the possible controlling mechanisms.

Temperature and salinity changes are detected by examining repeated hydrographic sections along 29.1°N in the Canary Region and 7.5°N and 24.5°N across the North Atlantic Ocean. Our results show that the warming of the intermediate and upper deep waters along 7.5°N, previously reported for the period 1957-1993, has continued until 2010; however, the cooling of deeper waters has been reversed. For the 24.5°N section, cooling (-0.15°C) is found between 1998 and 2004 in the 600-1800 db layer, which reverses the warming trend observed from 1957 to 1998. This change in the tendency of temperature, also presented in salinity, was corroborated using Argo data. In the Canary basin, a significant rise in temperature and salinity was found between 1500 and 2300 db for the 1997-2006 period, with respective maximum rates of 0.29°C and 0.047 per decade at 1600 db. Decomposition into changes on neutral surfaces and changes due to the vertical displacements of the isoneutrals reveals the latter mechanism as the principal contributor to the observed changes. Nevertheless, some water masses are changing. North Atlantic Central Water (NACW) arrived to the Canary region in 2006 in a cooler and fresher form than in 1997. Contrary, Antarctic Intermediate Water (AAIW) and Upper Circumpolar Water (UCPW) in the 7.5°N section were warmer and saltier in 2010 as compared with 1993.

Regarding the circulation variations, data from a current meter installed in the Lanzarote Passage in the eastern boundary of the subtropical North Atlantic Gyre were used to determine and quantify the 9-year mean transport and the inter-annual and seasonal mass transport variability for the three water masses present in the area. Time series analysis show a mean mass transport of -0.81 ± 1.48 Sv for the NACW, $+0.09 \pm 0.57$ Sv for the AAIW and -0.05 ± 0.17 Sv for the MW. The seasonal pattern obtained from the harmonic and wavelet analysis is characterized by opposite patterns for NACW and AAIW. A maximum southward transport in winter and spring has been observed for the NACW followed by a minimum one in summer and fall. Near zero values during winter and spring are found for AAIW, with a maximum northward value in summer and a negative value in fall, when this water mass reverses its flow. MW has a seasonal pattern similar to NACW.

Finally, the three-dimensional circulation in the Coastal Transition Zone off northwest Africa is described from the analysis of high-resolution data collected southeast of the Canary Islands during late winter 2006. The coastal transition zone is divided into upwelling, frontal and offshore regions based on their distinct physical and dynamic characteristics. We also quantify the different contributions to the vertical motion, namely vertical velocities induced by wind, mesoscale structures and the upwelling/diapycnal transfer. The absolute mesoscale

vertical velocities reach maximum local values, up to 18 m day^{-1} , but the integrated upwelling and diapycnal transports are largest (of order 0.1 Sv).

Resumen

El contenido de calor del océano se ha incrementado entre mediados de los cincuenta y de los noventa, reseñando el papel de los océanos en el sistema climático. Las observaciones realizadas a bordo de buques oceanográficos han evidenciado cambios substanciales de la temperatura y la salinidad en la termoclinia del Atlántico, aunque no son uniformes ni monotónicos. En esta tesis evaluamos la variabilidad reciente del océano Noratlántico tropical y subtropical en diferentes escalas espaciales y exploramos los posibles mecanismos que controlan dichos cambios.

Los cambios de temperatura y salinidad han sido detectados examinando secciones hidrográficas repetidas a lo largo de 29.1°N en la región canaria y, 7.5°N y 24.5°N a través del océano Atlántico Norte. Nuestros resultados muestran que el calentamiento que había sido documentado para el periodo de 1957-1993 en las aguas intermedias y en la parte superior de las aguas profundas existentes a lo largo de 7.5°N ha continuado hasta 2010; sin embargo, el enfriamiento de las aguas más profundas se ha detenido o incluso ha sido invertido. Para la sección a lo largo de 24.5°N, se observa un enfriamiento (-0.15°C) entre 1998 y 2004 en la capa de 600-1800 db, el cual invierte la tendencia de calentamiento observada entre 1957 y 1998. Este cambio de tendencia en la temperatura, también observado en la salinidad, es corroborado con datos Argo. En la cuenca Canaria se encontró un aumento significativo de temperatura y salinidad entre 1500 y 2300 db para el periodo 1997-2006, con una tasa máxima de 0.29°C and 0.047 por década a los 1600 bd. La descomposición de dichos cambios en cambios a lo largo de las superficies isoneutras y cambios debidos al desplazamiento vertical de las isoneutras revela que es este último mecanismo el principal contribuyente en los cambios observados. No obstante, existen masas de agua que están cambiando. El Agua Noratlántica Central llegó a la región Canaria en 2006 en una forma más fría y menos salada que en 1997. Por el contrario, el Agua Antártica Intermedia y el Agua Circumpolar Superior en la sección fueron más cálidas y saladas en 2010 en comparación a 1993.

En cuanto a la circulación, se utilizaron los datos de un correntímetro instalado en el Pasaje de Lanzarote, en la frontera este del giro subtropical del Noratlántico, para determinar y cuantificar el transporte medio durante los 9 años de datos, su variabilidad interanual y estacional para cada una de las masas de agua presentes en esta área. El análisis de la serie temporal mostró un transporte de masa medio de -0.81 ± 1.48 Sv para el Agua Noratlántica Central, $+0.09 \pm 0.57$ Sv para el Agua Antártica Intermedia y -0.05 ± 0.17 Sv para el Agua Mediterránea. El patrón estacional obtenido a partir de los análisis armónico y wavelet se caracteriza por patrones opuestos entre el Agua Noratlántica Central y el Agua Antártica Intermedia. Se observó un transporte máximo hacia el sur del Agua Noratlántica Central en invierno seguido de un mínimo en verano y otoño. Durante el invierno y la primavera se encontraron valores cercanos a cero para el Agua Antártica Intermedia, con valores máximos hacia el norte en verano y negativos en otoño, cuando esta masa de agua invierte su flujo. El Agua Mediterránea presentó un patrón estacional similar al Agua Noratlántica Central.

Finalmente, se describe la circulación tridimensional en la zona de transición costera del

noroeste de África a partir del análisis de datos de alta resolución recogidos al sureste de las Islas Canarias durante el verano de 2006. La zona de transición costera se divide en las regiones de afloramiento, frontal y de océano abierto en función de sus características físicas y dinámicas. Además, cuantificamos las diferentes contribuciones al movimiento vertical, es decir velocidades verticales inducidas por el viento, estructuras mesoscales y transferencia diapicna. Las velocidades verticales absolutas de la mesoscala alcanzan valores locales máximos, hasta 18 m día^{-1} , pero los transportes integrados de afloramiento y diapicno son mayores (del orden de 0.1 Sv).

Preface

This thesis is based on five papers which form chapters 2-6 of it. These papers have been published in or submitted to peer-reviewed journals. Below, I list them indicating my contribution in each one.

Paper I: Benítez-Barrios, V.M., Pelegrí, J.L., Emelianov, M. and Fraile-Nuez, E. Decadal changes in the tropical Atlantic along the 7.5°N section. *In prep.* After the MOC-equatorial cruise in April 2010, Benítez-Barrios did the data calibration and analysis of temperature and salinity variations along the 7.5°N section under the supervision of Pelegrí. The results were jointly interpreted by Pelegrí and Benítez-Barrios.

Paper II: Vélez-Belchí, P., Hernández-Guerra, A., Fraile-Nuez, E. and Benítez-Barrios, V.M. Changes in temperature and salinity tendencies of the upper subtropical North Atlantic Ocean at 24.5°N. *Journal of Physical Oceanography*, doi: 10.1175/2010JPO4410.1, 2010. Benítez-Barrios conducted the Matlab implementation of the methodology used to compute the isobaric variations and their decomposition. Furthermore, Benítez-Barrios helped in the interpretation of the results.

Paper III: Benítez-Barrios, V.M., Hernández-Guerra, A., Vélez-Belchí, P., Machín F. and Fraile-Nuez, E. Recent changes in subsurface temperature and salinity in the Canary Region. *Geophysical Research Letters*, volume 35, L07603, doi:10.1029/2008GL033329, 2008. The idea for this paper came from Hernández-Guerra, who also made the necessary data available. Implementation of the required methodology, data analysis and writing were carried out by Benítez-Barrios. Hernández-Guerra contributed ideas for analyses and helped in the interpretation of the results.

Paper IV: Fraile-Nuez, E., Machín F., Vélez-Belchí, P., López-Laatzén F., Borges, R., Benítez-Barrios, V.M. and Hernández-Guerra, A. Nine years of mass transport data in the eastern boundary of the North Atlantic subtropical gyre. *Journal of Geophysical Research*, volume 115, C09009, doi:10.1029/2010JC006161, 2010. Benítez-Barrios contributed to data collection and interpretation.

Paper V: Benítez-Barrios, V.M., Pelegrí, J.L., Hernández-Guerra, A., Lwiza, K.M.M., Gomis, D., Vélez-Belchí, P. and Hernández-León, S. Three-dimensional Circulation in the NW Africa Coastal Transition Zone. *Progress in Oceanography*, 2011, under review. During a doctoral stay in the Marine Sciences Research Center (State University of New York, Stony Brook, NY), Lwiza proposed the hydrographic data collected during the CONAFRICA survey was a good opportunity to compute vertical velocities due to their distribution and

high spatial resolution. Benítez-Barrios processed the data and performed the objective analysis following the recommendations given by Gomis and Vélez-Belchí. Subsequently, Pelegrí pointed to the interest of estimating and comparing the different contributions to the vertical velocity field. Benítez-Barrios and Pelegrí jointly interpreted the results and wrote the manuscript.

Contents

| | |
|---|-----------|
| 1 General introduction and motivation | 1 |
| 1.1 The Earth's climate system | 3 |
| 1.1.1 Climate vs weather | 3 |
| 1.1.2 Climate system components | 3 |
| 1.1.3 The Earth's energy balance | 5 |
| 1.1.4 The hydrological cycle | 6 |
| 1.2 The importance of oceans in the Earth's climate system | 7 |
| 1.2.1 The wind-driven circulation | 8 |
| 1.2.2 Thermohaline circulation | 10 |
| 1.2.3 Oceanic eddies | 11 |
| 1.3 Climate variability and climate change | 12 |
| 1.4 Thesis objectives and organization | 14 |
| | |
| I Tropical and Subtropical North Atlantic | 17 |
| | |
| 2 Decadal changes in the tropical Atlantic along the 7.5°N section | 19 |
| 2.1 Introduction | 21 |
| 2.2 Data and methods | 21 |
| 2.3 Results and discussion | 22 |
| 2.4 Conclusions | 27 |
| | |
| 3 Changes in temperature and salinity tendencies of the upper subtropical North Atlantic ocean at 24.5°N | 29 |
| 3.1 Introduction | 31 |
| 3.2 Data and methods | 32 |
| 3.3 Results | 35 |
| 3.3.1 Basin-wide changes | 35 |
| 3.3.2 Zonally averaged changes | 37 |
| 3.3.3 Isobaric change decomposition | 40 |
| 3.3.4 Annual and interannual variability | 42 |
| 3.4 Discussion and conclusions | 43 |
| | |
| II The Canary Region | 45 |
| | |
| 4 Recent changes in subsurface temperature and salinity in the Canary region | 47 |
| 4.1 Introduction | 49 |
| 4.2 Data Set and Method | 49 |
| 4.3 Results | 50 |

| | | |
|------------|---|-----------|
| 4.3.1 | θ/S isobaric changes | 50 |
| 4.3.2 | Isobaric change decomposition | 52 |
| 4.3.3 | Warming, freshening and heaving mechanisms | 52 |
| 4.4 | Discussion and conclusion | 55 |
| 5 | Nine years of mass transport data in the eastern boundary of the North Atlantic Subtropical Gyre | 57 |
| 5.1 | Introduction | 60 |
| 5.2 | Data | 61 |
| 5.2.1 | Current-meter description | 61 |
| 5.2.2 | Hydrographic data | 62 |
| 5.3 | Current-meter statistics | 62 |
| 5.4 | EOF analysis | 65 |
| 5.4.1 | Temporal EOFs with four moorings | 65 |
| 5.4.2 | Temporal EOFs for the nine-year record | 69 |
| 5.5 | Periodic signals | 69 |
| 5.5.1 | Harmonic analysis | 69 |
| 5.5.2 | Wavelet analysis | 72 |
| 5.6 | Variability in mass transport | 74 |
| 5.6.1 | Temporal variability | 74 |
| 5.6.2 | Seasonal variability | 77 |
| 5.6.3 | Inter-annual variability | 80 |
| 5.7 | Results and discussion | 82 |
| III | The NW African Upwelling System | 85 |
| 6 | Three-dimensional circulation in the NW Africa Coastal Transition Zone | 87 |
| 6.1 | Introduction | 90 |
| 6.2 | Data analysis | 92 |
| 6.2.1 | Dataset | 92 |
| 6.2.2 | Optimal statistical interpolation | 94 |
| 6.3 | Methodology to estimate vertical velocities | 95 |
| 6.3.1 | Quasi-geostrophic mesoscale vertical velocities | 96 |
| 6.3.2 | Wind-induced and diapycnal vertical velocities | 98 |
| 6.4 | Distribution and transport of properties | 99 |
| 6.4.1 | Horizontal structure | 99 |
| 6.4.2 | Vertical structure | 104 |
| 6.4.3 | Water transports | 106 |
| 6.4.4 | Vertical velocity fields | 108 |
| 6.5 | Discussion | 111 |
| 6.5.1 | The upwelling, frontal and offshore regions | 111 |
| 6.5.2 | Origin of mesoscale structures | 115 |
| 6.5.3 | Fluorescence distribution | 117 |

| | |
|--|------------|
| 6.6 Conclusions | 118 |
| 7 Conclusions and future work | 121 |
| 8 Resumen en español | 125 |
| 8.1 Introducción general y motivación | 127 |
| 8.1.1 El sistema climático de la Tierra | 127 |
| 8.1.2 La importancia de los océanos en el sistema climático | 130 |
| 8.1.3 Variabilidad y cambio climático | 134 |
| 8.1.4 Objetivos de la tesis y organización | 136 |
| 8.2 Síntesis de resultados | 138 |
| 8.2.1 Cambios decadales en el Atlántico tropical a lo largo de la sección 7.5°N (Capítulo 2) | 138 |
| 8.2.2 Cambios en las tendencias de temperatura y salinidad en la sección transatlántica 24.5°N (Capítulo 3) | 141 |
| 8.2.3 Variaciones de la temperatura y salinidad subsuperficiales en la región Canaria (Capítulo 4) | 145 |
| 8.2.4 Nueve años de datos del transporte de masa en el límite oriental del giro subtropical del Atlántico Norte (Capítulo 5) | 148 |
| 8.2.5 Circulación tridimensional en la zona de transición costera del noroeste de África (Capítulo 6) | 158 |
| 8.3 Conclusiones y futuras líneas de investigación | 172 |
| Bibliography | 177 |

List of Figures

| | | |
|-----|---|----|
| 1.1 | Schematic view of the components, processes and interactions in the Earth's climate system (Le Treut et al., 2007). | 4 |
| 1.2 | Earth's annual global energy balance (Le Treut et al., 2007, source: Kiehl and Trenberth (1997)). | 6 |
| 1.3 | Maps of the 1989 mean wind velocity and sea level pressure (upper panel) and the ocean surface circulation (lower panel). Source: Stewart (2005). | 8 |
| 1.4 | Simplified sketch of the global overturning circulation (from Kuhlbrodt et al. (2007)). Surface waters (red lines) flow towards the three main deep-water formation regions (yellow ovals) located in the northern North Atlantic, the Ross Sea and the Weddell Sea, where they initiate their recirculation as deep waters (blue lines) and bottom waters (purple lines). | 11 |
| 1.5 | Sea surface temperature image of the Gulf Stream current swirling warm-core and cold-core rings north and south of its mean path. | 12 |
| 2.1 | Location of stations occupied during the IGY in 1957 (black dots), the WOCE A06 line in 1993 (blue dots) and its revisit in 2010 under the MOC project (red crosses). | 21 |
| 2.2 | Potential temperature and salinity change on isobars between 2010 and 1993 sections. Red colors denote increasing property. The side partitions correspond to the zonally averaged changes for the periods 1957-1993 (blue line), 1993-2010 (red line) and 1957-2010 (black line). | 23 |
| 2.3 | Decomposition of temperature and salinity changes at constant pressure (black line) into changes along neutral surfaces (blue line) and change due to heaving (red line) for the period 1993-2010. The grey line denotes the sum of both components. Terms are zonally averaged for the western basin (48.45°W - 32°W) and the eastern basin (32°W - 17.45°W). | 25 |
| 2.4 | As for Figure 2.3 but for the period 1957-2010. | 26 |
| 3.1 | a) Positions of the CTD stations from the repeated hydrographic sections sampled across 24.5°N in 1957 (IGY), 1981, during WOCE in 1992 (A05) and in 1998 (AR01), and finally in 2004. To avoid overlapping between each section, a latitude offset has been added to each section, as indicated in the legend. (b) Locations of each Argo profile in the period between January 2003 and December 2008 used in this study. The 2006 Argo zonal 'synthetic' section obtained is also shown. The gray lines at 23°W and 70°W bound the longitude range where the Atlantic was effectively sampled at 24.5°N during the five occupations. | 33 |

- 3.2 Vertical zonal sections, on pressure surfaces, of potential temperature differences at 24.5°N in the Atlantic Ocean between the oceanographic sections carried out during: (a) 1998-1957 (i.e. between 1957 and 1998), (b) 2004-1957, (c) 2004-1998, (d) 2006 (Argo)-1957 and (e) 2006 (Argo)-1998. The gray lines at 23°W and 70°W bound the longitude range where the Atlantic was effectively sampled at 24.5°N during the five occupations. Positive values indicate warming. This convention has been used throughout the text, subtracting the older temperature section from the most recent one when computations refer to time periods. The same color scale has been used for the five panels. 36
- 3.3 Vertical zonal sections on pressure surfaces of salinity differences at 24.5°N in the Atlantic between the oceanographic sections carried out during: (a) 1998-1957 (i.e. between 1957 and 1998), (b) 2004-1957, (c) 2004-1998, (d) 2006(Argo)-1957 and (e) 2006(Argo)-1998. The gray lines at 23°W and 70°W bound the longitude range where the Atlantic was effectively sampled at 24.5°N during the five occupations. Positive values indicate increase in salinity. This convention has been used throughout the text, subtracting the older salinity section from the most recent one when computations refer to time periods. The same color scale has been used for the five panels. 38
- 3.4 Vertical zonal sections on pressure surfaces of salinity differences at 24.5°N in the Atlantic between the oceanographic sections carried out during: (a) 1998-1957 (i.e. between 1957 and 1998), (b) 2004-1957, (c) 2004-1998, (d) 2006(Argo)-1957 and (e) 2006(Argo)-1998. The gray lines at 23°W and 70°W bound the longitude range where the Atlantic was effectively sampled at 24.5°N during the five occupations. Positive values indicate increase in salinity. This convention has been used throughout the text, subtracting the older salinity section from the most recent one when computations refer to time periods. The same color scale has been used for the five panels. 39
- 3.5 Decomposition of the temperature changes along isobaric surfaces $d\theta/dt|_p$ (thick solid line), as the sum of changes along neutral surfaces, $d\theta/dt|_{\gamma_n}$ (gray line), and the changes due to vertical displacement of the isoneutral, $dp/dt|_{\gamma_n} \partial\theta/\partial p$ (thick dashed line). a) 1998-1957. b) 2004-1998 and c) 2006(Argo)-1998. Positive values indicate warming. 41
- 3.6 Time evolution of averaged (left) temperature and (right) salinity between 70°W and 23°W for the upper ocean, thermocline and intermediate waters. Vertical gray lines denote the CTD measurements (1957, 1981, 1992, 1998 and 2004), small black dots the annual Argo estimates (2005, 2006, 2007 and 2008), and gray dots the 2006 Argo synthetic section. 43

| | | |
|-----|--|----|
| 4.1 | (a) Hydrographic stations carried out during CANIGO (1997, crosses) and RAPROCAN (2006, dots) cruises. (b) Potential temperature differences on isobaric levels. Differences contoured at 0.2°C intervals. The side partition is the zonally averaged difference of the potential temperature. The dashed lines stand for the 95% confidence intervals. (c) As for Figure 1b but for salinity. Difference contours at 0.05 intervals. Shaded areas indicate rising temperature and salinity over time. | 51 |
| 4.2 | (a) Isobaric change from 1997 to 2006 ($\theta' _z$ and $S' _z$, black) decomposed into changes along neutral surfaces ($\theta' _n$ and $S' _n$, blue) and changes due to the vertical displacements of isoneutrals (-N θ_z and -NS $_z$, red) as a function of the average pressure of the neutral surfaces. The grey line denotes the sum of both components. (b) As for (a) but for salinity. (c) Change in pressure of neutral surfaces from 1997 to 2006. Positive displacements indicate downward movement over time. Dots represent zonally-averaged isoneutral pressures. | 53 |
| 4.3 | Mean θ/S curves for 2006 (red) and 1997 (blue) for (a) North Atlantic Central Water (NACW) and (b) Antarctic Intermediate Water (AAIW) and Mediterranean Water (MW). The dashed lines correspond to potential density anomaly isolines and the solid lines link points of equal pressure. | 54 |
| 4.4 | The variance explained for the case of pure warming (continuous), pure freshening (dashed) and pure heave (dashed-dotted) against the average pressure of the neutral surfaces. Four different pressure regimes are shown at the top of the figure. | 55 |
| 5.1 | Eastern boundary of the North Atlantic Subtropical Gyre. Eastern Boundary Current (EBC) mooring positions are represented in the map and in the upper inset (zoom), where the Lanzarote Passage is shown. A black line across the moorings indicates the 12 occupations of the same hydrographic section carried out during these 9 years. For reference, the 200-, 1000-, 2000- and 3000-m isobaths are shown (Smith and Sandwell, 1997). In the lower inset, a θ/S diagram shows the distributions of the three water masses present in the area and used for this study. | 63 |
| 5.2 | 9-year average velocity distributions along the maximum variance axis at (a) 150, (b) 300, (c) 500, (d) 870 and (e) 1230 m. The standard deviation is shaded in gray. | 66 |
| 5.3 | A spatial Empirical Orthogonal Function (EOF) analysis is carried out with the two years of data from the 4 mooring installed in the Lanzarote Passage (a). (b) shows the Monte Carlo Method in order to determine the significant oscillation modes, (c) to (f) together with the total explained variance for each mode. | 67 |
| 5.4 | Temporal amplitude corresponding to the EOF analysis over the four EBC moorings. | 68 |

| | | |
|------|---|-----|
| 5.5 | A temporal EOF analysis is carried out with the 9-year time series in the Lanzarote Passage. (a) shows the Monte Carlo Method to determine the two significant oscillation modes visible in (b), together with the total explained variance for each mode. | 70 |
| 5.6 | Amplitude corresponding to the EOF analysis for the EBC4 mooring. | 71 |
| 5.7 | The continuous wavelet power spectrum for the time series of each current-meter (2-5, a-d) at the EBC4 mooring. The thick black contour shows the 5% significance level against red noise, and the cone of influence (COI) where edge effects might distort the picture is shown as a lighter shade. | 75 |
| 5.8 | Estimated mass transport based at the EBC4 mooring for (a) NACW, (b) AAIW and (c) MW together with the geostrophic mass transport estimates from hydrographic stations in the Lanzarote Passage during the different surveys carried out from 1997 to 2006. The transports are smoothed with a 1-month running mean. The means and standard deviations are shown at the top of each subplot. The means are also shown as a horizontal dashed line in each subplot. Note that each subplot has a different scale. Dots represent the geostrophic mass transports computed with a level of no motion at $\gamma_n = 27.3 \text{ kg m}^{-3}$, circles show the geostrophic mass transports with a level of no motion at the bottom. | 76 |
| 5.9 | Estimated mass transport based on the EBC-4 mooring for NACW, and the estimates obtained from XBT data and a θ/S relation from historical CTD data. A running filter of 1-month has been applied to the mass transport from the EBC4 data. | 78 |
| 5.10 | Seasonal variability of the mass transport computed with daily means for each year for (a) NACW, (b) AAIW and (c) MW. Monthly variability is shown as a standard deviation for every month. Note that each subplot has a different scale. | 80 |
| 5.11 | Inter-annual variability of the mass transports computed as cumulative monthly means for each year for (a) NACW, (b) AAIW and (c) MW. | 81 |
| 6.1 | (Top) Study area (solid grey box) off NW Africa with the mean wind components during the CONAFRICA cruise period (22 March - 7 April 2006). (Bottom) Detail of the study area showing the CTD stations together with the 50, 200, 500, 1000 and 2000 m isobaths. | 93 |
| 6.2 | Time series of averaged daily winds over the surveyed area; the cruise period is highlighted. | 94 |
| 6.3 | (a) Satellite SST ($^{\circ}\text{C}$) image for March 29 with the geostrophic current vectors at the sea surface (relative to 500 db) as obtained using the cruise hydrographic data. (b) Satellite Chl a (mg m^{-3}) image for April 7. The white line corresponds to the 200 m isobath, approximately at the shelf break. | 100 |
| 6.4 | Distributions at 20 db of (a) dynamic height (dyn m; gray bar) and $\vec{v}_g (10^{-2} \text{ m s}^{-1})$, referred to 500 db; (b) <i>in situ</i> fluorescence (V; grey bar) and $\theta (^{\circ}\text{C})$ with 0.2°C contour intervals; (c) S with 0.04 contour intervals. The thick dashed black lines denote the dynamic height contours of 0.625 and 0.64 dyn m and the gray line shows the 200 m isobath. | 101 |

| | |
|---|-----|
| 6.5 Distributions of (top) dynamic height (dyn m) and \vec{v}_g (10^{-2} m s $^{-1}$), referred to 500 db, (middle) <i>in situ</i> fluorescence (V) and potential temperature (°C), and (bottom) ζ_g superimposed on the SST image for March 29, at 50 db, 110 db, 245 db and 410 db. Contour interval is 0.2°C for θ and 0.4×10^5 s $^{-1}$ for ζ_g . White lines represent the 0.625 and 0.64 dyn m isolines of dynamic height at 20 db. The bold contours in the θ field at 110 db is the 17.4 °C isotherm. | 103 |
| 6.6 θ-S diagram for all the stations performed during the cruise. Averaged θ-S curves for the upwelled, frontal and offshore waters. The colour scale represents the pressure of each gridpoint, and the dashed lines correspond to $\sigma_\theta=26.6, 26.8$ and 27.1 kg m^{-3} | 105 |
| 6.7 Across-shore sections of the (left) meridional v_g (10^{-2} m s $^{-1}$) and neutral density (kg m^{-3}), and (right) <i>in situ</i> fluorescence (V) and θ (°C) at (top) 27.95°N, (middle) 27.55°N and (bottom) 27.25°N. Dashed contours indicate southward velocities. The elongated upper left panels represent the surface zonal u_g (10^{-2} m s $^{-1}$) at each transect, with positive values indicating eastward flow. The bold contours in the θ field denote the 17.4 °C isotherm. The frontal position is indicated by arrows at the top of the left panels. | 107 |
| 6.8 (a) Layer-integrated mass transports for the north (crosses, solid line), south (x-marks, dotted line), east (stars, dashed-dotted line) and west (circle, solid line) sections of the grid. Mass conservation in the box is represented by the black line. Positive/negative signs are assigned for divergence/convergence flow out-of/into the box. (b) Accumulated mass transport at 27.7°N, beginning the integration at the African coast. Positive/negative accumulated mass transport values denote northward/sorthward flow for the Canary Upwelling Current (CUC) and the Canary Current (CC). | 109 |
| 6.9 Across-shore sections of w_{qg} (m day $^{-1}$) and the zonal u_g along (top) 27.95°N, (middle) 27.55°N and (bottom) 27.25°N. Gray lines represent isopycnals contoured at intervals of 0.05 kg m^{-3} . The frontal position is indicated by arrows at the top of each panel. | 112 |
| 6.10 Distributions of mesoscale vertical velocity w_{qg} (m day $^{-1}$) at 50 db, 110 db, 245 db and 410 db; red and blue areas respectively indicate upward and downward velocities. Superimposed are the ζ_g fields (solid/dashed gray lines indicate positive/negative values, plotted at 0.4×10^5 s $^{-1}$ intervals) together with the 0.625 and 0.64 dyn m isolines of dynamic height at 20 db (dashed black curves). | 113 |
| 6.11 (a) Distribution of ζ_g at 20 db with dots indicating the position of Dipole 1 and Dipole 2. Left and right panels in (b) through (d) correspond to the sections through Dipoles 1 and 2, respectively. (b) Sections of θ (°C; black lines) and <i>in situ</i> fluorescence (V; grey lines). Contour interval is 1°C for θ, and 0.4 V for fluorescence. (c) Sections of w_{qg} (m day $^{-1}$) and the zonal u_g (10^{-2} m s $^{-1}$), referred to 500 db. (d) Sections of w_{qg} (m day $^{-1}$) and the meridional v_g (cm s $^{-1}$), referred to 500 db. In panels (c) and (d) the gray lines represent isopycnals contoured at intervals of 0.1 kg m^{-3} | 116 |

List of Tables

| | | |
|-----|---|----|
| 3.1 | Mean temperature differences ($^{\circ}$ C) with respect to IGY 1957, between 23 $^{\circ}$ W and 70 $^{\circ}$ W. In the last column the value between brackets correspond to the results obtained if annual climatological temperature and salinity data from the World Ocean Atlas 2005 are used as a first guess for the objective analysis instead of data from the World Ocean Atlas 1994. | 40 |
| 5.1 | Summary of mooring information and mean flow statistics for the 9-year time series. Hernández-Guerra et al. (2003) values for the very first four years of the series are shown in parenthesis. | 64 |
| 5.2 | Frequencies contained in the 9-year time series of the component of the velocity along the direction of maximum variance. | 73 |
| 5.3 | Seasonal, annual and 9-year mean mass transports for NACW (surface-27.3 kg m $^{-3}$; 0-600 m) from 1997 to 2005. | 79 |
| 5.4 | Seasonal, annual and 9-year mean mass transports for AAIW (27.3-27.7 kg m $^{-3}$; 600-1100 m) from 1997 to 2005. | 79 |
| 5.5 | Seasonal, annual and 9-year mean mass transports for MW ($\gamma_n > 27.45 \text{ kg m}^{-3}$; 900-bottom) from 1997 to 2005. | 79 |

CHAPTER 1

General introduction and motivation

This chapter provides an overview of the Earth's climate system, which acts as a heat engine fueled by energy from the Sun. A brief description of the major components of the climate system, i.e. the atmosphere, the hydrosphere, the cryosphere, the geosphere and the biosphere, is given, as well as several examples to illustrate the complex non linear character of this system. We then discuss the importance of the ocean as a regulator of climate through its capacity to store and transport heat, freshwater and radiatively active gases exchanged with the atmosphere. We introduce the upper ocean circulation, the thermohaline circulation and the oceanic eddies, the three principal mechanisms by which the ocean accomplishes energy distribution. The chapter ends by briefly reviewing some climate-related research carried out in the tropical and subtropical Atlantic Ocean, and presenting the issues we tackle in this thesis.

Contents

| | | |
|------------|---|-----------|
| 1.1 | The Earth's climate system | 3 |
| 1.1.1 | Climate vs weather | 3 |
| 1.1.2 | Climate system components | 3 |
| 1.1.3 | The Earth's energy balance | 5 |
| 1.1.4 | The hydrological cycle | 6 |
| 1.2 | The importance of oceans in the Earth's climate system | 7 |
| 1.2.1 | The wind-driven circulation | 8 |
| 1.2.2 | Thermohaline circulation | 10 |
| 1.2.3 | Oceanic eddies | 11 |
| 1.3 | Climate variability and climate change | 12 |
| 1.4 | Thesis objectives and organization | 14 |

1.1 The Earth's climate system

1.1.1 Climate vs weather

The origin of the word climate is traced back to the ancient Greek word "klimat", which means inclination. The Greeks knew that there was a direct association between climate and the inclination of the Sun's rays on the Earth's surface; thus, the larger inclination the colder the climate. This definition, however, is unsatisfactory because local climate is more than a mere time-invariant function of latitude.

Then, what is climate in the modern climatology? The popular phrase "*Climate is what we expect, weather is what we get*", attributed to Robert A. Heinlein, reveals some intrinsic aspects of climate, as well as the differences with the common concept for weather. Definitions given by the Intergovernmental Panel on Climate Change (IPCC) clarify the distinction between them:

- *Weather, as we experience it, is the fluctuating state of the atmosphere around us, characterised by the temperature, wind, precipitation, clouds and other weather elements. This weather is the result of rapidly developing and decaying weather systems such as mid-latitude low and high pressure systems with their associated frontal zones, showers and tropical cyclones. Weather has only limited predictability. Mesoscale convective systems are predictable over a period of hours only; synoptic scale cyclones may be predictable over a period of several days to a week. Beyond a week or two, individual weather systems are unpredictable.*
- *Climate in a narrow sense is usually defined as the average weather, or more rigorously, as the statistical description in terms of the mean and variability of relevant quantities over a period of time ranging from months to thousands or millions of years. The classical period for averaging these variables is 30 years, as defined by the World Meteorological Organization. The relevant quantities are most often surface variables such as temperature, precipitation and wind. Climate in a wider sense is the state, including a statistical description, of the climate system.*

1.1.2 Climate system components

The climate state is determined by the **climate system**, a complex and interactive system consisting of the atmosphere, the hydrosphere, the cryosphere, the land surface and the biosphere, and the interactions between them (see Figure 1.1).

The **atmosphere** is an envelope of gases that surrounds the Earth. It is divided into four layers, being the two lowest, the troposphere (up to 18 km) and the stratosphere (up to 50 km), critical for climate. About 80% of the mass of the atmosphere is contained

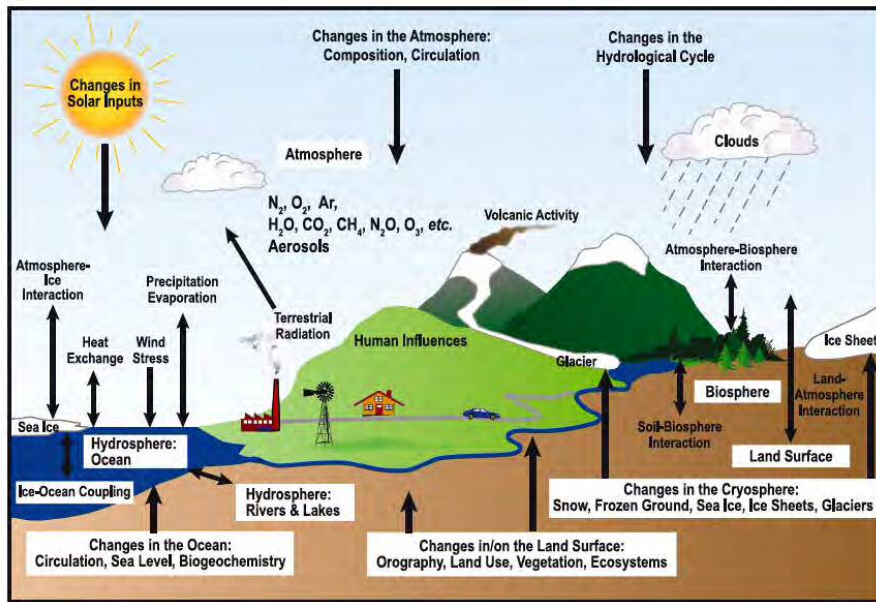


FIGURE 1.1: Schematic view of the components, processes and interactions in the Earth's climate system (Le Treut et al., 2007).

within the troposphere. The atmospheric air is primarily composed of nitrogen (78.08%), oxygen (20.94%) and argon (0.93%). These are the so called constant gases because their concentrations remain virtually constant over space and time. Contrary, the remaining gases are referred to variable gases, among which are the **greenhouse gases** such as water vapor, carbon dioxide, methane, nitrous dioxide and ozone. These components, even though they represent a trace amount of the atmosphere, may have important implications for climate. Unfiltered air samples may contain also trace amounts of dust, pollen and spores, sea spray, volcanic ash, and various industrial pollutants, such as mercury and chlorine, flourine and surfur compounds.

The **hydrosphere** comprises all the liquid water, surface and subterranean, fresh and saline; thus, it includes rivers, lakes, aquifers, oceans and seas. Among them, the oceans are those with the larger spatial coverage, about 70% of the Earth's surface. They transport heat, freshwater and dissolved gases such as carbon dioxide. Due to their heat capacity, the oceans store large amounts of heat acting as regulators of climate (see next section).

The **cryosphere** includes the ice sheets of Greenland and Antarctica, continental glaciers and snow fields, sea ice and permafrost. Its principal impact in the climate system lies on four main aspects: i) its high albedo produces the reflection of much of the solar radiation they receive; without the cryosphere, the global albedo would be considerably lower and, consequently more energy would be absorbed at the Earth's surface leading to higher

temperatures of the atmosphere; ii) it thermally insulates the ocean from the atmosphere and decouples the ocean from direct driving of the wind; iii) it represents the largest Earth's reservoir of freshwater constituting a source of variability in the volume of the oceans and global sea levels. The rate of global average sea-level rise during the 20th century has been estimated to be in the range from 1.0 to 2.0 mm/yr; however, the ice melt contribution is considerably low in comparison with the sea level rise produced by ocean thermal expansion; and iv) the formation of sea ice in polar regions, together with heat loss, increases the surface density and eventually, initiates deep water mass formation and, therefore the thermohaline circulation (see Section 1.2.2).

The **geosphere** consists of all the solid Earth, from the soils, the sediments and rocks of the Earth's land surface, to the continental and oceanic crust and the mantle. A principal role is to control how much energy received from the Sun is returned to the atmosphere. The geosphere is the reservoir in which important compounds and elements for the climate system have the longest residence times. Direct interaction with the atmosphere and the oceans occurs in volcanic eruption and hydrothermal activity. The material and gases transported into the atmosphere during a volcanic eruption can interact with the incoming radiation by reflecting it back and, consequently, reducing the energy available to the climate system. The geosphere defines the geographical boundaries of land, sea and air. Therefore, the roughness of the land also modifies the circulation of the atmosphere and ocean.

The **biosphere** consists of the marine and terrestrial biota. It influences the uptake and release of gases constituent of the atmosphere. The autotrophic biota, through the photosynthesis process, produces oxygen and incorporates significant amounts of carbon dioxide for their growth. In the case of marine phytoplankton, they can also sequester this inorganic carbon pool through sinking to deep oceanic levels, the so called biological pump. Therefore, the biosphere plays a crucial role in the carbon cycle, as well as in the cycling of tracer gases such as methane and nitrous oxide. Methane is produced in anaerobic conditions by bacterial decay and in digestive systems of animals (particularly ruminants), whereas nitrous oxide is a product of aerobic release of nitrogen within soils. The land biota also takes part in the hydrological cycle, for example moderating the rate at which precipitation enters the soil or determining the level of transpiration. It also reduces the atmospheric momentum dragging the wind as it flows through vegetation.

1.1.3 The Earth's energy balance

At the planetary scale, the climate system is driven primarily by the heat energy received from the Sun (Figure 1.2). The incoming solar radiation reaching the top of the Earth's atmosphere averages 342 W m^{-2} , mainly as shortwave radiation. About 30% is reflected back to the space by clouds, aerosols and areas with high albedo like snow, ice and desert. The remaining 70%, approximately 240 W m^{-2} , enters in the climate system; two-thirds are absorbed by the Earth's surface and one-third by the atmosphere. To achieve radiative balance, and maintain the temperature nearly constant through time, the Earth must radiate an

equal amount of energy back to the space. This heat loss occurs through outgoing longwave radiation. If 240 W m^{-2} were reflected back to the space, the Earth's surface would have an average temperature of -19°C , which is much colder than the present temperature. The explanation for this discrepancy lies on the **greenhouse effect**, whose principal basis is that longwave radiation emitted from the surface is trapped by atmospheric trace gases and clouds and then re-emitted to the Earth's surface. This results in an average surface temperature of 14°C , making the Earth habitable.

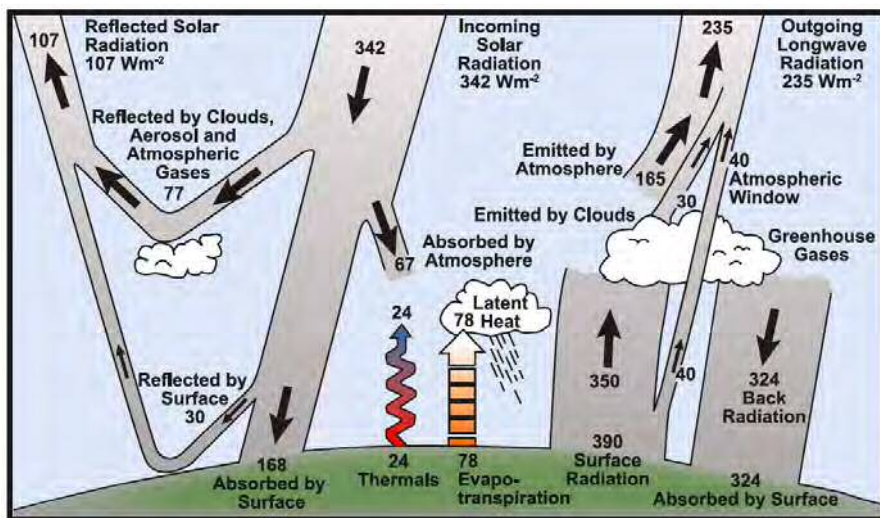


FIGURE 1.2: Earth's annual global energy balance (Le Treut et al., 2007, source: Kiehl and Trenberth (1997)).

Besides solar radiation, there are two other processes that transfer heat within the climate system. The first is *sensible heat*. The Earth's surface warmed by the Sun transfers heat through conduction to the lowermost layer of the atmosphere. The heated (therefore lighter) air then rises, convecting heat upward. The second form is the transfer of *latent heat*. This process involves a change of the water state, either from ice to water or from water to water vapor. The large amount of energy required in this transformation is latent in the water, and subsequently released in the opposite process.

1.1.4 The hydrological cycle

As seen in the previous section, the energy from the Sun drives water movement between the components of the climate system. This global circulation of water (liquid, vapor and ice phases) is called the **hydrological cycle** (see Figure 1.1). The water reserves on Earth are primarily stored in the oceans, glaciers and permanent snow cover and ground water. The

proportion of water in the atmosphere, soil and rivers is comparatively small. Water moves between these reservoirs by processes like evaporation, condensation, precipitation, deposition, runoff, infiltration, sublimation, transpiration and groundwater flow.

1.2 The importance of oceans in the Earth's climate system

Arthur C. Clarke once remarked "*How innapropriate to call this planet Earth when clearly It is ocean*". Indeed, oceans cover about 70% of the Earth's surface. Furthermore, they contain 97% of the free water on Earth and receive 78% of the global precipitation. This gives the ocean a heat capacity larger than any other component of the climate system. Just the top ca. 3 m of the ocean contain as much heat as the global atmosphere.

The response of the Earth's surface to the seasonal cycle of solar heating is a good example of the large heat capacity of the ocean. Landmasses heat (or cool) quickly because they neither store large amounts of heat nor conduct it down rapidly. In contrast, oceans heat (or cool) slowly due to their heat capacity and the mechanical stirring of solar heat by winds in the uppermost ca. 100 m. In other words, the ocean has high resistance to temperature change, i.e. its high thermal inertia implies that relatively small changes in temperature are associated to the gain or lose of large amounts of energy. Therefore, the ocean has a delayed response to non-random atmospheric influences, leading to gradual changes in climate.

Thus, the role of the oceans in the climate system is to store and redistribute heat, as well as freshwater and dissolved gases, providing a temporal memory for climate variations. The central questions are *how and when/where the ocean stores and distributes heat?*

In section 1.1 the global heat budget was explained on an Earth averaged basis. However, the incoming solar radiation and the reflection by the Earth surface vary with latitude. Low latitudes receive more radiation than the poles because of the direct angle of incidence of the solar rays; whereas high latitudes reflect more radiation due to the presence of surfaces with high albedo. As a result there is an excess of heat at low latitudes and a deficit at high latitudes. Hence, the energy balance in the climate system requires a meridional heat transport by the atmospheric and oceanic circulations.

The partitioning of poleward transport between the atmosphere and ocean suggests similar contributions, with the ocean dominating in the tropics and the atmosphere at high latitudes. Thus, a principal interest lies on the ocean mechanisms to distribute heat (and freshwater). Three mechanisms have been suggested to accomplish this task: i) the wind driven circulation, ii) the thermohaline circulation and iii) the oceanic eddies. A brief explanation of each of them is given below.

1.2.1 The wind-driven circulation

As its name suggests, the wind-driven circulation is the upper ocean circulation developed in each ocean basin as the response to the large-scale wind forcing. In fact, if we look at the circulation of low level winds in the atmosphere and the ocean surface currents, we will see the close relationship between them (Figure 1.3). This response may take place through the direct wind drag of the surface layers, moving the surface mixed layer of the ocean, or indirectly via convergence (divergence) of surface waters which escape into (arrive from) the permanent upper thermocline.

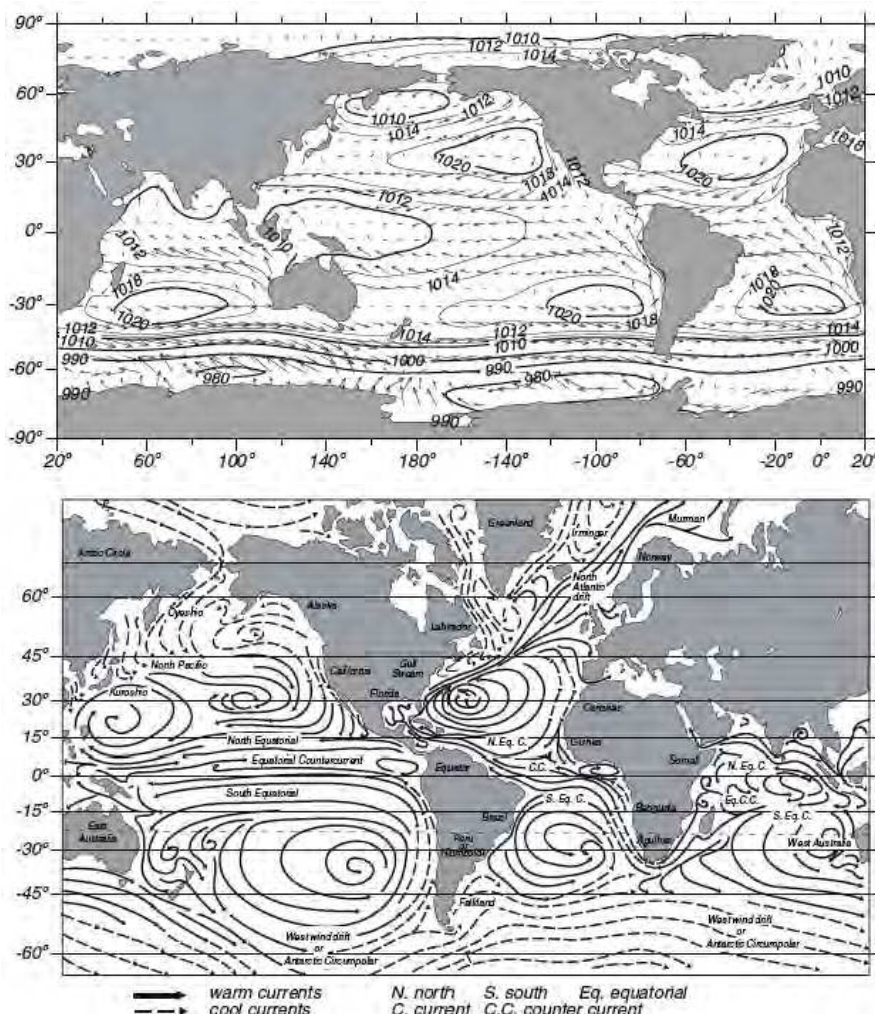


FIGURE 1.3: Maps of the 1989 mean wind velocity and sea level pressure (upper panel) and the ocean surface circulation (lower panel). Source: Stewart (2005).

Ekman (1905) was the first to present a satisfactory mechanical theory of wind-driven currents under the influence of the Earth's rotation. His results showed that the stress exerted by winds, through turbulent transfer of momentum at the ocean surface, leads to a surface current directed at an angle to the right (left) of the prevailing wind direction in the Northern (Southern) Hemisphere. This transport, called **Ekman transport**, is confined to the uppermost 10-100 m of the water column, often referred to as the **Ekman layer**. The Ekman layer is a quantity very difficult to precise, as it depends on hardly known coefficients such as the vertical eddy viscosity, and in practice it is replaced by the surface mixed layer, or the uppermost layer of the ocean which becomes well-mixed because of the input of momentum from the wind. So, it could be said that the direct effect of wind is only felt in the very surface of the ocean. However, how deep does its indirect effect reach?

The anticyclonic winds in the subtropical region results in convergence of Ekman transports, whereas in the subpolar ocean the cyclonic winds results in Ekman transport divergence. Since water can not accumulate or drain indefinitely, a vertical exchange of fluid takes place between the Ekman layer and the interior ocean. Hence, convergent flows induce downwelling or **Ekman pumping** (negative vertical velocities) and divergent flows induce upwelling or **Ekman suction** (positive vertical velocities). Such vertical motions determine the structure and circulation in the permanent thermocline through the Luyten-Pedlosky-Stommel model (Luyten et al., 1983), which combines surface Ekman pumping/suction with an interior thermocline geostrophic flow.

The θ -S properties of the water masses that make up the subtropical thermocline are set by ocean-atmosphere fluxes and subduction, i.e. by the transfer of surface water into the ocean interior. The water mass formation model proposed by Iselin (1939) showed that the structure of the thermocline is set through subduction of surface waters originated at higher latitudes, i.e. the vertical structure of the permanent thermocline reflects the meridional structure of the surface ocean. But it was Henry Stommel (Stommel, 1979) who showed how late winter mixed-layer waters may penetrate into the main thermocline, where they flow along isopycnals. Stommel remarked that during spring and summer waters do no penetrate into the thermocline due to the rapid deepening of the mixed-layer in autumn and winter.

As the water flows out of the surface mixed layer, into the interior ocean, the wind stress no longer has influence and the flow is initially subject to the surface pressure gradients set by the ocean-atmosphere heat exchange. We could imagine the resulting flow as driven by these pressure gradients and simultaneously experiencing the Coriolis force, which redistribute the density field until a steady-state flow is reached where the pressure gradients and the Coriolis force are in **geostrophic balance**. For this to happen the thermocline becomes tilted and the neutrally buoyant water parcels follow these sloping isopycnals, parallel to the local geopotential height contours. The result is a large-scale circular current system around a basin, known as subtropical and subpolar gyres (see Figure 1.3, lower panel). Tropical gyres also experience some of these elements but with significant modifications in the equatorial band, as the Coriolis force tends to zero at the equator.

Subpolar gyres present a cyclonic circulation at high latitudes of the Northern Hemisphere. The North Atlantic subpolar gyre involves the North Atlantic Current, the Irminger Current, the East and West Greenland Currents, and the Labrador Current. In the Southern Hemisphere, where these gyre systems cannot develop because of the absence of constraining continents, westerlies drive the energetic Antarctic Circumpolar Current through which transfers heat and mass between basins.

Subtropical gyres in the Northern and Southern hemispheres rotate in opposite directions approximately centered at 30° latitude. In the North Atlantic subtropical gyre, the Gulf Stream flows from the equator to about $40\text{--}45^{\circ}\text{N}$, where it continues east as the North Atlantic Current. The North Atlantic Current then splits into the Norwegian Current (which flows northeasterly) and the Azores Current which feeds the southward flow of the Canary Current. At approximately 15°N , the Canary Current merges with the North Equatorial Current, closing the gyre.

Western and eastern boundary currents have a very different nature. The western boundary currents (e.g. the Gulf Stream) are generally narrow (<100 km), deep (2 km) and intense, moving poleward up to 150-200 Sv of relatively warm waters at an average speed of about 1 m s^{-1} . On the other hand, the eastern boundary currents (e.g. the Canary Current) are broad (1000 km) and shallow (500 m), and relatively slow flows, transporting equatorward about 10-15 Sv of relatively cold waters at an average speed of $0.05\text{--}0.1 \text{ m s}^{-1}$. A special feature in eastern boundary currents is the presence of **coastal upwelling**. This process occurs when Ekman transport draws surface waters away from the coast which are then replaced by cold and nutrient-rich subsurface waters.

1.2.2 Thermohaline circulation

In addition to wind-driven circulation, the ocean exhibits the **thermohaline circulation**, a large-scale ocean circulation driven by changes in the sea water density arising from temperature (thermal) or salt (haline) effects. Intense heat loss and salt rejection during sea ice formation rise the density of the winter mixed layer waters in the high-latitude North Atlantic and Southern oceans. As a result the cold dense waters sink to form the deep and bottom waters which spread throughout the global ocean. Volume conservation in the North Atlantic requires a balance between the flow of cold deep waters towards the equator and the warm poleward flow in the thermocline.

The coupling of the surface and deep large-scale circulations is known as the **meridional overturning circulation** (Figure 1.4). Some 15 ± 12 Sv of North Atlantic Deep Water (NADW), produced in the northern North Atlantic Ocean, move southward along the American continental slope entraining Antarctic Intermediate Water (AAIW) and Antarctic Bottom Water (AABW) to reach a volume of 23 ± 12 Sv at 30°S . In the Southern Ocean, the deep water formation amounts to 21 ± 6 Sv of Circumpolar Deep Water (CDW), which approximately occupies the depth range of the lower NADW (Ganachaud and Wunsch,

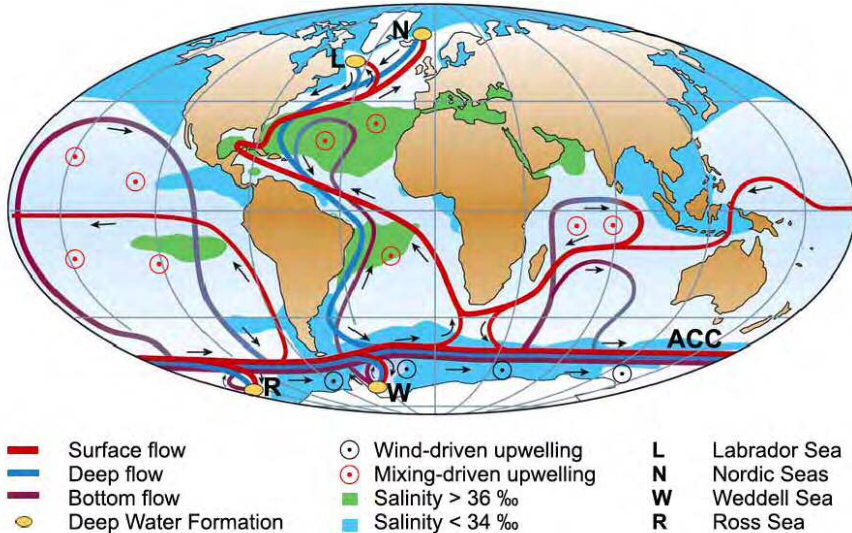


FIGURE 1.4: Simplified sketch of the global overturning circulation (from Kuhlbrodt et al. (2007)). Surface waters (red lines) flow towards the three main deep-water formation regions (yellow ovals) located in the northern North Atlantic, the Ross Sea and the Weddell Sea, where they initiate their recirculation as deep waters (blue lines) and bottom waters (purple lines).

2000). The NADW enters into the lower cell of the Southern Ocean and it is mixed with Antarctic waters to form denser bottom waters. Some AABW, including recently converted NADW, enters to the Indian and Pacific basins as the Circumpolar Deep Water (CDW) and/or modified NADW (Lumpkin and Speer, 2007). During their voyage, the inflows into the Indian and Pacific basins eventually upwell to form part of the wind driven circulation and eventually feed the shallow waters around Antarctica or follow, as near-surface currents, their trip back to the starting point in the northern North Atlantic. One cycle of this circuit takes about a thousand years. This implies that the involved water masses, which were isolated from the atmospheric influence at their formation time, sequester heat during such time. Therefore, variations in the operation of the global meridional overturning circulation may cause significant changes in the climate system.

1.2.3 Oceanic eddies

The oceanic eddies also play a substantial role in transporting heat and other climatically important properties. Although their global contribution is apparently small, it has been determined to be significant in western boundary currents, equatorial regions and the Antarctic Circumpolar Current. These currents become unstable, either by baroclinic or barotropic

processes, leading to the formation of meanders. As a meander grows it may eventually detach and form a **ring**. The meandering flow of the Gulf Stream results in the formation of two types of rings: cold-core rings (cyclonic eddies), made up of northern cold waters which detach into the warm southern side of the stream, and warm-core eddies (anticyclonic eddies), which bring southern warm waters across the current into the northern regions (see Figure 1.5). The movement of the rings formed north of the Gulf Stream is quite limited and they usually rejoin the main current; however, cold-core rings cover the Sargasso Sea.

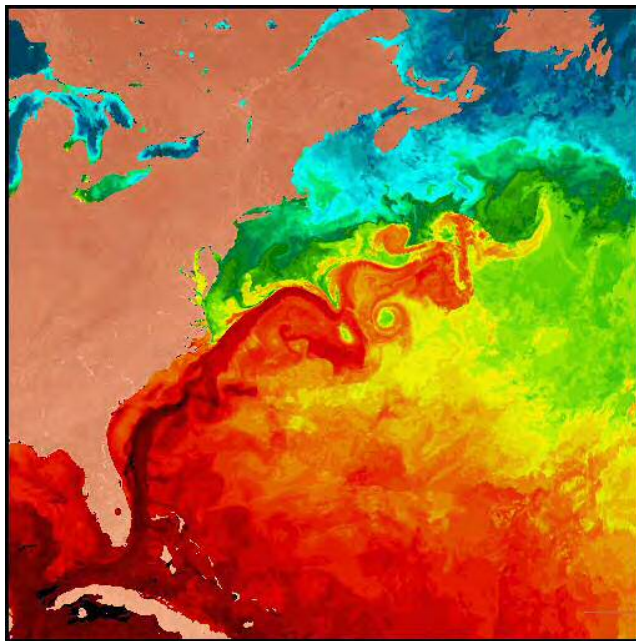


FIGURE 1.5: Sea surface temperature image of the Gulf Stream current swirling warm-core and cold-core rings north and south of its mean path.

1.3 Climate variability and climate change

The complexity of the climate system is such that the Earth's climate is continually evolving and, therefore, varying over multiple time and spatial scales (from weeks to millennia, and from regional to global scales). At this point, it is important to differentiate between **climate variability** and **climate change** (IPCC):

Climate variability refers to variations in the mean state and other statistics (such as standard deviations, the occurrence of extremes, etc.) of the climate on all spatial and temporal scales beyond that of individual weather events.

Climate change refers to a change in the state of the climate that can be identified (e.g., by using statistical tests) by changes in the mean and/or the variability of its properties, and that persists for an extended period, typically decades or longer.

Climate variability and change may result either because of alterations within the climate system, in its components and/or interactions, or from variations in natural or anthropogenic external forcing. Examples of external forcing include variations in solar radiation, in volcanic activity or in the amount of greenhouse gases caused by human activities. The response of the climate to these forcings is rather complex due to the non-linear interactions between components and feedbacks. A process is called **feedback** when it changes the sensitivity of the climate; therefore, it intensifies (positive feedback) or reduces (negative feedback) the climate response for a given forcing. For example, an important feedback mechanism is the water vapor feedback: as the Earth warms, evaporation increases leading to raised levels of water vapor in the atmosphere, which in turn amplify this warming through trapping of more radiation.

This thesis, as many studies on climate-change detection, deals with the identification of variability and trends in climate and the ascription of these changes to the causative mechanisms. This task requires long-term quality observations with sufficient spatial coverage. For example, ocean temperature and salinity are sensitive indicators for detecting climate variability and change, but available records are relatively short and spatially sparse. Despite this handicap, the great advances made in understanding oceanic climate have shown that the initial assumption of an steady-state ocean is wrong.

Chapter 5 of the IPCC Fourth Assessment Report (AR4), published in 2007 (Bindoff et al., 2007), concludes that the global ocean mean temperature has been increasing since 1961 in the 0-3000 m layer, leading to an increase in the ocean heat content much larger than any other component of the Earth climate system. Additionally to temperature changes, long-term salinity trends are characterized by a freshening in high latitude regions and increased salinity in more evaporative regions. Several observations support these results for the Atlantic ocean. In fact, inspection of the heat content time series for individual ocean basins point to the North Atlantic as a major contributor to such increase (Levitus et al., 2005).

Examination of repeated hydrographic sections have revealed the characteristics of temperature and salinity anomalies over the tropical and subtropical North Atlantic. Much of our knowledge on subtropical variability comes from the analysis along 24.5°N, the most surveyed transoceanic section in the world. The initial studies of Roemmich and Wunsch (1984) indicated warming of intermediate waters and cooling at deeper levels for the period 1957-1981. Subsequently, Parrilla et al. (1994) found that warming had continued until 1992 at a maximum rate of 1°C/century at 1100 db. For the 1992-2002 period, Vargas-Yáñez et al. (2004) reported a higher warming trend (2.7°C/century) for the eastern basin thermocline. The study of the 24.5°N section was finally extended by Cunningham and Alderson (2007), who concluded that waters shallower than 1750 db have been warming and saltening since at least 1981, leading to significantly warmer and saltier waters in 2004 than at any time since 1957. They also pointed that the warming in the western Atlantic thermocline since 1957,

at a rate of $1.11^{\circ}\text{C}/\text{century}$, dominated the transatlantic average. Decomposition of isobaric changes into water mass changes and changes due to the displacements of the isopycnals, have shown that this warming trend is the result of both contributions (Bryden et al., 1996; Arbic and Owens, 2001). Joyce and Robbins (1996) and Joyce et al. (1999) also found a warming trend since the late 1950's at Bermuda and along 52° and 66°W in the western North Atlantic.

In the tropical Atlantic, Arhan et al. (1998) found a similar pattern of change along 7.5°N . A comparison of the 1993 and IGY surveys revealed net warming of the intermediate and upper deep waters (maximum basin-averaged rate of $0.4^{\circ}\text{C}/\text{century}$ between 1000 and 2000 m) and cooling ($< 0.008^{\circ}\text{C}/\text{decade}$) of the deepest waters. Analysis of a section made in 2000 at a nominal latitude of 6.5°N , within the framework of the World Ocean Russian Federal Program, showed that the temperature continued increasing in the whole water column of the eastern basin especially at intermediate levels ($0.117^{\circ}\text{C}/\text{decade}$) (Sarafanov et al., 2007).

1.4 Thesis objectives and organization

This thesis aims at examining the recent response of the North Atlantic Ocean to climate variations on different spatial scales, and to explore the possible mechanisms causing the observed changes. Specifically, we have addressed the following research questions:

- *Have the temperature and salinity trends observed in the tropical (7.5°N) and subtropical (24.5°N) Atlantic continued or have they reversed?*
- *Have regional changes, in terms of thermohaline structure and circulation, occurred in the Canary basin during the last decade?*
- *How well do the gyre-scale and the regional-scale changes agree?*
- *What are the mechanisms responsible for the observed changes?*
- *What is the potential role of the Canary upwelling system as a buffer zone?*

To cope with these questions the thesis is divided into three parts:

- **Part I** (Chapters 2 and 3) focuses on the temperature and salinity interdecadal variability over the tropical and subtropical North Atlantic ocean since 1950's.

In **Chapter 2**, the temporal evolution between 1957 and 2010 of the water mass properties along the 7.5°N section is presented. In order to elucidate the controlling mechanisms, changes on isobaric surfaces are decomposed into changes on isoneutral surfaces and changes due to the vertical movement of the isoneutrals (Bindoff and McDougall, 1994).

In **Chapter 3**, an analysis similar to that used in Chapter 2 is performed for five repeated hydrographic sections across 24.5°N. Additionally, Argo data are used to corroborate the latest temperature and salinity tendencies presented within the subtropical waters.

- **Part II** (Chapters 4 and 5) concentrates on the variability of the water masses and circulation patterns in the Canary region during the last decade.

In **Chapter 4**, temperature and salinity variations are assessed on a section carried out in 1997 and 2006 north of the Canary Islands. Observed changes are interpreted in terms of variations in atmospheric forcing at the water mass source region, namely, variations in surface heat flux, surface evaporation minus precipitation or wind stress curl.

In **Chapter 5**, the mean transport of the eastern boundary of the North Atlantic subtropical gyre, and its seasonal and interannual variability, are determined based on a current-meter time series in the Lanzarote Passage.

- **Part III**

In **Chapter 6**, we present novel results from a univariate spatial objective analysis of high-resolution hydrographic data collected in the coastal transition zone off NW Africa. Three dynamically different regions are identified: the upwelling region, the frontal system and the offshore region. For each region we characterise the main dynamic elements, assess the different contributions to vertical motion in each of them (diapycnal, quasi-geostrophic vertical, and wind-induced vertical velocities) and compare these vertical motions with the near-surface fluorescence field.

Finally, **Chapter 7** collects the major conclusions of this thesis work and some suggestions for future research directions. A thesis summary written in Spanish is given in **Chapter 8**.

Part I

Tropical and Subtropical North Atlantic

CHAPTER 2

Decadal changes in the tropical Atlantic along the 7.5°N section

Verónica Benítez-Barrios¹, José Luis Pelegrí¹, Mikhail Emilianov¹, Eugenio Fraile-Nuez², Alonso Hernández-Guerra³, Jesús Peña-Izquierdo¹ and Miquel Rosell-Fieschi¹

¹ Institut de Ciències del Mar (CSIC), Barcelona, Spain.

² Instituto Español de Oceanografía, Centro Oceanográfico de Canarias, Santa Cruz de Tenerife, Spain.

³ Universidad de Las Palmas de Gran Canaria, Las Palmas, Spain.

Abstract

The transatlantic hydrographic section along 7.5°N is of great interest for climate studies as it represents a crucial region of the global overturning cell. It has been previously surveyed twice, during the 1957 International Geophysical Year and during 1993 as part of the World Ocean Circulation Experiment program under the denomination of A06 line. Comparison of these early realizations revealed moderate warming of the upper-thermocline and intermediate/upper-deep waters, and weak cooling of the bottom water. A third occupation of this section, during spring 2010, allows us to update the long-term hydrographic variations in the tropical water masses. As compared with 1993 the upper-thermocline and, to a lesser degree, the intermediate waters have continued warming and salinifying, and a clear signal of warmed and salty bottom waters has reached the western basin. Temperature and salinity changes at constant pressures are partitioned into changes on neutral surfaces and changes due to the vertical movement of the isoneutrals. Grossly speaking, advective changes dominate the intermediate layers while vertical motions are more significant in the permanent thermocline and deep/bottom waters.

KEYWORDS: WOCE A06 line, tropical Atlantic Ocean, ocean variability

In preparation.

Contents

| | | |
|------------|-------------------------------|-----------|
| 2.1 | Introduction | 21 |
| 2.2 | Data and methods | 21 |
| 2.3 | Results and discussion | 22 |
| 2.4 | Conclusions | 27 |

2.1 Introduction

The first transatlantic section in the tropical region of the North Atlantic Ocean, nominally at 8.25°N , was measured in May 1957 as part of the International Geophysical Year. Under the name of A06 line, an approximate reoccupation of this section along 7.5°N was conducted in February 1993 as a contribution to the World Ocean Circulation Experiment (see Figure 2.1). Comparison of the 1993 and 1957 surveys revealed a net warming of the intermediate and upper deep waters (maximum basin-averaged rate of $0.04^{\circ}\text{C}/\text{decade}$ between 1000 and 2000 m) and cooling ($< 0.008^{\circ}\text{C}/\text{decade}$) of the deeper waters (Arhan et al., 1998). In April-May 2010, as part of the Memoria Oceánica del Clima (MOC) project, the 7.5°N transatlantic section was repeated for the third time. In view of the previous results, here we concentrate on examining the temporal evolution of the water mass properties and its controlling mechanisms from 1957 to present.

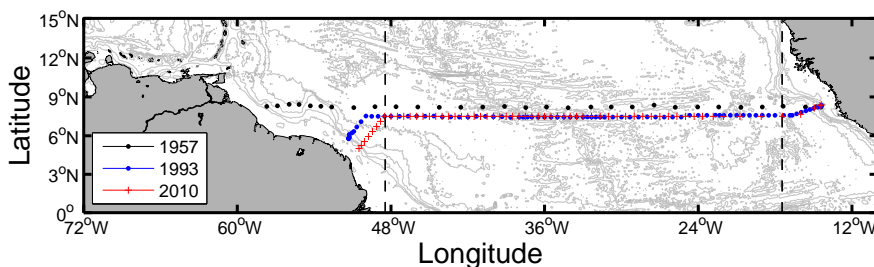


FIGURE 2.1: Location of stations occupied during the IGY in 1957 (black dots), the WOCE A06 line in 1993 (blue dots) and its revisit in 2010 under the MOC project (red crosses).

2.2 Data and methods

This study is based on the potential temperature (θ) and salinity (S) profiles obtained during the repeated sections along 7.5°N in 1957, 1993 and 2010. Because of differences in vertical and horizontal resolutions of the sampling, hydrographic data were linearly interpolated onto a common grid consisting of 300 vertical levels from 10 to 6000 db and from 48.45°W to 17.45°W at 0.5° intervals. The accuracy of temperature and salinity measurements for the 1957 cruise was reported as 0.1°C and 0.01, respectively (Fuglister, 1960). For the two more recent cruises the accuracy improves to 0.002°C and 0.002, although the results here presented we have not yet applied the salinity corrections available from the onboard Autosal (typically of the same order as the above accuracy).

Distinction of the mechanisms responsible of the observed changes is performed through the Bindoff and McDougall (1994) model, which states that changes in potential temperature and salinity on isobars can be decomposed into changes on neutral surfaces (Jackett and McDougall, 1997) and changes due to the vertical displacements of isoneutrals, referred to as heaving. Given the basin-dependent behaviour, the profiles of zonally averaged differences are computed east and west of the Mid Atlantic Ridge, approximately located at 32°W.

2.3 Results and discussion

Figure 2.2 shows the temperature and salinity differences on pressure surfaces when the 1993 values are subtracted from the 2010 data. Within the thermocline (the upper 1000 db), temperature and salinity differences are very large (up to $\pm 9^{\circ}\text{C}$) with alternating sign at scales of 3 degrees in longitude, especially in the west basin. Below 1000 db and extending to the bottom, there has been a near-uniform weak warming (about 0.05°C) along the section, except between 40°W and 45°W. Salinity follows a similar pattern in the thermocline and intermediate waters while the upper deep waters appear more patchy, with small values of alternating sign. Near bottom, in the western margin and close to the Mid-Atlantic Ridge, we find significant warming and salinification.

When averaged along isobars (side partition in Figure 2.2), the temperature difference between 1993 and 2010 (red line) shows the presence of warming through the water column. The most significant difference below the thermocline, on the basis of 95% confidence intervals, occurs near 4500 db with a maximum rate of $0.009^{\circ}\text{C}/\text{decade}$. This implies that the cooling trend between 1957 and 1993 (blue line) previously reported by Arhan et al. (1998) in the deep water column (> 3000 db) has been reversed over the past 17 years. However, the recent warming did not offset the preceding cooling leading to a net cooling in the 3000-4000 db pressure range (black line). The zonally-averaged salinity difference indicates a similar pattern of change as temperature, with maximum salinifying values in the permanent thermocline, and substantially large values in the intermediate and deep waters. A local maximum salinification of $0.0008/\text{decade}$ is found near 4500 db. However, for the 1993-2010 time period, waters from roughly 2000 to 4000 db present no significant salinity change on isobars.

The decomposition of the total temperature and salinity changes at a constant pressure level into changes along neutral surfaces (referred to as advective variations, θ_n and S_n) and changes due to the vertical displacements of isoneutrals (referred to as heaving, $-N\theta_z$ and $-NS_z$, where $N = dz/dt$ at constant neutral density), is used to diagnose variations in the outcropping region and, therefore, the forcing mechanisms of the observed changes.

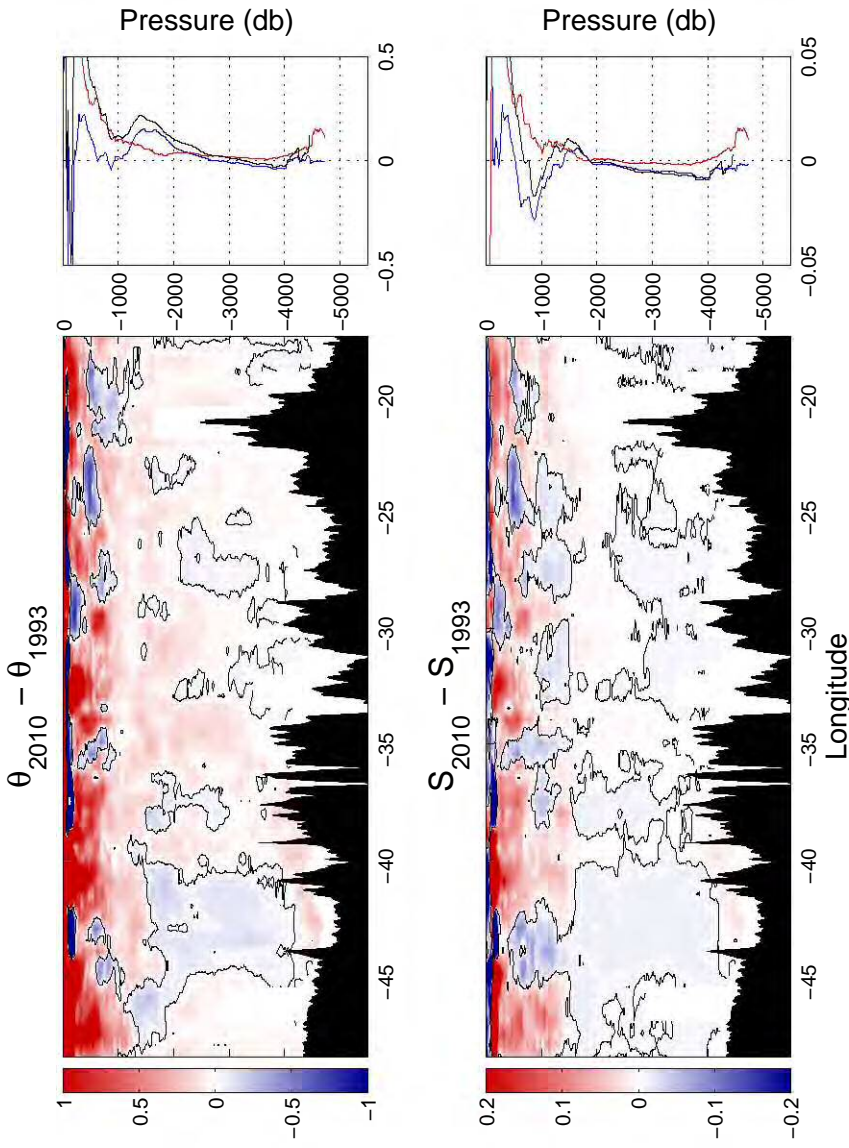


FIGURE 2.2: Potential temperature and salinity change on isobars between 2010 and 1993 sections. Red colors denote increasing property. The side partitions correspond to the zonally averaged changes for the periods 1957-1993 (blue line), 1993-2010 (red line) and 1957-2010 (black line).

Figure 2.3 display the isobaric temperature and salinity changes between 1993 and 2010, as well as each individual contribution (advection and heaving) and their sum. The sum of both contributions, for both the east and west basins fits well the original signal, therefore indicating that a succesful decomposition has been done.

In the western basin (left panels), the permanent thermocline increase of temperature and salinity at constant pressure is dominated by downward heave. The neutral surfaces were depressed 10-70 db between 100 and 1000 db, resulting in maximum rates of warming and salinification of $1.3164^{\circ}\text{C}/\text{decade}$ and $0.1506^{\circ}/\text{decade}$, respectively, at 150 db. Such variations have been previously attributed to oscillations, see review in Arhan et al. (1998). However, changes along isoneutrals surfaces have also contributed to the thermocline changes. At intermediate levels, there has been a pressure-averaged warming and salinification of $0.0524^{\circ}\text{C}/\text{decade}$ and $0.0098^{\circ}/\text{decade}$ in the Antarctic Intermediate Water (AAIW) and Upper Circumpolar Water (UCPW). In the deep water column (between 2000 and 4000 db), the North Atlantic Deep Water (NADW) underwent a warming of $0.0140^{\circ}\text{C}/\text{decade}$ on isobars mainly due to isoneutral displacements at a rate of 28.96 db/decade, with a minor offsetting from the water mass changes. Salinity changes in this pressure range were of order of its accuracy measurement. The abyssal layers show a warming and salinification of $0.0587^{\circ}\text{C}/\text{decade}$ and $0.0056^{\circ}/\text{decade}$ within the Antarctic Bottom Water (AABW), caused by an isoneutral deepening up to 165 db over the past two decades.

For the eastern basin (right panels) the upper warming and salinification due to heaving of isoneutrals affect only the first 500 db with moderate intensity (maximum rates of $0.1458^{\circ}\text{C}/\text{decade}$ and $0.0192^{\circ}/\text{decade}$). Within the 500-2000 db pressure range, occupied by the intermediate waters and the uNADW, the average temperature change is $0.0583^{\circ}\text{C}/\text{decade}$, partitioned approximately equal between changes along isoneutrals of $0.0236^{\circ}\text{C}/\text{decade}$ and changes due to the deepening of isoneutrals of $0.0336^{\circ}\text{C}/\text{decade}$. In contrast, the salinity changes associated to heaving cause freshening, significant but uncapable of offsetting the $0.0004/\text{decade}$ rate of salinification caused by flow along isoneutrals. Below 2500 db, at the mNADW-INADW levels, the temperature increased by $0.0095^{\circ}\text{C}/\text{decade}$ on constant pressure surfaces caused by heaving, whereas the salinity changes were again comparable to the measurement accuracy.

Figure 2.4 display the components of the isobaric changes between 1957 and 2010. The decomposition for both basins is similar to that observed for the 1993-2010 period. The only difference is the cooling in the waters deeper than 3000 db of the eastern basin, apparently as the result of an increasing importance of water mass changes.

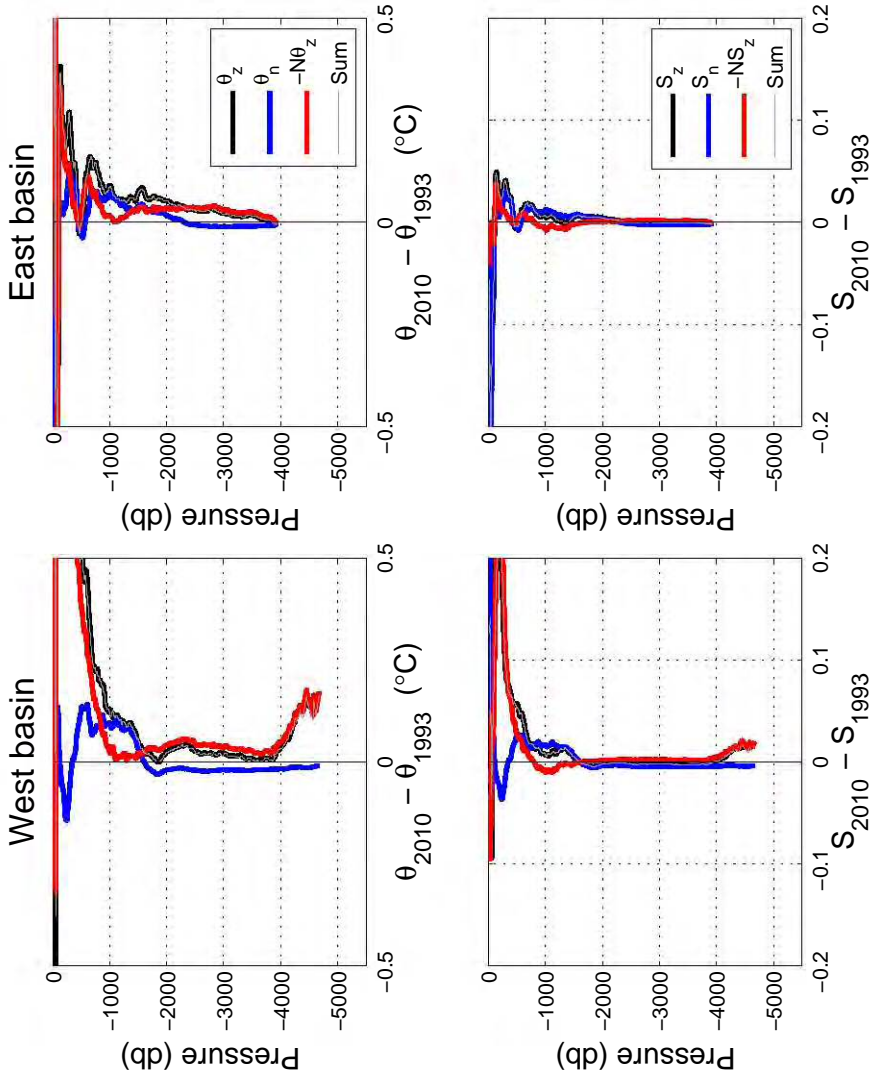


FIGURE 2.3: Decomposition of temperature and salinity changes at constant pressure (black line) into changes along neutral surfaces (blue line) and change due to heaving (red line) for the period 1993-2010. The grey line denotes the sum of both components. Terms are zonally averaged for the western basin (48.45°W - 32°W) and the eastern basin (32°W - 17.45°W).

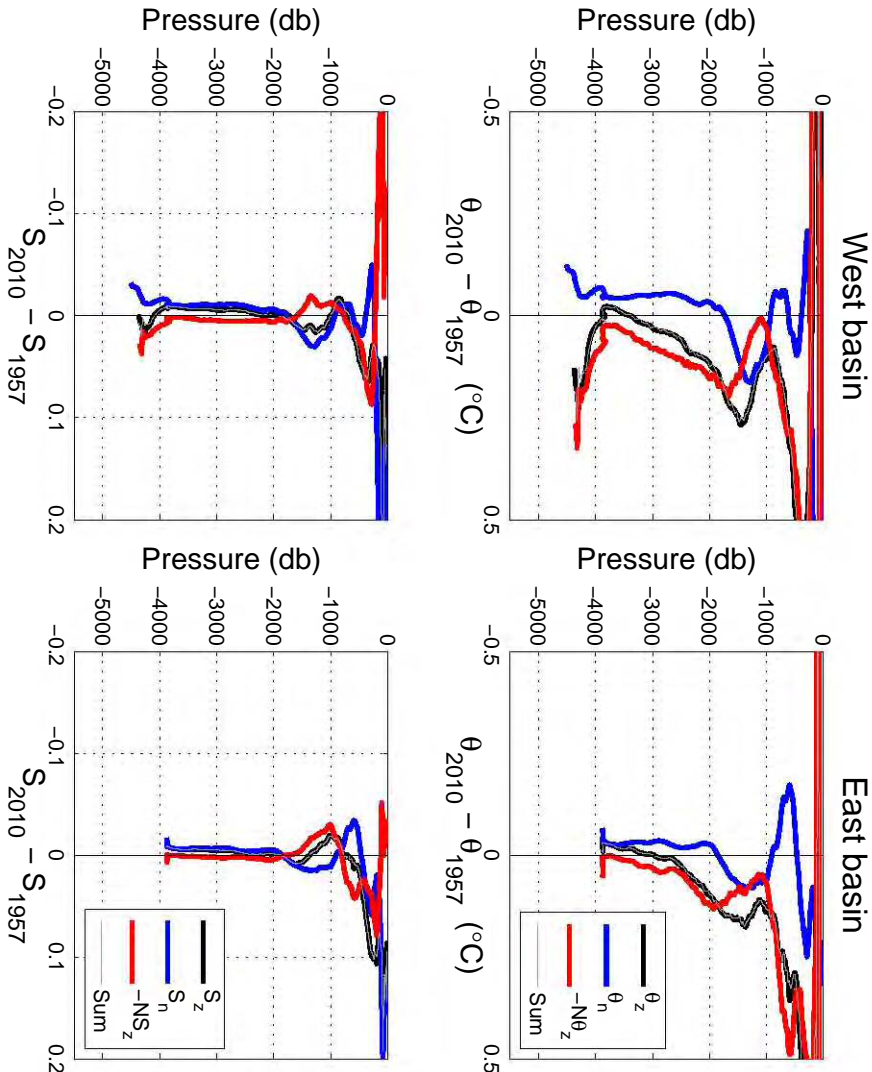


FIGURE 2.4: As for Figure 2.3 but for the period 1957-2010.

2.4 Conclusions

We have shown that the Atlantic tropical waters along 7.5°N have continued warming since 1993 over the entire water column but especially intense within the thermocline, intermediate and bottom waters. These same layers have experienced salinification but, in contrast, the pressure range between 2000 and 4000 db has remained approximately invariant.

Although water mass changes were important at intermediate levels, the observed changes were dominated by the vertical displacements of the isoneutrals. The greatest variation below the thermocline is found in the AABW which forms the abyssal waters of the western basin. A study of the AABW variability pointed at the synchrony of the AABW temperature trends with a quasi-annual transport cycle (Hall et al., 1997). Thus, further work is needed to verify whether we are looking at interannual or annual oscillations. The consistency of the physical properties changes along 7.5°N and 24.5°N (see for example Vélez-Belchí et al., 2010), presumably due to the meridional propagation of the anomalies, allows us to predict the observation of warming of AABW in a future revisit of the 24.5°N section.

CHAPTER 3

Changes in temperature and salinity tendencies of the upper subtropical North Atlantic ocean at 24.5°N

Pedro Vélez-Belchi¹, Alonso Hernández-Guerra², Eugenio Fraile-Nuez¹, and Verónica Benítez-Barrios²

¹ Instituto Español de Oceanografía, Centro Oceanográfico de Canarias, Santa Cruz de Tenerife, Spain.

² Facultad de Ciencias del Mar, Universidad de Las Palmas de Gran Canaria, Las Palmas, Spain.

Abstract

Strong interest in multi-decadal changes in ocean temperature and heat transport has resulted in the occupation of the North Atlantic hydrographic transect along 24.5°N five times since 1957, more than any other transoceanic section in the world. This latitude is chosen since it is where the northward ocean transport of heat in the Atlantic reaches its maximum. An analysis of the five oceanographic cruises at this latitude shows that there has been a significant cooling of -0.15°C in the upper ocean (600-1800 dbar range) over the last seven years, from 1998 to 2004. In contrast to the warming of 0.27°C observed from 1957 to 1998. Salinity shows a similar change in tendency, with freshening since 1998. For the upper ocean at 24.5°N, 1998 was the warmest and saltiest year since 1957. Data from the Argo network are used to corroborate the strong cooling and freshening since 1998, showing a -0.13°C cooling in the period between 1998 to 2006, and revealing interannual variability between 2005 and 2008 to be much smaller than the decadal variability estimated using the transect. The results also demonstrate that Argo is an invaluable tool for observing the oscillations in the tendencies of the ocean.

KEYWORDS: Temperature, Salinity, North Atlantic Ocean, Ship observations, Multidecadal variability

Journal of Physical Oceanography, volume 40, 2546–2555, doi: 10.1175/2010JPO4410.1, 2010.

Contents

| | | |
|------------|------------------------------------|-----------|
| 3.1 | Introduction | 31 |
| 3.2 | Data and methods | 32 |
| 3.3 | Results | 35 |
| 3.3.1 | Basin-wide changes | 35 |
| 3.3.2 | Zonally averaged changes | 37 |
| 3.3.3 | Isobaric change decomposition | 40 |
| 3.3.4 | Annual and interannual variability | 42 |
| 3.4 | Discussion and conclusions | 43 |

3.1 Introduction

The Atlantic Meridional Overturning Circulation contributes to the moderation of climate in Europe through the northward transport of 25% of the global heat flux, which is maximum (1.5 PW) at around 24.5°N (Lavín et al., 2003). Consequently, transatlantic oceanographic sections at this latitude have become a benchmark for monitoring long-term changes in temperature in the Atlantic (Parrilla et al., 1994), and to study the nature and causes of climate change (Bindoff et al., 2007).

The first oceanographic section across the North Atlantic subtropical gyre at 24.5°N was carried out during the 1957 International Geophysical Year (IGY) (Fuglister, 1960). Since then, four additional occupations have been carried out: one in 1981 (Roemmich and Wunsch, 1985); two during the World Ocean Circulation Experiment (WOCE), in 1992 Parrilla et al. (1994) and 1998 (Baringer and Molinari, 1999); and finally one in 2004 (Cunningham and Alderson, 2007).

Examination of these hydrographic sections over the subtropical North Atlantic Ocean reveals that in 1992 the subtropical Atlantic along 24.5°N was warming at 0.65°C/century, with a maximum of 1°C/century in the intermediate waters at 1100 dbar, between 1981 and 1992 (Parrilla et al., 1994). For the 2002-1992 period this warming was higher (2.7°C/century) in the eastern basin thermocline (Vargas-Yáñez et al., 2004). According to Cunningham and Alderson (2007), who focused on the differences between the western (65°W-75°W) and the eastern (25°W-35°W) basins, the warming in the western Atlantic thermocline since 1957, at a rate of 1.11°C/century, dominated the transatlantic average, while deep water cooled and freshened. These authors concluded that waters shallower than 1750 dbar had been warming and salterning since at least 1981, and that in 2004 were significantly warmer and saltier than at any time since 1957.

From 1957 to 1981, the observed warming and increase in salinity was principally due to the downward heave of isopycnals, while from 1981 to 1992 it was dominated by changes in water mass characteristics (Bryden et al., 1996). The analyses of the 1992 and 2004 sections also indicated that upper ocean changes dominate over deep ocean changes (Parrilla et al., 1994; Cunningham and Alderson, 2007).

In addition to these five oceanographic sections, the global array of temperature/salinity free-drifting profiling floats, known as Argo, provides continuous monitoring of temperature and salinity in the upper 2000 dbar at regular 10-day intervals (Team, 1998). These data are made publicly available within hours of their collection. Argo has evolved to the point that the goal of 3000 free-drifting profiling floats has been recently achieved.

This paper reports that, on average, waters shallower than 2000 dbar across 24.5°N have cooled and freshened between 1998 and 2006. These results were obtained using two independent data sets: the repeated ocean cruises described above and the Argo network at its full capacity of large spatial and temporal coverage. The results also confirm the usefulness of the Argo network to study long-term variability in ocean properties and to permit basin-wide views of the changes. The remainder of the paper is organized as follows: in section 2 the data set and methods are described. Section 3 shows the results found in the comparison of the hydrographic sections and the Argo data, and finally in section 4 the results are discussed and the conclusions presented.

3.2 Data and methods

Each of the five hydrographic sections extends from the African continental shelf to the Bahamas. However, while the 1957 and 1992 sections follow the 24.5°N parallel over the entire Atlantic, the 1981, 1998 and 2004 sections angle south-westward from the African continental shelf at about 28°N to reach the target latitude at around 23°W and again angle north-westward at about 70°W to continue the section along 26.5°N (Figure 3.1a). As a result, up to 2° differences in the latitudes of the sections may be found west of 70°W and east of 23°W.

The five transatlantic sections also differ in the details of their sampling scheme. The 1957 section consisted of 38 stations, with a mean distance between stations of 230 km, and was sampled with Nansen bottles at 25 depth levels; the 1981 section was carried out with continuous CTD measurements for 90 profiles with a mean spatial resolution of 79 km; and finally, the 1992, 1998 and 2004 sections were carried out with continuous CTD measurements at a similar distance between stations, around 70 km.

In order to compare the five hydrographic sections in the longitude range at 24.5°N that was effectively sampled during the five occupations, only the CTD casts between 23°W and 70°W are used. This avoids comparison of sampling at different latitudes over the African and Bahamas continental shelves, where there are up to 2 degrees difference in latitude between the different sections. Additionally, and given the different sampling grid for each trans-oceanic section, temperature and salinity data from each survey have been linearly interpolated to 101 pressure levels between the surface and 2000 dbar, and bilinearly each 0.5 degrees in longitude. The use of other interpolating yields the same results.

All available good quality Argo data in the North Atlantic between January 2003 and December 2008 are used. The Argo data system (Team, 2002) provides real-time quality control and delayed mode quality control, when available. Additionally, the

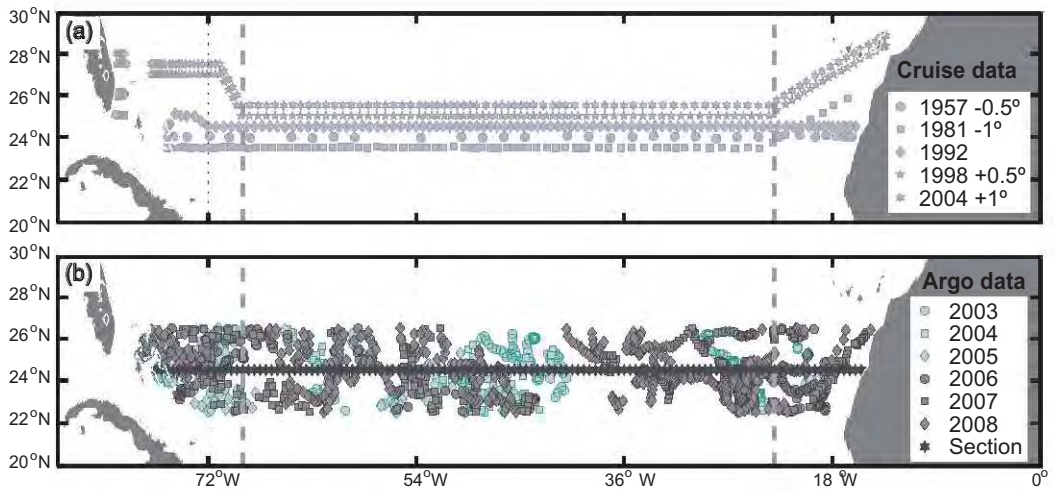


FIGURE 3.1: a) Positions of the CTD stations from the repeated hydrographic sections sampled across 24.5°N in 1957 (IGY), 1981, during WOCE in 1992 (A05) and in 1998 (AR01), and finally in 2004. To avoid overlapping between each section, a latitude offset has been added to each section, as indicated in the legend. (b) Locations of each Argo profile in the period between January 2003 and December 2008 used in this study. The 2006 Argo zonal ‘synthetic’ section obtained is also shown. The gray lines at 23°W and 70°W bound the longitude range where the Atlantic was effectively sampled at 24.5°N during the five occupations.

data passed a more stringent quality control procedure developed by the present authors. This quality control includes visual inspection of all the temperature and salinity profiles used, comparing them with their neighboring profiles by means of objective analysis. All floats with suspicious profiles either in temperature or salinity were inspected individually. Those profiles from floats with suspicious behavior, or on the Argo graylist (Team, 2002), have been excluded from the data. As a result, only 2048 from an initial set of 2411 profiles within the region of interest (80°W–8°W, and 20°N–40°N) are used (Figure 3.1b). The data were initially downloaded in May 2009, but similar results are obtained with data downloaded in March 2010, demonstrating the robustness of the method.

After our quality control step, the Argo data were objectively interpolated onto a hypothetical zonal ‘section’ at 24.5°N, using an updated version of the method of optimal statistical interpolation employed previously by Fraile-Nuez and Hernández-Guerra (2006). This statistical approach is commonly used to obtain climatological fields since it is designed to minimize the noise-to-signal ratio. Noise is defined as any non-resolved scale, and in transoceanic sections it is mainly attributed to eddies

(Gomis and Pedder, 2005; Pedder, 1993). For the objectively interpolated temperature and salinity fields, the annual climatological temperature and salinity data from the World Ocean Atlas 1994 (Levitus et al., 1994a; Levitus and Boyer, 1994b) are used as a first guess to ensure that the anomaly field (data minus climatology) is a stationary, zero-mean random function of the location. A sensitivity study using the annual climatological temperature and salinity fields from the World Ocean Atlas 2005 (Levitus, 2006) as a first guess yielded similar results, as described in the next section. However, the analysis carried out with the first guess obtained from the World Ocean Atlas 1994, which does not include the 2004 CTD data, ensures the independence of the Argo synthetic section from the 2004 CTD data.

The large amount of data and the 6-year span of the observations allow the ocean ‘eddy’ noise, always present in single hydrographic sections, to be greatly reduced. In this sense, the synthetic Argo section is less affected by eddy noise than the hydrographic sections at 24.5°N. This is demonstrated by the fact that the noise-to-signal ratio obtained during the objective analysis of the Argo section is an order of magnitude smaller than that for a single hydrographic section. In particular, the ratio is 0.08 for the Argo temperature section, but it is 1.27 and 0.68 for the WOCE A05 1992 and the WOCE AR01 1998 sections, respectively.

The resulting Argo synthetic zonal section is composed of temperature and salinity profiles every 0.5 degree between 23°W and 70°W, at 101 pressure levels between the surface and 2000 dbar. The computed mean date is 2006 and, therefore, this synthetic Argo section would be considered as the sixth occupation of 24.5°N, in 2006. This synthetic Argo section was used by Hernández-Guerra et al. (2009) to show that the transport estimates derived from Argo data have significantly less eddy noise than those estimated from individual hydrographic sections. Hernández-Guerra et al. (2009) have also shown that, within the estimation error, the upper limb of the Atlantic MOC has not changed significantly since 1957.

Synthetic sections with computed mean times for 2005, 2006, 2007 and 2008 are also obtained by objectively analyzing all the Argo data between January and December of the respective year, following the procedure described above. Similar results regarding the annual variability were obtained using yearly estimations based on data centered on the target year extending over a two to three year time period.

The model proposed by Bindoff and McDougall (1994) is used to interpret temperature and salinity variations in the water column. Using a Taylor expansion and assuming that vertical gradients of temperature are constant in time, these authors showed that for small displacements, temporal changes of potential temperature (θ) on isobars can be split into two components:

$$\frac{d\theta}{dt} \Big|_p = \frac{d\theta}{dt} \Big|_{\gamma_n} - \frac{dp}{dt} \Big|_{\gamma_n} \frac{\partial\theta}{\partial p} \quad (3.1)$$

where the p subscript denotes isobaric rates of change; the γ_n subscript denotes rates of change along neutral surfaces, $dp/dt|_{\gamma_n}$ denotes the isoneutral displacement, and $\partial\theta/\partial p$ the vertical temperature gradient. The equation represents the observed changes of temperature along isobaric surfaces as the sum of two independent contributions: changes along neutral surfaces and changes due to vertical displacements of the isoneutral surface itself. The latter is referred to as heaving (Jackett and McDougall, 1997). Two mechanisms can contribute to heaving: changes in isopycnal thickness by changing renewal rates and changes in the gyre circulation strength resulting from changes in wind stress curl. On the other hand, changes on isoneutral surfaces are representative of variability in the surface heat fluxes in the water formation area (Jackett and McDougall, 1997; Arbic and Owens, 2001). Salinity differences on isobars can be decomposed in a similar manner, but for the sake of brevity this decomposition is not presented here.

3.3 Results

3.3.1 Basin-wide changes

Contoured sections of the temperature differences on isobaric surfaces for the periods 1998-1957 (i.e. between 1957 and 1998), 2004-1957, 2004-1998, 2006(Argo)-1957 and 2006(Argo)-1998 are presented in Figure 3.2. The temperature difference sections have been smoothed using a 300 km low-pass Gaussian filter to eliminate eddy variability from the cruise sections.

Temperature differences between the WOCE 1998 and IGY 1957 surveys (Figure 3.2a) reveal that the subtropical North Atlantic at 24.5°N warmed during this 41-year period at a similar rate, 0.65°C/century, as that found in 1992 (Parrilla et al., 1994). The warming occurred almost basin-wide, with a maximum of up to 1°C found between 800 and 1000 dbar.

Temperature differences between the 2004 and 1957 sections (Figure 3.2b) show that the Atlantic interior in 2004 was warmer than in 1957. However, the magnitude of the warming is lower than in 1998, especially in waters deeper than 400 dbar, where the warming of up to 1°C found in 1998 was reduced to less than 0.5°C in 2004, and even lower in the eastern central Atlantic (20°W-45°W). This recent cooling, reversing the previous long-term warming trend, is clearly observed in the temperature differences between the 2004 and the WOCE AR01 1998 sections (Figure 3.2c). The cooling in the

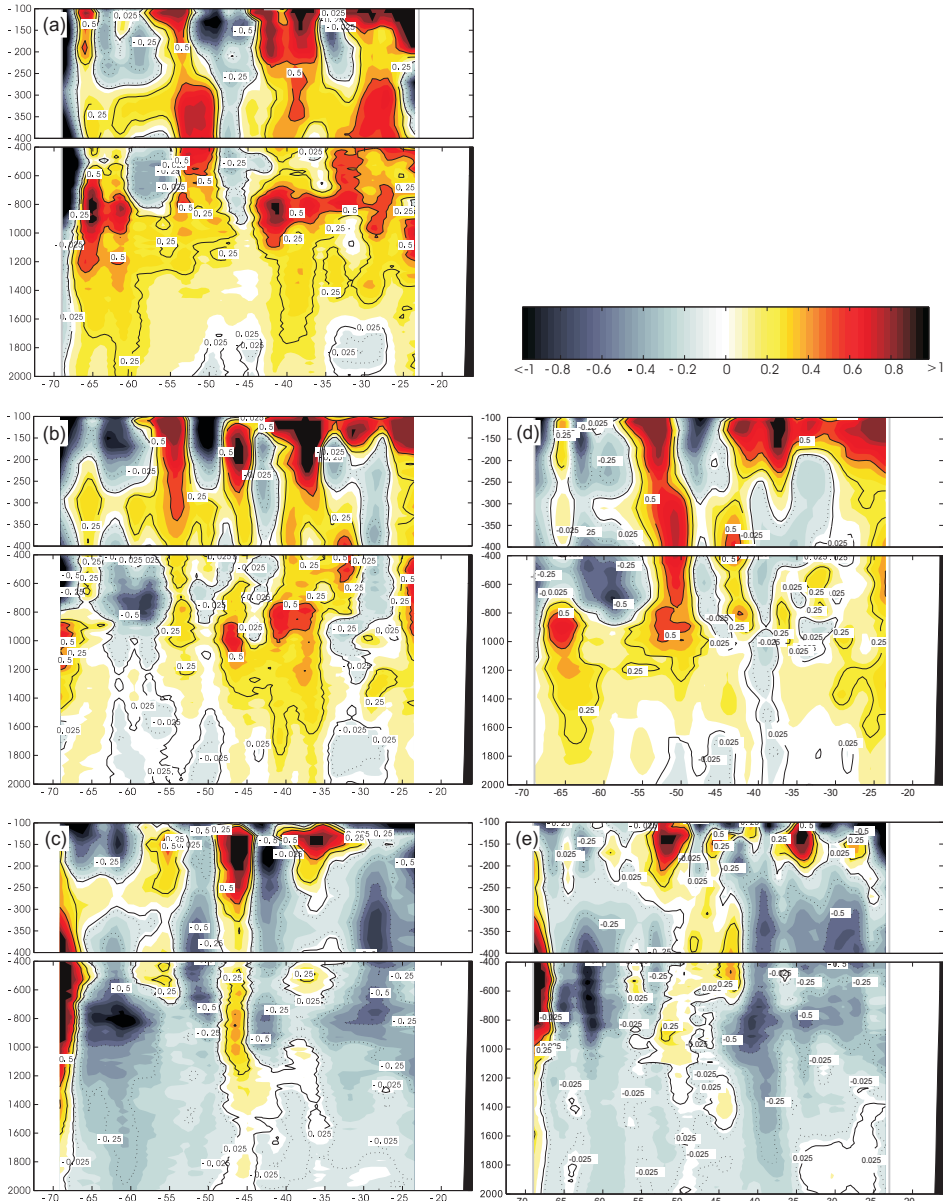


FIGURE 3.2: Vertical zonal sections, on pressure surfaces, of potential temperature differences at 24.5°N in the Atlantic Ocean between the oceanographic sections carried out during: (a) 1998-1957 (i.e. between 1957 and 1998), (b) 2004-1957, (c) 2004-1998, (d) 2006 (Argo)-1957 and (e) 2006 (Argo)-1998. The gray lines at 23°W and 70°W bound the longitude range where the Atlantic was effectively sampled at 24.5°N during the five occupations. Positive values indicate warming. This convention has been used throughout the text, subtracting the older temperature section from the most recent one when computations refer to time periods. The same color scale has been used for the five panels.

period 2004-1998 was basin-wide except for the central Atlantic (40°W - 55°W), where a 0.70°C warming in the upper levels (<200 dbar) is found. This warming extends to 1200 dbar but decreases to less than 0.05°C in the waters deeper than 1200 dbar. The observed 2004-1998 cooling had maximum values of -0.5°C at 800 dbar between 55°W and 65°W in the western basin and at 350 dbar between 25°W and 25°W in the eastern basin.

Temperature differences for 2006-1957 and 2006-1998 using the synthetic Argo section for 2006 (Figures 3.2d and 3.2e) show changes similar to those found using the CTD data for the same periods. This confirms, using an independent dataset, the usefulness of the Argo data for long-term studies. In particular, the observed maximum cooling at 800 dbar between 55°W and 65°W in the western basin, as well as the slight warming in the central Atlantic (40°W - 55°W), are clearly observed in the temperature difference section for the period between 1998 and 2006 (Argo).

Regarding salinity changes at 24.5°N , there was an increase between 1957 and 1998, with the larger changes occurring in the top 1200 dbars (Figure 3.3a). Maximum values of up to 0.2 are found in the top 300 dbars, decreasing, almost linearly, to 0.02 at 1000 dbar. Salinity differences between the 2004 and IGY 1957 sections (Figure 3.3b) show that the Atlantic interior in 2004 was saltier than in 1957, with a similar pattern to that found during 1998. However, the increase in salinity was lower than that found in 1998, especially in waters deeper than 300 dbar, since the waters in 2004 are just 0.05 saltier than in 1957. This recent freshening, reversing the previous long-term salt increase tendency, is clearly observed in the salinity differences between the 2004 and the WOCE AR01 1998 sections (Figure 3.3c). During this period, the freshening was higher in the top 800 dbar, except for the central Atlantic (40°W - 55°W), where a 0.05 salt increase in the upper levels (<300 dbar) and intermediate levels is found. Around 800 dbar, there is a relative maximum in the freshening with values of up to -0.1. Salinity differences for the periods 2006 (Argo)-1957 and 2006 (Argo)-1998 (Figures 3.3d and 3.3e) show changes similar to those found using the CTD. This also confirms the observed freshening by means of an independent dataset.

3.3.2 Zonally averaged changes

Vertical profiles of zonally averaged temperature differences between 1957 and the five occupations (Figure 3.4a) confirm and quantify the changes in the tendency observed in the basin-wide sections. A warming between the first occupation in 1957 and the sections sampled in 1981, 1992 and 1998 is observed. The maximum warming shifted from 900 dbar in 1981, to 1000 dbar in 1992 and back to 900 dbar in 1998.

The maximum warming with respect to 1957 occurs in 1998, with an averaged warming of 0.27°C for the upper ocean (600-1800 dbar), 0.24°C for the thermocline waters

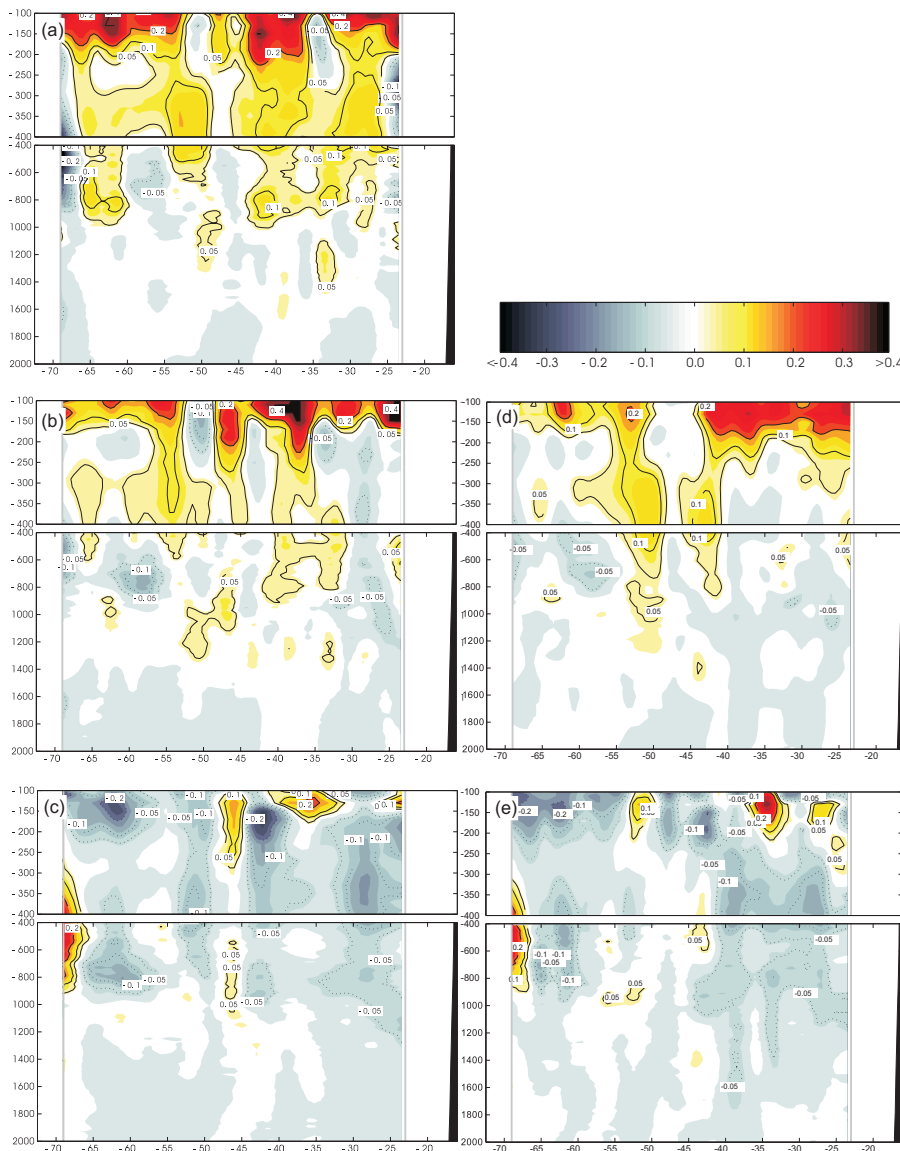


FIGURE 3.3: Vertical zonal sections on pressure surfaces of salinity differences at 24.5°N in the Atlantic between the oceanographic sections carried out during: (a) 1998-1957 (i.e. between 1957 and 1998), (b) 2004-1957, (c) 2004-1998, (d) 2006(Argo)-1957 and (e) 2006(Argo)-1998. The gray lines at 23°W and 70°W bound the longitude range where the Atlantic was effectively sampled at 24.5°N during the five occupations. Positive values indicate increase in salinity. This convention has been used throughout the text, subtracting the older salinity section from the most recent one when computations refer to time periods. The same color scale has been used for the five panels.

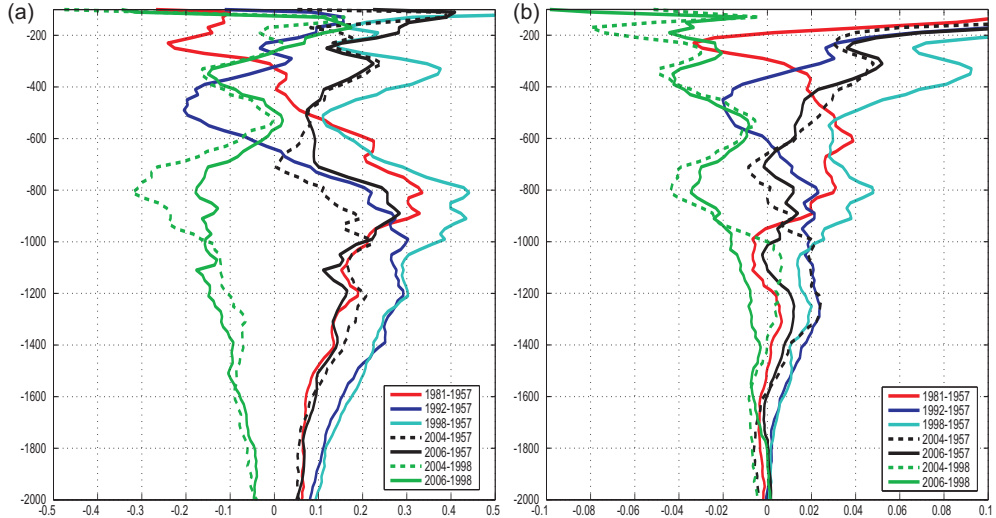


FIGURE 3.4: Vertical zonal sections on pressure surfaces of salinity differences at 24.5°N in the Atlantic between the oceanographic sections carried out during: (a) 1998-1957 (i.e. between 1957 and 1998), (b) 2004-1957, (c) 2004-1998, (d) 2006(Argo)-1957 and (e) 2006(Argo)-1998. The gray lines at 23°W and 70°W bound the longitude range where the Atlantic was effectively sampled at 24.5°N during the five occupations. Positive values indicate increase in salinity. This convention has been used throughout the text, subtracting the older salinity section from the most recent one when computations refer to time periods. The same color scale has been used for the five panels.

(300-800 dbar) and 0.27°C for the intermediate waters (800-1800 dbar) (Table 3.1). From 1998 to 2004, the zonally averaged temperatures decreased, with the maximum cooling of -0.3°C found at 800 dbar. The thermocline waters cooled by -0.15°C, while the intermediate waters cooled by -0.13°C. The observed cooling between 1998 and 2004 is statistically significant and represents almost 50% of the warming found from 1957 to 1998. As a result, between 1957 and 2004 period the thermocline waters warmed, on average, by 0.09°C, the intermediate waters by 0.14°C and the upper-ocean layer by 0.12°C (Table 3.1). This statistically significant 0.12°C mean temperature increase since 1957 for the upper ocean layer is less than half of that found during the 1998-1957 period and is lower than the mean upper ocean temperature increase observed in 1981. Once again, the results obtained using the synthetic Argo section are very similar to those obtained with CTD data. The differences between the mean temperature increases obtained with the 2006 Argo data and the 2004 CTD data in the three layers used is much smaller than the changes occurring between 1998 and 2004, and therefore confirm the robustness of the method and the validity of using the Argo

network to observe long-term changes. Specifically, for the upper ocean the mean cooling between the 1998 and 2004 CTD sections was -0.15°C, while the differences between the 2004 CTD section and the 2006 Argo synthetic section was 0.02°C (Table 3.1).

TABLE 3.1: Mean temperature differences (°C) with respect to IGY 1957, between 23°W and 70°W. In the last column the value between brackets correspond to the results obtained if annual climatological temperature and salinity data from the World Ocean Atlas 2005 are used as a first guess for the objective analysis instead of data from the World Ocean Atlas 1994.

| | 1981 | 1992 | 1998 | 2004 | 2006 Argo |
|-------------------------------------|------|-------|------|------|-------------|
| Upper Ocean (600-1800 dbar) | 0.16 | 0.20 | 0.27 | 0.12 | 0.14 (0.15) |
| Thermocline waters (300-800 dbar) | 0.14 | -0.05 | 0.24 | 0.09 | 0.05 (0.05) |
| Intermediate Waters (800-1800 dbar) | 0.14 | 0.22 | 0.27 | 0.14 | 0.16 (0.17) |

Zonally averaged profiles of salinity differences (Figure 3.4b) confirm the increase in salinity before 1998 and the decrease afterwards. The CTD data show that 1998 was the saltiest year. Although the maximum values are found in the top 400 dbar, there is a subsurface maximum at 800 dbar, with values of up to 0.05 in 1998, but decreasing to almost zero in 2004. The freshening occurred between 1998 and 2004 also had a subsurface maximum of -0.04 at 800 dbar.

The Argo data show that the vertical profiles of the zonally-averaged temperature and salinity differences for the periods 2006 (Argo)-1957 and 2006 (Argo)-1998 are very similar to those obtained using the 2004 CTD data. Moreover, the differences between the sections and the zonally averaged values for the 2004 and 2006 (Argo) datasets are much smaller than the changes that occurred in the period 2004-1998.

The associated changes in steric sea level since 1957 over the 800-1800 dbar interval, reached a maximum of 3.3 cm in 1998, and then decreased given the observed ocean cooling and freshening to 1.8 cm in 2004.

3.3.3 Isobaric change decomposition

The decomposition of the temperature changes along isobaric surfaces as the sum of changes along neutral surfaces is shown in Figure 3.5.

Between 1957 and 1998 the main contribution to the warming in the upper ocean (600-1800 dbar) was due to a deepening of the isoneutral surfaces (Figure 3.5a). This

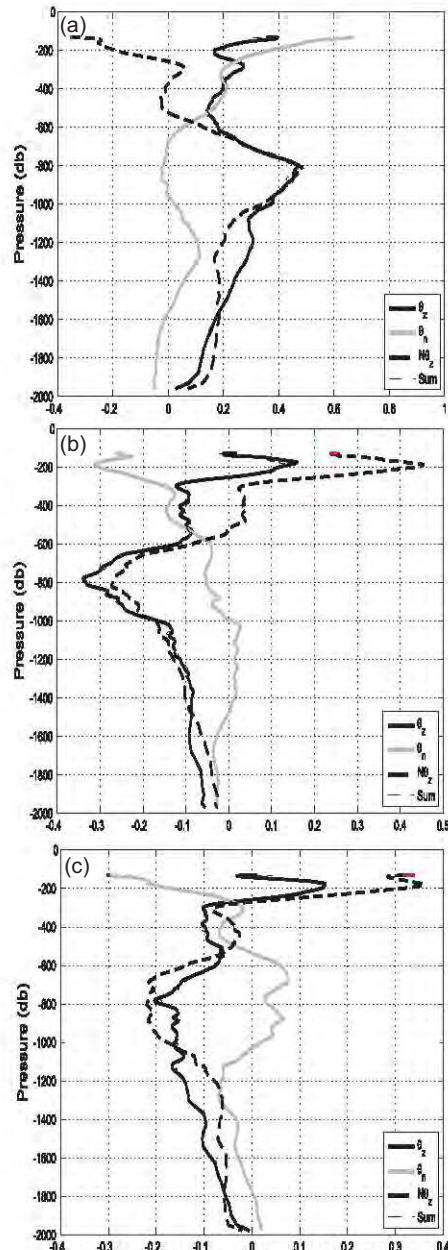


FIGURE 3.5: Decomposition of the temperature changes along isobaric surfaces $d\theta/dt|_p$ (thick solid line), as the sum of changes along neutral surfaces, $d\theta/dt|_{\gamma_n}$ (gray line), and the changes due to vertical displacement of the isoneutral, $dp/dt|_{\gamma_n} \partial\theta/\partial p$ (thick dashed line). a) 1998-1957. b) 2004-1998 and c) 2006(Argo)-1998. Positive values indicate warming.

deepening occurred during each individually-observed period between 1957 and 1998, except in the period from 1981 to 1992 (not shown) that is dominated by changes in water masses.

Between 1998 and 2004, the main contribution to the cooling of the upper ocean came from shallowing of the isoneutral surfaces (Figure 3.5b). Only the intermediate waters show some significant contribution from changes along neutral surfaces. This is consistent with the fact that in the eastern basin the intermediate waters are mainly Mediterranean Outflow Waters (1200 dbar), which have shorter time-scales of variability, and well-known mesoscale activity related to Meddies.

The decomposition of the temperature changes obtained from the 2006 Argo synthetic section is very similar to that obtained from the 2004 CTD section (Figure 3.5c).

3.3.4 Annual and interannual variability

The coverage of the Argo network in 2005, 2006, 2007 and 2008 permits the estimation of yearly synthetic sections for each of these years, hence providing an estimate of interannual variability at 24.5°N. This estimates in turn gives the first insight into the extent to which the observed changes at the 24.5°N transects may be related to decadal variability or to interannual variability aliased by the decadal sampling period.

Figure 3.6 shows the time evolution of the mean temperature and salinity between 70°W and 23°W for the upper ocean, thermocline and intermediate waters for the five CTD occupations, the four yearly synthetic Argo sections and the 2006 Argo synthetic section described in the previous paragraphs.

The interannual variability of the Argo synthetic sections between 2005 and 2008 is much smaller than the variability observed from the hydrographic sections. For instance, the standard deviation of the mean upper ocean temperatures for the five hydrographic sections is 0.096, while this value decreases to 0.008 for the four Argo estimates. Similarly, the standard mean temperature of the thermocline (intermediate) waters is 0.106 (0.101) and 0.032 (0.013) for the Argo estimates.

The mean temperature and salinity for the synthetic section obtained with Argo data in the period 2003-2008, equivalent to year 2006, is very similar to that obtained with data just for the year 2006, confirming the robustness of the Argo method.

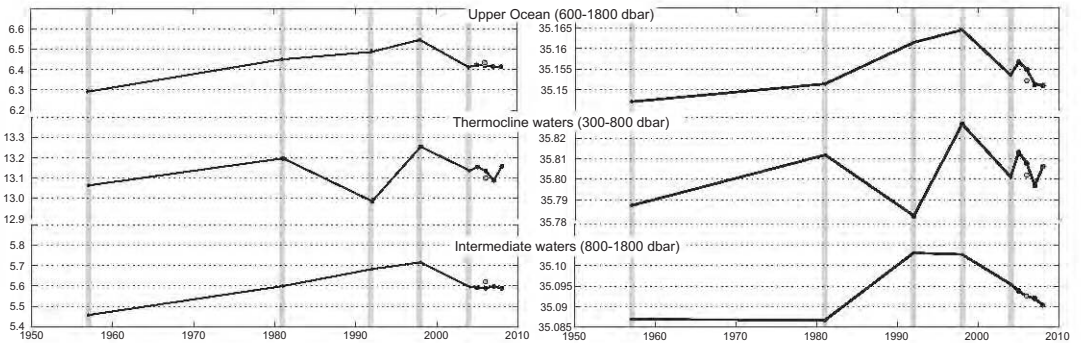


FIGURE 3.6: Time evolution of averaged (left) temperature and (right) salinity between 70°W and 23°W for the upper ocean, thermocline and intermediate waters. Vertical gray lines denote the CTD measurements (1957, 1981, 1992, 1998 and 2004), small black dots the annual Argo estimates (2005, 2006, 2007 and 2008), and gray dots the 2006 Argo synthetic section.

3.4 Discussion and conclusions

In terms of century-scale tendencies the subtropical North Atlantic along 24.5°N warmed until 2004 at a rate of 0.25°C/century. This tendency differs, significantly, from the 0.57°C/century observed with the data until 1992. Parrilla et al. (1994) also used data ending in 1992 to obtain a tendency of 0.65°C/century, the small difference resulting from the use of slightly different layers and zonal limits.

Our analysis of the temperature data from the most recent transatlantic section at 24.5°N (2004) reveals a mean cooling of the upper ocean of -0.15°C between 1998 and 2004. Data from the Argo network, an independent data set, also reveal a mean cooling of the upper ocean of -0.13°C for the same period. This observed cooling significantly reduces the post-IGY warming in the subtropical Atlantic. Between 1957 and 1998, the upper ocean warmed 0.27°C, while by 2004 this value decreased to 0.12°C (0.14°C as obtained using the Argo data).

These results clearly show, from the available hydrographic sections, that the upper ocean in 1998 was significantly warmer and saltier than in any transoceanic measurements at 24.5°N since 1957.

Between 1957 and 1998, the warming in the upper ocean was mainly caused by deepening of the isoneutral surfaces, while the cooling found between 1998 and 2004 (2006 for the Argo synthetic section) was mainly due to shallowing of the isoneutral surfaces. The present dataset do not permit discrimination between the two

mechanisms that contribute to heaving, and therefore the forcing for the observed changes since 1957 could be either wind-driven ocean forcing or changes in the renewal rates at the formation areas. The interdecadal shifts from warming to cooling likely reflect intrinsic ocean-atmosphere variability that complicates the understanding of ocean climate change (Kerr, 2008; Keenlyside et al., 2008). Such variability has been shown in a trans-Indian hydrographic section across 32°S (Bryden et al., 2003), and in the Mediterranean Sea (López-Jurado et al., 2005). Bryden et al. (2003) showed that salinity presented an increase that almost reversed the freshening of mode waters observed from 1960 to 1987, and López-Jurado et al. (2005) showed that 2005 presented a reversal of the long-term progressive warming observed from 1957 to 2005 in Western Mediterranean Deep Waters.

Additionally, our Argo data show that the changes in the 24.5°N hydrographic zonal sections are a good proxy for decadal changes, since the interannual variability in the period with Argo synthetic sections (i.e. from 2005 to 2008) was small and therefore the interannual variability aliased by the decadal sampling period is likely negligible. Without regular observations, oceanographers have little understanding of the scales of variability in water mass properties that can mask evidence of anthropogenic climate change. Sampling has been the central problem for all similar studies of decadal change based on repeated hydrographic transects anywhere in the global ocean, and our results highlight the invaluable contribution of the Argo system for understanding long-term variability of the ocean's interior.

Part II

The Canary Region

CHAPTER 4

Recent changes in subsurface temperature and salinity in the Canary region

Verónica Benítez-Barrios¹, Alonso Hernández-Guerra¹, Pedro Vélez-Belchí², Francisco Machín³ and Eugenio Fraile-Nuez²

¹ Facultad de Ciencias del Mar, Universidad de Las Palmas de Gran Canaria, Las Palmas, Spain.

² Instituto Español de Oceanografía, Centro Oceanográfico de Canarias, Santa Cruz de Tenerife, Spain.

³ Institut de Ciències del Mar (CSIC), Barcelona, Spain.

Abstract

Based on hydrographic sections carried out during the last decade in the Canary region at 29°–10°N, we show that there has been a statistically significant rise in temperature and salinity on isobars between 1500 and 2300 db. The maximum increase, found at 1600 db, is occurring at a rate of 0.29°C and 0.047 per decade. Isobaric change decomposition into changes on neutral surfaces and changes due to the vertical displacement of the isoneutrals was performed. Results reveal that the lower part of North Atlantic Central Water (NACW) cooled and freshened on neutral surfaces, suggesting changes in the freshwater fluxes at the outcropping region. However, the signal in deep waters (1500–2300 db) was principally due to a downward displacement of the isoneutrals, although water mass modification is observed in the range of Mediterranean Water (MW) influence.

KEYWORDS: Canary Islands, ocean variability, temperature changes

Geophysical Research Letters, volume 35, L07603, doi:10.1029/2008GL033329, 2008.

Contents

| | | |
|------------|--|-----------|
| 4.1 | Introduction | 49 |
| 4.2 | Data Set and Method | 49 |
| 4.3 | Results | 50 |
| 4.3.1 | θ/S isobaric changes | 50 |
| 4.3.2 | Isobaric change decomposition | 52 |
| 4.3.3 | Warming, freshening and heaving mechanisms | 52 |
| 4.4 | Discussion and conclusion | 55 |

4.1 Introduction

A suite of observations over different scales and regions supports an unequivocal conclusion: the climate system is changing. Temperature increase in the oceans, sea level rise and melting glaciers are some of the known responses to natural and/or anthropogenic forcing which highlight the important role of the ocean in climate change (Bindoff et al., 2007). The evaluation of long-term variations in the ocean is one of the keys for understanding how climate is changing and to identify the controlling mechanisms.

Examination of repeated hydrographic sections over the subtropical North Atlantic have revealed a temperature increase at depths from 800 to 2500 m since the late 1950s (Roemmich and Wunsch, 1984; Parrilla et al., 1994; Vargas-Yáñez et al., 2004; Cunningham and Alderson, 2007). Decomposition of the isobaric changes into water mass changes and changes due to the displacements of the isopycnals have shown that this warming trend is the result of both contributions (Bryden et al., 1996; Arbic and Owens, 2001).

In this paper we report that the Canary region has also undergone temperature and salinity changes in recent years. We analyze them in order to decompose these changes and interpret them in terms of variations in the surface forcing at the outcropping region.

4.2 Data Set and Method

During the project Canary Islands Azores Gibraltar Observations (CANIGO) carried out in the 1990s, a section north of Canary Islands was accomplished on a seasonal basis (Machín et al., 2006a). In February 2006, the Canary Deep Hydrographic Section (RAPROCAN) repeated the January 1997 CANIGO section with casts in both surveys coincident (Figure 1a). A total of 16 full-depth CTD stations were occupied, where spatial separation for the deep-water stations was 35 km, reduced to 15 km for the inner stations. Temperature and salinity profiles averaged over a 2-db interval were obtained using a CTD/rosette (Neil Brown in 1997 and SeaBird 911+ with dual sensors in 2006). Water samples were analyzed on a Guidline salinometer to calibrate the conductivity sensor, and showed an accuracy better than 0.002 for single samples (hereafter salinity is expressed in the Practical Salinity Scale). Temperature and pressure sensors were calibrated using WOCE standards.

To evaluate the temperature and salinity variations in the water column, we have applied the model proposed by Bindoff and McDougall (1994). They relate the variations in both pressure and density surfaces through the following equation:

$$\frac{d\psi}{dt} \Big|_z = \frac{d\psi}{dt} \Big|_{\gamma_n} - \frac{dp}{dt} \Big|_{\gamma_n} \frac{\partial\psi}{\partial p} \quad (4.1)$$

which represents the observed changes in a scalar quantity ψ along isobaric surfaces as the sum of two independent contributions: changes along neutral surfaces (Jackett and McDougall, 1997) and changes due to vertical displacement of the isoneutrals, referred to as heaving. $dp/dt|_{\gamma_n}$ denotes the isoneutral displacement and $\partial\psi/\partial p$ the vertical gradient of the quantity which is assumed to be constant over time. This allows the decomposition test by comparing the sum of the two components to the isobaric change.

In order to apply the above methodology, temperature and salinity are interpolated onto a grid with a pressure interval of 50 db and 0.01 kg m^{-3} for neutral density, from the surface to 3000 db. Thus, differences and means along the transect are computed in both the geopotential and neutral coordinate frames. The 95% confidence intervals of the mean differences are based on a Student's t-test and take into account the loss of degrees of freedom at each pressure/neutral density surface due to eddy field autocorrelation.

4.3 Results

4.3.1 θ/S isobaric changes

Figures 1b and 1c display temperature and salinity differences and their zonal average to emphasize the principal changes. At first sight, both hydrographic variables follow a similar pattern characterized by a decrease of the property in the shallowest layer (0-100 db) with a remarkable homogeneity over the whole transect, this being statistically significant on the basis of 95% confidence intervals. This conspicuous decrease could be attributed to the influence of the atmosphere immediately above, which deepened the winter mixed layer 30 m more in 2006 than in 1997, cooling the surface to approximately 18°C . Below the mixed layer, North Atlantic Central Water (NACW) extends down to 600 db, defining the main thermocline. Within this water mass the principal changes are: (i) a pronounced increase in temperature and salinity (only significant for the latter) between 100 and 350 db, where values as large as 1.92°C and 0.46 are found in three patches along the section, and (ii) a decrease in salinity from 350 to 600 db while temperature remained unaffected. These differences imply that there have been changes which do not involve conservation of the θ/S properties.

From 600 down to 1500 db, corresponding to intermediate layers, two well-differentiated water masses are evident: Antarctic Intermediate Water (AAIW) identified by a relative salinity minimum, and Mediterranean Water (MW) clearly distinguished by its salinity maximum (Machín et al., 2006a). At these levels positive and negative differences alternate yielding a non-significant zonal average.

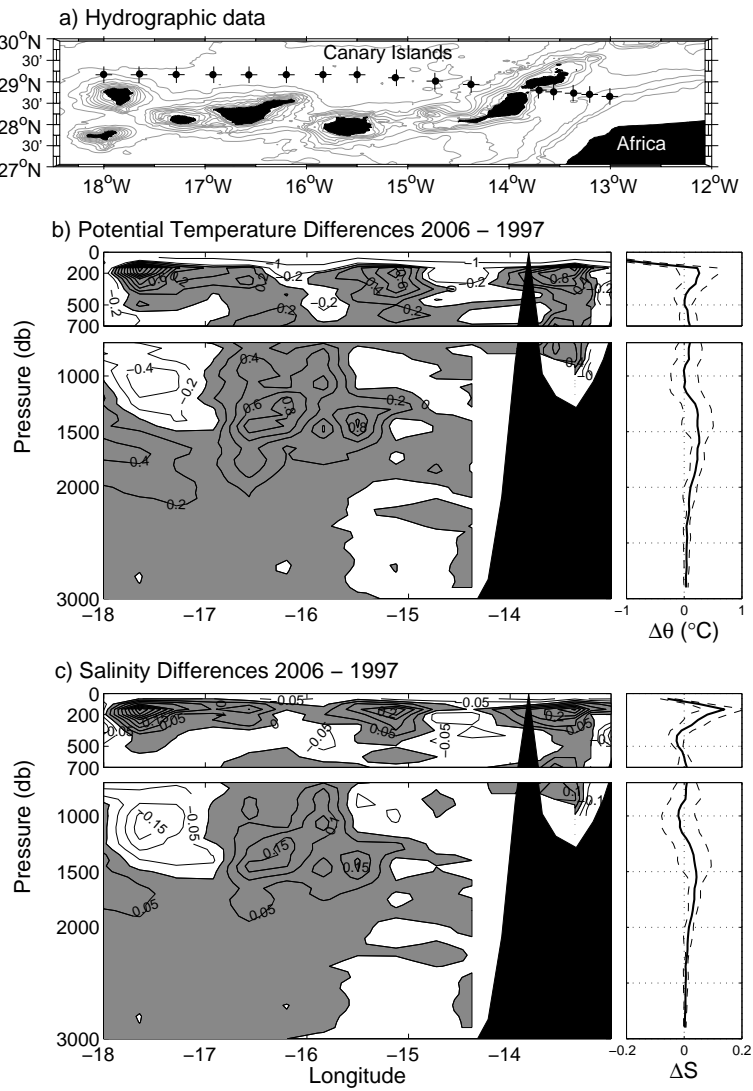


FIGURE 4.1: (a) Hydrographic stations carried out during CANIGO (1997, crosses) and RAPROCAN (2006, dots) cruises. (b) Potential temperature differences on isobaric levels. Differences contoured at 0.2°C intervals. The side partition is the zonally averaged difference of the potential temperature. The dashed lines stand for the 95% confidence intervals. (c) As for Figure 1b but for salinity. Difference contours at 0.05 intervals. Shaded areas indicate rising temperature and salinity over time.

In deep layers (>1500 db) consisting of North Atlantic Deep Water (NADW), a basin-wide band of warmer and saltier water is observed. This increment is statistically

significant from 1500 to 2300 db, reaching the maximum of both difference-fields at about 1600 db where temperature and salinity rose at rates of 0.29°C and 0.047 per decade, respectively.

4.3.2 Isobaric change decomposition

The temperature and salinity isobaric changes, their decomposition and the sum of the two components are plotted in Figures 4.2a and 4.2b. Except for the near surface, the sum of the components compares reasonably well with the isobaric change indicating that the decomposition has been successfully performed. In the thermocline waters, a subsurface layer of increased temperature and salinity on neutral surfaces led to significant salinification in the isobaric field. Conversely, the lower part of NACW cools and freshens on isoneutrals at a maximum rate of -0.26°C and -0.07 per decade, respectively. Hence, the mean θ/S diagram (Figure 4.3a), obtained from the zonally averaged temperature and salinity profiles at fixed pressure, reveals a cooler and fresher NACW curve in 2006. The lines linking points of equal pressure do not lie parallel to the isopycnals, indicating that displacement of neutral surfaces has occurred as observed in Figure 4.2c. Thus, the deepening of the neutral surfaces offsets the changes along neutral surfaces, resulting in non-significant changes on isobars at these levels.

In intermediate waters, neither isobaric changes nor water mass changes are statistically significant (Figures 4.2a and 4.2b). Nevertheless, differences in temperature and salinity on neutral surfaces show negative values for AAIW and positive values for the MW as well as changes in their θ/S relationship (Figure 4.3b). Although these changes are not large enough to be significant, it can be seen from the lines linking points of equal pressure that they are influenced by the displacement of the isoneutrals. Thus, Figure 2a and 2b show isoneutral displacements from 1200 to 2300 db ($27.78 < \gamma_n < 28.01 \text{ kg m}^{-3}$), with an averaged deepening of 30 db (Figure 4.2c), as the only significative contribution to the isobaric change in this pressure range. This is the principal reason for the increment in temperature and salinity along isobars in deep layers.

4.3.3 Warming, freshening and heaving mechanisms

Bindoff and McDougall (1994) proposed three processes for interpreting the observed changes: pure warming, pure freshening and pure heave, involving their respective change in atmospheric forcing in the water mass source region. The first two are related to heat and freshwater fluxes, changing the water mass characteristics, and the third one is related to wind stress curl, renewal rates of water masses or internal waves. The relative strength of each process, in terms of percentage variance explained (A^w , A^f and A^h , where w , f and h stand for warming, freshening and heave, respectively), can

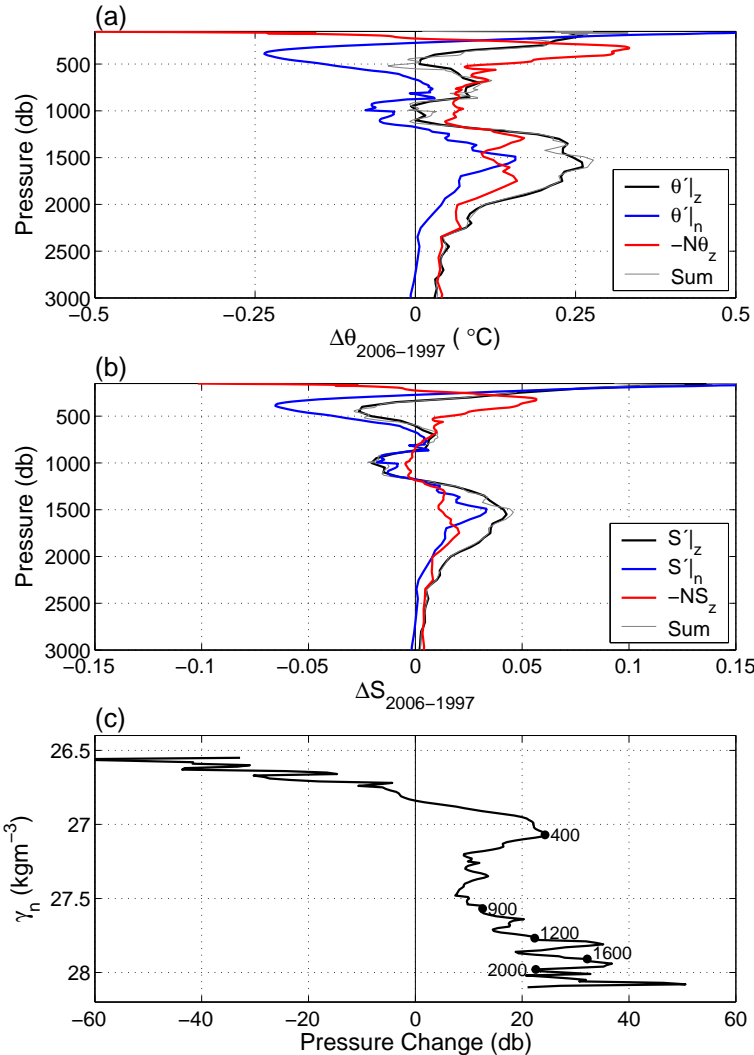


FIGURE 4.2: (a) Isobaric change from 1997 to 2006 ($\theta'|_z$ and $S'|_z$, black) decomposed into changes along neutral surfaces ($\theta'|_n$ and $S'|_n$, blue) and changes due to the vertical displacements of isoneutrals ($-N\theta_z$ and $-NS_z$, red) as a function of the average pressure of the neutral surfaces. The grey line denotes the sum of both components. (b) As for (a) but for salinity. (c) Change in pressure of neutral surfaces from 1997 to 2006. Positive displacements indicate downward movement over time. Dots represent zonally-averaged isoneutral pressures.

be estimated solving the following equations (Bindoff and McDougall, 1994):

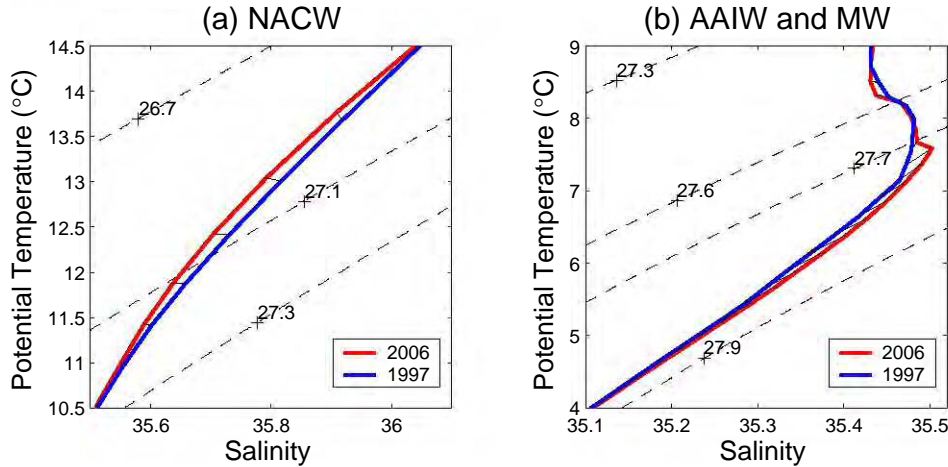


FIGURE 4.3: Mean θ/S curves for 2006 (red) and 1997 (blue) for (a) North Atlantic Central Water (NACW) and (b) Antarctic Intermediate Water (AAIW) and Mediterranean Water (MW). The dashed lines correspond to potential density anomaly isolines and the solid lines link points of equal pressure.

$$\frac{\rho^{-1} \rho'|_z}{R_\rho - 1} \begin{pmatrix} -(R_\rho - 1) & 0 & -R_\rho \\ 1 & R_\rho & 0 \\ R_\rho & R_\rho & R_\rho \\ 0 & (R_\rho - 1) & -1 \\ 1 & R_\rho & 0 \\ 1 & 1 & 1 \end{pmatrix} \times \begin{pmatrix} A^w \\ A^f \\ A^h \end{pmatrix} = \begin{pmatrix} \alpha\theta'|_z \\ \alpha\theta'|_n \\ N'\alpha\theta_z \\ \beta S'|_z \\ \beta S'|_n \\ N'\beta S_z \end{pmatrix} \quad (4.2)$$

where $\rho^{-1} \rho'|_z$ is the density anomaly at fixed pressure, N' is the change in pressure of a neutral density surface, $|_z$ denotes changes on isobars, $|_n$ denotes changes along isoneutrals, and R_ρ ($R_\rho = \alpha\theta_z/\beta S_z$) is the stability ratio defined from the thermal expansion and the haline contraction coefficients, α and β , respectively, and the vertical gradients of temperature and salinity, θ_z and S_z . Although Equation (2) is an ill-posed system, the proportion of the variance explained by each process can be assessed by making the assumption that only a single process is acting and applying an inverse method. We have distinguished four pressure regimes where a single process tends to dominate (Figure 4). In Regime I (350-600 db), corresponding to the lower levels of NACW, pure freshening explains more than 95% of the variance, suggesting water mass modification at the outcropping region. This result is expected based on the shift of the θ/S relationship shown in Figure 3a. Between 600 and 900 db (Regime II), the observed changes can be explained by pure heave and by pure freshening in Regime III (900-1200 db), both statistically significant at the 90% level. At deeper layers (Regime IV) the percentage of the overall variance resolved drops. However, pure heave explains 60-90% of the

signal over the deepest levels of intermediate waters and NADW.

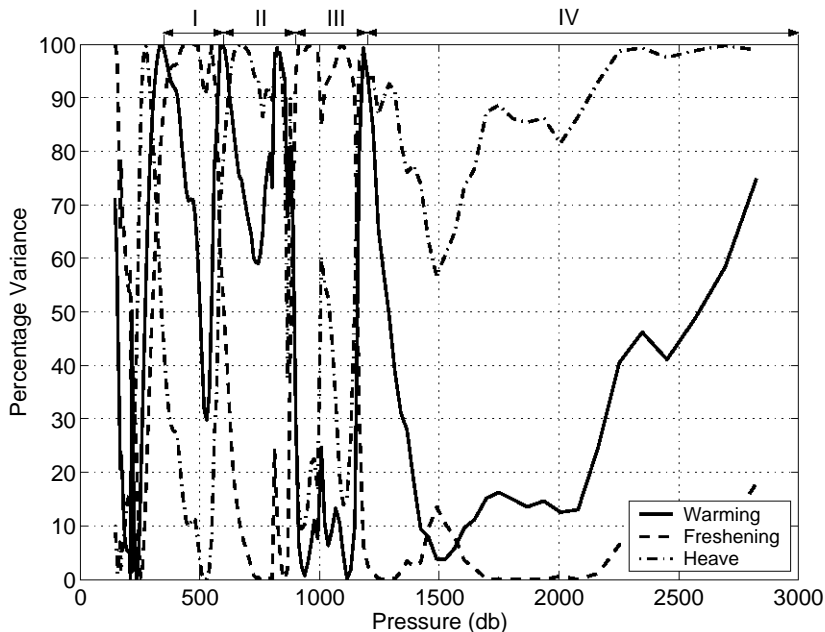


FIGURE 4.4: The variance explained for the case of pure warming (continuous), pure freshening (dashed) and pure heave (dashed-dotted) against the average pressure of the neutral surfaces. Four different pressure regimes are shown at the top of the figure.

4.4 Discussion and conclusion

We analyze the temperature and salinity changes that occurred in the Canary region from two hydrographic sections carried out in 1997 and 2006 by decomposing the isobaric changes into changes along isoneutrals and changes due the vertical movement of the neutral surfaces. In order to interpret them we compute the percentage of the variance explained by pure warming, pure freshening and pure heaving mechanisms. The results found here concur with the variations for the subtropical North Atlantic Ocean and its large scale circulation.

The NACW presents a subsurface layer (100-350 db) of temperature and salinity increases on isoneutrals, whereas its lower part (350-600 db) is cooled and freshened at a maximum rate of -0.26°C and -0.07 per decade leading to a shift in the θ/S relationship. The latter is in agreement with findings by Vargas-Yáñez et al. (2004) and Cunningham and Alderson (2007) of temperature and salinity decrease along

the isoneutrals of the 24°N eastern thermocline between the 1990s and early 2000. Moreover, the salinity diminution in NACW has been documented previously; e.g., Pérez et al. (1995) noted that the salinity on $\sigma_0 = 27.1$ dropped 0.2 between 1974 and 1982, remaining fresh until 1990. Since pure freshening explains more than 95% of the data variance, we suggest that this might be caused by changes in the balance of precipitation and evaporation taking place in the formation region of NACW, which was subsequently transported into the Canary region by circulation.

The rise in temperature and salinity on isobars found in the range 1500-2300 db has been reported in previous studies. Roemmich and Wunsch (1984) were the first to estimate long-term changes along 24°N and 36°N, making a direct comparison of temperature on isobars between 1981 and the International Geophysical Year (IGY) surveys in the late 1950s. They found that the temperature had increased between 700 and 3000 m, with a maximum difference of 0.2°C at 1000-1500 m. The study of the 24°N changes was extended by Parrilla et al. (1994), adding a survey carried out in 1992. They found that the warming had continued with a maximum increment of 0.32°C at 1100 m over the period 1957-1992, equivalent to an increase rate of 0.1°C/decade. Our results show an increase in temperature three times higher than that estimated from Parrilla et al. (1994). However, when splitting the North Atlantic sections into western and eastern basins, our isobaric trend of temperature and salinity match remarkably well those reported by Arbic and Owens (2001) for the eastern part of 24°N between 1981 and 1992. These authors found that both downward movement of the isopycnals and water mass changes (higher temperature and salinity on isopycnal surfaces) contributed to the changes along isobars. This result is consistent with the pure heave regime observed from 1200 to 3000 db in this study, the downward displacement of the isoneutrals being the main reason for the isobaric change. We also found increments in temperature and salinity on neutral surfaces which could be associated with the warming and salinification of the waters from the Mediterranean, revealed in recent studies (Millot et al., 2006; Potter and Lozier, 2004). Therefore, the MW modification and mixing with the upper levels of NADW during its southward flow, could be a plausible explanation for the percentage of variance explained by pure warming at these levels.

All these studies underline the fact that changes do not occur uniformly over time and space. Hence, similar repeated observations on regional and larger scales should continue in order to assess climate change. This will enable us to gain a better understanding about the relationship of regional to global changes.

CHAPTER 5

Nine years of mass transport data in the eastern boundary of the North Atlantic Subtropical Gyre

Eugenio Fraile-Nuez¹, Francisco Machín², Pedro Vélez-Belchí¹, Federico López-Laatzen¹, Rafael Borges³, Verónica Benítez-Barrios³ and Alonso Hernández-Guerra³

¹ Instituto Español de Oceanografía, Centro Oceanográfico de Canarias, Santa Cruz de Tenerife, Spain.

² Institut de Ciències del Mar (CSIC), Barcelona, Spain.

³ Facultad de Ciencias del Mar, Universidad de Las Palmas de Gran Canaria, Las Palmas, Spain.

Abstract

One of the longest current-meter time series in the Lanzarote Passage in the eastern boundary of the North Atlantic Subtropical Gyre has been used to determine and quantify the 9-year mean transport, the inter-annual and seasonal mass transport variability for the three water masses present in the area. Results show North Atlantic Central Water (NACW) flowing southward in the upper levels with a mean mass transport of -0.81 ± 1.48 Sv, Antarctic Intermediate Water (AAIW) flowing northward at intermediate levels with a mean transport of $+0.09 \pm 0.57$ Sv and Mediterranean Water (MW) flowing southward in the deep part of the Passage with a mean transport of -0.05 ± 0.17 Sv. Harmonic and wavelet analysis show the presence of a seasonal pattern in the Passage for the three water masses. A maximum southward transport in winter and spring has been observed for the NACW followed by a minimum in summer and fall. Near zero values during winter and spring are found for AAIW, with a maximum northward value in summer and a negative value in fall, when this water mass reverses its flow. MW has a similar seasonal pattern to NACW. The vertical structure in the Lanzarote Passage can be approximated by four significant oscillatory modes which cumulatively explain 86.4% of the variance. The strong transport fluctuation found at the seasonal and inter-annual timescales demonstrates that the Eastern Boundary Current transport has a strong impact on Meridional Overturning

estimates, thus indicating that to understand MOC variability, these transport estimates at the eastern Atlantic margin are necessary.

KEYWORDS: Canary Islands, Eastern Boundary Current, Meridional Overturning Circulation

Journal of Geophysical Research, volume 115, C09009, doi:10.1029/2010JC006161, 2010.

Contents

| | | |
|------------|--|-----------|
| 5.1 | Introduction | 60 |
| 5.2 | Data | 61 |
| 5.2.1 | Current-meter description | 61 |
| 5.2.2 | Hydrographic data | 62 |
| 5.3 | Current-meter statistics | 62 |
| 5.4 | EOF analysis | 65 |
| 5.4.1 | Temporal EOFs with four moorings | 65 |
| 5.4.2 | Temporal EOFs for the nine-year record | 69 |
| 5.5 | Periodic signals | 69 |
| 5.5.1 | Harmonic analysis | 69 |
| 5.5.2 | Wavelet analysis | 72 |
| 5.6 | Variability in mass transport | 74 |
| 5.6.1 | Temporal variability | 74 |
| 5.6.2 | Seasonal variability | 77 |
| 5.6.3 | Inter-annual variability | 80 |
| 5.7 | Results and discussion | 82 |

5.1 Introduction

The Azores Current is the northernmost current in the Eastern North Atlantic Subtropical Gyre which turns south, splitting into several branches. The easternmost branch flows east of Madeira and supplies the Canary Current (Siedler and Onken, 1996; Paillet and Mercier, 1997; Láiz et al., 2001; Machín et al., 2006a). The Canary Current, flowing southwestward forced by the curl of the wind stress (Fraile-Nuez and Hernández-Guerra, 2006) and the meridional blocking of the African continent, constitutes the major Eastern Boundary Current (EBC) of the North Atlantic Subtropical Gyre.

Particular effort was made during the CANIGO project (Canary Islands Azores Gibraltar Observations) (Parrilla et al., 2002) to improve our understanding of the physics, biogeochemistry, and paleoceanography of the portion of the EBC that flows through the channel between the island of Lanzarote and the African coast (hereafter Lanzarote Passage, Figure 6.1) (Hernández-Guerra et al., 2001; Knoll et al., 2002; Hernández-Guerra et al., 2002; Hernández-Guerra et al., 2003; Machín et al., 2006a).

The Lanzarote Passage is about 1300 m deep, and contains three water masses. The predominant upper-thermocline North Atlantic Central Water (NACW) is characterized by a close clustering of points in the θ/S diagram (Wright and Worthington, 1970; Tomczak, 1981). It spans from the surface to the approximate neutral density value of 27.3 kg m^{-3} (roughly 600 m depth; neutral density, γ_n , as defined by Jackett and McDougall (1997) is used as the density variable throughout this work) (Hernández-Guerra et al., 2001). At intermediate levels, two water masses interleave in the EBC: Antarctic Intermediate Water (AAIW) and Mediterranean Water (MW). AAIW is found below the NACW, mainly between the layers 27.3 and 27.7 kg m^{-3} (roughly 600-1100 m depth) with its core centered at 27.6 kg m^{-3} (roughly 900 m depth). AAIW is characterized by a minimum in salinity ($S < 35.3$). The MW reaches deeper than AAIW, roughly from 900 m to the bottom of the passage ($\gamma_n > 27.45 \text{ kg m}^{-3}$) (van Aken, 2000; Hernández-Guerra et al., 2003; Machín and Pelegrí, 2009). The MW is characterized by maximum salinity ($S > 35.5$) values (Arhan et al., 1994; Hernández-Guerra et al., 2005; Machín et al., 2006a). In the 1990s, several large-scale horizontal distributions of salinity, oxygen, and silica suggested a narrow northward penetration of AAIW along the eastern margin of the North Atlantic Subtropical Gyre, as the constant property lines stretch northeast along the African coastline. However, these were produced with rather low spatial resolution data that did not permit the identification of the spreading path (Kawase and Sarmiento, 1985; Reid, 1994; Lozier et al., 1995). Recently, this relatively fresh water flowing northward has been detected along the African slope as far north as 34°N during fall (Machín and Pelegrí, 2009).

An element of the CANIGO project in the Lanzarote Passage was the deployment of four moorings with a total of 19 current meters from January 1997 to January 1999.

Results from these observations, together with hydrographic and XBT cruises, gave a fairly comprehensive new picture of the circulation at the Eastern Boundary. The water masses found in the Passage had a mean annual mass transports of -0.8 ± 1.1 Sv for NACW, $+0.1 \pm 0.4$ Sv for AAIW and -0.05 ± 0.09 Sv for MW (Hernández-Guerra et al., 2001; Knoll et al., 2002; Hernández-Guerra et al., 2002; Hernández-Guerra et al., 2003). After the CANIGO experiment, measurements in the Lanzarote Passage were continued with just one mooring representative of the whole Passage (Hernández-Guerra et al., 2003).

The main purpose of the present study is on the one hand, to determine the seasonal and inter-annual dynamic variability of the EBC of the North Atlantic Subtropical Gyre and on the other hand, to demonstrate that the eastern Atlantic margin are necessary to understand the MOC variability. After a brief presentation of the collected hydrographic data in section 5.2 and current-meter statistics in section 5.3, we will describe the vertical variability of the EBC in terms of a Empirical Orthogonal Function analysis in section 5.4, while the harmonic signals obtained in the time series are presented in section 5.5. The 9-year mean, the seasonal and inter-annual variability of the mass transport, are described in section 5.6 and our final results and discussion are given in section 5.7.

5.2 Data

5.2.1 Current-meter description

From January 1997 to January 1999, 19 current meters were installed on four moorings (Figure 5.1). The shallowest three current meters of each mooring were deployed at the thermocline water level occupied by NACW, the next (the next two for the case of EBC-2) at AAIW level, and the last for EBC-3 and EBC-4 at the MW level (Hernández-Guerra et al., 2003). Mooring EBC-4 is still maintained but we only show data until February 2006 due to a large gap of data from March 2006 to February 2008. Thus, a 9-year time series of velocity, temperature, salinity and pressure has been obtained from mooring EBC-4 from January 1997 to February 2006. The full 9-year record is analyzed in this study. Mooring EBC-4 is located at $28^{\circ}44'N$, $13^{\circ}28'W$ in water of 1280 m depth (Figure 5.1). EBC-4 was initially equipped with 5 Aanderaa Rotor current meters, at approximately 150, 300, 520, 870 and 1230 m depth. During these 9 years the mooring has been recovered and deployed 11 times for maintenance.

The sampling time interval for all current meters was 2 hours. All current meters returned good data for the 9 years with only minor gaps, except for the shallowest one where the gaps are substantial. Hence, the shallowest current-meter is not used for the harmonic analysis and mass transport variability shown in sections 5.5 and 5.6.

The time series were low-pass filtered with a cutoff period of 40 h to eliminate tidal and inertial signatures from the time series. Velocities were rotated to the principal angle, along which the sum of the squares of the normal distance to the data points is minimum (Emery and Thomson, 1998) as previously used in the Lanzarote Passage (Hernández-Guerra et al., 2003).

5.2.2 Hydrographic data

From January 1997 to February 2006, the Lanzarote Passage has been occupied on 12 occasions (January and October 1997, March and July 1998, January and May 1999, April 2000, February 2001, February and September 2003, February both in 2005 and 2006). SeaBird 911+ CTD stations taken along this section were carried out from surface to bottom (Figure 6.1).

Geostrophic transport is calculated for each occupation using two different levels of no motion, one located at the neutral density of 27.3 kg m^{-3} and a second one at the bottom. $\gamma_n = 27.3 \text{ kg m}^{-3}$ marks the limit between the NACW flowing southward and the AAIW flowing northward in the study area, so a level of no motion may be expected at this density level (Hernández-Guerra et al., 2003). Section 5.6 will compare these geostrophic transports to the transport time series from EBC-4.

5.3 Current-meter statistics

Table 5.1 shows the deployment information for each current meter for the mooring EBC-4. Also shown are the mean duration, velocity, direction, zonal and meridional components of the velocity, velocity projected to the principal angle and its root mean square, temperature, salinity, kinetic energy and the directional stability of the flow. Table 5.1 shows values quite similar to those reported by Hernández-Guerra et al. (2003) for the first four years of the series, but several minor differences are observed. The current-meter located at the shallowest part of the water column now shows an increase of the kinetic energy and the stability for the current at this layer. The current-meter at 500 m depth shows a decrease in the kinetic energy compared to the first four years of the series.

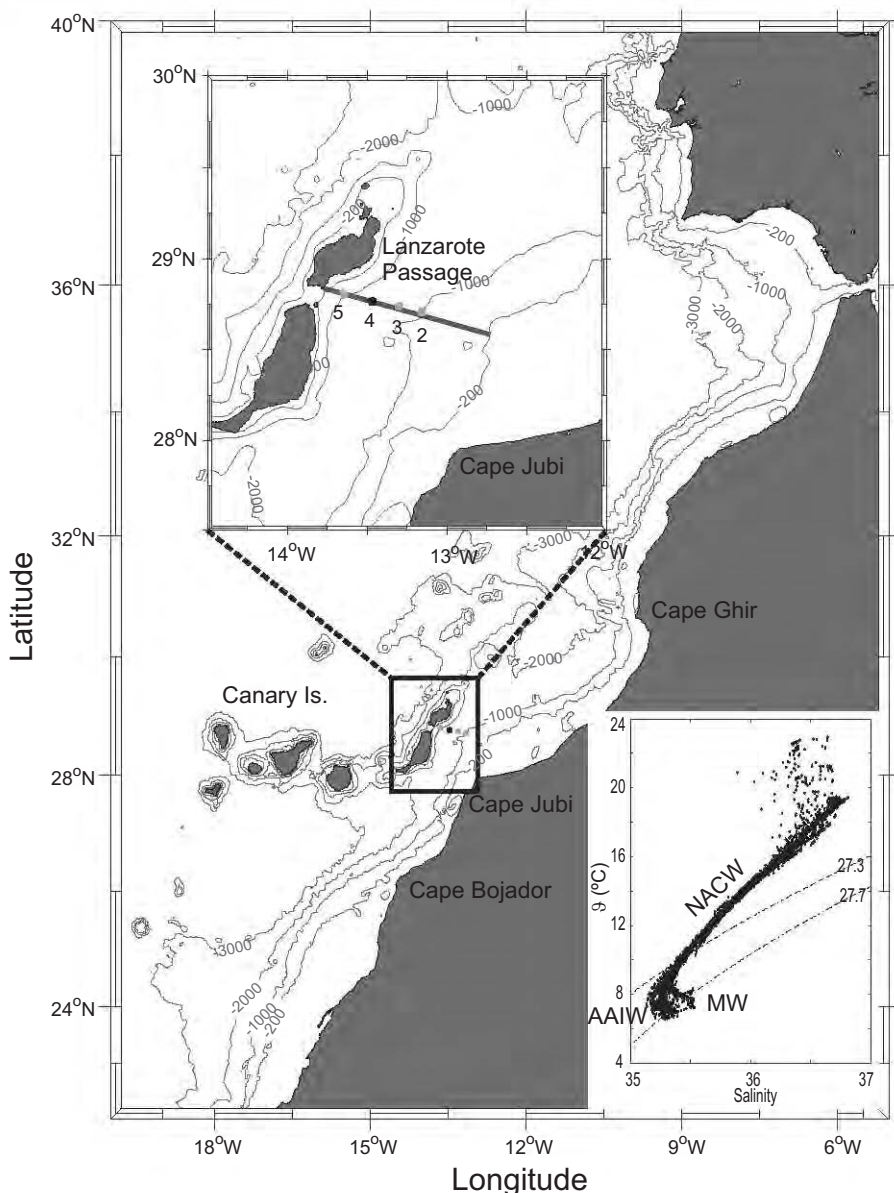


FIGURE 5.1: Eastern boundary of the North Atlantic Subtropical Gyre. Eastern Boundary Current (EBC) mooring positions are represented in the map and in the upper inset (zoom), where the Lanzarote Passage is shown. A black line across the moorings indicates the 12 occupations of the same hydrographic section carried out during these 9 years. For reference, the 200-, 1000-, 2000- and 3000-m isobaths are shown (Smith and Sandwell, 1997). In the lower inset, a θ /S diagram shows the distributions of the three water masses present in the area and used for this study.

TABLE 5.1: Summary of mooring information and mean flow statistics for the 9-year time series. Hernández-Guerra et al. (2003) values for the very first four years of the series are shown in parenthesis.

| Depth m | Duration days | SPD cm s^{-1} | DIR $^{\circ}\text{N}$ | u cm s^{-1} | v cm s^{-1} | vel_{mv} cm s^{-1} | $\text{rms}_{(vel_{mv})}$ cm s^{-1} | T $^{\circ}\text{C}$ | S | FKE $\text{cm}^2 \text{s}^{-2}$ | STAB |
|------------|------------------|---------------------------|---------------------------|----------------------------|----------------------------|----------------------------------|---|-------------------------|------------------------|------------------------------------|------|
| 150 | 1797.0 | 6.1 ± 8.7 (3.9) | 233.0 (216) | -4.9 ± 6.1 (-3.8±5.6) | -3.7 ± 6.2 (-0.6±4.9) | -6.0 ± 6.4 (-0.6±4.9) | 8.8 | 17.2 ± 0.7 (27.6) | 36.3 ± 0.1 (0.57) | 37.9 | 0.71 |
| 300 | 3135.0 | 4.2 ± 7.4 (4.1) | 232.6 (254) | -3.3 ± 5.3 (-4.0±6.1) | -2.5 ± 5.2 (-1.1±4.2) | -4.1 ± 6.0 (-1.1±4.2) | 7.3 | 14.3 ± 0.5 (27.9) | 36.2 ± 0.2 (0.61) | 27.5 | 0.64 |
| 520 | 3001.1 | 2.0 ± 6.4 (2.1) | 250.1 (268) | -1.8 ± 4.7 (-2.1±4.4) | -0.7 ± 4.3 (-0.1±3.2) | -1.8 ± 5.2 (0.9±3.5) | 5.5 | 11.6 ± 0.2 (14.8) | 35.7 ± 0.1 (0.47) | 20.6 | 0.39 |
| 870 | 3152.7 | 0.9 ± 5.3 (1.1) | 7.9 (33) | 0.1 ± 3.9 (0.6±4.5) | 0.9 ± 3.5 (0.9±2.7) | 0.7 ± 4.5 (-1.0±3.2) | 4.6 | 8.3 ± 0.3 (13.5) | 35.3 ± 0.1 (0.27) | 13.9 | 0.21 |
| 1230 | 2274.3 | 1.2 ± 4.3 (1.3) | 210.8 (238) | -0.6 ± 2.8 (-1.1±3.7) | -1.0 ± 3.2 (-0.7±2.4) | -1.2 ± 3.9 (-0.7±2.4) | 4.1 | 7.3 ± 0.3 (9.9) | 35.4 ± 0.1 (0.35) | 9.1 | 0.35 |

SPD and DIR stand for the current mean speed and direction. Vel_{mv} indicates the velocity component projected to the principal angle along which the sum of the squares of the normal distance to the data points is minimum. FKE indicates the fluctuating part of vector variance or the kinetic energy per unit mass. STAB indicates the directional stability of the flow defined by the ratio of the magnitude of the mean vector to the mean speed.

9-year mean southward velocities in the range $5\text{--}10 \text{ cm s}^{-1}$ are found at the first ($\sim 150 \text{ m}$) and second ($\sim 300 \text{ m}$) current meters, more intense during spring and weaker in summer and fall (Figure 5.2). The current meter located at 500 m depth has a mean velocity below 5 cm s^{-1} with a similar seasonality as the shallower current meters. On the other hand, the velocity pattern for the current meter located at the depth of the AAIW ($\sim 870 \text{ m}$) changes drastically. Near zero velocities with a small northward trend are found during February to June but from July to November a notable northward intensification of the velocity is found, with values up to $4\text{--}5 \text{ cm s}^{-1}$. From November to late December a drastic southward change of the direction of the velocity is found with sharp values around $5\text{--}6 \text{ cm s}^{-1}$. Finally, the signal found at the deeper current meter, 1230 m , is very variable and practically null although a southward net trend is found during November and December.

5.4 EOF analysis

A previous study in the area suggests a clear vertical structure as defined by NACW, AAIW and MW (Müller and Siedler, 1992). In this section, we apply an Empirical Orthogonal Function (EOF) analysis to determine, firstly, to what extent the current in the Passage can be described as either a two or three-layer domain and, secondly, the influence of the upwelling off northwest Africa on the dynamics of the Lanzarote Passage (Hernández-Guerra and Nykjaer, 1997).

5.4.1 Temporal EOFs with four moorings

A temporal EOF analysis has been done with the nineteen time series available for the passage from 1997 to 1999 (Figure 5.3a). The main aim of this EOF analysis is to find common oscillation patterns at all current meters, in order to describe the processes that force the observed variability of the time series and then try to quantify them.

A Monte Carlo method has been applied as a significance test in order to determine the significant modes in the EOF analysis (Hammersley and Handscomb, 1964). EOF analysis is performed 100 times with nineteen random time series with the same dimension of the original velocity time series. For every analysis, we store the different eigenvalues obtained from the noisy signal, so eigenvalues are considered as significant when they are above 95% of the eigenvalues generated from the noisy signal. Figure 5.3b presents the eigenvalues obtained from the original time series and from the random ones, where we can observe that four eigenvalues fall above the bounds given by the Monte Carlo analysis. These four significant oscillation modes cumulatively explain 86.4% of the overall variance.

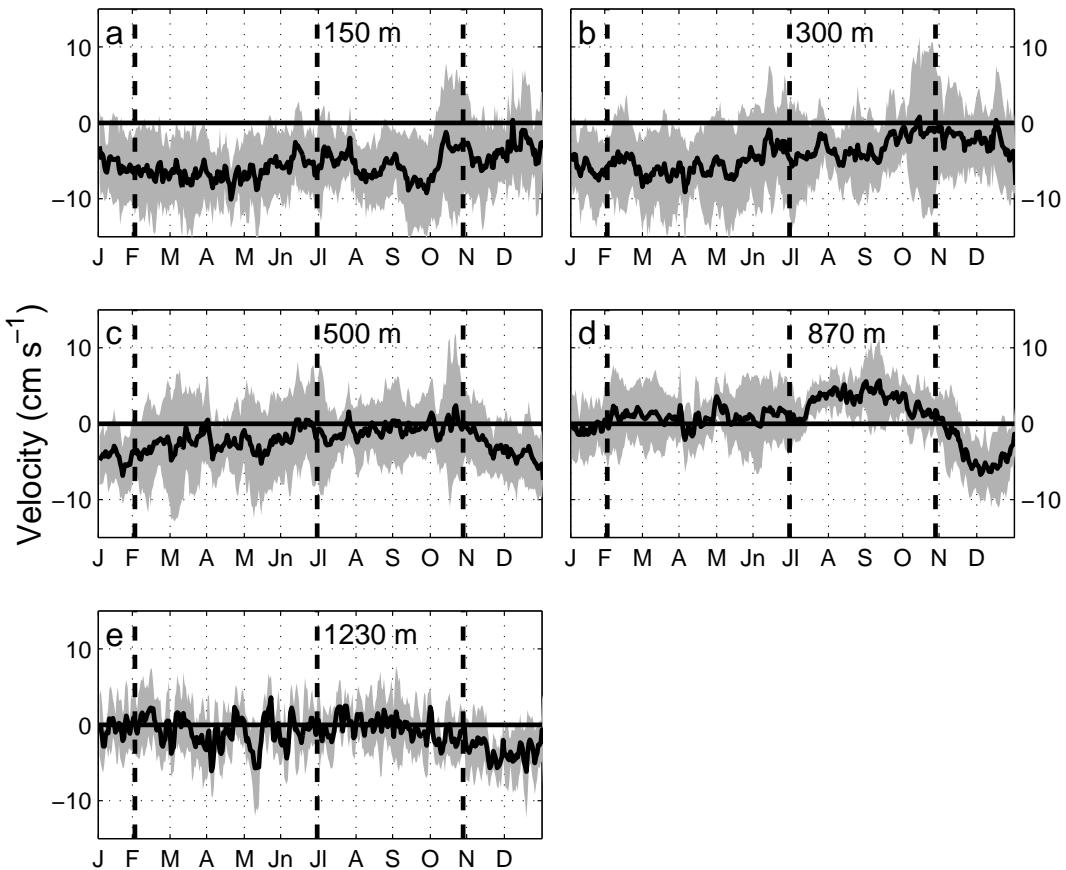


FIGURE 5.2: 9-year average velocity distributions along the maximum variance axis at (a) 150, (b) 300, (c) 500, (d) 870 and (e) 1230 m. The standard deviation is shaded in gray.

Figure 5.3c shows the first significant EOF that explains 56.9% of the variance of the data. This EOF contains positive values in the whole channel, with higher eigenvalues between 400-600 m depth and in the center of the passage, where EBC-4 is located. This pattern seems to be the combination of the barotropic mode with the first baroclinic mode of the quasi-geostrophic dynamics (Müller and Siedler, 1992). The second significant mode that explains 13.2% of the variance, shows a double-cell circulation structure where the upper layer flows in the opposite direction to the intermediate one (Figure 5.3d). The depth of the interface between them roughly matches up with the lower part of the NACW in the passage (Hernández-Guerra et al., 2003). The depth of the interface is shallower at the eastern part of the passage where the upwelling off northwest Africa is located. The third significant mode explaining 11.2% of the data

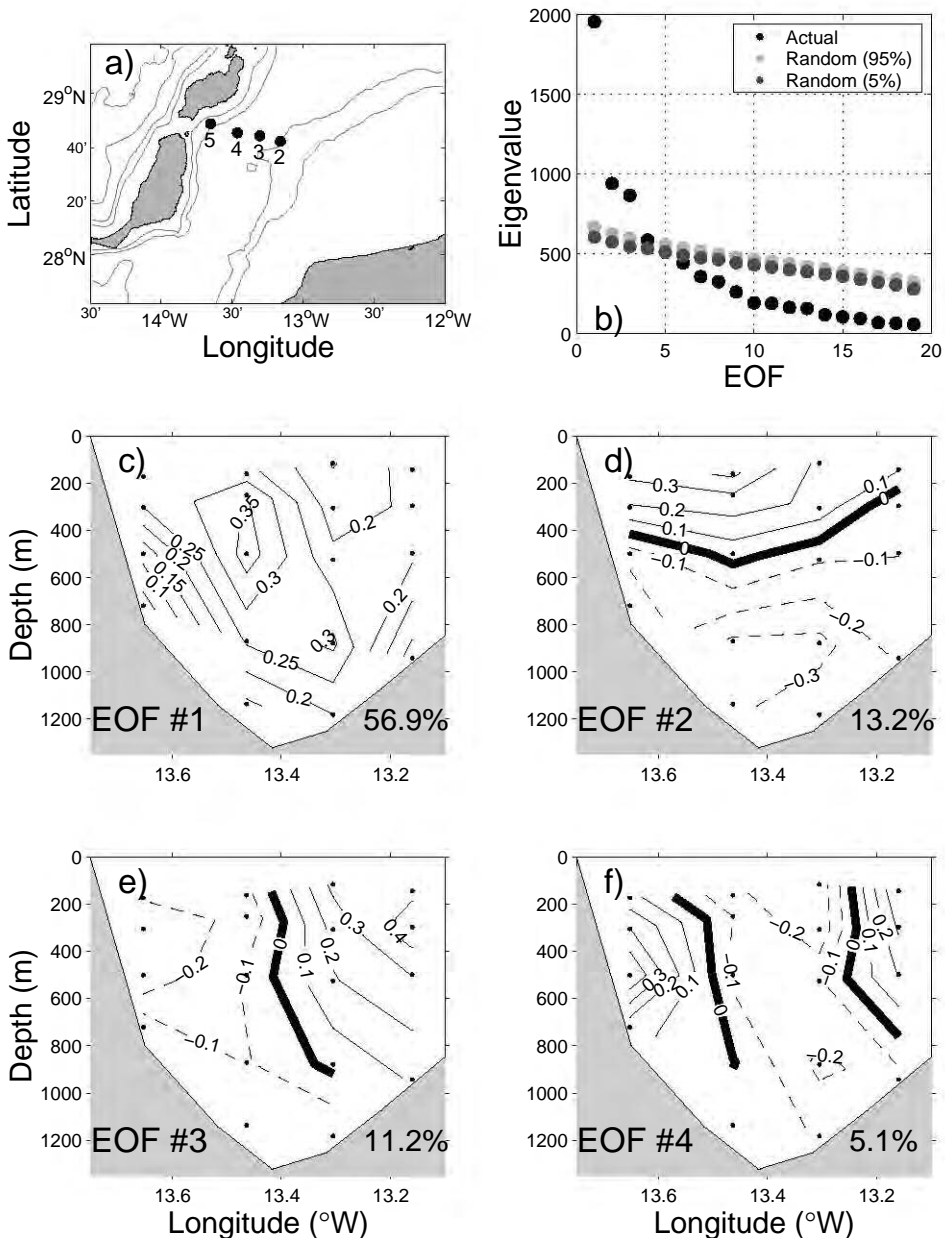


FIGURE 5.3: A spatial Empirical Orthogonal Function (EOF) analysis is carried out with the two years of data from the 4 mooring installed in the Lanzarote Passage (a). (b) shows the Monte Carlo Method in order to determine the significant oscillation modes, (c) to (f) together with the total explained variance for each mode.

variance, marks a difference between the waters close to the continental slope and those close to the Canary Islands (Figure 5.3e). It seems to be related to the different dynamics between the northwest African upwelling system and the Canary Current. It is worth mentioning that the maximum values are found in the upper layer of the upwelling. The fourth significant mode, that explains just 5.1% of the data variance, presents a complex pattern with three vertical regions, one close to the islands, another at the center of the passage and finally one close to the continental shelf (Figure 5.3f).

The amplitudes related to these EOFs are given in Figure 5.4. On the one hand, this figure shows the higher amplitude in the first two modes with respect to the last two, indicating the greater importance of EOFs 1 and 2. On the other hand, a large temporal variability is observed in all of them, as was also observed in the original dataset.

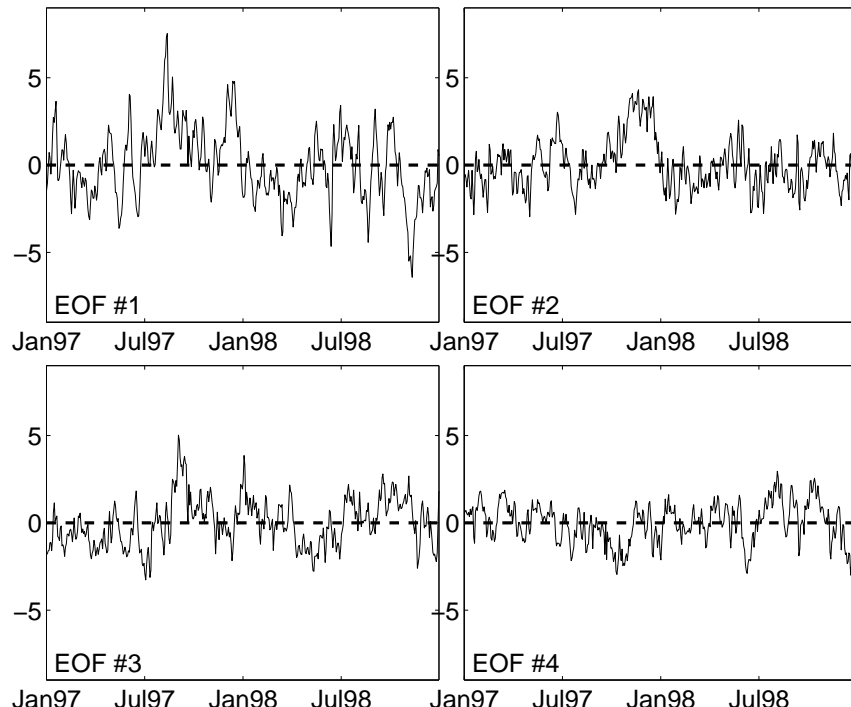


FIGURE 5.4: Temporal amplitude corresponding to the EOF analysis over the four EBC moorings.

5.4.2 Temporal EOFs for the nine-year record

A temporal EOF analysis has been done with the 9-year EBC-4 time series applying the same method as that for the previous section. Figure 5.5a shows the significance test applied to the 9-year time series of the velocities. On this occasion, only two oscillation modes are significant. Figure 5.5b shows the vertical distribution of significant eigenvectors. These two first significant oscillation modes have a similar interpretation as described in section 5.4.1 for the EOF analysis applied to the whole passage. The first mode seems to be a combination of the barotropic mode and the first baroclinic mode of the quasi-geostrophic dynamics. The second one marks the double-cell circulation structure with the NACW flowing southward and the AAIW flowing northward. Temporal amplitudes are given in Figure 5.6 and show a notable temporal variability, similar to that described in the original dataset.

Section 5.4.1 showed that the third significant mode in the previous EOF analysis was related to the upwelling dynamics and it is not present in the temporal EOF analysis. This fact suggests that the upwelling dynamics does not introduce relevant variability at the EBC4 mooring.

Therefore, combining the spatial and temporal EOF analyses, the circulation in the passage can be described as a double-cell circulation, with the upper layer occupied by NACW and a small influence of the upwelling, and the second layer for the intermediate waters occupied by AAIW and MW. Most variability (56%) is related to the barotropic circulation and the first baroclinic mode, while the double-cell circulation and the effect of the upwelling have a weaker influence ($\sim 11\text{-}12\%$).

5.5 Periodic signals

The length of these time series is optimal for detecting long-term periodic phenomena in the passage, from seasonal to inter annual variability. Here we try first a harmonic study, complemented later with a Wavelet analysis.

5.5.1 Harmonic analysis

Due to the fact that our 9-year time series has several gaps, a Fast Fourier Transform can not be used as a method to extract the harmonics in the EBC4 records. We have instead used the technique developed by Lomb (1976) and Scargle (1982) to detect the presence and significance of periodic signals in the unevenly sampled data. The justification for the use of this technique is that it provides a reasonably good approximation of the spectrum obtained by fitting sine waves using least squares to

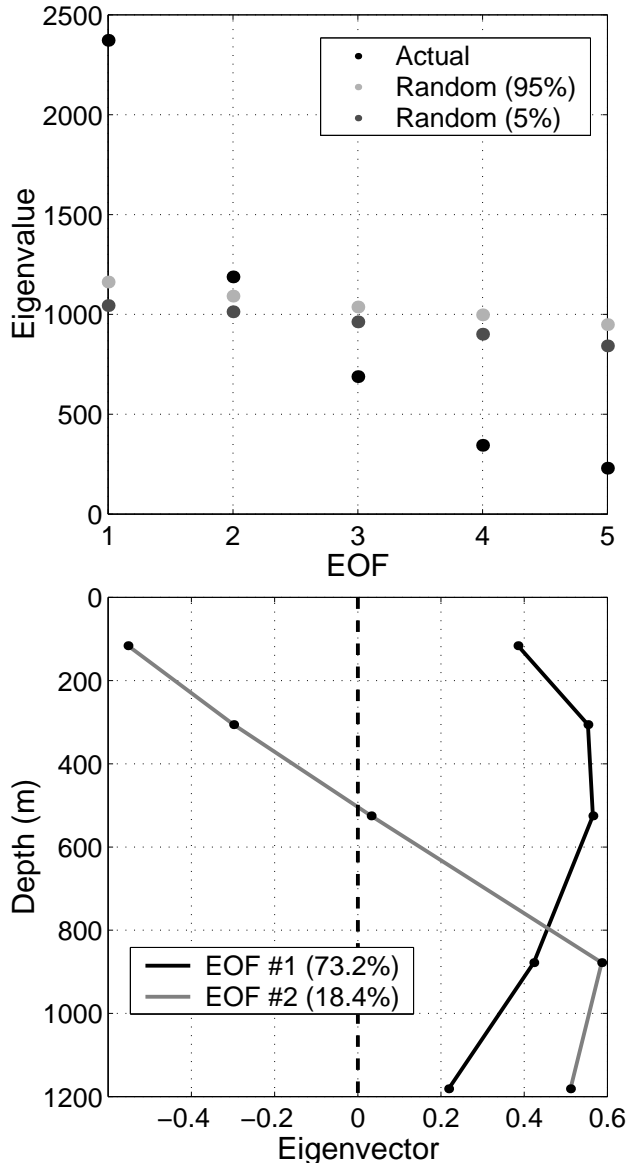


FIGURE 5.5: A temporal EOF analysis is carried out with the 9-year time series in the Lanzarote Passage. (a) shows the Monte Carlo Method to determine the two significant oscillation modes visible in (b), together with the total explained variance for each mode.

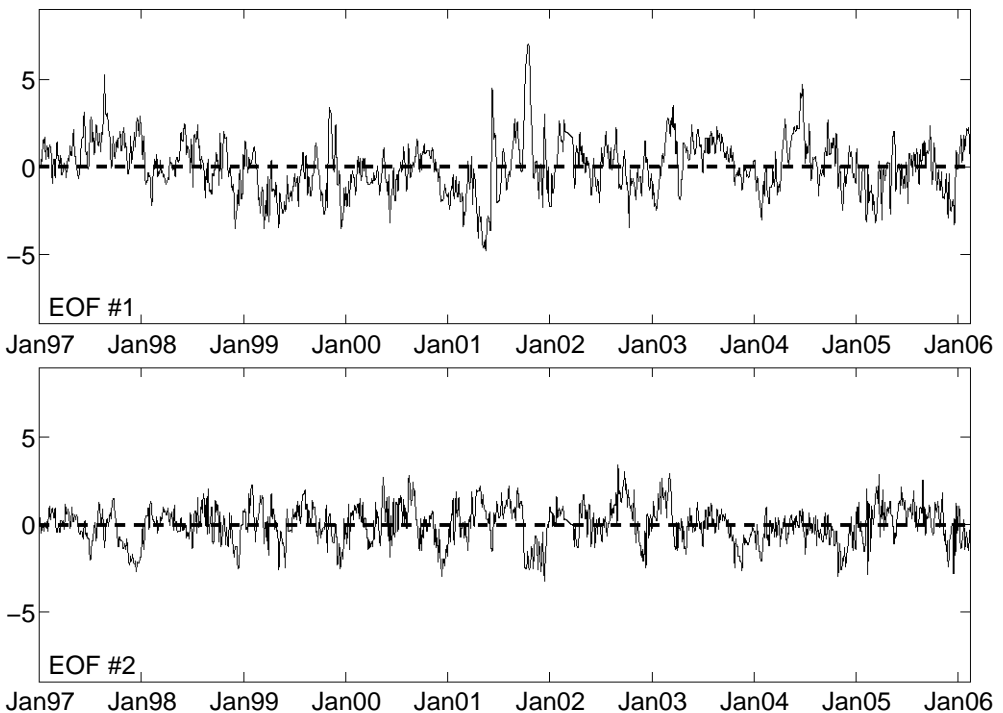


FIGURE 5.6: Amplitude corresponding to the EOF analysis for the EBC4 mooring.

the data and plotting the reduction in the sum of the residuals against frequency. This least-squares spectrum provides the best measure of the power contributed by the different frequencies to the overall variance of the data and can be regarded as the natural extension of Fourier methods to non-uniform data. It reduces to the Fourier power spectrum in the limit of equal spacing. This method has already been applied to the very first four years of this time series (Hernández-Guerra et al., 2003), and we now extend it to the nine-year record in order to detect longer period signals. The only inconvenience in this method is that it is subject to spectral leakage, i.e., the dominant peak appears at the highest frequency and also at other frequencies. Thus, a harmonic function with a period equal to the highest frequency must be subtracted from the original data. The residual is then used to compute the periodogram again and the next frequency of the data is obtained (Lomb, 1976; Scargle, 1982; Hernández-Guerra et al., 2003).

Table 5.2 shows the results of these calculations together with the amplitude, phase

and total variance explained for each frequency contained in every time series. Recall that the shallowest current-meter is not considered in this calculation because of the high number of gaps in the time series. The level of significance of each frequency shown in Table 5.2 is 99.9%. The strongest signal for the time series corresponding to the 300, 520 and 870 m depths is the annual period. Although the annual period also appears in the time series at 1230 m depth, the total variance explained for this period is less than the semi-annual signal, which seems to be dominant in the intermediate and deeper parts of the passage. A significant signal at a period of 3 months appears for each time series. The total variance explained for this period is different between the thermocline and the intermediate-deep waters. This difference is from 10% to 13% at the thermocline waters to 5.4% to 5.6%, at the intermediate and deep waters. This fact shows that the seasonal signal is very important over the whole water column, especially within the thermocline. A significant signal at a period of 2 months is present in the thermocline waters with a low contribution to the total explained variance. Finally, two more signals are present in the time series, the longest one, with an 18-month period at 300 m depth with a total explained variance of 7.3%, and the 9-month period signal that appears at 520 and 870 m depth. The contribution of this last period to the total explained variance is quite small, 1.8% and 2.3%, respectively, but significant.

5.5.2 Wavelet analysis

Once we have examined the periodicities in the frequency domain that have implicitly assumed that the underlying processes are stationary in time, a Wavelet analysis is applied in order to transform the expanded time series into time-frequency space, so that we can find localized intermittent periodicities (Torrence and Compo, 1998; Torrence and Webster, 1999; Grinsted et al., 2004).

Many statistical tests assume that the probability density function (pdf) is close to normal. Different authors point out that series far from the normal distribution produce rather unreliable and less significant results. Occasionally it can therefore be a good idea to transform the pdf of the time series. However, we caution against rashly changing the pdf. The Continuous Wavelet Transform (CWT) is applied to each EBC4 current-meter, immersed in the different water masses found in the Lanzarote Passage (NACW, AAIW and MW).

Figures 5.7a and 5.7b show the continuous wavelet power spectrum for the current-meter immersed in the NACW. There are clearly common features in the wavelet power of the two time series such as the high power for the \sim 1-year (371 days) band over the whole time period, though in 2002 where the presence of this band practically disappears. Two significant peaks in this band are centered around 2000-2002 and 2003-2005 in both current-meters. Both series also have high power in the \sim 9-month

TABLE 5.2: Frequencies contained in the 9-year time series of the component of the velocity along the direction of maximum variance.

| Current meter depth (m) | Frequency months (days) | Amplitude (cm s ⁻¹) | Phase ^a (days) | Total variance explained (%) |
|----------------------------|----------------------------|------------------------------------|------------------------------|---------------------------------|
| 300 | 18 (557) | 1.5 | 183 | 7.3 |
| | 12 (371) | 2.1 | 16 | 11.7 |
| | 6 (196) | 1.2 | -43 | 6.0 |
| | 3 (79) | 1.3 | -60 | 10.0 |
| | 2 (57) | 1.4 | -54 | 4.7 |
| 520 | 12 (371) | 1.6 | 69 | 15.0 |
| | 9 (278) | 0.8 | 62 | 1.8 |
| | 6 (165) | 1.0 | 53 | 4.2 |
| | 3 (79) | 1.2 | -73 | 13.0 |
| | 2 (57) | 1.1 | -35 | 2.9 |
| 870 | 12 (371) | 2.3 | -75 | 19.5 |
| | 9 (278) | 0.8 | -30 | 2.3 |
| | 6 (185) | 2.1 | 10 | 16.0 |
| | 3 (90) | 0.9 | -79 | 5.4 |
| 1230 | 12 (352) | 0.9 | 19 | 3.7 |
| | 6 (188) | 1.1 | 69 | 8.0 |
| | 3 (94) | 1.3 | -81 | 5.6 |

The amplitude and phase correspond to the harmonics matching the data.

^aPhase is relative to January 1.

(278 days) band in the period from 2000-2002, though for the deeper time series the power is not above the 5% significance level. Two significant peaks in the \sim 6-month (165-196 days) band are localized around 2001-2002 for the shallower current-meter and around 2002-2003 for the deeper time series in the NACW. Finally, similar patterns in the \sim 3-month (90 days) bands are found around 2000 for both current-meters, and just one significant peak in 2005 for the shallower current-meter.

Figure 5.7c shows the CWT for the AAIW current-meter time series with three well marked significant bands. The first one is located at the \sim 1-year (371 days) period from 1999-2005, except for the period of time around 2002 where the significance of the band is not above the 5% level. The second one is located in the \sim 6-month (185 days) period from 2000-2004 and finally, the third significant peak in the \sim 3-month (90 days) band is distributed along the time series with 3 significant peaks in 2000, 2001 and 2002.

Figure 5.7d shows the CWT for the MW current-meter time series. The wavelet power pattern for this current-meter is quite different for the shallower current-meters. The \sim 1-year (352 days) band is significant and appears just at the end of the time series around 2003-2005. A significant peak at the \sim 6-month (188 days) band is evident in 2000-2001. A significant peak that does not appear in the harmonic analysis is present in the wavelet power pattern centered at the \sim 135-day band and around 2003. Finally, two significant peaks at the \sim 3-month (94 days) band are seen in 2004 and 2005.

The results obtained from this analysis agree well with the periodicities shown in Table 5.2 for all the current-meters. However, the results add completely new information about the location in time of the periodicities first obtained.

5.6 Variability in mass transport

In this section, we describe the variability in the mass transport according to both the vertical structure in the passage obtained from the EOF analysis and from the significant periodicities presented in section 5. Mass transports are estimated for the whole Lanzarote Passage by using the polynomial function obtained by Hernández-Guerra et al. (2003) in the three water masses present in the area. These water masses have been selected following the definition in the introduction.

5.6.1 Temporal variability

Figure 5.8 shows the temporal variability of mass transport for the NACW, AAIW and MW, respectively. Figure 5.8a shows the time mass transport for the thermocline

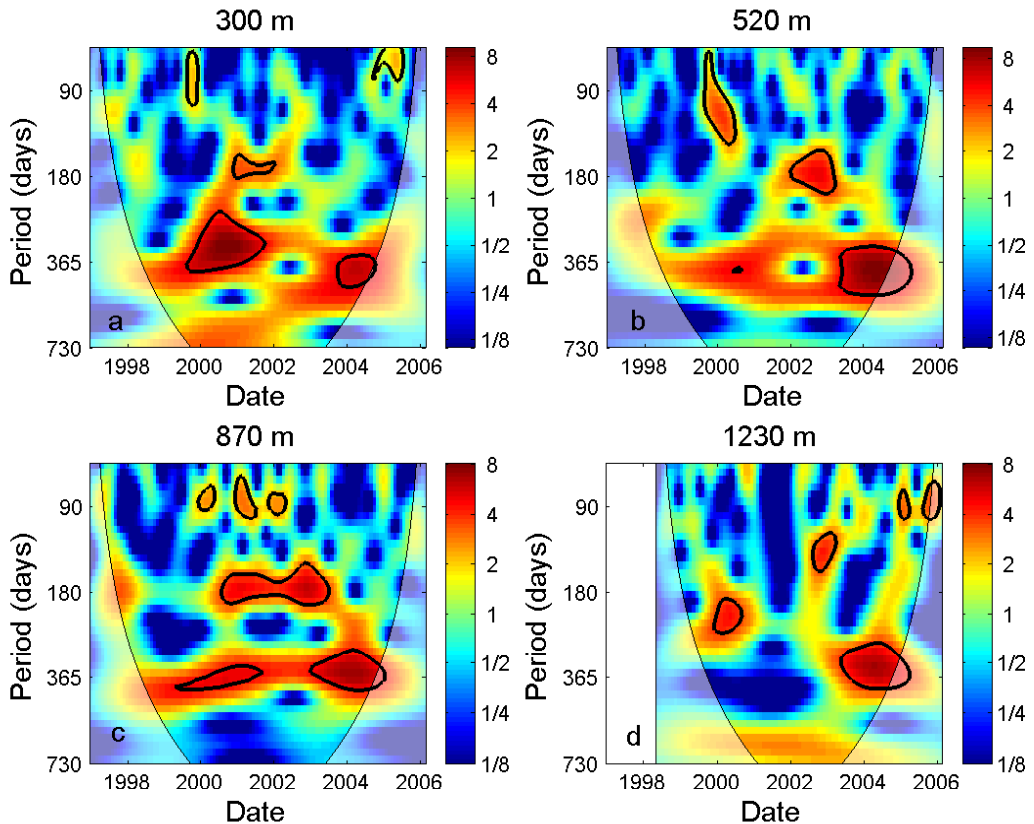


FIGURE 5.7: The continuous wavelet power spectrum for the time series of each current-meter (2-5, a-d) at the EBC4 mooring. The thick black contour shows the 5% significance level against red noise, and the cone of influence (COI) where edge effects might distort the picture is shown as a lighter shade.

water from January 1997 to February 2006. The mean mass transport is -0.81 ± 1.48 Sv, which agrees well with that obtained by Hernández-Guerra et al. (2003) for the first four years of the data (-0.80 ± 1.1 Sv). This fact demonstrates that the mean mass transport for the thermocline waters has not changed in the last 5 years compared with the first four. Fluctuations of the transport time series on a short time scale are large, with a maximum range from -6.65 Sv southward to +6.45 Sv northward.

Figure 5.8b shows the 9-year variability of the mass transport for AAIW in the Lanzarote Passage with a mean value of $+0.09 \pm 0.57$ Sv. This value also agrees with that obtained by Hernández-Guerra et al. (2003), indicating that the mean mass transport for AAIW in the Lanzarote Passage has not significantly changed in the last

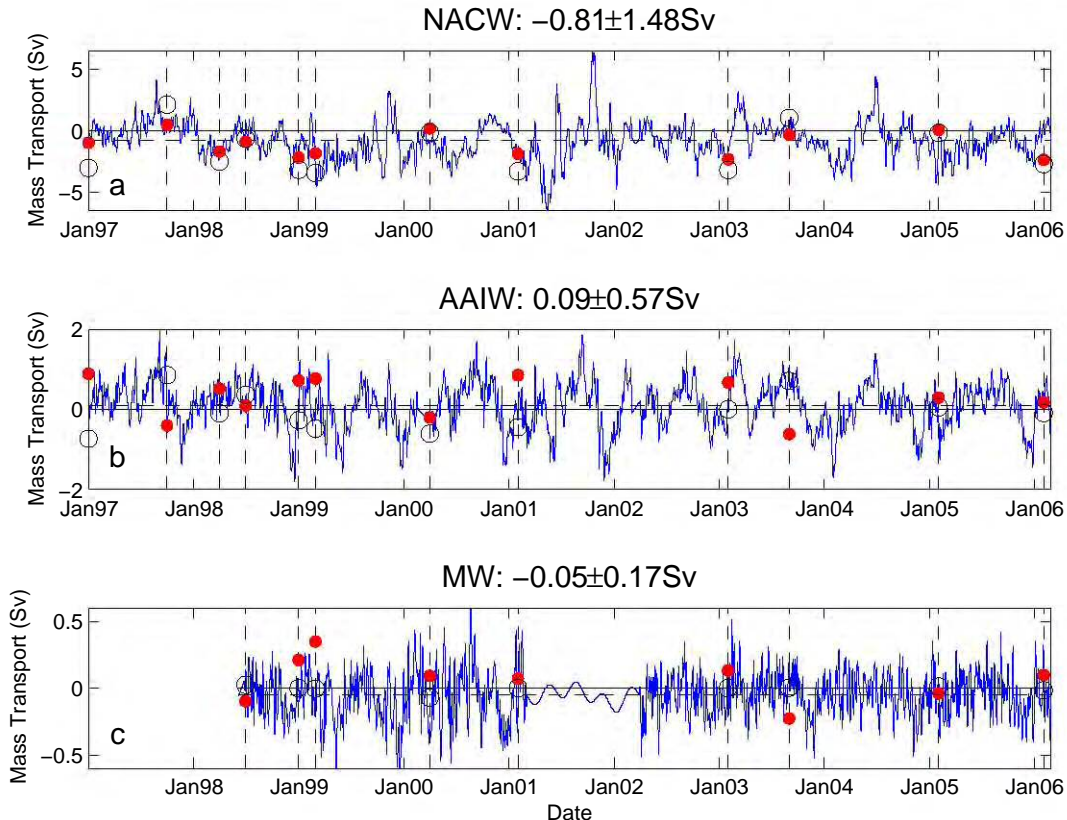


FIGURE 5.8: Estimated mass transport based at the EBC4 mooring for (a) NACW, (b) AAIW and (c) MW together with the geostrophic mass transport estimates from hydrographic stations in the Lanzarote Passage during the different surveys carried out from 1997 to 2006. The transports are smoothed with a 1-month running mean. The means and standard deviations are shown at the top of each subplot. The means are also shown as a horizontal dashed line in each subplot. Note that each subplot has a different scale. Dots represent the geostrophic mass transports computed with a level of no motion at $\gamma_n = 27.3 \text{ kg m}^{-3}$, circles show the geostrophic mass transports with a level of no motion at the bottom.

5-year compared with the first four. The range for AAIW is from 2.0 to -2.0 Sv.

Mass transport for MW is shown in figure 5.8c with a mean value of -0.05 ± 0.17 Sv. This value, as for NACW and AAIW, agrees with that obtained by Hernández-Guerra et al. (2003). Two significant gaps are present in the series, the first from January 1997 to June 1998 and the second from February 2001 to March 2002. The beginning of this series is considered to be at the end of the first gap (June 1998); the second gap has been interpolated using the three significant periods obtained in section 5.5. The range for the MW is from -0.6 to 0.6 Sv.

Figure 5.8 also shows the geostrophic mass transports obtained from the hydrographic stations in the Lanzarote Passage as described in section 5.2.2. Ekman transports obtained across the Lanzarote Passage have been estimated at weekly intervals based on ERS-2 data (January 1997-June 1999) and QuikScat data (July 1999-February 2006). Ekman transport has been added to the very first layer in order to take into account the effect of the wind component on the geostrophic mass transport. Geostrophic mass transports obtained using a level of no motion at the neutral density level located between NACW and AAIW have better agreement with the 9-year mass transport of the EBC4 than those using the bottom level.

Hernández-Guerra et al. (2002) estimated the mass transport in the thermocline layer from XBT data in the Lanzarote Passage. They estimated the mass transport every two months for two years using a θ/S relation from historical CTD data. Figure 5.9 shows that the XBT mass transport and the mass transport estimated from EBC4 present a similar shape, indicating that the mass transport obtained with EBC4 is in good agreement with results obtained previously with other types of data.

5.6.2 Seasonal variability

A canonical year is generated by averaging daily mean values over the nine years of data in order to obtain the mean monthly and seasonal variability of mass transport for NACW, AAIW and MW (Figure 5.10). The quantification of the seasonal mass transport for NACW, AAIW and MW during the last nine years are presented in Tables 5.3, 5.4 and 5.5, respectively.

Figure 5.10a shows that the monthly mean mass transports for NACW are southward throughout the year except from late October to the beginning of November, when it is approximately null. As shown in Table 5.3, the seasonal mass transport is maximum in winter (-1.30 ± 1.29 Sv), decreasing in spring (-0.99 ± 1.59 Sv) and summer (-0.57 ± 1.13 Sv), and having its minimum value in fall (-0.44 ± 1.50 Sv).

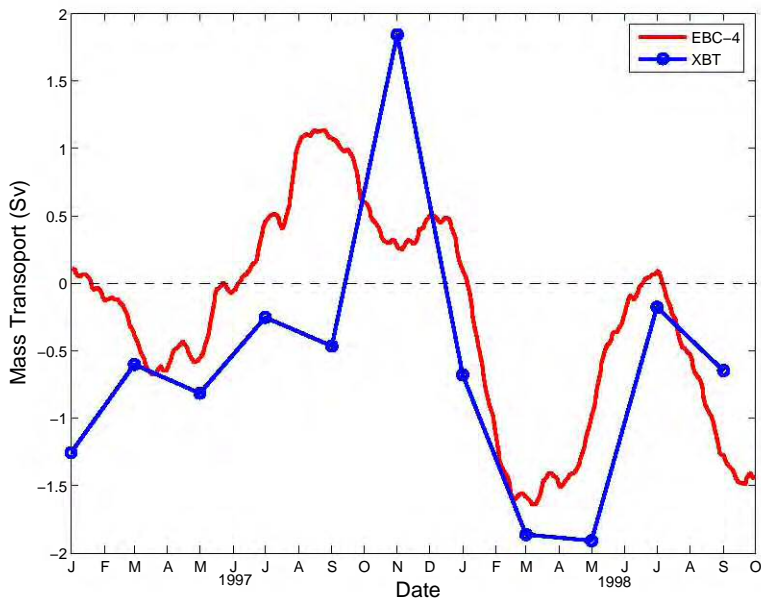


FIGURE 5.9: Estimated mass transport based on the EBC-4 mooring for NACW, and the estimates obtained from XBT data and a θ/S relation from historical CTD data. A running filter of 1-month has been applied to the mass transport from the EBC4 data.

Monthly mass transports for AAIW are shown in figure 5.10b that present a different pattern than NACW. Northward transport is observed along the year except from November to January. December is the month with maximum southward transport of -0.65 Sv. Maximum northward transports of +0.53 Sv and +0.50 Sv are found in August and September, respectively. At the seasonal scale, Table 5.4 shows that winter has a practically null mass transport of $+0.02 \pm 0.47$ Sv. During spring and summer, mass transport of AAIW is northward with a mean value of $+0.12 \pm 0.48$ Sv and $+0.44 \pm 0.37$ Sv, respectively. In contrast, winter has a southward transport of -0.23 ± 0.57 Sv.

Figure 5.10c shows the monthly mean transport for MW. Transport is very low with a maximum southward transport in December (-0.19 ± 0.15 Sv). Mean seasonal transport is always southward (Table 5.5) ranging from -0.01 ± 0.10 Sv in summer to -0.04 ± 0.11 Sv in spring. Nonetheless, southward mass transport in fall is three times greater than that found in spring (-0.12 ± 0.12 Sv).

TABLE 5.3: Seasonal, annual and 9-year mean mass transports for NACW (surface-27.3 kg m⁻³; 0-600 m) from 1997 to 2005.

| Years | Winter | Spring | Summer | Fall | Annual |
|--------|------------|------------|------------|------------|------------|
| 1997 | -0.24±0.45 | -0.28±0.78 | +0.92±0.78 | +0.48±0.59 | +0.22±0.83 |
| 1998 | -1.25±0.90 | -0.62±0.81 | -0.84±0.77 | -0.98±1.07 | -0.92±0.92 |
| 1999 | -1.69±1.42 | -2.21±0.42 | -1.32±0.96 | -0.91±2.15 | -1.53±1.47 |
| 2000 | -1.42±0.81 | -1.77±0.80 | -1.41±0.87 | +0.51±0.42 | -1.02±1.16 |
| 2001 | -1.78±0.94 | -2.66±2.73 | -0.96±1.31 | +0.86±2.52 | -1.14±2.41 |
| 2002 | -0.89±1.05 | -0.43±0.80 | -0.42±0.74 | -1.26±0.85 | -0.75±0.93 |
| 2003 | -0.00±1.69 | -0.07±0.78 | -0.03±0.48 | -0.89±0.39 | -0.25±1.04 |
| 2004 | -2.31±0.76 | +0.36±0.71 | -0.42±1.35 | -0.55±0.91 | -0.73±1.56 |
| 2005 | -2.13±0.92 | -1.21±0.71 | -0.61±0.61 | -1.25±0.82 | -1.30±0.94 |
| 9-year | -1.30±1.29 | -0.99±1.59 | -0.57±1.13 | -0.44±1.50 | -0.81±1.48 |

TABLE 5.4: Seasonal, annual and 9-year mean mass transports for AAIW (27.3-27.7 kg m⁻³ ; 600-1100 m) from 1997 to 2005.

| Years | Winter | Spring | Summer | Fall | Annual |
|--------|------------|------------|------------|------------|------------|
| 1997 | +0.24±0.23 | +0.34±0.35 | +0.68±0.38 | -0.23±0.36 | +0.26±0.47 |
| 1998 | +0.20±0.17 | +0.36±0.23 | +0.29±0.36 | -0.28±0.63 | +0.14±0.46 |
| 1999 | +0.22±0.36 | -0.48±0.50 | +0.27±0.25 | -0.26±0.56 | -0.06±0.54 |
| 2000 | -0.21±0.28 | +0.06±0.38 | +0.64±0.33 | +0.00±0.68 | +0.13±0.54 |
| 2001 | -0.26±0.33 | -0.08±0.59 | +0.59±0.48 | -0.36±0.77 | -0.03±0.68 |
| 2002 | +0.14±0.47 | -0.03±0.32 | +0.34±0.34 | -0.06±0.48 | +0.10±0.43 |
| 2003 | +0.45±0.61 | +0.12±0.38 | +0.57±0.27 | -0.32±0.37 | +0.20±0.55 |
| 2004 | -0.43±0.47 | +0.45±0.42 | +0.19±0.28 | -0.26±0.52 | -0.02±0.55 |
| 2005 | -0.20±0.35 | +0.31±0.23 | +0.44±0.27 | -0.33±0.53 | +0.05±0.49 |
| 9-year | +0.02±0.47 | +0.12±0.48 | +0.44±0.37 | -0.23±0.57 | +0.09±0.57 |

TABLE 5.5: Seasonal, annual and 9-year mean mass transports for MW ($\gamma_n > 27.45 \text{ kg m}^{-3}$; 900-bottom) from 1997 to 2005.

| Years | Winter | Spring | Summer | Fall | Annual |
|--------|------------|------------|------------|------------|------------|
| 1997 | — | — | — | — | — |
| 1998 | — | +0.01±0.01 | -0.03±0.08 | -0.12±0.10 | -0.04±0.08 |
| 1999 | -0.05±0.15 | -0.13±0.15 | -0.01±0.09 | -0.21±0.17 | -0.10±0.16 |
| 2000 | +0.01±0.15 | -0.09±0.19 | +0.05±0.20 | -0.14±0.16 | -0.04±0.19 |
| 2001 | -0.04±0.15 | -0.04±0.04 | -0.02±0.04 | -0.09±0.03 | -0.04±0.09 |
| 2002 | -0.07±0.06 | -0.09±0.12 | -0.02±0.11 | -0.10±0.08 | -0.07±0.10 |
| 2003 | +0.01±0.10 | -0.03±0.10 | +0.03±0.07 | -0.13±0.11 | -0.03±0.11 |
| 2004 | -0.01±0.10 | -0.01±0.08 | -0.05±0.11 | -0.13±0.12 | -0.05±0.11 |
| 2005 | -0.07±0.10 | +0.01±0.08 | -0.01±0.08 | -0.14±0.11 | -0.05±0.11 |
| 9-year | -0.03±0.11 | -0.04±0.11 | -0.01±0.10 | -0.12±0.12 | -0.05±0.17 |

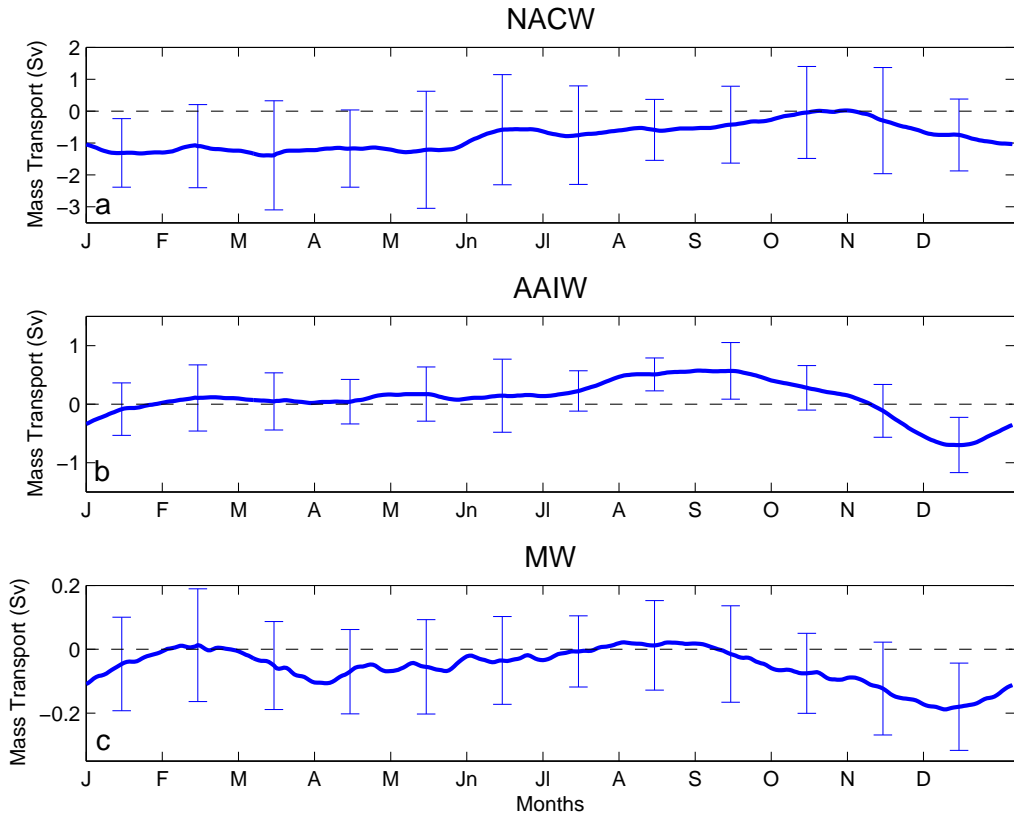


FIGURE 5.10: Seasonal variability of the mass transport computed with daily means for each year for (a) NACW, (b) AAIW and (c) MW. Monthly variability is shown as a standard deviation for every month. Note that each subplot has a different scale.

5.6.3 Inter-annual variability

Figure 5.11 shows the inter-annual variability of mass transports computed as cumulative monthly mass transports for each water mass. 9-year time series have been divided into 5 different periods of time: P1, from January 1997 to September 1998, P2, from September 1998 to July 2000, P3, from July 2000 to March 2003, P4, from March 2003 to November 2003 and P5, from November 2003 to February 2006. These different periods correspond to changes in the cumulative mass transport trends respect to the 9-years mean mass transports for the different water masses.

Figure 5.11a shows a practically null accumulated mass transport for NACW for the period P1. During P2, there is a clear monotonic increase of accumulated mass

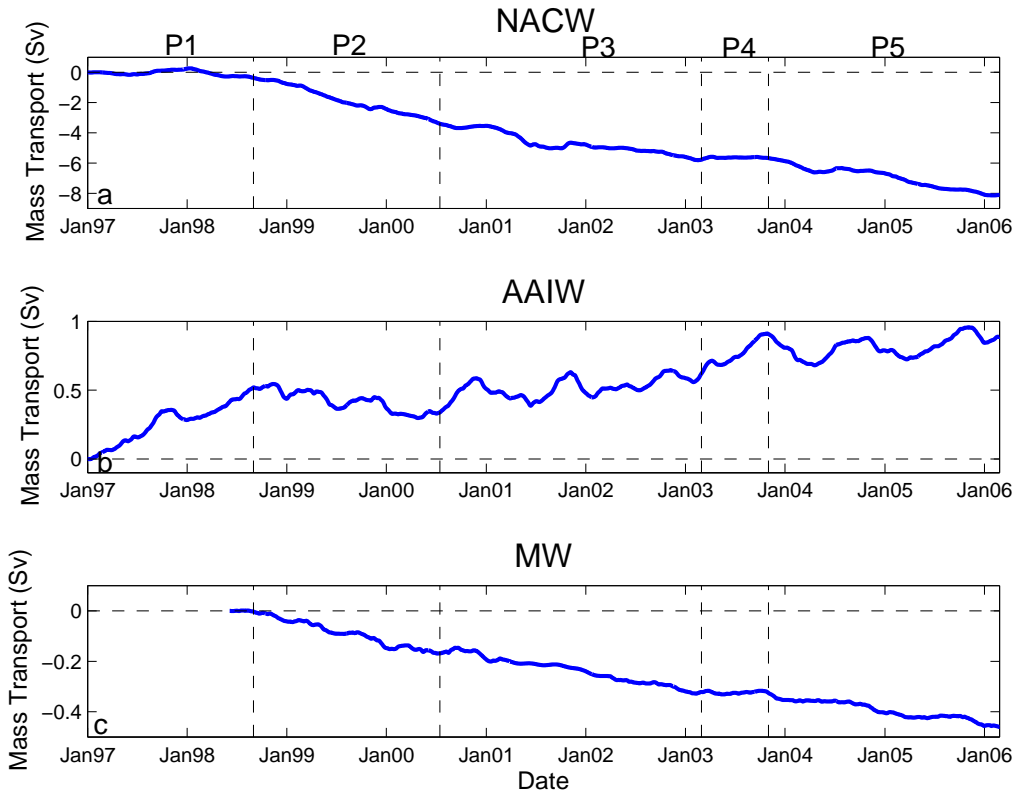


FIGURE 5.11: Inter-annual variability of the mass transports computed as cumulative monthly means for each year for (a) NACW, (b) AAIW and (c) MW.

transport. The yearly mean in this period, -1.50 Sv, is double the 9-year mean. During P3, the slope of the NACW accumulated mass transport decreases and the yearly mean, -0.83 Sv, is close to the 9-year mean. P4 has a null accumulated mass transport, similar to P1. During P5, the yearly mean mass transport is similar to the 9-year mean mass transport.

Figure 5.11b shows a tripling of the AAIW mass transport trend during P1, with a mean value around +0.28 Sv. During P2, a change of sign in the AAIW trend is found with a mean value of -0.09 Sv. This change in the sign of the trend is followed by a new change in the trend during P3, when the 9-year mean trend for AAIW is recovered. P4 is characterized by a quadrupling of the mean trend, with a value around +0.39 Sv. Finally, during P5, the cumulative mass transport of AAIW keeps increasing its value following the 9-year mean trend. The cumulative mass transport of AAIW clearly shows the maximum values obtained for this water mass during November over the

whole time series, as well as the minimum values in January.

Figure 5.11c shows the cumulative mass transport of MW, which follows the same pattern as the cumulative mass transport of NACW. A gap in the initial velocities is found in P1, so the mass transport could not be obtained. During P2, the mean trend almost doubles the 9-year mean of MW mass transport, -0.08 Sv. P3 and P5 follow the 9-year mean of the mass transport, with a mean value of -0.05 Sv. During P4 a practically null mean mass transport in the MW is found.

5.7 Results and discussion

In this study, one of the longest current-meter velocities time series in the Eastern North Atlantic Subtropical Gyre have been used to quantify the 9-year, inter-annual and seasonal mass transport variability for NACW, AAIW and MW measured in the Lanzarote Passage. Hernández-Guerra et al. (2003) published the annual mean mass transport in the Passage for the first four years of the full data record. These values were -0.8 ± 1.1 Sv to the south for NACW, $+0.1 \pm 0.4$ Sv to the north for AAIW, and -0.05 ± 0.09 Sv to the south for MW. At present, the EBC4 mooring record has 5 more years of information, and reveals that the yearly mean mass transport for the three water masses present in the area has not changed significantly over the last 5 years. The new annual mean mass transports quantified in this study are: -0.81 ± 1.48 Sv for NACW, $+0.09 \pm 0.57$ Sv for AAIW and -0.05 ± 0.17 Sv for MW. Two different data sets have corroborated the mass transports obtained at the EBC4 mooring in the Lanzarote Passage. Firstly, geostrophic mass transports obtained from 12 hydrographic sections in the Passage during 1997-2006 and, secondly, the computed mass transports for NACW obtained from XBT data and the θ/S relation from historical CTD data, which demonstrated for the first time the NACW flow reversal in November in the Lanzarote Passage.

A canonical year has been generated by averaging daily mean values over the nine years of data in order to obtain the mean monthly and seasonal variability of the mass transport for the three water masses present in the Lanzarote Passage. The NACW seasonal pattern is characterized by a maximum southward transport in winter (-1.30 ± 1.29 Sv), decreasing in spring and summer, with the minimum mass transport in fall (-0.44 ± 1.50 Sv). This pattern differs from that expected given the Trade winds seasonal variability, which presents its maximum intensity during summer. The offshore diversion of the southward Canary Current at Cape Ghir might be a plausible explanation for this seasonal pattern found in the Lanzarote Passage (Navarro-Pérez and Barton, 2001). On this basis, Pelegri et al. (2005a) have also suggested that by late fall, southward transport of the Canary Current is maximum and the flow becomes unstable and separates from the coast, retaking its southward motion further west between the central or western Canary Islands. At this time, the Lanzarote Passage

might support northward transports as shown in table 5.3. Similar results has been obtained by a high resolution numerical model in the area of study (Mason, 2009).

Seasonal mass transport for AAIW shows notable differences with respect to the NACW pattern. During winter, when the NACW mass transport reaches its maximum southward value, AAIW mean mass transport is practically zero ($+0.02 \pm 0.47$ Sv) although the root mean square is 0.28 Sv. This fact reflects that during winter, the mass transport of AAIW has a mean intensity of 0.28 Sv with a north/south direction (northward $+0.25$ Sv / southward -0.28 Sv). During spring and summer, the mass transport of AAIW is northward with a 9-year mean values of around $+0.12 \pm 0.48$ Sv and $+0.44 \pm 0.37$ Sv, respectively. August and September are the summertime months where a maximum northward AAIW flow is found over the whole time series. After this northward intensification of AAIW mass transport, a southward transport is found in December over the whole time series, with a mean value of -0.66 ± 0.49 Sv. MW over the first half of a year has seasonal mean mass transports of -0.03 ± 0.11 Sv and -0.04 ± 0.11 Sv, for winter and spring, respectively. During summer, a reduction of a flow is found with a mean value of -0.01 ± 0.10 Sv rapidly increasing in fall to a mean value of -0.12 ± 0.12 Sv. The maximum value is reached in December, -0.19 ± 0.15 Sv. The two deepest current-meters and salinity records of the EBC4 mooring for the same period of time of our study have been used by Machín and Pelegri (2009); Machín et al. (2010) to explain the seasonal variability of the intermediate waters. These authors have confirmed by means of a Sverdrup-type model that the summer northward progression of AAIW by a fall intense flow reversal of MW is associated to stretching or shrinking of the intermediate water strata.

The inter-annual variability of the mass transport suggests the existence of 5 different periods of time where the cumulative monthly mass transport trend changes for the three water masses present in the area (P1-P5, Figure 5.11). During the P1 and P4 time periods the mass transport for NACW and MW is practically null; however, during the same period of time, the AAIW 9-year mean trend mass transport increases by factors of 3 and 4, respectively. During P2, the accumulated mass transport trend for NACW and MW starts increasing by a factor of 2, while the AAIW trend changes its sign. Finally, during P3 and P5, NACW, AAIW and MW return to the normal 9-year mean trend.

The P-Periods described in this study seem to be related to the instability of the Canary Current north of the Canary Archipelago, as we have commented on above, together with the combination of the different phases of the North Atlantic Oscillation (NAO) index. Positive NAO phases are found during all of the periods except P2. During these positive phases, the predominant northeastern Trade Winds are intensified (Czaja and Marshall, 2000), reducing the southward NACW mass transport at the Lanzarote Passage and favoring the northward mass transport of the AAIW. During late 1998 to mid 2000 (P2), a negative NAO phase is found which might be related to the increasing

of the NACW mean mass transport trend. However, further investigation is needed in order to demonstrate the significance of this relationship.

Results from the first year of the RAPID/MOCHA array have demonstrated the ability of the observing system to continuously measure the strength and vertical structure of the Atlantic MOC (Kanzow et al., 2007; Chidichimo et al., 2010). The inter-annual variability in the Atlantic MOC should be defined with a resolution of 1.5 Sv (Cunningham and Alderson, 2007) because that is the order of magnitude of mass transport fluctuation in the Lanzarote Passage. On this basis, and in order to conclude this study, the strong transport fluctuations at seasonal and inter-annual time scales in the Eastern Boundary Current of the North Atlantic Subtropical Gyre demonstrates that the Eastern Boundary Current transport has a significant impact on Meridional Overturning estimates, indicating that in order to understand MOC variability, transport estimates in the eastern Atlantic margin are necessary.

Part III

The NW African Upwelling System

CHAPTER 6

Three-dimensional circulation in the NW Africa Coastal Transition Zone

Verónica Benítez-Barrios¹, Jose Luis Pelegrí², Alonso Hernández-Guerra¹, Kamazima M.M. Lwiza³, Damiá Gomis⁴, Pedro Vélez-Belchí⁵ and Santiago Hernández-León¹

¹ Facultad de Ciencias del Mar, Universidad de Las Palmas de Gran Canaria, Las Palmas, Spain.

² Institut de Ciències del Mar (CSIC), Barcelona, Spain.

³ School of Marine and Atmospheric Sciences, State University of New York, Stony Brook, NY, USA

⁴ Institut Mediterrani d'Estudis Avançats (CSIC-UIB), Palma de Mallorca, Spain

⁵ Instituto Español de Oceanografía, Centro Oceanográfico de Canarias, Santa Cruz de Tenerife, Spain.

Abstract

High-resolution data collected southeast of the Canary Islands during late winter 2006 are analyzed to describe the hydrography and three-dimensional circulation in the coastal transition zone off NW Africa. The data are optimally interpolated over a regular grid and the Q-vector formulation of the omega equation is used to compute the quasi-geostrophic (QG) mesoscale vertical velocity. The coastal transition zone is divided into upwelling, frontal and offshore regions from their physical and dynamic characteristics. The upwelling region is characterized by cold and weakly stratified waters flowing towards the equator, with a poleward undercurrent of approximately 0.05 m s^{-1} over the continental slope. The frontal region is characterized by a southwestward baroclinic jet associated with cross-shore raising isopycnals; the jet transport is close to 1 Sv , with maximum velocities of 0.18 m s^{-1} at surface decreasing to 0.05 m s^{-1} at 300 db . Vertical sections across the frontal region show the presence of deep eddies probably generated by the topographic blocking of the islands to the southward current, as well as much shallower eddies that likely have arisen as instabilities of the baroclinic upwelling jet. The QG mesoscale vertical velocity field is patchy, ranging from -18 to 12 m day^{-1} , with the largest absolute values corresponding to an anticyclonic eddy located south of Fuerteventura island. These values are significantly larger than the diapycnal vertical velocities associated with the frontal region (mean value of about 5 m day^{-1}); they are

also larger than the wind-induced vertical velocities generated offshore, as a result of the wind stress horizontal divergence (a fraction of a meter per day), and in the upwelling region, due to the coastal constraint (about 2 m day^{-1}). However, the patchiness in the QG mesoscale vertical velocity causes the integrated mesoscale vertical transport (0.01 Sv) to be one order of magnitude smaller than either the coastal Ekman transport (0.07 Sv), the integrated Ekman pumping (-0.05 Sv) or the diapycnal transfer (0.18 Sv). The pattern of the near-surface fluorescence field is a good indicator of these different contributions, with large homogeneous values in the coastal upwelling region and a patchy structure associated with the offshore mesoscale structures.

KEYWORDS: Eastern boundaries; Canary Upwelling System; Quasi-geostrophic Omega Equation; Vertical velocity; Frontal system; Nutrient supply

Under revision in *Progress in Oceanography*.

Contents

| | | |
|------------|--|------------|
| 6.1 | Introduction | 90 |
| 6.2 | Data analysis | 92 |
| 6.2.1 | Dataset | 92 |
| 6.2.2 | Optimal statistical interpolation | 94 |
| 6.3 | Methodology to estimate vertical velocities | 95 |
| 6.3.1 | Quasi-geostrophic mesoscale vertical velocities | 96 |
| 6.3.2 | Wind-induced and diapycnal vertical velocities | 98 |
| 6.4 | Distribution and transport of properties | 99 |
| 6.4.1 | Horizontal structure | 99 |
| 6.4.2 | Vertical structure | 104 |
| 6.4.3 | Water transports | 106 |
| 6.4.4 | Vertical velocity fields | 108 |
| 6.5 | Discussion | 111 |
| 6.5.1 | The upwelling, frontal and offshore regions | 111 |
| 6.5.2 | Origin of mesoscale structures | 115 |
| 6.5.3 | Fluorescence distribution | 117 |
| 6.6 | Conclusions | 118 |

6.1 Introduction

The most prominent characteristic of the coastal transition zone (CTZ) off NW Africa is the presence of a coastal upwelling frontal system, a transition region between stratified offshore waters and relatively homogeneous upwelled waters. The visible, sea-surface, expression of this frontal system is usually simply referred as front (Bowman and Iverson, 1978). This CTZ has received considerable attention in the past. Major research started during the Cooperative Investigation of the Northern Part of the Eastern Central Atlantic (CINECA), held between 1970 and 1977, with nearly one hundred scientific cruises aimed at studying the upwelling region off NW Africa (e.g. Hughes and Barton, 1974; Mittelstaedt et al., 1975; Brockman et al., 1977; Tomczak, 1978; Manríquez and Fraga, 1982; Mittelstaedt, 1983). During the eighties the focus of the research turned to the deep ocean, partly motivated by regional political instability and partly because of the global objectives of the World Ocean Circulation Experiment (e.g. Käse et al., 1986; Krauss, 1986; Fiekas et al., 1992; Müller and Siedler, 1992; Arhan et al., 1994). Since the beginning of the nineties major attention shifted to the physical and biological characteristics of mesoscale structures, eddies and filaments, either associated to the Canary Islands or to the upwelling region (e.g. Arístegui et al., 1994; Hagen et al., 1996; Barton et al., 1998; Sangrà et al., 2005; Sangrà et al., 2007, 2009).

During the late nineties the Canary Islands Azores Gibraltar (CANIGO) project had sufficient spatial coverage and resolution to investigate the CTZ off NW Africa (Parrilla et al., 2002). In the lifetime of CANIGO, permanent moorings, scientific and opportunity cruises, and remote sensing data provided an improved view of the spatio-temporal variability of the NW Africa system (e.g. Van Camp et al., 1991; Nykjaer and van Camp, 1994; Hernández-Guerra and Nykjaer, 1997; Pacheco and Hernández-Guerra, 1999; Hernández-Guerra et al., 2001; Knoll et al., 2002; Tejera et al., 2002; Hernández-Guerra et al., 2003; Pelegrí et al., 2005a; Pelegrí et al., 2005b; García-Muñoz et al., 2005; Machín et al., 2006a). One of the main outcomes of the CANIGO program was to realize that a major fraction of the eastern boundary recirculation of central waters, or Canary Current (CC), occur in the CTZ, a relatively narrow region where intense transfer takes place between subsurface and surface waters. This easternmost branch of the CC, linked to the coastal upwelling jet, has been referred as the Canary Upwelling Current (CUC) (Pelegrí et al., 2005b, 2006). The existence of such localized along-slope, equatorward, transport has also been realized and described for another major eastern boundary region, the California Current System (e.g. Huyer et al., 1998, , and references therein).

All the above studies have greatly contributed to the knowledge of the CTZ in terms of physico-biogeochemical water properties and meso- and large-scale structures, horizontal circulation and spatio-temporal variability. Nevertheless, the delicate interplay of horizontal and vertical motions in the CTZ yet remains quite unknown.

The complexity of estimating the three-dimensional (3D) flow lies on the difficulty to measure the vertical velocity. Horizontal velocities in the CTZ have been determined either from drifters (Barton et al., 2004; Sangrà et al., 2005; Sangrà et al., 2007), altimetry data (Sangrà et al., 2009), moored current-meters (Hernández-Guerra et al., 2003), ship-borne ADCP (Knoll et al., 2002) or by applying the thermal wind relation to density profiles (Hernández-Guerra et al., 2001; Barton et al., 2004; Hernández-Guerra et al., 2005; Sangrà et al., 2007). The vertical velocity associated to the internal wave field may reach up to $O(10^{-2}) \text{ m s}^{-1}$, therefore also being a measurable variable (van Aken et al., 2007). However, these are relatively fast motions, with time scales from minutes to hours. Mesoscale and wind-driven vertical velocities, with time scales from days to weeks, are notoriously difficult to measure because of their small magnitude, typically five to six orders of magnitude less than the horizontal velocities. They have to be inferred indirectly, from a laborious analysis of the distribution of other measured variables, hence very little is yet known about their spatial structure in the CTZ. Hereafter, when we refer to vertical motions we will always be talking about those related to mesoscale and wind-induced processes.

Vertical motions at the CTZ may arise from several mechanisms: (1) as the result of wind forcing via both normal-to-shore Ekman transport and Ekman pumping, (2) through diapycnal mixing at the upwelling frontal system, and (3) because of ageostrophic imbalances associated to mesoscale dynamics. Inhomogeneities in Ekman transport, either because of the coastal constraint or because of spatial variations in surface winds, induce Ekman convergence or divergence. Such convergent and divergent motions lead to vertical displacements of the isopycnals, e.g. in the CTZ divergence causes upwelling and the appearance of cold waters at the surface. First, the wind-induced contribution may be directly estimated from the local winds. Second, the frontal region is often critically stable (Kundu and Beardsley, 1991), i.e. the gradient Richardson number is close to a critical value, and may undergo intense diapycnal mixing. This contribution is difficult to assess and here we will estimate it by assuming that the net vertical transfer has to close the large-scale horizontal balance, essentially the same procedure followed by inverse models (e.g. Machín et al., 2006a). Finally, there are vertical motions associated with different phases of mesoscale structures, analogous to what happens in atmospheric motions (Keyser and Shapiro, 1986). We will assess them through the Q-vector version of the quasi-geostrophic (QG) omega equation (Hoskins et al., 1978), a procedure widely used in the literature (Tintoré et al., 1991; Pollard and Regier, 1992; Allen and Smeed, 1996; Rudnick, 1996; Gomis et al., 2002; Mouriño et al., 2004; Shearman et al., 1999).

This work aims at investigating the 3D circulation in the CTZ off NW Africa, with special attention to two aspects. First, we explore the characteristics of the different dynamic regimes encountered as we move in the cross-shore direction away from the continental platform. In particular, we demonstrate that the frontal region not only separates upwelling from offshore waters but is also a source of shallow baroclinic

mesoscale features, substantially different from the more barotropic eddies generated through the interaction of the CC with the islands. Secondly, we quantify the different contributions to the vertical motion, namely vertical velocities induced by wind, mesoscale structures and the upwelling/diapycnal transfer.

To examine these ideas we concentrate in a relatively small region south of the Canary Islands, using data with high spatial resolution from an oceanographic cruise carried out in late winter 2006. This cruise was part of CONAFRICA, a multidisciplinary research project focused on the zooplankton and ictioplankton drift within filaments emanating from the NW African upwelling region. Section 6.2 presents the dataset and the interpolation method used to map the measured hydrographic variables onto a regular grid. The interpolation is critical when high-order derived variables such as vertical velocity are to be obtained from the mapped observed variables. Section 6.3 describes the methodology used to assess the different contributions to vertical motion, with emphasis on the QG omega equation. Section 6.4 presents a general view of the horizontal and vertical hydrographic structure of the CTZ obtained from observations. Section 6.5 analyzes the results and discusses the main dynamic processes associated with the distinct regions of the CTZ, as well as their influence on the fluorescence distribution. We close the paper in Section 6.6 by summarizing the major findings and the remaining uncertainties.

6.2 Data analysis

6.2.1 Dataset

During the R/V Hespérides survey (22 March - 7 April 2006) 81 Conductivity-Temperature-Depth (CTD) stations were performed in a $200 \times 100 \text{ km}^2$ domain located south of the eastern Canary Islands. The stations were distributed along transects parallel to the African coast (Figure 6.1) with a meridional and zonal spacing of about 20 km. The CTD profiles were obtained with a SeaBird 911Plus, equipped with a fluorometer. Raw profiles were interpolated on a 2-db interval and generally restricted to the top 500 m (or the sea bed where shallower).

Wind data from the SeaWind scatterometer onboard the QuikSCAT satellite were downloaded from the CERSAT site (<http://www.ifremer.fr/cersat/>). Data are available on gridded fields of 0.5° latitude and 0.5° longitude at daily resolutions. Both the spatial distribution of the mean winds during the time of the cruise (Figure 6.1a) and the time series of wind speed and direction averaged over the survey area (Figure 6.2; the averaging area is highlighted as a gray rectangle in Figure 6.1) show the dominance of upwelling favourable conditions. Sporadic downwelling-favourable winds occurred at the beginning and end of February, and just before the cruise, but the sampling was

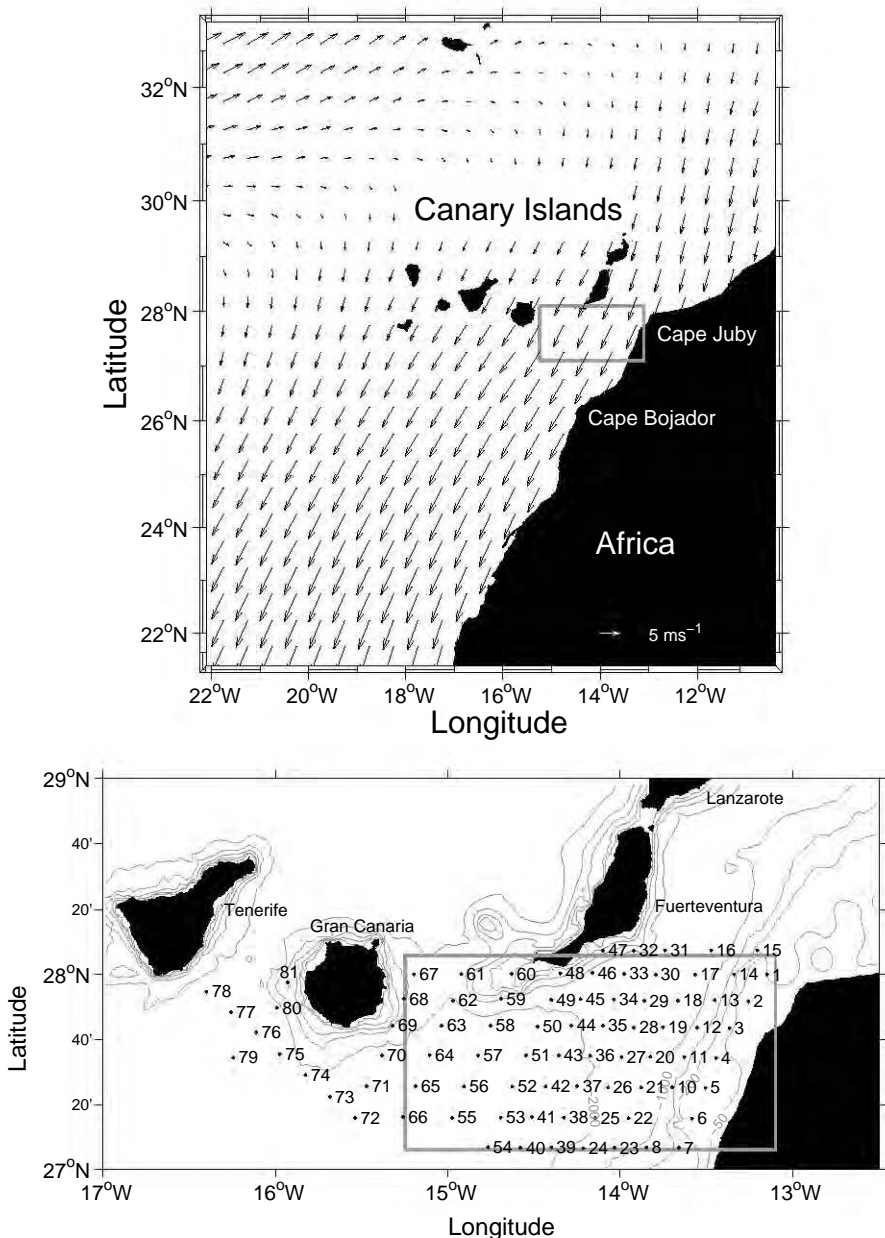


FIGURE 6.1: (Top) Study area (solid grey box) off NW Africa with the mean wind components during the CONAFRICA cruise period (22 March - 7 April 2006). (Bottom) Detail of the study area showing the CTD stations together with the 50, 200, 500, 1000 and 2000 m isobaths.

carried out during an upwelling event.

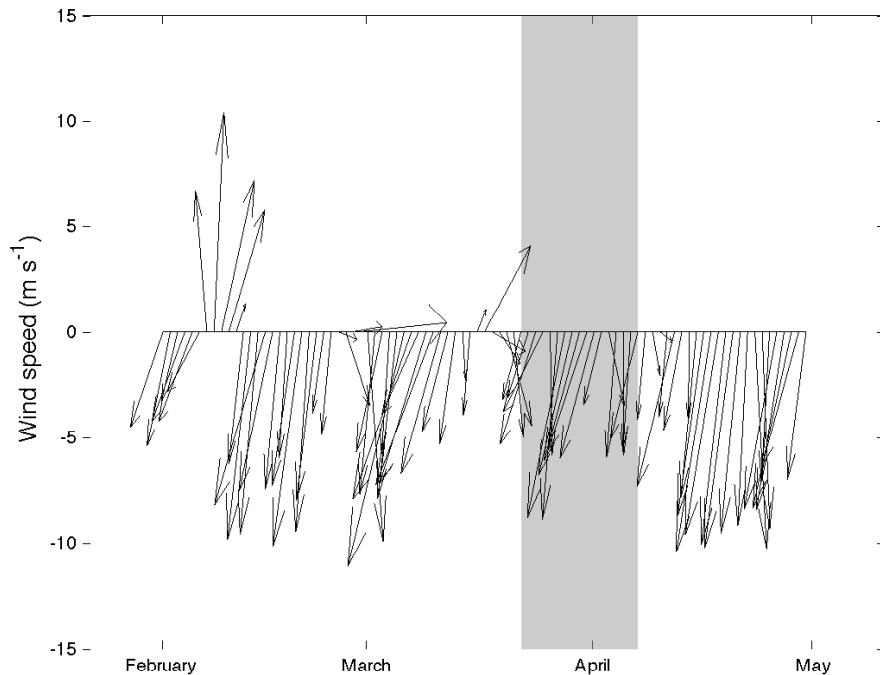


FIGURE 6.2: Time series of averaged daily winds over the surveyed area; the cruise period is highlighted.

During the cruise near real-time Chlorophyll-a (Chl-a) estimates, derived from the Seaviewing Wide Field-of-view Sensor (SeaWiFS), were processed by the Remote Sensing Center at the University of Las Palmas and used onboard to guide the sampling. Sea Surface Temperature (SST) images from the Advanced Very High Resolution Radiometer (AVHRR) and Chl-a images are used in this study to help understand the physical processes occurring in the region.

6.2.2 Optimal statistical interpolation

In order to compute spatial derivatives of the observed variables and hence to diagnose the vertical velocity field, the hydrographic variables are to be interpolated from the unevenly distributed observations points onto a 3D regular grid. A widely applied method is the Optimal Statistical Interpolation (OSI) scheme, originally developed by

Gandin (1965) for meteorological data and first described in an oceanographic context by Bretherton et al. (1976) (for a more recent review see Gomis et al., 2001).

The output grid consists of 21×44 points separated approximately 5 km in the offshore and alongshore directions. The grid point spacing is a compromise between the spatial resolution and interpolation accuracy. On one hand, the spatial resolution of the output field is constrained by the station separation but has to be good enough to resolve the spatial scales of interest. On the other hand, the interpolation errors increase with the density of the grid and determine the accuracy of spatial derivatives. In the vertical direction we use 34 levels equally spaced at 15 db and covering from 5 to 500 db. The mean field for all variables is computed by fitting a second order polynomial to the observations. The horizontal characteristic scale of the correlation model (related to the size of the dominant structures) and the noise-to-signal ratio are set to 20 km and 0.01, respectively. Additionally, in order to avoid aliasing problems, the spatial scales that cannot be resolved by the sampling are filtered out by convolving the classical OSI scheme with a normal-error filter (see Gomis et al., 2001); the cut-off wavelength of the filter is set to 40 km (twice the separation distance between stations).

The described interpolation scheme can be readily applied to temperature T and salinity S , from which other variables such as potential temperature θ , potential density (referred to the sea surface) ρ_θ and neutral density γ_n (Jackett and McDougall, 1997) may be calculated. To calculate the dynamic height we set 500 db as the reference level, which is our deepest sampled water depth. This is not far from the lowest limit of the North Atlantic Central Water (NACW), about 600-700 m, and is close to no-motion reference levels suggested by other authors for the area south of the Canary Islands (Olbers et al., 1985; Pelegrí et al., 2006; Pastor et al., 2008). Since the surveyed area included shelf stations, we chose the layer thickness (dynamic height referred to the level immediately below) as the variable to be interpolated onto the grid points. Following this simple procedure effectively sets the no-motion reference level to continue onshore along the sea bottom, as in Csanady (1979). The dynamic height is then determined by integrating down to the reference level, and other dynamical variables can be easily derived from the interpolated density and dynamic height fields through finite differences. Hereafter, despite differences are very small, we will always present θ and γ_n rather than T and ρ_θ distributions. Potential temperature is the proper variable when considering adiabatic motions while neutral density is the most accurate one to examine budgets of water mass and other properties.

6.3 Methodology to estimate vertical velocities

Vertical velocity may be expressed as the addition of three components: the motion associated with the rising/lowering of isopycnals, epipycnal (along-isopycnals) motion

and diapycnal (across-isopycnal) motion. The first two components imply no mass transfer between isopycnal layers. Here we use the simplest possible approach to evaluate these components: we assume that the rising/lowering of isopycnals and epipyccnal vertical motion result from both ageostrophic motions that tend to restore departures from geostrophic balance, and may be diagnosed through the adiabatic QG theory, and Ekman convergence-divergence in the upper mixed-layer, which arise entirely from wind-induced forcing. Diapycnal velocities, on the other hand, will be estimated by adjusting the water balances in isopycnal layers: any imbalance has to be satisfied through transfer from one layer to another.

6.3.1 Quasi-geostrophic mesoscale vertical velocities

Vertical velocities associated to mesoscale structures can be inferred by solving the Q-vector form of the omega equation. For this purpose we partition the velocity field into geostrophic and ageostrophic components $\vec{v} = (u, v, w) = (u_g, v_g, 0) + (u_a, v_a, w_{qg})$ and define the Rossby number as the normalized relative vorticity field, $\zeta/f \equiv (\partial v / \partial x - \partial u / \partial y) / f$, where $f = 2\Omega \sin \phi$ is the planetary vorticity, with Ω the Earth's angular velocity and ϕ the latitude; we take ϕ as constant and equal to the mean latitude of our study area so that f is also constant.

Assuming the Rossby number is small ($\text{Ro} \ll 1$), we may approximate the rate of change following a particle as $D_g/Dt = \partial/\partial t + u_g(\partial/\partial x) + v_g(\partial/\partial y)$. Thus, the QG momentum equations may be written as

$$\frac{D_g u_g}{Dt} - fv_a = 0 \quad (6.1)$$

$$\frac{D_g v_g}{Dt} + fu_a = 0 \quad (6.2)$$

The mass conservation for an incompressible flow is

$$\frac{D_g \rho}{Dt} + w_{qg} \frac{\partial \rho}{\partial z} = 0 \quad (6.3)$$

where ρ is the water density. Under the hydrostatic approximation ($\partial p / \partial z = -\rho g$, where p is pressure and g is the gravity acceleration) equation (6.3) becomes

$$\frac{1}{\rho_0} \frac{D_g}{Dt} \frac{\partial p}{\partial z} + N^2 w_{qg} = 0 \quad (6.4)$$

where $N^2 = (-g/\rho) \partial \rho / \partial z$ is the squared buoyancy frequency.

Using the geostrophic relation ($fu_g = (-1/\rho_0)\partial p/\partial y$ and $fv_g = (1/\rho_0)\partial p/\partial x$) to eliminate the time derivatives between (6.1), (6.2) and, (6.4) we obtain

$$\frac{\partial}{\partial x}(N^2 w_{qg}) - f^2 \frac{\partial u_a}{\partial z} = Q_x \quad (6.5)$$

$$\frac{\partial}{\partial y}(N^2 w_{qg}) - f^2 \frac{\partial v_a}{\partial z} = Q_y \quad (6.6)$$

where Q_x and Q_y are the horizontal components of the QG \vec{Q} vector given by

$$\vec{Q} = (Q_x, Q_y) = 2 \frac{g}{\rho_0} \left(\frac{\partial \vec{u}_g}{\partial x} \cdot \vec{\nabla}_h \rho, \frac{\partial \vec{u}_g}{\partial y} \cdot \vec{\nabla}_h \rho \right) \quad (6.7)$$

Finally, using the continuity equation to eliminate the horizontal ageostrophic velocities yields

$$\nabla_h^2(N^2 w_{qg}) + f_0^2 \frac{\partial^2 w_{qg}}{\partial z^2} = \vec{\nabla}_h \cdot \vec{Q} \quad (6.8)$$

This 3D elliptic equation for w_{qg} is known as the Q-vector formulation of the QG omega equation (Hoskins et al., 1978) and it can be solved provided that appropriate boundary conditions are specified and the vertical forcing at every grid point of the domain is known. The forcing term (right-hand-side of equation 8) is equal to the horizontal divergence of the Q vector and, therefore, may be determined from the density and geostrophic velocity fields.

Regarding boundary conditions, w_{qg} is usually set equal to 0 (Dirichlet conditions) at the upper and lower boundaries, of the domain, here taken to be the sea surface and 500 m. Near the sea surface w_{qg} does not have to be exactly zero. Instead, this vertical velocity should match some externally provided condition, such as arising from wind-induced convergence/divergence in the surface mixed-layer. We will later see, however, that this value turns out to be substantially smaller than the w_{qg} values attained at depth, and is therefore safely approximated to zero. The choice $w_{qg} = 0$ at the lower boundary implies that mesoscale motions there are very much reduced. We will later see that the T and S vertical displacements are very much reduced near 500 m depth, hence supporting this assumption.

Lateral boundary conditions are usually set in a more arbitrary way, here we use Dirichlet conditions at all boundaries. It may be shown that, provided the horizontal scale of the structures is smaller than the size of the domain, the ellipticity of equation (8) causes the interior solution for w_{qg} to be relatively insensitive to the imposed conditions (see for instance Gomis and Pedder, 2005). In our case the mesoscale structures are indeed smaller than the domain, and we have verified this statement to be true when these structures are located at least a few grid points away from the boundary.

6.3.2 Wind-induced and diapycnal vertical velocities

Wind-driven vertical motions may be induced by two processes that depend on the sea-surface horizontal wind-stress vector: Ekman pumping and normal-to-shore Ekman transport (e.g. Pickett and Paduan, 2003). The sea-surface horizontal wind-stress vector is defined as $\vec{\tau} = (\tau_x, \tau_y, 0)$, with east-west (τ_x) and north-south (τ_y) components. This vector field can be derived from the QuikSCAT wind field using the Liu et al. (1996) algorithm. In the open ocean the relevant contribution is Ekman pumping, which results from the convergence/divergence generated in the surface mixed-layer by the wind stress curl. The linear Ekman pumping velocities, w_{ek} , are calculated as $w_{ek} = (1/\rho f) \vec{k} \cdot (\nabla \times \vec{\tau})$, where $\nabla \times \vec{\tau}$ is the curl of the mean wind stress during the cruise period and can be derived by applying finite differences to the QuikSCAT wind stress field. Non-linear Ekman pumping is neglected, as the geostrophic relative vorticity $\zeta_g = (\partial v_g / \partial x - \partial u_g / \partial y)$ remains always significantly smaller than f .

Nearshore, however, the presence of the coast makes Ekman coastal divergence to be the relevant contribution to vertical motion. In order to estimate the associated vertical velocities, the offshore component of Ekman transport at each grid point is computed from the cruise mean wind stress vector closest to the coast (roughly 30 km offshore). The normal-to-shore Ekman transport per unit length is hence given by $U = \tau_p / (\rho f)$, where τ_p is the wind stress component parallel to coast. To obtain the upwelling vertical velocity w_{up} we also need the width of the area where the coastal constraint applies, L_x , so that $w_{up} = U/L_x$. An estimate of the extent of the coastal constraint comes from the internal Rossby radius of deformation for an idealized two-layer upwelling system, given by $(gh)^{1/2}/f$, where h is the thickness of the upper layer and $g = g(\rho_2 - \rho_1)/\rho_1$, with ρ_1 and ρ_2 being the densities of the upper and lower layers. Using $\rho_2 - \rho_1 = 0.3 \text{ kg m}^{-3}$ and $h = 150 \text{ m}$ as typical values for the region (see Section 6.4.3) we obtain this two-layer Rossby radius to be close to 100 km, similar to the observed width of the upwelling area. Therefore we set L_x equal to the width of the observed upwelling area, calculated as the mean distance between the 200 m isobath and the frontal region (as defined through selected dynamic-height contours at 20 db, see Section 6.4.2).

Finally, vertical velocities also result from turbulent mixing. In a stratified fluid the presence of positive vertical velocities implies transformation of kinetic into potential energy. This is possible in critically stable regions, with sufficiently large vertical shear, which frequently occur within frontal systems in upwelling regions (Pelegrí and Richman, 1993; Kundu and Beardsley, 1991). These vertical velocities are often parameterized in terms of the gradient Richardson number, with a large degree of uncertainty. Here we use a simpler approximation based on several works which have shown that 500 m is a good reference level to determine the principal features of the alongshore currents in the upwelling region south of the Canary Islands as far as Cape Blanc (Olbers et al., 1985; Machín et al., 2006a; Pelegrí et al., 2006; Pastor et al., 2008). A geostrophic mass imbalance in any layer is hence viewed as the result of

horizontal convergence/divergence that has to be supplied by the neighbouring layers via diapycnal velocities w_{dia} . This concept is useful in assessing water exchange between adjacent layers in idealized box-type models, as discussed below.

6.4 Distribution and transport of properties

6.4.1 Horizontal structure

Figure 6.3 displays the SST and surface Chl-a fields on March 29 and April 7, respectively, obtained from AVHRR and SeaWiFS sensors. The insets show how the far-field is characterized by relatively warm and unproductive offshore waters, in contrast with the cool and productive waters of the CTZ that occupy a band of about 100 km from the coastline. The main images illustrate our region of interest, south of the eastern islands. This mesoscale picture bears a great similarity to that depicted by Barton et al. (2004) for essentially the same region in August 1999. It is characterized by the existence of filaments stretching from the coastal region and a remarkable mesoscale activity reflected in both SST and Chl-a fields. Two filaments (F1 and F2) appear as offshore extensions of cold and productive water attached to the shelf break near Capes Bojador and Juby. Barton et al. (2004) pointed to the relation between F1 and a quasi-permanent cyclonic eddy trapped in the trough south of the inner islands, as well as between F2 and an intermittent anticyclonic eddy southeast of Fuerteventura island, to form systems that favour the exchange between the continental shelf and open ocean waters. Between F1 and F2 we may identify the A1-C1 eddy dipole which leads to onshore flow in between.

Figure 6.4 shows the circulation and water properties distribution at 20 db. The dominant signature is the baroclinic coastal upwelling jet entering the region through the northeastern margin (Figure 6.4a) and meandering southwestwards to the southern end of the domain where it loses strength and turns southeast. The largest geostrophic velocities (about 0.18 m s^{-1}) are related to the sharper horizontal gradients in dynamic height at 20 db referenced to 500 db, $D_{20/500}$. In Figure 6.4a we show these to be bound by the 0.625 and 0.64 dyn m isolines, located approximately 100 km off the African coast. These velocity values are in agreement with wintertime observations and inverse model results for the flow along the passage east of Lanzarote Island (Machín et al., 2006a).

The property distributions are consistent with the classical two-dimensional vertical upwelling cell (e.g. Gill and Clarke, 1974). A shelf-break front roughly follows the 200 m isobath and separates relatively dense (cold and fresh) and pigment-enriched waters, adjacent to the African coast, from the offshore region (Figures 6.4b,c). A southward along-slope jet, which brings relatively cold and fresh waters of northern

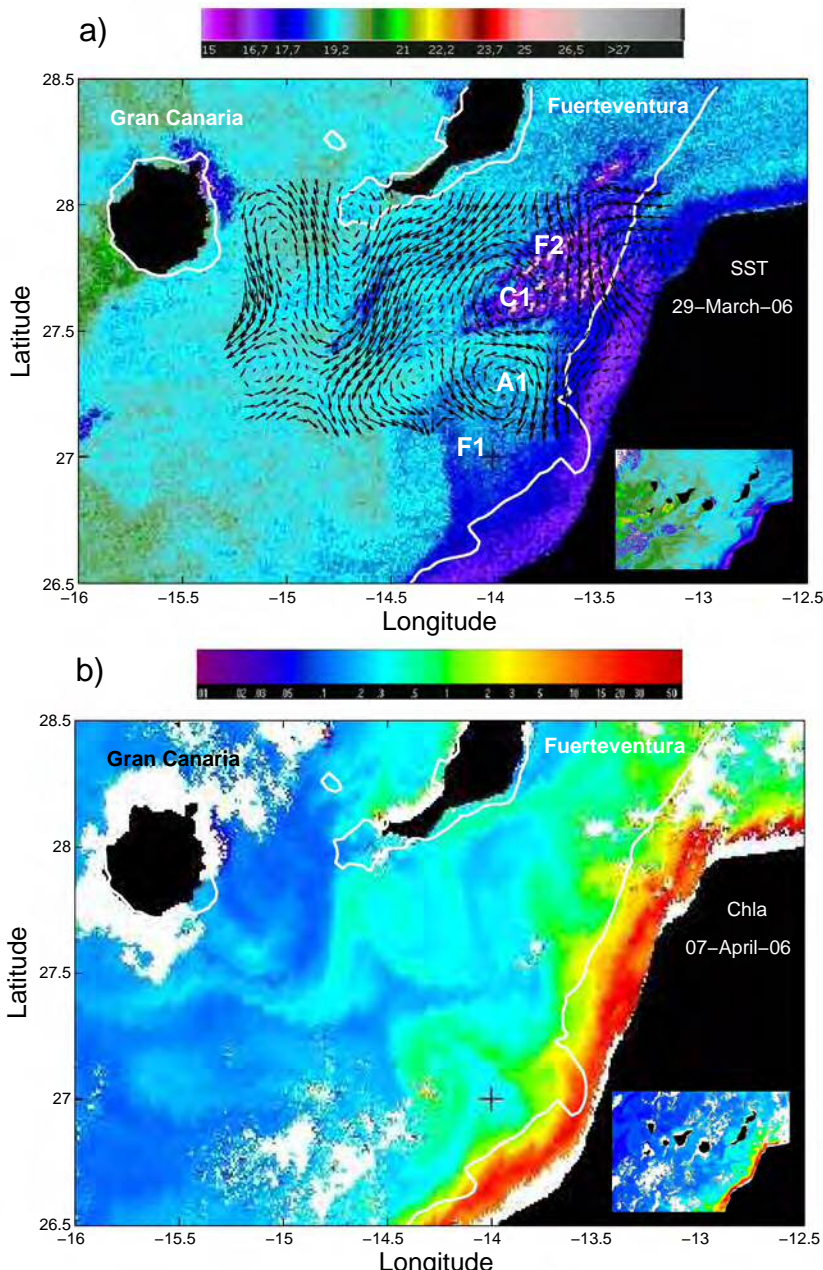


FIGURE 6.3: (a) Satellite SST ($^{\circ}$ C) image for March 29 with the geostrophic current vectors at the sea surface (relative to 500 db) as obtained using the cruise hydrographic data. (b) Satellite Chl a (mg m^{-3}) image for April 7. The white line corresponds to the 200 m isobath, approximately at the shelf break.

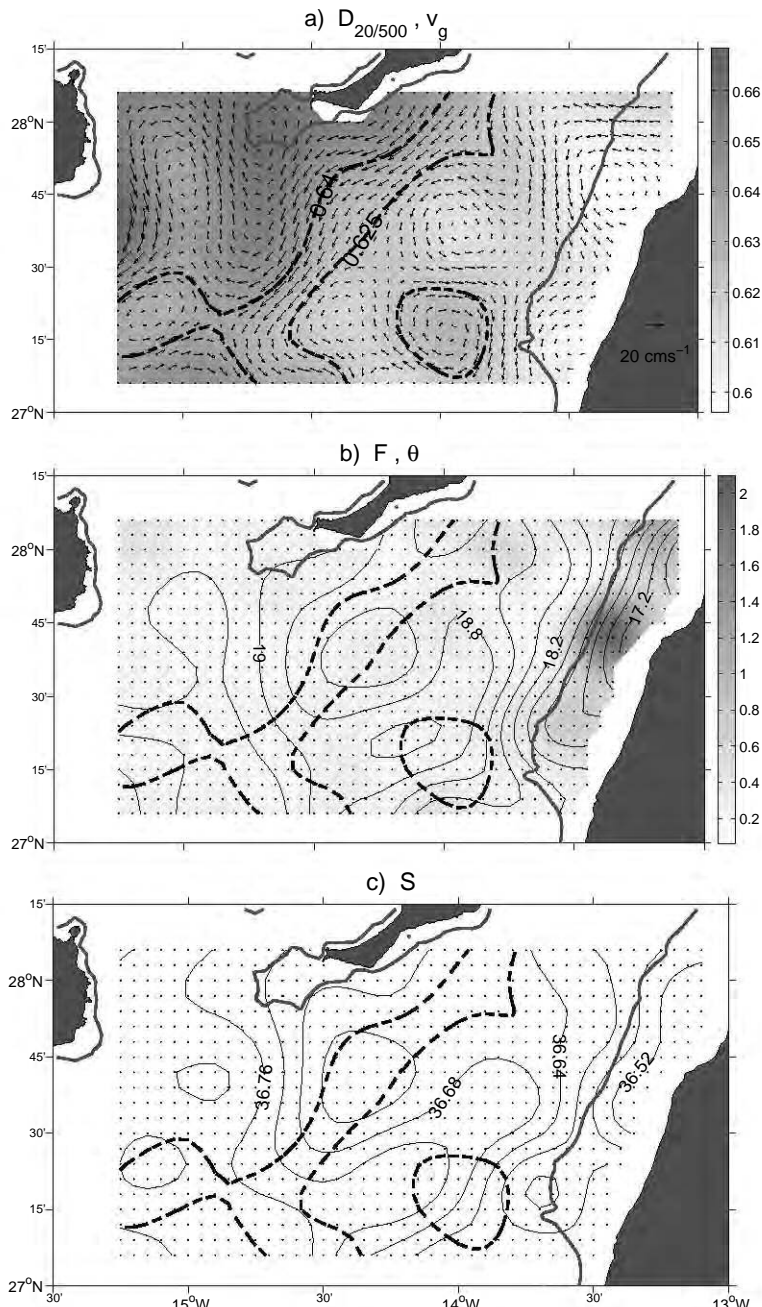


FIGURE 6.4: Distributions at 20 db of (a) dynamic height (dyn m; gray bar) and v_g (10^{-2} m s^{-1}), referred to 500 db; (b) *in situ* fluorescence (V; grey bar) and θ (°C) with 0.2°C contour intervals; (c) S with 0.04 contour intervals. The thick dashed black lines denote the dynamic height contours of 0.625 and 0.64 dyn m and the gray line shows the 200 m isobath.

origin, appears to be associated with this front. The maximum cross-frontal horizontal gradients are found to the north, where θ and S decrease about 1.4°C and 0.12 over a distance of 50 km.

Figure 6.5 (top and middle panels) shows the dynamic height and the corresponding \vec{v}_g fields at 50, 110, 245 and 410 db (relative to 500 db), together with the θ and fluorescence fields. The S fields are not shown since they have very similar patterns to the θ fields, as expected from the very tight θ - S relation in surface and central waters (Figure 6.6, see next subsection). A relatively cold and fresh surface tongue extends west of Cape Juby, along 27.8°N until the southwestern tip of Fuerteventura Island (14.5°W) from where it stretches south (Figures 6.3a and 6.4c). This surface feature is a shallow filament, as it fades out by 50 db (middle panels in Figure 6.5). The high cross-jet θ gradients are maintained and with depth, depicting an intense frontal system that reaches down to at least 245 db and marks the real boundary between coastal upwelled and offshore waters.

The geostrophic circulation pattern follows the position of the near-surface (20 db) jet (Figure 6.4a), which persists invariant down to 245 db (upper panels in Figure 6.5). The jet itself is linked to the frontal system, as is apparent from the 110 and 245 db θ fields, flowing roughly parallel to the slope. The jet and all eddies have similar speeds down to 110 db. At 245 db we still find intense currents along the jet axis and in the cyclonic and anticyclonic eddies located between Fuerteventura and Gran Canaria, while some of those eddies east of the jet become relatively weak. At 410 db the jet weakens but there are still appreciable flows around the Fuerteventura and Gran Canaria eddies.

The distribution of *in situ* fluorescence at 20 db (Figure 6.4b) shows maximum values over the continental platform, in concordance with the cold and high-pigment platform waters visible in the remote sensing images (Figure 6.3). Figure 6.5 (middle panels) displays the *in situ* fluorescence distributions at 50, 110, 245 and 410 db, with significant differences when compared to the 20 db field. At 50 db the maximum values ($> 1.2 \text{ V}$) do not correspond to shelf waters ($< 0.8 \text{ V}$) rather they have a patchy distribution located on a band along the upwelling coastal front, immediately offshore the 17.4°C isotherm. At 110 db the maximum values are found further offshore but the distribution remains patchy, pointing at the possibility of localized downwelling linked to some phases of eddies and meanders in the region. This point will be re-examined in Section 6.5.3. Further deep, at 245 and 410 db, the fluorescence values are much smaller, likely not significant.

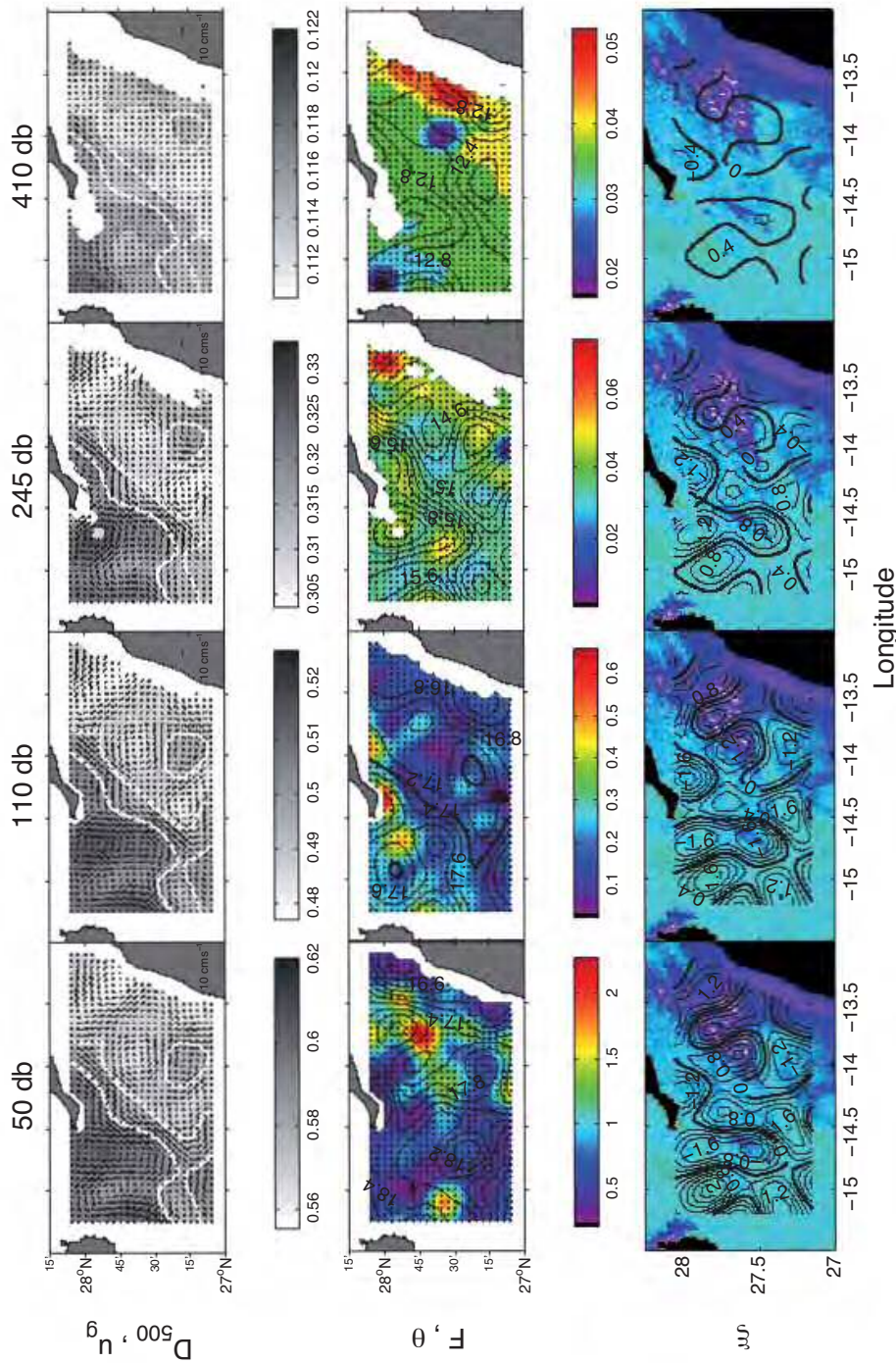


FIGURE 6.5: Distributions of (top) dynamic height (dyn m) and v_g (10^{-2} m s^{-1}), referred to 500 db, (middle) *in situ* fluorescence (V) and potential temperature (°C), and (bottom) ζ_g superimposed on the SST image for March 29, at 50 db, 110 db, 245 db and 410 db. Contour interval is 0.2°C for θ and $0.4 \times 10^5 \text{ s}^{-1}$ for ζ_g . White lines represent the 0.625 and 0.64 dyn m isolines of dynamic height at 20 db. The bold contours in the Θ field at 110 db is the 17.4 °C isotherm.

Figure 6.5 (lower panels) illustrates the ζ_g fields superimposed on the SST image of March 29. Relative ζ_g maxima and minima are associated with cyclonic and anticyclonic structures, with length scales similar to the Rossby deformation radius (about 20 km, Pelegri et al., 2005b). The zero ζ_g line roughly defines a streamline for the jet core, as well as the edges of mesoscale eddies. The geostrophic Rossby number, defined as $Ro = \zeta_g/f$, ranges from -0.3 to 0.3 at surface and weakens slowly with depth. Although QG theory may only strictly be used when $Ro \ll 1$, several studies on the applicability of this theory have shown that relative errors in directly derived quantities such as \vec{v}_g and ζ_g are of the same order as Ro (Shearman et al., 1999; Gomis et al., 2001). Hence, for our study we expect these errors to not exceed 30%, typically much less away from the center of eddies. However, as the mesoscale vertical velocity field w_{qg} depends on non-linear combinations of the second derivatives of density and geostrophic velocity, it is difficult to assess what the associated errors would be. These relative errors are likely of the same order as the maximum Ro values, important but possibly no much larger than other errors inherent to the horizontal grid resolution and the survey's lack of sinopticity (Gomis and Pedder, 2005). We conclude we may trust the w_{qg} fields but with some caution, therefore only accepting the calculated spatial patterns and gross numbers.

6.4.2 Vertical structure

The Θ -S diagram shows the presence of NACW as the principal water mass in the sampled depth range (Figure 6.6). NACW is identified by a linear Θ -S relationship, from near-surface waters down to the isoneutral $\gamma_n \approx 27.38 \text{ kg m}^{-3}$ (roughly 700 m depth, Hernández-Guerra et al., 2005), therefore completely covering the upper 500 m of the ocean as shown in Figure 6.6. Since the cruise was done during late winter, when the atmosphere-ocean heat flux has just began to increase (e.g. Hsiung, 1986), the offshore waters hardly show a seasonal thermocline. Nevertheless the Θ -S scattering in the upper layers reflects the differences between the near-slope upwelled waters, which are central waters that have recently reached the sea surface, and the offshore surface waters, which have been close to the surface long enough to be modified through air-sea interaction.

In order to sort out the surface water types, we have superimposed three mean Θ -S curves constructed by clustering the stations as a function of their $D_{20/500}$ values (see Figure 6.4a). The ranges $D_{20/500} \leq 0.625$, $0.625 \leq D_{20/500} \leq 0.64$ and $D_{20/500} \geq 0.64$ have been chosen to represent the upwelled, frontal and open-ocean waters, respectively. With this division the mean curves become well differentiated and the three Θ -S domains, defined by data points within one standard deviation of these mean curves, hardly overlap. Below this surface layer, the three curves are indistinguishable and correspond to the eastern NACW. This unique relation between Θ and S is what, for the permanent upper-thermocline, allows a direct inference of the S from Θ data (e.g. it

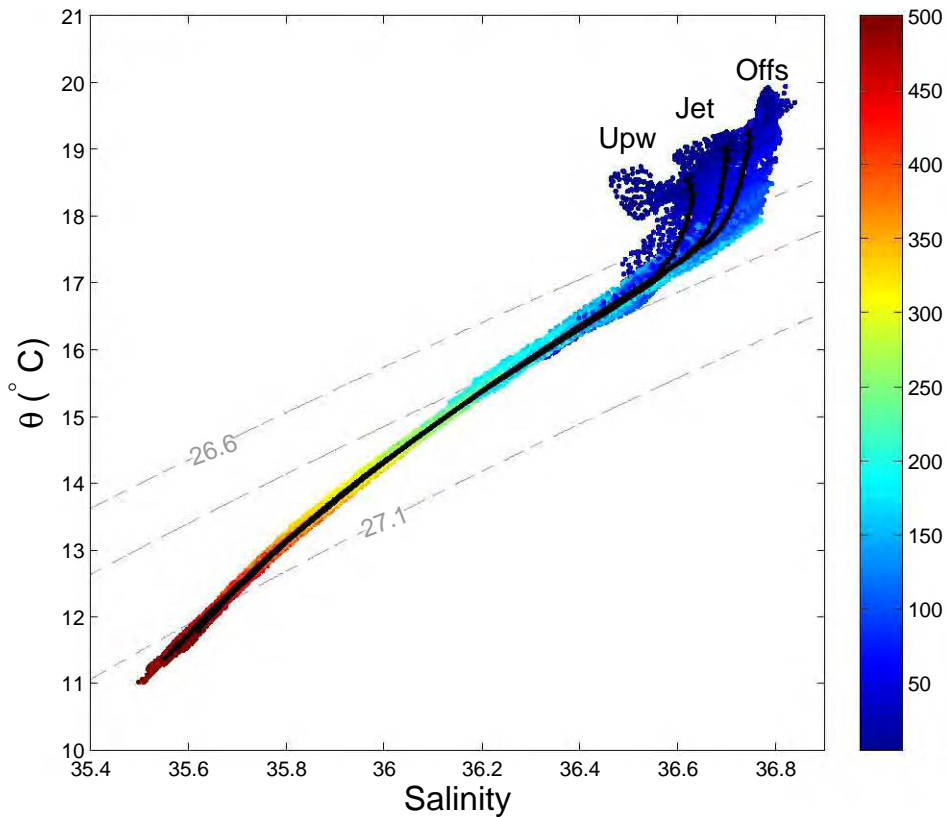


FIGURE 6.6: θ -S diagram for all the stations performed during the cruise. Averaged θ -S curves for the upwelled, frontal and offshore waters. The colour scale represents the pressure of each gridpoint, and the dashed lines correspond to $\sigma_\theta=26.6, 26.8$ and 27.1 kg m^{-3} .

allows to infer the S distributions from the middle panels in Figure 6.5).

Figure 6.7 shows vertical sections of γ_n , meridional geostrophic velocity, v_g , θ and fluorescence along 27.95°N , 27.55°N and 27.25°N . Geostrophic velocities, relative to 500 db, reveal the close association between the front and the jet current. A southward baroclinic jet flows separated from the coast, over a region of rising isoneutrals. Maximum jet velocities about 0.18 m s^{-1} are observed at surface, decreasing to 0.05 m s^{-1} at 300 db. This confirms that the largest fraction of the jet's baroclinic signal is confined to the upper layers, i.e. the surface geostrophic velocities would not change much if we had chosen a reference level at 400 db. East of this front the isoneutrals dip against the continental slope, inducing a poleward undercurrent, its core located at about $\gamma_n=26.8 \text{ kg m}^{-3}$. In the southern section (27.25°N) the southward jet actually

appears to split around the poleward undercurrent (see also the \vec{v}_g field at 245 db in Figure 6.4a). Cross-shore geostrophic velocities are generally weak, well within the $\pm 0.1 \text{ m s}^{-1}$ range.

Lifting of isotherms, isohalines and isoneutrals is noticeable within 100 km from the coast, influencing approximately the top 300 db of the water column (Figure 6.7). For example, the 17°C isotherm is lifted by approximately 150 db over 100 km at 27.55°N and 27.95°N (middle and top panels of Figure 6.7) giving an average isotherm slope of about 1.5×10^{-3} . The correspondence between the 17.4°C isotherm and the deep fluorescence maximum (DFM) layer, located at the top of the nutricline (Tett et al., 2002), is remarkable (Figure 6.7).

6.4.3 Water transports

We have calculated the mass transports entering or leaving the domain by simply integrating the velocity through each outer section of the grid, i.e. across each outer section and from 500 db, or the sea floor if shallower, to the sea surface. A surface mixed layer depth ranging from 12 to 76 m is obtained by following the procedure proposed by Kara et al. (2000). Thus, the water column is divided into three layers by isoneutrals 26.65 , 26.85 and 27.162 kg m^{-3} . These layers are identical to those proposed by Ganachaud (2003) for the North Atlantic Ocean except for the first one which here is selected to be slightly heavier to match the maximum observed mixed-layer depth (76 m), thus it contains all the wind-induced Ekman transports (see below). The middle layer reaches down to about 15°C , near 300 db far offshore, so it includes most of the water column that upwells towards the coast. The deep layer goes down to about 11.5°C , near the 500 db level. This deep layer is essentially unaltered by the vertical motions; it is far from the direct influence of the wind and has relatively weak currents, therefore it should not experience substantial mixing with the overlying layer. Figure 6.7 is useful to visualize the density (left panels) and thermal (right panels) structure of the water column down to 500 db.

Ekman transports are computed from the relations $T_{Ex} = \tau_y / (\rho f)$ and $T_{Ey} = -\tau_x / (\rho f)$, where τ_x and τ_y are the zonal and meridional mean wind stress during the cruise period as determined from QuikSCAT. T_E amounts to 0.07, 0.12 and -0.11 Sv for the northern, western and southern sections, respectively ($1 \text{ Sv} = 10^6 \text{ m}^3 \text{ s}^{-1} \sim 10^9 \text{ kg s}^{-1}$). These transports are assumed to exclusively take place in the surface layer. Further, the water transports in the deepest layer are imposed to balance out by assuming a barotropic velocity of $-2.3 \times 10^{-3} \text{ m s}^{-1}$ at the northern section. Such a small negative reference velocity is coherent with inverse model results obtained for the passage east of Lanzarote island by Machín et al. (2006a). These authors found an annual-mean reference velocity close to -0.01 m s^{-1} at about 800 db, but with substantial temporal

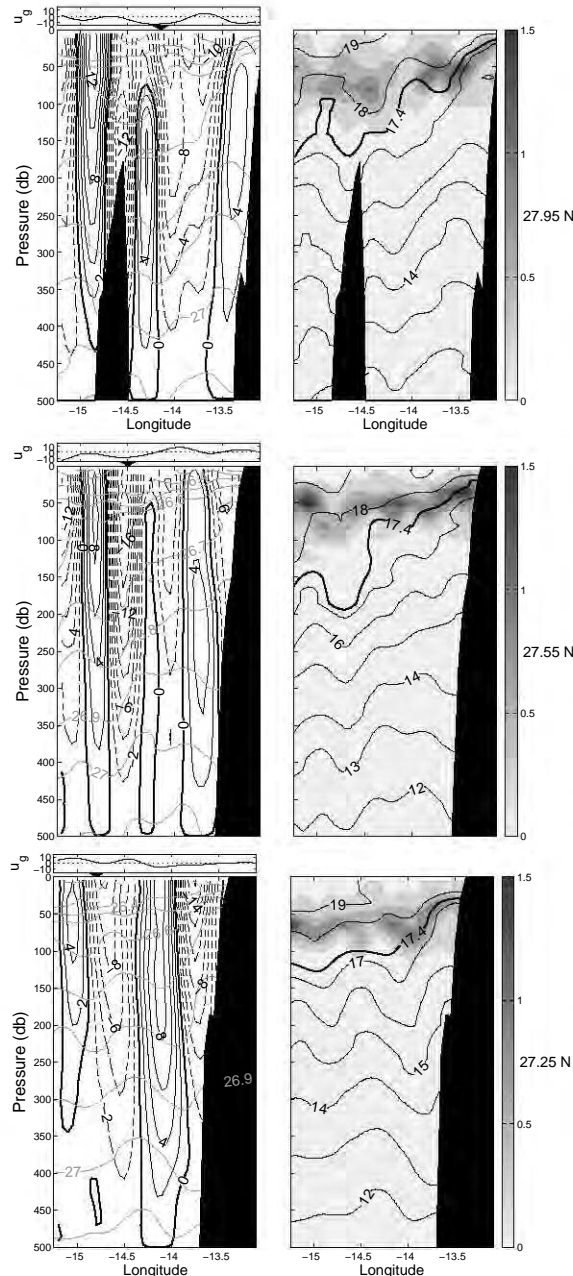


FIGURE 6.7: Across-shore sections of the (left) meridional v_g (10^{-2} m s^{-1}) and neutral density (kg m^{-3}), and (right) *in situ* fluorescence (V) and θ ($^{\circ}\text{C}$) at (top) 27.95°N , (middle) 27.55°N and (bottom) 27.25°N . Dashed contours indicate southward velocities. The elongated upper left panels represent the surface zonal u_g (10^{-2} m s^{-1}) at each transect, with positive values indicating eastward flow. The bold contours in the θ field denote the 17.4°C isotherm. The frontal position is indicated by arrows at the top of the left panels.

variability.

Figure 6.8a shows the layer integrated mass transport in each section. Adding the transports in all three layers (0.34, 0.57 and 0.27 Sv through the upper, middle and deep layers, respectively) gives a total of 1.18 Sv flowing through the north section, with about 1.0 Sv corresponding to the transport of NACW by the CUC between the islands and the African coast. This result is in good agreement with the mean transport through this passage as determined from expandable bathythermograph (XBT) and CTD casts (Hernández-Guerra et al., 2001, 2002; Knoll et al., 2002). It also agrees with the transport in the top 600 m as estimated from an eastern boundary mooring located in the middle of the channel between the eastern Canary Islands and the African continental slope (Hernández-Guerra et al., 2003). A recent estimate based on 10 years of current-meter data from this passage shows a mean value close to our result but with rather large variability, -0.81 ± 1.48 Sv (Fraile-Nuez et al., 2010).

Off NW Africa the background upper-thermocline boundary current is the CC, embracing the whole Canary Archipelago and beyond (approximately 1000 km), with a transport of order 5 Sv within 700 m of NACW (Käse et al., 1985, 1986; Stramma and Siedler, 1988). An important fraction of its transport occurs close to the continental slope, as the CUC, linked to the coastal upwelling frontal system (Pelegrí et al., 2005a; Pelegrí et al., 2005b; Machín et al., 2006a). Figure 6.8b shows the southward transport across 27.7°N , with a maximum increase over the frontal region. This figure illustrates the presence of significant southward transport both over the upwelling region (about 0.4 Sv of barotropic contribution) and over the frontal system itself (about 1 Sv of baroclinic contribution), beyond which the transport increases more slowly as the CUC merges with the offshore CC.

6.4.4 Vertical velocity fields

The 1.18 Sv input through the north section is approximately balanced by 1.36 Sv leaving the box through the west section (0.99 Sv distributed as 0.37, 0.34 and 0.28 Sv for the upper, middle and deep layers, respectively) and, to a lesser extend, through the south section (0.37 Sv distributed as 0.20, 0.19 and -0.02 Sv for the upper, middle and deep layers, respectively) (Figure 6.8a). The net mass imbalance, 0.18 Sv, mainly reflects flow convergence in the middle layer and divergence in the top one. This result implies diapycnal transfer from the middle into the surface layer, as expected to occur in upwelling regions (Pelegrí and Richman, 1993). If we assume that most of this transfer occurs in the frontal region, about 30 km wide and 100 km long, then it implies a diapycnal velocity $w_{dia} = 6 \times 10^{-5} \text{ m s}^{-1}$ [5.2 m day^{-1}]. Maximum values are certain to be much greater than this average value, most likely responding to subcritical stages of the baroclinic upwelling jet (Kundu and Beardsley, 1991; Pelegrí

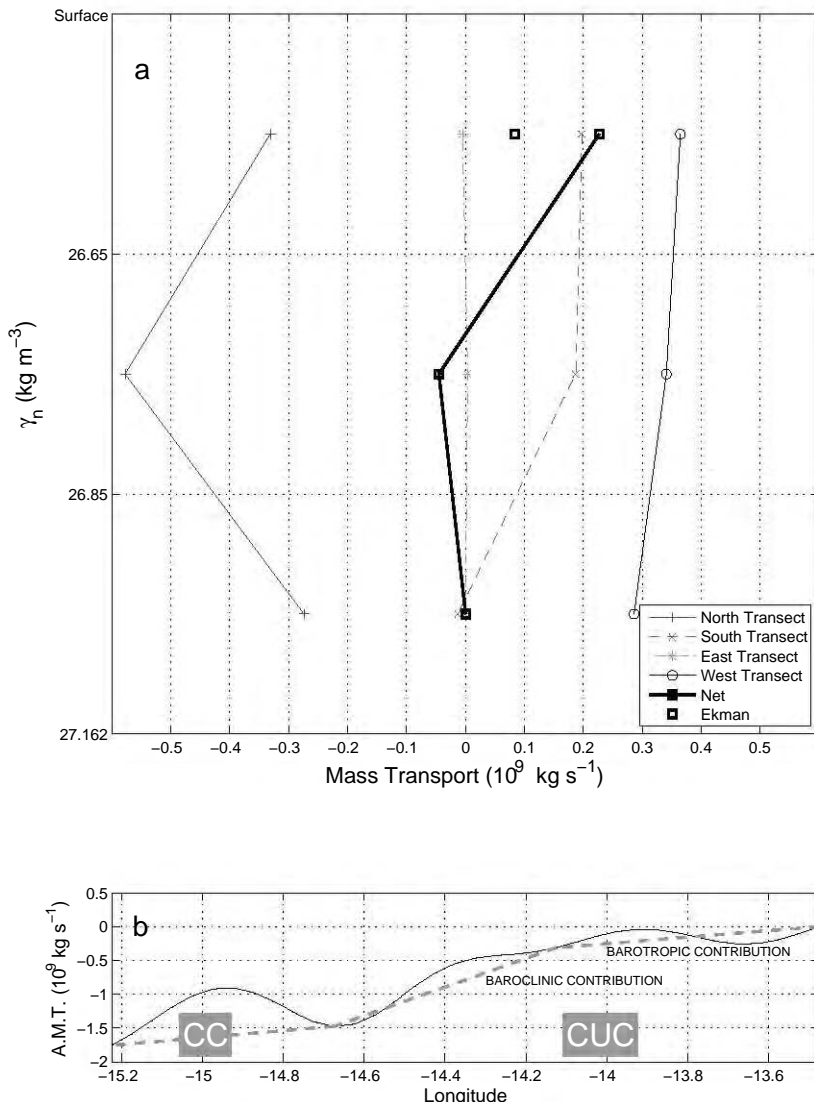


FIGURE 6.8: (a) Layer-integrated mass transports for the north (crosses, solid line), south (x-marks, dotted line), east (stars, dashed-dotted line) and west (circle, solid line) sections of the grid. Mass conservation in the box is represented by the black line. Positive/negative signs are assigned for divergence/convergence flow out-of/into the box. (b) Accumulated mass transport at 27.7°N , beginning the integration at the African coast. Positive/negative accumulated mass transport values denote northward/sorthward flow for the Canary Upwelling Current (CUC) and the Canary Current (CC).

and Richman, 1993).

Adding the Ekman transports through all transects bounding our domain shows the mean Ekman balance to be about 0.08 Sv. Divided by the upwelling area (100 km width and the length of our coastline) gives an upwelling velocity of $w_{up} = 0.8 \times 10^{-5}$ m s $^{-1}$ [0.7 m day $^{-1}$]. As a first estimate this velocity should affect the whole width of the upwelling region and down to the 15 °C isotherm.

The Ekman pumping velocity calculated for each point of the domain leads to a mean negative w_{ek} of -0.3×10^{-5} m s $^{-1}$ [-0.26 m day $^{-1}$]. This value, despite being small, is consistent with negative Ekman pumping values that must occur within the subtropical gyre (e.g. Leetma and Bunker, 1978). Integrated over the whole domain this corresponds to a downward transport of -0.05 Sv, of the same order as the coastal Ekman transport but of opposite sign.

The \vec{v}_g and ζ_g fields (Figures 6.9 and 6.10) illustrate a meandering jet that gives rise to baroclinic eddies on both flanks, with positive ζ_g towards the coast and negative values in the open ocean side. The jet core, which should have zero vorticity, actually corresponds to the wide band of moderately low ζ_g values in Figure 6.10. The w_{qg} field changes slowly with depth within the frontal region, with maximum velocities (of order 10 m day $^{-1}$) occurring between 100 and 150 db. Furthermore, it has much smaller length scales than the ζ_g field, being linked to certain phases of the meanders and eddies. However, the w_{qg} field is so patchy that its associated net transport at any depth is estimated to be of order 0.01 Sv.

The vertical velocities within the upwelling region are controlled by the coastal constraint, which induces a 2D vertical cell along a normal-to-shore section. This vertical cell results in the cross-shore transfer of subsurface waters, from the 100 to 300 db stratum into the surface layer. In the previous subsection we estimated this upwelling velocity w_{up} to be about 2 m day $^{-1}$. Superposed onto this mean vertical flow there are some QG vertical velocities w_{qg} (Figures 6.9 and 6.10), with a patchy structure and moderate values.

In summary, the w_{dia} is relatively large (about 5 m day $^{-1}$) but occurs in a relatively narrow frontal region therefore contributing to a moderate transport of 0.18 Sv. The offshore Ekman pumping is -0.05 Sv and, as it occurs over the whole domain, leads to small vertical velocities w_{ek} of about 0.3 m day $^{-1}$. The coastal Ekman divergence is about 0.08 Sv and leads to vertical velocities w_{up} of about 1 m day $^{-1}$ over the upwelling region. In our region, transports due to either coastal Ekman divergence or offshore Ekman pumping are small but their joint effect is even smaller. Finally, the w_{qg} peak values (Figures 6.9 and 6.10) are much larger than either w_{up} or w_{ek} and even larger than w_{dia} , i.e. order 10 m day $^{-1}$ instead of order 0.1 to 1 m day $^{-1}$, but their

patchiness leads to a very small transport of order 0.01 Sv.

6.5 Discussion

6.5.1 The upwelling, frontal and offshore regions

Off NW Africa, sustained equatorward trade winds drive offshore Ekman transport in the surface layer, leading to the upwelling of cold, fresh and nutrient-rich subsurface waters. The result is the formation of a frontal system with isopycnals outcropping near-shore, a baroclinic system over which a relatively shallow upwelling jet flows along-shore. A near steady-state system, with constant intensity jet and outcropping isopycnals at some offshore distance, is eventually possible because of the along-shore resistance of the lower layers and as offshore Ekman transport is maintained via cross-shore vertical motions, both along (epipycnal) and across (diapycnal) the upwelling isopycnals.

The frontal system is the dominating baroclinic structure in the CTZ. It is a relatively narrow and shallow feature, typically about 30 km wide and some 250-300 m deep (Pelegrí et al., 2005a; Pelegrí et al., 2005b; Pastor et al., 2008), which divides the CTZ in three regions: upwelled waters, frontal region and offshore ocean. The upwelled waters may be idealized as a near-homogeneous water column that reaches all the way from the sea surface to the sea bottom. The motion of this deep water column represents a near-barotropic transport, a contribution with relatively large inertia that slowly changes its momentum through the large-scale wind regime. This barotropic water transport attains significant values because of the large water depth, despite the presence of relatively small horizontal velocities. The frontal waters, on the other hand, reach much larger horizontal velocities but they go to near-zero at the base of the frontal system (left panels in Figure 6.7). Hence, this baroclinic contribution has much less inertia than its barotropic counterpart. Its transport depends on intermittent events (of the order of several days to a few weeks) that cause the intensification/weakening of upwelling and, consequently, the acceleration/slowing down of the current associated with the frontal upwelling system. The different character of both contributions has been discussed by Pelegrí and Richman (1993).

The above idealized 2D picture is modified by many factors, such as along-shore changes in wind/bathymetry and the interaction with eastern boundary currents (either the CC or the poleward undercurrent). There are also numerous instabilities, in the form of meanders, filaments and eddies, generated at the front itself or by the blockage effect of the islands to the current (Machín and Pelegrí, 2006b), which may form an intense mesoscale eddy field (Arístegui et al., 1994). All these factors are responsible for the existence of significant spatial variability, with localized regions of intense

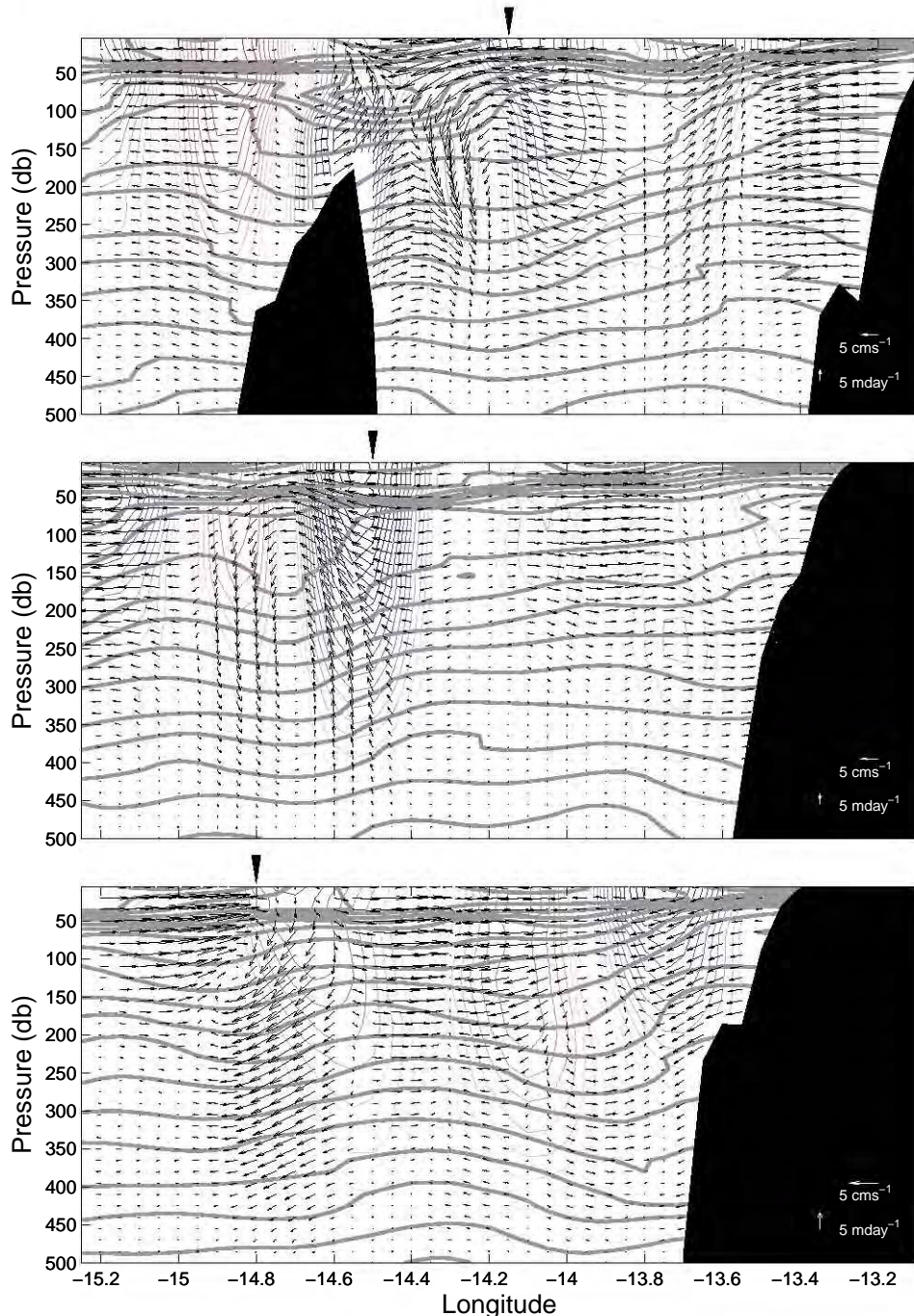


FIGURE 6.9: Across-shore sections of w_{qg} (m day^{-1}) and the zonal u_g along (top) 27.95°N , (middle) 27.55°N and (bottom) 27.25°N . Gray lines represent isopycnals contoured at intervals of 0.05 kg m^{-3} . The frontal position is indicated by arrows at the top of each panel.

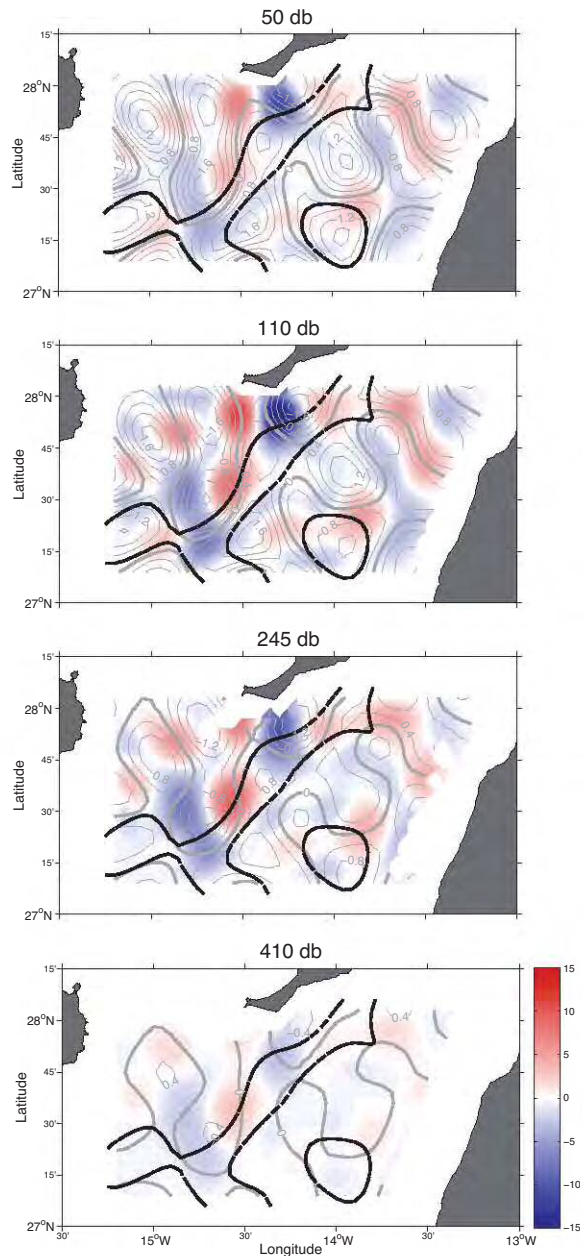


FIGURE 6.10: Distributions of mesoscale vertical velocity w_{qg} (m day $^{-1}$) at 50 db, 110 db, 245 db and 410 db; red and blue areas respectively indicate upward and downward velocities. Superimposed are the ζ_g fields (solid/dashed gray lines indicate positive/negative values, plotted at $0.4 \times 10^5 \text{ s}^{-1}$ intervals) together with the 0.625 and 0.64 dyn m isolines of dynamic height at 20 db (dashed black curves).

vertical motions, as discussed next.

The satellite images in Figure 6.3 illustrate the presence of the upwelling region adjacent to the coast, characterized by very cold and productive waters. The coldest and most productive waters are actually located over the platform, but its influence extends well beyond the 200 m isobath (e.g. Figure 6.3). From these images, as well as from the horizontal sections in Figure 6.5, we may locate the offshore extreme of the upwelling region as the 17.4 °C isotherm at 110 db, approximately 100 km off the African continental slope.

The distribution of γ_n , \vec{v}_g (relative to 500 db) and θ in three sections normal to shore (27.95°N, 27.55°N and 27.25°N) is very informative (Figure 6.7). In the upwelling region the upper isotherms (down to about 16 °C) rise towards the sea surface. Further deep the isopycnals downwell towards the slope in what constitutes the core of the poleward undercurrent. At 27.95°N the poleward undercurrent is adjacent to the platform but further south it appears to flow above a deeper slope isobath. At 27.55°N a near-barotropic southward flow of about 0.06 m s^{-1} occupies the water column onshore from this undercurrent. At 27.25°N an anticyclone (also visible in Figure 6.3) appears as the dominant feature adjacent to the slope.

From the vertical sections in Figure 6.7 and 6.9 we may appreciate that the width of the frontal system is about 30 km. Most isoneutrals in the frontal system do not reach the surface, and their largest horizontal gradients occur at near-surface levels, typically at about 50 db. In some instances, however, these large gradients are found at deeper levels, e.g. near 200 db along 27.55°N (Figure 6.7b). The baroclinic jet is associated to this front, its main baroclinicity reaching down to some 300 db. This jet is most intense at 27.55°N with maximum values of 0.18 m s^{-1} and least intense at 27.25°N where it only reaches 0.10 m s^{-1} , apparently because of the nearshore anticyclone which also displaces the jet offshore.

As a first approximation the zero ζ_g lines should give an idea of the extension of the frontal region and the beginning of the offshore region. The offshore region would be located seaward from the frontal system, where the baroclinicity has substantially decreased and ζ_g goes to zero. The zero ζ_g lines in Figure 6.10 define a wide frontal system, apparently squeezing the offshore region to a minimum expression southwest of Fuerteventura Island.

In the absence of mesoscalar features we would anticipate the offshore region to display a relatively weak southward flow, the Canary Current, reflected by the isoneutrals rising gently towards the coast. However, this background situation is completely masked by the presence of mesoscale features. Because of these features, a second zero ζ_g line intrudes far west of the jet core zero contour. Figure 6.10 underscores the

predominance of mesoscale features in our region of interest, which are cause offshore ζ_g values as large as those found in the other two regions.

Figures 6.9 and 6.10 indeed illustrate the presence of several mesoscale structures, particularly eddies near the islands, with large QG mesoscale vertical velocities. In the anticyclonic structure attached south of Fuerteventura Island there is a dominance of downwelling (negative) w_{qg} . In the other vortices, located further away from the islands, there are alternating areas, or phases, with positive and negative values. This agrees with the idea that young eddies, i.e. shortly after their generation by the islands, are still undergoing vertical adjustment, so that cyclones/anticyclones must have predominant positive/negative vertical velocities (Sangrà et al., 2007). However, once the vortices reach QG equilibrium then vertical motions of both signs appear in both cyclones and anticyclones. These maxima are located on the edges of eddies, as a result of the convergence/divergence of \vec{Q} , which then force the w_{qg} estimates (Bower, 1989; Gomis et al., 2001).

6.5.2 Origin of mesoscale structures

South of the Canary Islands, the presence of an important mesoscalar activity has been traditionally ascribed to the topographic generation by the Islands blocking the southward CC (Arístegui et al., 1994, 1997; Barton et al., 1998, 2004; Sangrà et al., 2005; Sangrà et al., 2007, 2009). Jiménez et al. (2008) have found that this topographic mechanism may be supported through wind-driven Ekman pumping at the islands' wakes. However, the nearby presence of the frontal system raises the possibility that some eddies may arise from instabilities of the associated baroclinic jet.

In order to elucidate the origin of the observed eddies, we examine the vertical distributions of θ along two different transects which cross two anticyclonic-cyclonic eddy pairs, or dipoles, located in the offshore (Dipole 1) and upwelling (Dipole 2) regions (Figures 6.11a,b). Note Dipole 2 is formed by the C1 feature in Figure 6.3 and an anticyclone found further northeast, not visible in the SST image. The number of mesoscale structures is abundant (e.g. Figures 6.10 and 6.11a) and many other combinations are certainly possible. However, based on the sections in Figures 6.7 and 6.9, we have selected these two dipoles as representative of what we identify as two different types of eddies, barotropic and deep (Dipole 1) versus baroclinic and shallow (Dipole 2). The paths shown in Figure 6.11a follow the grid points that best cross the center of the eddies.

The two dipoles display significantly distinct thermal patterns, which are most evident in the θ differences between the adjacent eddy cores as displayed in the right-hand-side of these figures. The isotherms in Dipole 1 have near-constant slope down to about 400 db, suggesting a dominance of the barotropic component and, therefore, it is

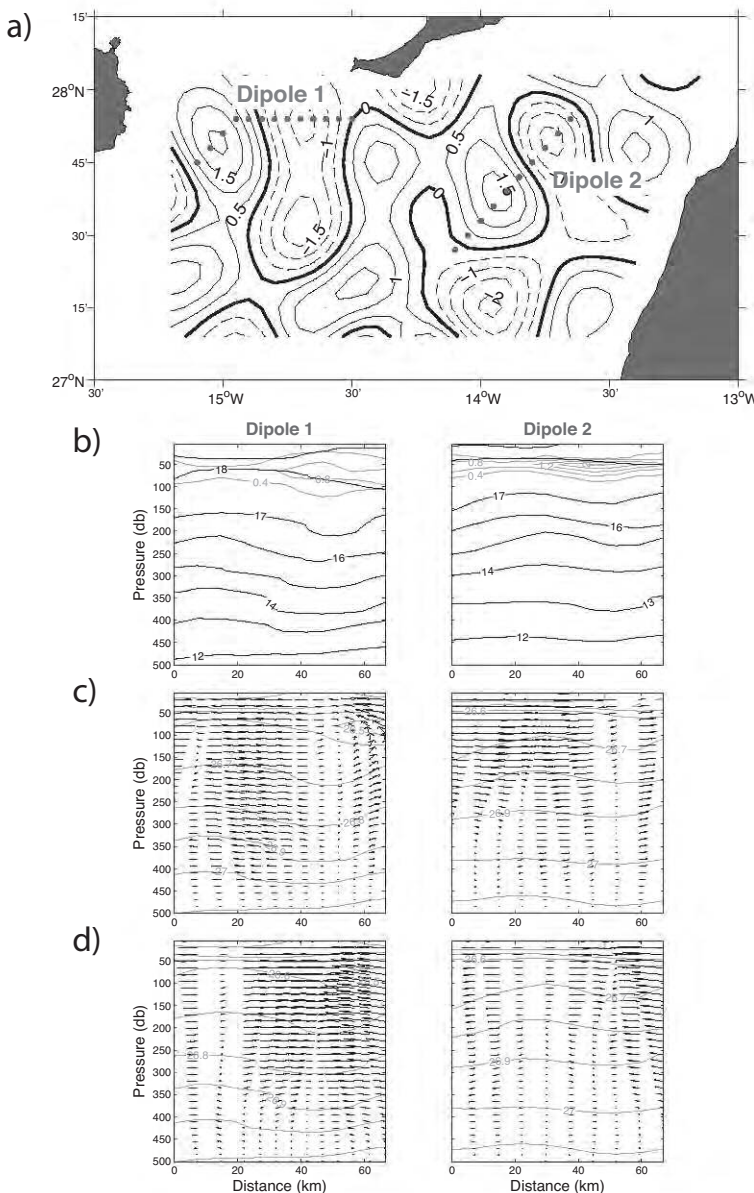


FIGURE 6.11: (a) Distribution of ζ_g at 20 db with dots indicating the position of Dipole 1 and Dipole 2. Left and right panels in (b) through (d) correspond to the sections through Dipoles 1 and 2, respectively. (b) Sections of θ ($^{\circ}\text{C}$; black lines) and *in situ* fluorescence (V ; grey lines). Contour interval is 1°C for θ , and 0.4 V for fluorescence. (c) Sections of w_{qg} (m day^{-1}) and the zonal u_g (10^{-2} m s^{-1}), referred to 500 db. (d) Sections of w_{qg} (m day^{-1}) and the meridional v_g (cm s^{-1}), referred to 500 db. In panels (c) and (d) the gray lines represent isopycnals contoured at intervals of 0.1 kg m^{-3} .

indicative of island-generated eddies. Contrary, Dipole 2 exhibits substantial flattening of isotherms from 250 db, thus its generation is apparently associated to baroclinic instabilities at the upwelling front. If we were to examine the dipole formed by the C1 and A1 features in Figure 6.3 we would have found it to be of mixed type, as A1 also has isotherms with significant slopes until near the bottom of the sampled water column (see bottom panels, along 27.25°N, in both Figures 6.7 and 6.9).

These differences are also quite clear in the velocity distribution through the two dipoles (Figures 6.11a,c,d). Dipole 1 exhibits a \vec{v}_g field with magnitude quite constant with depth, only changing very close to 500 db (left panels of Figures 6.11c,d). On the contrary, Dipole 2 has a clear baroclinic structure, with the magnitude of \vec{v}_g rapidly decreasing between 200 and 300 db (right panels of Figures 6.11c,d). The different character of both dipoles is also visible in the w_{qg} field, now with the offshore dipole having greater velocities than the near-shore dipole. Therefore, both the θ and velocity fields point at a different origin, with a near-barotropic Dipole 1 likely originating through the blockage of the CC by the islands and a baroclinic Dipole 2 resulting from the instability of the baroclinic frontal jet.

Recently, Sangrà et al. (2009) reported the region south of the Canary Islands to be a main source for long-lived westward propagating eddies, which lasted over six months while travelling over 2000 km. This region was found to be the origin for over 40% of the long-lived eddies observed in the northeastern subtropical Atlantic, with an average formation rate between 3 and 4 eddies per year. These authors used remote sensing techniques to identify the source region but the imagery lacked enough resolution near coast. Therefore, they emphasized the importance of the island effect but raised the possibility that some of the mesoscale activity was generated at the CTZ. Our results, however, support the idea that the instability of a coastal baroclinic zone is potentially a very important eddy generation mechanism. Our data suggests that this is the likely source of the northeastern eddies in the study area: C1 in Figure 6.3, which is the cyclone of Dipole 2 in Figure 6.11, and the anticyclone and cyclone located to the right of this cyclone as shown in Figures 6.10 and 6.11.

6.5.3 Fluorescence distribution

Early research has indicated that frontal regions, as transition zones between different water masses with high mesoscale activity, are sites of enhanced primary production (Holligan, 1981; Jones and Halpern, 1981; Falkowski et al., 1991). Indeed, satellite images (Pacheco and Hernández-Guerra, 1999) and field data from the Canary region (Arístegui et al., 1997; Barton et al., 1998, 2004) have shown that chlorophyll may be enhanced when associated with specific mesoscale structures. The principal factors influencing phytoplankton growth are the availability of solar radiation and inorganic nutrients, the latter supplied through both vertical movements and horizontal transport

from the upwelling region (e.g. filaments in Figure 6.3). Regarding the first factor, the depth of the euphotic zone has been reported to be quite constant in our study area, i.e. about 100 m (Neuer et al., 2007). Therefore, it does not appear to play a key role on the spatial distribution of primary production. Since no nutrient data are available from the cruise we cannot justifiably address the second issue, i.e. nutrient supply. However, based on the available fluorescence distributions, we can make some brief considerations on the potential role of mesoscale structures in modulating primary production.

Physical processes in mesoscale structures may either accumulate/retain the existing biomass or stimulate in situ growth of phytoplankton. Cyclones dome isopycnals and, therefore, tend to upwell subsurface nutrients into the euphotic zone; conversely anticyclones depress isopycnals making difficult the conection between the nutrients and light (Arístegui et al., 1997). However, the role of isopycnals doming or deepening on the nutrients supply can only be effective during relatively short periods immediately after eddy generation. After some time, typically of the order of a few eddy revolutions or about 10-20 days (Sangrà et al., 2005; Sangrà et al., 2007), the eddy is fully formed and the maximum isopycnal displacements have been attained. Beyond this time the eddy starts to decay and the isopycnal displacements decrease. At these later stages the mean tangential flow is closely in geostrophic balance so that vertical and radial advective motions are negligible, and vertical secondary circulations within the eddy may only arise as a result of diffusive processes. This is possibly a reason for differences in behaviour between the cyclonic and anticyclonic eddies: the proximity of subsurface nutrients in cyclonic eddies likely favours diapycnal transfer, contrary to what happens in anticyclonic eddies.

These ideas are supported by our data set. We find a substantial correlation between the vertical profiles of fluorescence and w_{qg} down to 110 db in those regions with high mesoscale activity ($r \geq |\pm 0.6|$, $p \leq 0.1$). This result fundamentally points to the isopycnals (and DFM) as caused by the vertical velocities w_{qg} associated to mesoscale structures. As indicated earlier (Section 6.4.2), the depth of the 17.4 °C isotherm approximately follows the base of the surface mixed layer. Since the depths of the surface mixed-layer shoals towards the coast, we expect there should be a correlation between the depth of the 17.4 °C isotherm and DFM depth. We indeed find such a high correlation, $r = 0.68$, $p \leq 0.01$. Nevertheless, the intensity of the DFM does not remain constant. There is a negative correlation ($r = -0.37$, $p \leq 0.01$) between the depth of the 17.4 °C isotherm and the intensity of the DFM, indicating that the shallower the DFM the more intense it become, e.g. cyclonic eddies appear with higher fluorescence levels.

6.6 Conclusions

We have examined the characteristics of the CTZ, with special emphasis on the 3D circulation patterns, in a 100 km long and 200 km wide region south of the Canary

Islands. The dominant characteristic is the coastal upwelling frontal system, some 30 km wide and occupying the top 300 db of the water column. This frontal region is characterized by an intense baroclinic jet, whose intensity decreases from 0.18 to 0.05 m s⁻¹ between the sea surface and 300 db, that separates upwelled waters from the offshore region.

Over the slope, between the frontal region and the continental platform, we find upwelled waters which are relatively homogeneous down to the sea floor. At pressures less than 200-300 db we find a weak southward flow that changes little with pressure, which we identify as the barotropic contribution of the CUC. Just below and down to some 400-500 m we find the poleward undercurrent, a region of order 10-20 km wide characterized by isoneutrals deepening towards the sea bottom with associated northward flow.

A traditional perspective of the offshore region would anticipate isopycnals gently rising towards the coast, the large-scale signature of the CC. However, in our relatively small region this picture is masked by the presence of substantial mesoscale activity. An important finding is that these vortices have two different origins: approximately barotropic vortices are generated through the traditional topographic mechanism, i.e. the interaction of the CC and the Canary Islands, and more baroclinic vortices originate through instabilities of the frontal system, in the form of meanders that eventually detach as vortices to both sides of the front. These vortices, and those generated by the interaction of the CC and the Canary Islands, characterize the offshore region.

The mesoscale and wind-induced vertical velocity field is characterized by a patchy field superposed onto a zonal gradient. The distribution of QG mesoscale vertical velocities is intermittent all over the domain, changing with horizontal and vertical position. These velocities become very intense in phases of meanders and vortices, up to -18 m day⁻¹ and 12 m day⁻¹, but their patchy spatial structure causes the associated transport to be small, of order 0.01 Sv. This contrasts with other non-zero mean contributions to the vertical velocity field (upwelling, Ekman pumping and diapycnal), that change with distance from the coast. The upwelling vertical field, positive in the upwelling region, has mean values of 0.7 m day⁻¹ and a total contribution of 0.08 Sv. The diapycnal velocity w_{dia} is mostly located in the frontal region, as a result of its subcritical character, with an estimated total transport of 0.18 Sv that corresponds to mean positive velocities of 5.2 m day⁻¹. Ekman pumping is the slowest one, about 0.3m day⁻¹, as it takes place over a potentially large offshore region. An observed increase of DFM values in the frontal and upwelling regions suggest a potentially important role played by these diapycnal and upwelling processes. Further offshore a moderate increase in DFM appears to be associated with peaks of QG mesoscale vertical velocity w_{qg} , intermittently developing at different phases of the evolving eddies.

CHAPTER 7

Conclusions and future work

The major conclusions arising from this thesis are:

1. Examination of hydrographic sections over the tropical and subtropical North Atlantic suggests that waters between 600 and 1800 db have been warming and salinifying since 1957, although there is a clear evidence of considerable interdecadal variability superimposed on the long-term trend.
 - (a) The warming reported for the period 1957-1993 of the intermediate and upper deep waters along 7.5°N, has continued until 2010; however the cooling of deeper waters have been halted or partly reversed.
 - (b) The warming trend of the upper ocean (600-1800 db) observed along 24.5°N between 1957 and 1998 was reversed between 1998 and 2004. A similar change in tendency was observed in salinity. The upper waters warmed 0.27°C from 1957 to 1998, the warmest and saltiest year since 1957. Then, a cooling of -0.15°C occurred in the period between 1998 and 2004.
 - (c) The Canary region waters present a significant rise in temperature and salinity on isobars between 1500 and 2300 db. The maximum increase (at 1600 db) is occurring at a rate of 0.29°C and 0.047 per decade, which are much higher than the observed changes averaged zonally along the eastern basin of the 24.5°N section.
2. Isobaric change decomposition into changes on neutral surfaces and changes due to the vertical displacements of the isoneutrals revealed the former mechanism as the principal contributor of the observed changes. Nevertheless, some water masses are changing. North Atlantic Central Water arrived to the Canary region in 2006 in a cooler and fresher form than in 1997. Contrary, Antarctic intermediate Water and Upper Circumpolar Water in the 7.5°N section were warmer and saltier in 2010 as compared to 1993.

3. Data from Argo network have corroborated the latest patterns of change at 24.5°N, thus demonstrating the value of Argo data as a tool for observing oceanic variability. Moreover, its use offers the advantages of i) data availability in near real time, ii) large spatial coverage, iii) a small eddy noise compared to that of hydrographic sections and iv) enabling the inspection of changes at relatively short temporal scales.
4. Analysis of the 9-year currentmeter times series in the Lanzarote Passage has revealed an annual mean mass transport of -0.81 ± 1.48 Sv for the NACW, $+0.09 \pm 0.57$ Sv for the AAIW and -0.05 ± 0.17 Sv for the MW.
 - (a) Seasonal variability of these water masses are characterized by a maximum southward transport of NACW in winter and spring, followed by a minimum in summer and fall. Near zero values during winter and spring are found for AAIW, with a maximum northward value in summer and a negative value in fall, when this water mass reverses its flow. MW has a similar seasonal pattern to NACW.
5. Exploration of high-resolution data collected southeast of the Canary Islands during late winter 2006 showed that the costal transition zone off northwest Africa was divided into three different regions based on their physical and dynamic characteristics: the upwelling, frontal and offshore regions.
 - (a) The upwelling region was characterized by cold and weakly stratified waters flowing towards the equator, with a poleward undercurrent of approximately 5 cm s^{-1} over the continental slope.
 - (b) The frontal region was characterized by a southwestward baroclinic jet associated with cross-shore raising isoneutrals; the jet transport is close to 1 Sv, with maximum velocities of 18 cm s^{-1} at surface decreasing to 5 cm s^{-1} at 300 db.
 - (c) The frontal region showed the presence of deep eddies probably generated by the topographic blocking of the islands to the southward Canary Current, as well as much shallower eddies that likely have arisen as instabilities of the baroclinic upwelling jet.
 - (d) The quasi-geostrophic vertical velocities, ranging from -18 to 12 m day $^{-1}$, were larger than the diapycnal vertical velocities associated with the frontal region (mean value of about 5 m day $^{-1}$), the wind-induced vertical velocities generated offshore, as a result of the wind stress horizontal divergence (a fraction of a meter per day), and in the upwelling region, due to the

coastal constraint (about 2 m day^{-1}). However, its patchiness in the quasi-geostrophic vertical velocity caused the integrated vertical transport (0.01 Sv) to be one order of magnitude smaller than either the coastal Ekman transport (0.07 Sv), the integrated Ekman pumping (-0.05 Sv) or the diapycnal transfer (0.18 Sv).

The results reported in this thesis point to different directions in order to improve our understanding of the long-term variations of water properties in the North Atlantic Ocean. The analysis has to be largely based on our improved skill to gather large amounts of data, either through conventional cruises or innovative systems such as Argo profilers, and the very much enhanced computational skills to jointly analyze these large data sets. In particular, oceanographic data has to be viewed in conjunction with meteorological data, in order to track back in time the origin of the observed thermohaline anomalies, and also with numerical models, so that we may predict the future path for such changes.

A brief outline of some of these lines of future research follows :

1. To use the recently completed 24°N section in order to distinguish whether the observed changes are interannual/interdecadal oscillations or they do represent actual long-term trends;
2. Further study the ocean variability at shorter temporal scales, particularly the presence of large thermocline oscillations that are visible in the transatlantic sections;
3. To remove the oscillations which perturb the thermohaline fields within upper and intermediate waters along 7.5°N, and repeat the analysis of temperature and salinity changes;
4. To explore the relationship between the observed hydrographic changes and the long-term variations in the atmospheric patterns;
5. To further study the large scale covariation of the patterns of circulation and the physical properties in the Canary region from CTD and/or currentmeter data;
6. Lastly, to investigate the time evolution of the northwest African upwelling, in terms of both the extension and properties of the upwelled waters, through observed and model data, in order to estimate possible range of variation and its potential role as regional and global thermoregulator.

CHAPTER 8

Resumen en español

En este último capítulo se realiza una síntesis de la tesis. Primero se describe el sistema climático y la importancia de los océanos en el mismo. Seguidamente se realiza una revisión de la variabilidad climática observada en el océano Nortatlántico, lo que nos llevará a establecer los objetivos y estructura adoptada en la tesis. Después de exponer los principales resultados de cada uno de los capítulos, se presentan las conclusiones derivadas de los mismos y se proponen futuras líneas de trabajo.

Contents

| | |
|---|------------|
| 8.1 Introducción general y motivación | 127 |
| 8.1.1 El sistema climático de la Tierra | 127 |
| 8.1.2 La importancia de los océanos en el sistema climático | 130 |
| 8.1.3 Variabilidad y cambio climático | 134 |
| 8.1.4 Objetivos de la tesis y organización | 136 |
| 8.2 Síntesis de resultados | 138 |
| 8.2.1 Cambios decadales en el Atlántico tropical a lo largo de la sección 7.5°N (Capítulo 2) | 138 |
| 8.2.2 Cambios en las tendencias de temperatura y salinidad en la sección transatlántica 24.5°N (Capítulo 3) | 141 |
| 8.2.3 Variaciones de la temperatura y salinidad subsuperficiales en la región Canaria (Capítulo 4) | 145 |
| 8.2.4 Nueve años de datos del transporte de masa en el límite oriental del giro subtropical del Atlántico Norte (Capítulo 5) | 148 |
| 8.2.5 Circulación tridimensional en la zona de transición costera del noroeste de África (Capítulo 6) | 158 |
| 8.3 Conclusiones y futuras líneas de investigación | 172 |

8.1 Introducción general y motivación

Esta sección ofrece un resumen del sistema climático de la Tierra, el cual actúa como una máquina térmica alimentada por la energía del Sol. Se describen brevemente los principales componentes del sistema climático, es decir, la atmósfera, la hidrosfera, la criosfera, la geosfera y la biosfera; y también se aportan ejemplos que ilustran el complejo carácter no lineal de este sistema. Seguidamente discutimos la importancia del océano como un regulador del clima por su capacidad de almacenar y transportar calor, agua dulce y gases radiativamente activos que han sido intercambiados con la atmósfera. Introducimos la circulación del océano superior, la circulación termohalina y los remolinos oceánicos; los tres mecanismos principales por los que el océano lleva a cabo la distribución de energía. La sección termina haciendo una revisión de la investigación climática realizada en el océano Atlántico tropical y subtropical y presentando las cuestiones a las que nos enfrentaremos en esta tesis.

8.1.1 El sistema climático de la Tierra

Clima y tiempo

El origen de la palabra clima se remonta a la antigua palabra griega "klimat", que significa inclinación. Los griegos sabían que existía una relación directa entre el clima y la inclinación de los rayos del Sol sobre la superficie de la Tierra; de modo que, a una mayor inclinación, más frío es el clima. Sin embargo, esta definición resulta insatisfactoria pues el clima local es más que una mera función estacionaria de la latitud.

Entonces, ¿qué significa clima en el climatología actual? La popular frase "*Clima es lo que esperamos, tiempo es lo que conseguimos*", atribuida a Robert A. Heinlein, revela algunos aspectos intrínsecos del clima, así como las diferencias respecto del concepto tiempo. Las definiciones dadas por el Grupo Intergubernamental de Expertos sobre el Cambio Climático aclara las distinción entre ellos:

- *El tiempo, tal y como lo experimentamos, es el estado fluctuante de la atmósfera alrededor de nosotros, caracterizado por la temperatura, el viento, la precipitación, las nubes y otros elementos de tiempo. Este tiempo es el resultado de sistemas de tiempo que se desarrollan y caen rápidamente tales como los sistemas de altas y bajas presiones en latitudes medias con sus correspondientes zonas frontales, lluvias y ciclones tropicales. El tiempo tiene una predictabilidad limitada. Los sistemas mesoscales convectivos son predecibles en un período de horas solamente; los ciclones a escala sinóptica se pueden predecir en un período de varios días a una semana. Más allá de una semana o dos, los sistemas individuales de tiempo son impredecibles.*
- *El clima se suele definir como el tiempo promedio, o más rigurosamente, como la descripción estadística en términos de la media y la variabilidad de las cantidades*

relevantes en un período de tiempo que oscila desde meses a miles o millones de años. El período clásico para promediar estas variables es de 30 años, tal y como define la Organización Meteorológica Mundial. Las cantidades relevantes suelen ser variables superficiales como temperatura, precipitación y viento. El clima en un sentido más amplio es el estado, incluyendo una descripción estadística, del sistema climático.

Componentes del sistema climático

El estado del clima está determinado por el **sistema climático**, un sistema complejo e interactivo que consta de la atmósfera, la hidrosfera, la criósfera, la geosfera y la biosfera, y de las interacciones entre ellos (ver Figura 1.1).

La **atmósfera** es la envoltura de gases que rodea la Tierra. Está dividida en cuatro capas, siendo las dos más bajas, la troposfera (hasta 18 km) y la estratosfera (hasta 50 km), críticas para el clima. Cerca del 80% de la masa de la atmósfera está contenida en la troposfera. El aire atmosférico está principalmente compuesto por nitrógeno (78.08%), oxígeno (20.94%) y argón (0.93%). Éstos son los llamados gases constantes porque su concentración permanece prácticamente constante en el espacio y en el tiempo. Al contrario, los restantes gases son llamados gases variables, entre los que se encuentran los **gases invernadero** tales como el vapor de agua, dióxido de carbono, metano, dióxido nitroso y ozono. Estos componentes, aunque se encuentren en cantidades traza en la atmósfera, pueden tener grandes implicaciones en el clima. Las muestras de aire no filtradas pueden contener también cantidades traza de polvo, polen y esporas, spray marino, ceniza volcánica, y varios contaminantes industriales, como mercurio y cloro, flúor y componentes de azufre.

La **hidrosfera** comprende todo el agua líquida de superficie y subterránea, dulce y salada; por tanto, incluye ríos, lagos, acuíferos, océanos y mares. Entre ellos, los océanos son los que tienen mayor cobertura espacial, aproximadamente el 70% de la superficie de la Tierra. Los océanos transportan calor, agua dulce y gases disueltos como el dióxido de carbono. Debido a su alta capacidad calorífica, los océanos almacenan grandes cantidades de calor, actuando como reguladores del clima (ver la siguiente sección).

La **criósfera** incluye las capas de hielo de Groenlandia y la Antártida, los glaciares continentales y los campos de nieve, el hielo marino y el permafrost. Su principal impacto en el sistema climático reside en cuatro aspectos: i) su alto albedo produce la reflexión de gran parte de la radiación solar que reciben; sin la criósfera, el albedo global sería considerablemente más bajo y, por consiguiente, la superficie de la Tierra absorbería más energía dando lugar a temperaturas más altas en la atmósfera; ii) aisla térmicamente al océano de la atmósfera y desacopla el océano del efecto directo del viento; iii) representa el mayor reservorio de agua dulce de la Tierra, constituyendo una fuente de variabilidad en el volumen de los océanos y los niveles globales del mar. La tasa promedio global del aumento del nivel del mar durante el siglo XX ha sido estimada en 1.0-2.0 mm/año; sin embargo, la contribución de la fusión de los hielos es considerablemente pequeña en comparación con el aumento del

nivel del mar producido por la expansión térmica del océano; and iv) la formación de hielo marino en regiones polares, junto con la pérdida de calor, incrementan la densidad superficial y eventualmente, inician la formación de masas de agua profundas y por tanto, la circulación termohalina (ver sección 8.1.2).

La **geosfera** consiste en la parte sólida de la Tierra, desde los suelos, los sedimentos y las rocas de la superficie de la Tierra, hasta las cortezas continentales y oceánicas y el manto. Su papel principal es el de controlar cuánta de la energía recibida desde el Sol es devuelta a la atmósfera. La geosfera es el reservorio en el que elementos y compuestos importantes para el sistema climático tienen los mayores tiempos de residencia. La interacción directa con la atmósfera y los océanos ocurre a través de las erupciones volcánicas y la actividad hidrotermal. El material y los gases transportados hacia la atmósfera en una erupción volcánica pueden interaccionar con la radiación que llega reflejándola y, por consiguiente, reduciendo la energía disponible en el sistema climático. La geosfera define fronteras geográficas en la tierra, el mar y el aire; por tanto, también modifica la circulación de la atmósfera y del océano.

La **biosfera** consiste en la biota marina y terrestre. Influye sobre el consumo y la producción de gases contituyentes de la atmósfera. La biota autotrófica, a través del proceso de fotosíntesis, produce oxígeno e incorpora cantidades significativas de dióxido de carbono para su crecimiento. En el caso del fitoplancton marino, además pueden secuestrar este carbono inorgánico a través de su hundimiento hacia niveles oceánicos más profundos, proceso conocido como bomba biológica. Por tanto, la biosfera juega un papel crucial en el ciclo del carbono, así como en los de gases traza como el metano y el óxido nitroso. El metano se produce en condiciones anaeróbicas por la decomposición bacteriana y en los sistemas digestivos de ciertos animales (particularmente rumiantes), mientras que el óxido nitroso es un producto de la liberación aeróbica de nitrógeno dentro de los suelos. La biota terrestre también participa en el ciclo hidrológico, por ejemplo moderando la tasa a la cual la precipitación entra en el suelo o determinando el nivel de transpiración. También reduce el momento atmosférico debido al efecto de resistencia que produce la vegetación cuando el viento fluye a través de ella.

El balance de energía en la Tierra

A escala planetaria, el sistema climático está impulsado por la energía térmica recibida desde el Sol (Figura 1.2). El promedio de la radiación solar entrante que alcanza la parte superior de la atmósfera es de 342 W m^{-2} , la cual es principalmente radiación de onda corta. Aproximadamente el 30% es reflejado hacia el espacio por las nubes, aerosoles y áreas con un alto albedo como son la nieve, el hielo y el desierto. El 70% restante, alrededor de 240 W m^{-2} , entra en el sistema climático; dos tercios son absorbidos por la superficie de la Tierra y un tercio por la atmósfera. Para alcanzar un balance radiativo, y mantener la temperatura aproximadamente constante a lo largo del tiempo, la Tierra debe radiar una cantidad de energía igual hacia el espacio. Esta pérdida de calor ocurre a través de radiación saliente de onda larga. Si se reflejaran 240 W m^{-2} , la superficie de la Tierra tendría una temperatura media de -19°C , la cual es mucho menor de la actual. La explicación a esta discrepancia es el **efecto invernadero**, cuya base principal es que la radiación de onda larga

emitida desde la superficie es atrapada por los gases traza de la atmósfera y las nubes y luego es re-emitida a la superficie de la Tierra. Esto resulta en una temperatura superficial media de 14°C, haciendo la Tierra un lugar habitable.

Además de la radiación solar, existen otros dos procesos que transfieren calor dentro del sistema climático. El primero es el **calor sensible**. La superficie de la Tierra, que ha sido calentada por el Sol, transfiere calor por conducción a la capa más baja de la atmósfera. El aire calentado (y por tanto menos denso) luego asciende transmitiendo el calor hacia arriba por convección. El segundo proceso es la transferencia de **calor latente**. Este proceso implica un cambio en el estado del agua, ya sea desde hielo a agua líquida o desde agua líquida a vapor de agua. La gran cantidad de energía requerida en esta transformación permanece latente en el agua, y es liberada posteriormente en el proceso contrario.

El ciclo hidrológico

Como vimos en la sección anterior, la energía del Sol dirige el movimiento del agua entre los componentes del sistema climático. Esta circulación global de agua (en sus fases líquida, vapor o hielo) se denomina **ciclo hidrológico** (ver Figura 1.1). Las reservas de agua en la Tierra son principalmente almacenadas en los océanos, glaciares y coberturas de nieve persistentes, y en aguas subterráneas. La proporción de agua en la atmósfera, suelos o ríos es comparativamente más pequeña. El agua se mueve entre estos reservorios por procesos como: evaporación, condensación, precipitación, deposición, escorrentías, infiltración, sublimación, transpiración y flujo de aguas subterráneas.

8.1.2 La importancia de los océanos en el sistema climático

Arthur C. Clarke una vez dijo "*Qué inapropiado es llamar a este planeta Tierra cuando claramente es océano*". Efectivamente, los océanos ocupan aproximadamente el 70% de la superficie de la Tierra. Además, contienen el 97% del agua libre de la Tierra y reciben el 78% de la precipitación global. Esto confiere al océano una capacidad calorífica mucho mayor que la de cualquier otro componente del sistema climático. Solamente los primeros 3.2 m del océano contienen el mismo calor que toda la atmósfera.

La respuesta de la superficie de la Tierra al ciclo estacional del calentamiento solar es un buen ejemplo de la alta capacidad calorífica del océano. Las masas de tierra se calientan (o enfrián) rápidamente debido a que no pueden almacenar grandes cantidades de calor ni conducirlo de forma rápida. Al contrario, los océanos se calientan (o enfrián) lentamente por su alta capacidad calorífica y la mezcla mecánica inducida por los vientos en los primeros 100 m de la columna de agua. En otras palabras, el océano tiene una alta resistencia a cambios de temperatura, es decir, su alta inercia térmica da lugar a que pequeños cambios en temperatura estén asociados a la ganancia o pérdida de grandes cantidades de energía. Por tanto, el océano presentará una respuesta tardía a las influencias atmosféricas no aleatorias, produciendo cambios graduales del clima.

Luego, el papel de los océanos en el sistema climático es el de almacenar y distribuir calor, así como agua dulce y gases disueltos, al mismo tiempo que actúa como memoria de las variaciones climáticas. Por tanto, las preguntas son ¿cómo y cuándo/dónde el océano almacena y distribuye el calor?

En la sección 1.1 el balance de energía global fue explicado en base al promedio para toda la Tierra. Sin embargo, la radiación solar entrante y la reflexión por parte de la superficie terrestre varían con la latitud. Las bajas latitudes reciben más radiación que los polos debido a un ángulo de incidencia más directo de los rayos solares; mientras que las altas latitudes reflejan más radiación debido a la presencia de superficies con un alto albedo. Como resultado, existe un exceso de calor a bajas latitudes y un déficit a altas latitudes. De ahí que para alcanzar un balance de energía sea necesario que las circulaciones atmosférica y oceánica realicen un transporte meridional de calor.

El porcentaje de transporte de calor hacia los polos de la atmósfera y el océano sugiere que realizan contribuciones similares, siendo dominante el océano en los trópicos y la atmósfera a altas latitudes. De este modo, el interés permanece sobre los mecanismos del océano para distribuir el calor (y el agua dulce). Se han sugerido tres mecanismos por los cuales se realiza esta tarea: i) la circulación conducida por el viento, ii) la circulación termohalina y iii) los remolinos oceánicos. A continuación se explican brevemente cada uno de estos tres procesos.

La circulación conducida por el viento

Tal como su nombre sugiere, la circulación conducida por el viento es la circulación desarrollada en la capa superior del océano en cada una de las cuencas oceánicas como respuesta al forzamiento a larga escala de los vientos. De hecho, si miramos la circulación de los vientos en los niveles bajos de la atmósfera y a las corrientes oceánicas superficiales, veremos la gran relación existente entre ellos (Figura 1.3).

Ekman (1905) fue el primero en presentar una teoría mecánica satisfactoria acerca de las corrientes dirigidas por el viento bajo la influencia de la rotación de la Tierra. Sus resultados mostraron que el estrés ejercido por los vientos, a través de la transferencia turbulenta de momento según fluyen sobre la superficie del océano, produce una corriente superficial dirigida a un ángulo a la derecha (izquierda) de la dirección en la que prevalecen los vientos en el hemisferio norte (sur). Este transporte, llamado **transporte de Ekman**, está limitado a los primeros 10-100 m de la columna de agua, a la cual se refiere como **capa de Ekman**. Entonces, podríamos decir que el efecto directo del viento solamente se siente en una parte muy superficial del océano. Sin embargo, ¿hasta dónde llega su efecto indirecto?

Siguiendo la teoría de Ekman (para el hemisferio norte), los vientos anticiclónicos en la región subtropical resultan en transportes de Ekman dirigidos hacia el interior, mientras que en el océano subpolar, los vientos ciclónicos resultan en transportes de Ekman

dirigidos hacia afuera. Puesto que el agua no se puede acumular indefinidamente, tiene lugar una transferencia de fluido entre la capa de Ekman y el océano interior. De esta manera los flujos convergentes inducen hundimiento o **bombeo de Ekman** y los flujos divergentes inducen afloramiento o **succión de Ekman**. Estos movimiento verticales determinan la estructura y circulación en la termoclinia permanente a través del modelo de Sverdrup (cita).

Las propiedades θ -S de las masas de agua que componen la termoclinia subtropical son establecidas por los flujos océano-atmósfera y la subducción, es decir, la transferencia de agua en el océano interior. El modelo de formación de masas de agua propuesto por Iselin (1939) mostró que el bombeo de Ekman a finales de invierno fuerza la penetración de las aguas de la capa de mezcla en la termoclinia principal, donde fluyen a lo largo de las isopicnas. Los fundamentos por los que el océano interior refleja las propiedades de finales de invierno fueron posteriormente explicados por Stommel (1979). Este autor indicó que durante la primavera y el verano las aguas no penetran en la termoclinia debido al rápido hundimiento de la capa de mezcla en otoño e invierno. De ahí que el periodo de subducción efectiva esté limitado al final del invierno.

Además, la velocidad vertical inducida por el viento (bombeo o succión de Ekman) inclina la termoclinia. Ello genera gradientes horizontales de presión, los cuales eventualmente se balancearán con la fuerza de Coriolis dando lugar a **flujos geostróficos**. El flujo gesotrófico, que es paralelo a los contornos de altura geopotencial, produce sistemas de corrientes circulares a larga escala alrededor de las cuencas conocidos como **giros** (ver Figura 1.3, panel inferior).

Los **giros subpolares** presentan una circulación ciclónica a altas latitudes en el hemisferio norte. El giro subpolar noratlántico comprende la Corriente Noratlántica, las Corrientes este y oeste de Groenlandia y la Corriente del Labrador. En el hemisferio sur, donde el sistema de giros no se puede desarrollar por la ausencia de limitación continental, los vientos del oeste dirigen la enérgica Corriente Circumpolar Antártica, a través de la cual se realiza la transferencia de calor y masa entre las cuencas oceánicas.

Los **giros subtropicales** en los hemisferios norte y sur rotan en direcciones opuestas centrados aproximadamente a 30° de latitud. En el giro subtropical del Atlántico norte, la corriente del Golfo fluye desde el ecuador hasta cerca de $40\text{--}45^{\circ}\text{N}$, donde continúa hacia el este como la Corriente Noratlántica. La Corriente Noratlántica posteriormente se divide en la Corriente de Noruega (que fluye hacia el norte) y la Corriente de Azores que alimenta el flujo hacia el sur de la Corriente de Canarias. Aproximadamente a 15°N , la Corriente de Canarias se une a la Corriente Norecuatorial cerrando el giro.

Puesto que el efecto de Coriolis sobre las corrientes se incrementa con el aumento de la latitud, las corrientes de frontera oeste y este tienen una naturaleza muy diferente. La corrientes de frontera oeste (p.e. la Corriente del Golfo) son generalmente estrechas (<100 km), profundas (2 km) e intensas, transportando hacia los polos unos 150-200 Sv de aguas cálidas a una velocidad promedio de 1 ms^{-1} . Por otro lado, las corrientes de frontera este (p.e.

la Corriente de Canarias) son anchas (1000 km), someras (500 m) y lentes, transportando hacia los polos cerca de 10-15 Sv de aguas frías a una velocidad promedio de $0.05\text{--}0.1 \text{ ms}^{-1}$. Una característica particular de los sistemas de frontera este es la presencia del **afloramiento costero**. Este proceso ocurre cuando el transporte de Ekman empuja las aguas superficiales lejos de la costa. El agua empujada hacia afuera es reemplazada por agua subsuperficial más fría y rica en nutrientes.

La circulación termohalina

Además de la circulación conducida por el viento, existe en el océano la **circulación termohalina**, una circulación a larga escala dirigida por cambios en la densidad del agua de mar que surgen por efectos en la temperatura (termo) o en la salinidad (halinos). La gran pérdida de calor y el rechazo de sal que tiene lugar durante la formación de hielo marino, hace aumentar la densidad de las aguas de la capa de mezcla invernal a altas latitudes en los océanos Atlántico y Austral. Como resultado, estas aguas más densas se hunden para formar las aguas profundas y abisales, las cuales se extienden a través del océano global. La conservación de volumen en el Atlántico norte requiere por tanto un balance entre el flujo de las aguas frías y profundas que viajan hacia el ecuador y el flujo cálido de la termoclina que viaja hacia el polo.

El acoplamiento entre las circulaciones superficial y profunda de larga escala se conoce como **circulación meridional** (Figura 1.4). Aproximadamente $15 \pm 12 \text{ Sv}$ de Agua Profunda del Noratlántico, producida en el norte del Océano Noratlántico, se mueven hacia el sur a lo largo del talud continental americano incorporando Agua Antártica Intermedia y Agua Antártica de Fondo hasta alcanzar un volumen de $23 \pm 12 \text{ Sv}$ at 30°S . En el Océano Austral, la formación de agua profunda asciende a $21 \pm 6 \text{ Sv}$ de Agua Circumpolar Profunda, la cual aproximadamente ocupa el rango de profundidades del Agua Noratlántica Profunda inferior (Ganachaud and Wunsch, 2000). El Agua Noratlántica Profunda entra en la célula menor del Océano Austral y se mezcla con las aguas antárticas para formar aguas abisales más densas. Una parte de Agua Antártica de Fondo, incluyendo la recientemente formada Agua Noratlántica Profunda, entra en las cuencas Índica y Pacífica como Agua Circumpolar Profunda y/o Agua Noratlántica Profunda modificada (Lumpkin and Speer, 2007). Durante su viaje, las entradas hacia las cuencas Índica y Pacífica terminan aflorando para formar parte de la circulación dirigida por el viento y finalmente alimentan las aguas someras que fluyen alrededor de la Antártida o bien, siguen su camino de vuelta hacia el punto de inicio en el Océano Noratlántico como corrientes cercanas a la superficie. Un ciclo de este circuito lleva un tiempo aproximado de mil años. Esto implica que las masas de agua involucradas en el mismo, las cuales se aislan de la influencia atmosférica en su momento de formación, secuestran calor durante dicho periodo de tiempo. Por consiguiente, variaciones en el funcionamiento de la circulación meridional global pueden causar cambios significativos en el sistema climático.

Remolinos oceánicos

Los remolinos oceánicos también juegan un papel importante en el transporte de calor y otras propiedades climáticamente importantes. A pesar de que su contribución global es aparentemente pequeña, se ha determinado que es significativa en las corrientes de frontera oeste, regiones ecuatoriales y en la corriente Circumpolar Antártica. Estas corrientes se vuelven inestables, bien por procesos baroclinos o barotrópicos, dando lugar a la formación de meandros. El meandro puede crecer hasta que finalmente se separa y forma un **anillo**. El flujo serpenteante de la Corriente del Golfo resulta en dos tipos de anillos: anillos de núcleo frío (remolinos ciclónicos), formados a partir de las aguas frías del norte que se desprenden en el lado cálido al sur de la corriente, y los anillos de núcleo cálido (remoclinos anticiclónicos), los cuales llevan aguas cálidas del sur hacia la región norte de la corriente (ver Figura 1.5). El movimiento de los anillos que se forman al norte de la Corriente del Golfo es bastante limitado por lo que normalmente se vuelven a unir a la corriente principal; sin embargo, los anillos de núcleo frío se dispersan por el Mar de los Sargazos.

8.1.3 Variabilidad y cambio climático

La complejidad del sistema climático es tal que el clima de la Tierra está continuamente evolucionando y, por tanto, variando en múltiples escalas espaciales y temporales (desde semanas a milenios, y desde escalas regionales a globales). Llegados a este punto, es importante diferenciar entre **variabilidad climática** y **cambio climático** (IPCC):

La variabilidad climática se refiere a variaciones en el estado medio y otras características (tales como las desviaciones estándar, la ocurrencia de eventos extremos, etc.) del clima en todas las escalas espaciales y temporales más allá de aquellas de eventos de tiempo individuales.

El cambio climático se refiere a un cambio en el estado del clima que puede ser identificado (p.e. usando tests estadísticos) por cambios en la media y/o en la variabilidad de sus propiedades, y que persiste por un periodo extenso, típicamente décadas o más.

La variabilidad climática y el cambio climático pueden resultar bien por alteraciones dentro del sistema climático, en sus componentes y/o interacciones, o por variaciones naturales o antropogénicas del forzamiento externo. Ejemplos de variaciones en el forzamiento externo son las variaciones en la radiación solar, en la actividad volcánica o en la cantidad de gases de efecto invernadero causados por las actividades humanas. La respuesta del clima a cualquier forzamiento es bastante compleja debido a las interacciones no lineales entre los componentes y los procesos de retroalimentación. Un proceso es llamado de **retroalimentación** cuando cambia la sensibilidad del clima; por tanto, intensifica (retroalimentación positiva) o reduce (retroalimentación negativa) la respuesta del clima a un forzamiento dado. Por ejemplo, un mecanismo importante de retroalimentación es el del vapor de agua: a medida que se calienta la Tierra, la evaporación se incrementa produciendo un aumento de los niveles

del vapor de agua en la atmósfera, el cual atrapa más radiación amplificando a su vez el calentamiento.

Esta tesis, al igual que muchos estudios sobre la detección de cambio climático, se dedica a la identificación de la variabilidad y tendencias en el clima y la atribución de estos cambios a los mecanismos causantes. Esta tarea necesita de observaciones de calidad durante largos períodos y con suficiente cobertura espacial. Por ejemplo, la temperatura y salinidad oceánicas son indicadores sensibles a la varibilidad y cambio climático, aunque las medidas disponibles son relativamente cortas y dispersas en el espacio. A pesar de este inconveniente, los grandes avances que se han realizado en el entendimiento del clima del océano han mostrado que la suposición inicial de un océano en estado estacionario era errónea.

El capítulo 5 del cuarto informe de evaluación del IPCC, publicado en 2007 (Bindoff et al., 2007), concluye que la temperatura media del océano global se ha estado incrementando desde 1961 en la capa de 0-3000 m, produciendo un incremento en el contenido de calor del océano mucho mayor que en cualquier otro componente del sistema climático. Además de los cambios en temperatura, se han detectado cambios a larga escala en la salinidad caracterizados por un endulzamiento en regiones de latitudes altas y un incremento en la salinidad en regiones donde predomina la evaporación. Numerosas observaciones apoyan este resultado para el Océano Atlántico. De hecho, la inspección de las series temporales del contenido de calor para cada cuenca apuntan al Noratlántico como principal contribuyente de dicho incremento (Levitus et al., 2005).

El análisis de secciones hidrográficas repetidas ha revelado las características de las anomalías de temperatura y salinidad sobre el Noratlántico tropical y subtropical. Gran parte de nuestro conocimiento acerca de la variabilidad subtropical se debe al análisis a lo largo de 24.5°N, la sección transoceánica que se ha muestreado más veces en el mundo. Los estudios pioneros de Roemmich and Wunsch (1984) indicaron un calentamiento de las aguas intermedias y un enfriamiento de las aguas más profundas para el periodo 1957-1981. Posteriormente, Parrilla et al. (1994) encontró que el calentamiento había continuado hasta 1992 a una tasa máxima de 1°C/siglo en los 1100 db. Para el periodo 1992-2002, Vargas-Yáñez et al. (2004) encontró una mayor tendencia de calentamiento (2.7°C/siglo) para la termoclinia de la cuenca este. El estudio de la sección 24.5°N fue extendido finalmente por Cunningham and Alderson (2007), quien concluyó que las aguas menos profundas de 1750 db se han estado calentando e incrementando su salinidad desde 1981, produciendo que las aguas en 2004 fueran significativamente más cálidas y salinas que en ninguna observación desde 1957. Estos autores también señalaron que el calentamiento en la termoclinia oeste del Atlántico desde 1957, a una tasa de 1.11°C/siglo, dominó la media translantánica. La descomposición de los cambios isobáricos en cambios en las masas de agua y cambios debidos al desplazamiento de las isopícnas, han mostrado que esta tendencia de calentamiento es el resultado de ambas contribuciones (Bryden et al., 1996; Arbic and Owens, 2001). Joyce and Robbins (1996) y Joyce et al. (1999) también encontraron una tendencia de calentamiento desde finales de los años cincuenta en la estación Bermuda y a lo largo de 52° y 66°W en el oeste del Atlántico norte.

En el Atlántico tropical, Arhan et al. (1998) encontró un patrón de cambio similar a lo largo de 7.5°N. La comparación de las campañas realizadas en 1993 y durante el Año Geofísico Internacional reveló un calentamiento de las aguas intermedias y capas superiores de las aguas profundas (tasa máxima promediada para el transecto de 0.4°C/siglo entre 1000 and 2000 m) y un enfriamiento (< 0.008°C/década) de las aguas más profundas. El análisis de una sección realizada en 2000 a una latitud nominal de 6.5°N, dentro del marco del Programa Federal Ruso del Océano Global, mostró que la temperatura siguió aumentando en toda la columna de agua de la cuenca este, especialmente a niveles intermedios (0.117°C/década) (Sarafanov et al., 2007).

8.1.4 Objetivos de la tesis y organización

Esta tesis tiene como objetivo examinar la respuesta reciente del Océano Noratlántico a variaciones climáticas en diferentes escalas espaciales, y explorar los posibles mecanismos causantes de los cambios observados. Concretamente, nosostros hemos abordado las siguientes preguntas:

- *¿Han continuado las tendencias en la temperatura y la salinidad observadas en el Atlántico tropical (7.5°N) y subtropical (24.5°N), o se han invertido?*
- *¿Qué cambios regionales han ocurrido en la Cuenca Canaria durante la última década en términos de estructura termohalina y circulación?*
- *¿Concuerdan los cambios a escala de giro y regionales?*
- *¿Cuáles son los mecanismos responsables de los cambios observados?*
- *¿Cuál es el papel potencial del sistema de afloramiento canario como una zona de amortiguamiento?*

Para este fin, hemos dividido la tesis en tres partes:

- **Parte I** (Capítulos 2 and 3) se centra en la variabilidad interdecadal de temperatura y salinidad en el Océano Noratlántico tropical y subtropical desde los años 50.

En el **Capítulo 2** se presenta la evolución temporal entre 1957 y 2010 de las propiedades de las masas de agua a lo largo de una sección transoceánica en 7.5°N. Con el fin de dilucidar los mecanismos que controlan dichos cambios, los cambios en superficies isobáricas son descompuestos en cambios a lo

largo de superficies isoneutras y cambios debidos al desplazamiento vertical de la isoneutras (Bindoff and McDougall, 1994).

En el **Capítulo 3**, se realiza un análisis similar al desarrollado en el Capítulo 2 para las cinco secciones hidrográficas llevadas a cabo a lo largo de 24.5°N. Además, se hace uso de datos Argo para corroborar las últimas tendencias en temperatura y salinidad presentadas por las aguas subtropicales.

- * **Parte II** (Capítulos 4 and 5) se concentra en la variabilidad en las masas de agua y en la circulación en la región canaria durante la última década.

En el **Capítulo 4**, se evalúan las variaciones de temperatura y salinidad en una sección al norte de las Islas Canarias llevada a cabo en los años 1997 y 2006. Los cambios observados son intrepretados en términos de variaciones en el forzamiento atmosférico en la zona de formación de las masas de agua, es decir, variaciones en el flujo de calor, evaporación menos precipitación o en el rotacional del estrés del viento.

En el **Capítulo 5**, se determinan el transporte medio de la corriente de frontera este del giro subtropical del Atlántico Norte y su varibilidad estacional e interanual a partir de series temporales de correntímetros instalados en el Pasaje de Lanzarote.

· **Parte III** (Capítulo 6)

En el **Capítulo 6**, presentamos resultados novedosos de un análisis espacial objetivo univariable aplicado a datos hidrográficos de alta resolución recogidos en la zona de transición costera del noroeste de África. Se identifican tres regiones dinámicamente diferentes: la región de afloramiento, el sistema frontal y la región de océano abierto. Para cada una de estas regiones caraterizamos los principales elementos dinámicos, estimamos las diferentes contribuciones al movimiento vertical (velocidades verticales diapicinas, quasi-geostróficas e inducidas por el viento) y las comparamos con el campo de fluorescencia cerca de superficie.

Finalmente, el **Capítulo 7** reúne las conclusiones más importantes de este trabajo de tesis y algunas sugerencias de trabajo futuro. Cada uno de estos capítulos se resumen en la siguiente sección.

8.2 Síntesis de resultados

8.2.1 Cambios decadales en el Atlántico tropical a lo largo de la sección 7.5°N (Capítulo 2)

OBJETIVO

El capítulo 2 está dirigido al análisis de la evolución temporal de las propiedades de las masas de agua y los mecanismos que la controlan desde 1957 hasta la actualidad a lo largo del transecto transoceánico 7.5°N.

MATERIAL Y MÉTODOS

Este estudio se basa en los perfiles de temperatura potencial (θ) y salinidad (S) obtenidos durante las secciones repetidas a lo largo de 7.5°N en 1957, 1993 y 2010. Debido a las diferencias en las resoluciones verticales y horizontales del muestreo, los datos hidrográficos fueron interpolados linealmente a una malla común que consistió en 300 niveles verticales desde 10 a 6000 db y desde 48.45°W a 17.45°W en intervalos de 0.5°. La precisión de las medidas de temperatura y salinidad para la campaña de 1957 fue de 0.1°C y 0.01, respectivamente (Fuglister, 1960). Para las dos campañas más recientes la precisión mejoró a 0.002° y 0.0002, aunque no hemos aplicado la corrección a la salinidad para los resultados que se presentan aquí.

La distinción de los mecanismos responsables de los cambios observados se realiza a través del modelo de Bindoff and McDougall (1994), el cual establece que los cambios de la temperatura potencial y la salinidad en isóbaras pueden ser descompuestos en cambios en las superficies neutrales (Jackett and McDougall, 1997) y cambios debidos al desplazamiento vertical de las isoneutras. Dada la dependencia en comportamiento de ambas cuencas, los perfiles de diferencias promediadas zonalmente se calcularon al este y oeste de la dorsal mesoatlántica, aproximadamente localizada a 32°W.

RESULTADOS

La Figura 2.2 muestra las diferencias de temperatura y salinidad en superficies de presión cuando los valores de 1993 son restados a los de 2010. Dentro de la termoclinia (los primeros 1000 db), las diferencias de temperatura y salinidad son muy grandes (hasta $\pm 9^{\circ}\text{C}$) con alternancia de signos a escalas de 3 grados en longitud, especialmente en la cuenca oeste. Debajo de 1000 db y exteniéndose hasta el fondo, hay un

calentamiento débil (alrededor de 0.05 °C) de forma bastante uniforme a lo largo de la sección, excepto entre 40°W and 45°W. La salinidad sigue un patrón similar en la termoclina y las aguas intermedias mientras que en las aguas profundas superiores aparece más parcheado, con pequeños valos de signo cambiante. Cerca del fondo, en el margen oeste y cerca de la dorsal mesoatlántica, encontramos un calentamiento y salinificación significativos.

Cuando promediamos a lo largo de las isóbaras (partición en la Figura 2.2), la diferencia de temperatura entre 1993 y 2010 (línea roja) muestra la presencia de un calentamiento a través de la columna de agua. La diferencia más significativa bajo la termoclina, en base a los intervalos de confianza al 95%, ocurre cerca de 4500 db con una tasa máxima de 0.009 °C/decade. Esto implica que la tendencia de enfriamiento entre 1957 y 1993 (línea azul) previamente documentada por Arhan et al. (1998) en la columna de agua profunda (> 3000 db) se ha invertido en los últimos 17 años. Sin embargo, este reciente calentamiento no compensó el anterior enfriamiento dando lugar a un enfriamiento neto en el rango de presiones de 3000-4000 db (línea negra). La diferencia de salinidad promediada zonalmente indica un patrón de cambio similar al de la temperatura, con valores máximos de salinificación en la termoclina permanente y cambios substanciales en las aguas intermedias y profundas. Encontramos un máximo local de salinificación de 0.0008/década a 4500 db. Sin embargo, para el periodo de 1993-2010, las aguas entre 2000 y 4000 db no presentan un cambio significativo en isóbaras.

La descomposición de los cambios totales de temperatura y salinidad en niveles de presión constante en cambios a lo largo de superficies neutrales (referidas como variaciones advectivas, θ_n y S_n) y cambios debido al desplazamiento vertical de las isoneutras ($-N\theta_z$ and $-NS_z$, donde $N = dp/dt$ evaluado en densidades neutrales contantes), se usa para diagnosticar variaciones en la zona de formación de la masa de agua y por tanto, los mecanismos que están forzando los cambios observados.

La Figura 2.3 exhibe los cambios isobáricos de temperatura y salinidad entre 1993 y 2010, así como cada contribución y su suma. La suma de ambas contribuciones tanto para la cuenca este como para la oeste se ajusta bastante bien a la señal original, indicando por tanto que la descomposición se ha realizado con éxito.

En la cuenca oeste (paneles izquierdos), el incremento de temperatura y salinidad en la termoclina permanente está dominado por el desplazamiento de las isoneutras, las cuales se hundieron 10-70 db entre 100 y 1000 db dando lugar a tasas máximas de calentamiento y salinificación

de $1.3164^{\circ}\text{C/década}$ and 0.1506 /década , respectivamente, a 150 db. Dichas variaciones se han atribuido previamente a oscilaciones, ver la revisión realizada en Arhan et al. (1998). No obstante, los cambios a lo largo de las superficies neutrales también han contribuido a los cambios en la termoclinia. En niveles intermedios, ha habido un calentamiento y salinificación promediada en presión de $0.0524^{\circ}\text{C/década}$ y 0.0098 /década en las aguas Antártica Intermedia y Circumpolar Superior. En la columna de agua profunda (entre 2000 y 4000 db), el agua Noratlántica Profunda sufrió un calentamiento en las isóbaras de $0.0140^{\circ}\text{C/década}$ debido principalmente al desplazamiento de las isoneutras a una tasa de 28.96 db/década, con un pequeño contrarrestado por cambios en la masa de agua. Los cambios de salinidad en este rango de presiones fueron del orden de la precisión de su medida. Las capas abisales muestran un calentamiento y salinificación de $0.0587^{\circ}\text{C/década}$ y 0.0056 /década causado por un hundimiento de las isoneutras de 165 db en las dos últimas décadas.

Para la cuenca este (paneles derechos) el calentamiento y salinificación superior debido al desplazamiento de las isoneutras afecta solamente a los primeros 500 db con una intensidad moderada (tasas máximas de $0.1458^{\circ}\text{C/década}$ and 0.0192 /década). En el rango de presiones 500-2000 db, ocupado por las aguas intermedias y el Agua Noratlántica Profunda superior, el cambio de temperatura promedio es $0.0583^{\circ}\text{C/década}$, el cual se divide de forma aproximadamente equitativa entre cambios a lo largo de la isoneutras de $0.0236^{\circ}\text{C/década}$ y cambios debidos al hundimiento de las superficies de densidad constante de $0.0336^{\circ}\text{C/década}$. Al contrario, los cambios en salinidad asociados al desplazamiento de las isoneutras provocaron un endulzamiento, significativo pero incapaz de contrarrestar la tasa de salinificación de $0.0004/\text{década}$ a lo largo de las isoneutras. Por debajo de 2500 db, en los niveles del Agua Noratlántica Profunda media e inferior, la temperatura se incrementó $0.0095^{\circ}\text{C/década}$ en isóbaras por desplazamiento de las isoneutras, mientras que los cambios en salinidad fueron nuevamente comparables a la precisión de su medida.

La Figura 2.4 muestra las componentes de los cambios isobáricos entre 1957 y 2010. La descomposición para ambas cuencas es similar a la observada para el periodo 1993-2010. La única diferencia es el enfriamiento en las aguas más profundas de 3000 db de la cuenca este, aparentemente como resultado de un aumento en la importancia de los cambios en las masas de agua.

8.2.2 Cambios en las tendencias de temperatura y salinidad en la sección transatlántica 24.5°N (Capítulo 3)

OBJETIVO

El capítulo 3 se centra en el análisis de la evolución temporal desde 1957 de las propiedades de las masas de agua a lo largo del paralelo 24.5°N. Dicha sección fue escogida por ser la latitud a la cual el transporte de calor hacia el norte realizado por el océano en el Atlántico es máximo (Lavín et al., 2003). Es por ello que se ha convertido en un punto de referencia para detectar cambios de temperatura en el Atlántico y estudiar las causas del cambio climático (Bindoff et al., 2007).

MATERIAL Y MÉTODOS

Para llevar a cabo este objetivo se utilizaron datos hidrográficos y datos Argo. Los datos hidrográficos provienen de las cinco secciones oceanográficas que se han realizado en 24.5°N desde 1957. Éstas se restringieron al rango longitudinal donde todas las campañas coincidían, es decir, entre 23°W y 70°W. Además fueron interpolados a 101 niveles verticales de presión entre la superficie y 2000 db, y bilinealmente interpolados cada 0.5 grados en longitud. En cuanto a los datos Argo, después de pasar los controles de calidad, se seleccionaron todos aquellos comprendidos entre enero de 2003 y diciembre de 2008. Éstos fueron interpolados objetivamente a una sección hipotética a lo largo de 24.5°N usando una versión actualizada del método de interpolación óptima empleado previamente por Fraile-Nuez and Hernández-Guerra (2006). Para la interpolación de los campos de temperatura y salinidad se utilizaron los valores climatológicos anuales del World Ocean Atlas 1994 como primera aproximación, asegurando de esta manera que el campo de anomalías (el datos menos el valor climatológico) es una función aleatoria de la posición, estacionaria y de media cero. La gran cantidad de datos Argo obtenidos durante los 6 años en que se extienden las observaciones hacen que el ruido mesoscalar se reduzca considerablemente y, por tanto, estén menos afectados por el mismo que las secciones hidrográficas. Esta sección sintética de datos Argo, cuya media se asigna al año 2006, consta de perfiles de temperatura y salinidad interpolados a la misma malla que los datos hidrográficos, por lo que puede considerarse como la sexta ocupación de la sección 24.5°N. También se calcularon secciones sintéticas para los años 2005, 2006, 2007 y 2008 interpolando objetivamente los datos Argo entre enero y diciembre del año correspondiente.

Las variaciones de temperatura y salinidad son interpretadas según el

modelo propuesto por Bindoff and McDougall (1994). Estos autores mostraron que, para pequeños desplazamientos, usando una expansión de Taylor y asumiendo que los gradientes verticales son constantes en el tiempo, los cambios temporales de temperatura potencial (θ) a lo largo de las isóbaras se pueden descomponer en cambios a lo largo de superficies isoneutras (Jackett and McDougall, 1997) y cambios debidos al desplazamiento vertical de las superficies isoneutras:

$$\frac{d\theta}{dt} \Big|_p = \frac{d\theta}{dt} \Big|_{\gamma_n} - \frac{dp}{dt} \Big|_{\gamma_n} \frac{\partial\theta}{\partial p} \quad (8.1)$$

donde p denota la tasa de cambio en isóbaras; γ_n la tasa de cambio a lo largo de superficies neutrales, $dp/dt|_{\gamma_n}$ el desplazamiento isoneutral y $\partial\theta/\partial p$ el gradiente vertical de temperatura. La ecuación representa los cambios observados en las isóbaras como suma de dos contribuciones independientes. La primera contribución se debe a cambios en el flujo de calor en la zona de formación de la masa de agua. La segunda contribución, sin embargo, puede resultar de cambios en el espesor de isoneutras debido a cambios en las tasas de renovación, o bien a cambios en la fuerza de la circulación del giro por cambios en el estrés del viento. Las diferencias en salinidad a lo largo de las isóbaras se pueden descomponer de la misma manera.

RESULTADOS

Se calcularon las diferencias de temperatura en superficies isobáricas para los períodos 1998-1957, 2004-1957, 2004-1998, 2006(Argo)-1957 y 2006(Argo)-1998 (Figura 3.2). Las diferencias de temperatura entre 1998 y 1957 (Figura 3.2a) muestran un calentamiento en el noratlántico subtropical a lo largo de 24.5°N a una tasa de 0.65°C/siglo, similar a la encontrada en 1992 (Parrilla et al., 1994). Este calentamiento se observa prácticamente en toda la cuenca, con un máximo de 1°C entre 800 y 1000 db. Las diferencias de temperatura entre 2004 y 1957 muestran que el interior del océano Atlántico estaba más caliente en 2004 que en 1957; sin embargo, la magnitud de dicho calentamiento fue inferior que en 1998, especialmente a profundidades mayores de 400 db, donde los máximos calentamientos de hasta 1°C se ven reducidos a 0.5°C e incluso valores más bajos en el Atlántico centro este (20°W-45°W). Dicho enfriamiento, que invierte la anterior tendencia de calentamiento, se observa claramente en las diferencias de temperatura entre 2004 y 1998 (Figura 3.2c). Este enfriamiento fue general para la cuenca, excepto en la zona central (40°W-55°W) donde se observa un calentamiento de 0.70°C en los niveles superiores (< 200 db) que disminuye a menos de

0.05°C en aguas más profundas de 1200 db. La máximas diferencias negativas para el periodo 2004-1998 se encuentran a 800 db en la cuenca oeste entre 55°W y 65°W y a 350 db en la cuenca este entre 25°W y 35°W. Las diferencias de temperatura calculadas para los periodos 2006-1957 y 2006-1998 usando la sección sintética construida a partir de datos Argo (Figuras 3.2d y 3.2e) muestran cambios similares a los encontrados con datos de CTD. Por tanto, se confirma el uso de datos Argo para estudios a largo plazo.

En cuanto a la salinidad, mostró un patrón semejante al de la temperatura (Figura 3.3); un aumento entre 1957 y 1998 con los mayores cambios en los primeros 1200 db (Figura 3.3a), seguido de una disminución entre 1998 y 2004 (Figura 3.3c). Durante este periodo las mayores diferencias se encuentran en los primeros 800 db, excepto en el Atlántico central donde se aprecia un incremento de la salinidad en los niveles superiores e intermedios. Las diferencias de salinidad con las secciones sintéticas Argo confirman esta tendencia de disminución de la salinidad en la última década.

La representación de los perfiles verticales del promedio zonal de las diferencias de temperatura entre 1957 y el resto de ocupaciones (Figura 3.4a) confirman y cuantifican los cambios en la tendencias observadas en las secciones de toda la cuenca. Se observa un calentamiento entre la primera ocupación en 1957 y las secciones muestreadas en 1981, 1992 y 1998. La profundidad a la cual tiene lugar el máximo calentamiento se ha desplazado desde 900 db en 1981, pasando a 1000 db en 1992 y regresando a 900 db en 1998. El máximo calentamiento respecto a 1957 ocurre en 1998, con un promedio de 0.27°C para el océano superior (600-1800 db), 0.24°C para las aguas de la termoclina (300-800 db) y 0.27 para las aguas intermedias (800-1800 db) (Tabla 3.1). Desde 1998 a 2004, las temperaturas promediadas zonalmente decrecieron con un enfriamiento máximo de -0.3°C a 800 db. Las aguas de la termoclina se enfriaron -0.15°C y las intermedias -0.13°C. El enfriamiento encontrado entre 1998 y 2004 es estadísticamente significativo y representa casi el 50% del calentamiento encontrado desde 1957 a 1998. Como resultado tenemos que entre 1957 y 2004 las aguas de la termoclina se calentaron 0.09°C, las intermedias 0.14°C y la capa superior 0.12°C (Tabla 3.1). Una vez más, los resultados obtenidos a partir de la sección sintética Argo son muy similares a los encontrados con los datos de CTD. Las diferencias entre el incremento medio obtenido con los datos de las secciones Argo 2006 y CTD 2004 en las tres capas es mucho menor que los cambios ocurridos entre 1998 y 2004, confirmando, por tanto, la robustez del método y la validez de los datos Argo para la observación de cambios a larga escala. Las diferencias de salinidad promediadas

zonalmente (Figure 3.4b) confirman un incremento de salinidad antes de 1998 y un descenso después de éste. Los datos de CTD muestran que el año 1998 presentó las salinidades más elevadas. Aunque los máximos valores se encuentran en los primeros 400 db, existe un máximo subsuperficial a 800 db con valores de hasta 0.05 en 1998 aunque decrecen hasta casi hacerse nulos en 2004. El descenso en salinidad ocurrido entre 1998 y 2004 también tiene un máximo subsuperficial de -0.04 a 800 db. Los cambios en el nivel del mar asociados a los cambios observados en la temperatura y la salinidad desde 1957 para la capa de 800-1800 db alcanzó un máximo de 3.3 cm en 1998, y luego decreció a 1.8 cm en 2004.

Una vez conocidos los cambios en las superficies de presión, éstos fueron descompuestos como la suma de los cambios a lo largo de las isoneutras y los cambios debidos al desplazamiento de las superficies neutrales (Figura 3.5). Entre 1957 y 1998, la principal contribución al calentamiento en el océano superior (600-1800 db) fue el hundimiento de la superficies isoneutras (Figura 3.5a). Este hundimiento tuvo lugar en cada uno de los periodos analizados entre 1957 y 1998 excepto para el periodo 1981-1992 (no se muestra), el cual estuvo dominado por cambios en las masas de agua. Entre 1998 y 2004, la principal contribución al enfriamiento del océano superior fue la elevación de la susperficies isoneutras (Figura 3.5b). Únicamente las aguas intermedias muestran cambios a lo largo de las isoneutras. Este resultado es consistente con el hecho de que, en la cuenca este, las aguas intermedias están compuestas esencialmente por Agua Mediterránea (1200 db), la cual tiene cortas escalas de variabilidad y una conocida actividad mesoescalar relacionada con los meddies. La descomposición de los cambios de temperatura realizada con la sección sintética Argo 2006 muestra resultados similares a los obtenidos con la sección de 2004 (Figura 3.5c).

Para finalizar, se examina la variabilidad interanual en 24.5°N utilizando las secciones Argo sintéticas de los años 2005, 2006, 2007 y 2008. Esta estimación nos da información de si los cambios observados en las secciones realizadas en 24.5°N están relacionados con la variabilidad decadal o la variabilidad interannual enmascarada por un muestreo decadal. La Figura 3.6 muestra la evolución temporal de la temperatura y salinidad medias entre 70°W y 23°W para el océano superior, la termoclinia y las capas intermedias, para las ocupaciones llevadas a cabo con CTD, las cuatro secciones sintéticas Argo construidas anualmente y la sección sintética Argo 2006. Se puede observar que la variabilidad interanual de las secciones sintéticas Argo entre 2005 y 2008 es mucho más pequeña que la observada a partir de las secciones hidrográficas. Por ejemplo, la desviación estándar de las temperaturas medias en el océano

superior de las cinco secciones hidrográficas es de 0.096, mientras que este valor decrece a 0.008 para las cuatro estimas de Argo. Del mismo modo, la desviación estándar de la temperatura media para las aguas de la termoclina (intermedias) es 0.106 (0.101) y 0.032 (0.013) para Argo.

8.2.3 Variaciones de la temperatura y salinidad subsuperficiales en la región Canaria (Capítulo 4)

OBJETIVO

En el capítulo 4 se documentan los cambios de temperatura y salinidad ocurridos en aguas de la región Canaria durante la última década. Los cambios observados son descompuestos en cambios en las masas de agua y cambios debidos al movimiento vertical de las isoneutras, e interpretados en base a variaciones en el forzamiento superficial en la zona de formación de las masas de agua.

MATERIAL Y MÉTODOS

Durante el proyecto Canary Islands Azores Gibraltar Observations (CANIGO), llevado a cabo en los años 90, se realizó una sección hidrográfica al norte de las Islas Canarias con carácter estacional (Machín et al., 2006a). En febrero de 2006, el proyecto Radial Profunda de Canarias (RAPROCAN) repitió las estaciones realizadas durante la campaña CANIGO de enero de 1997. Se ocuparon un total de 16 estaciones de CTD con una resolución espacial de 35 km para las estaciones profundas, que se redujo a 15 km para las estaciones más someras. La calibración del sensor de conductividad a partir del análisis de muestras de salinidad en un salinómetro Guidline mostró una precisión superior a 0.002 para las muestras individuales. Los sensores de temperatura y salinidad se calibraron utilizando estándares WOCE.

Para evaluar las variaciones de temperatura y salinidad en la columna de agua, se aplicó el modelo propuesto por Bindoff and McDougall (1994), el cual relaciona las variaciones ocurridas en las superficies de presión y densidad constantes a través de la siguiente ecuación:

$$\frac{d\psi}{dt} \Big|_z = \frac{d\psi}{dt} \Big|_{\gamma_n} - \frac{dp}{dt} \Big|_{\gamma_n} \frac{\partial\psi}{\partial p} \quad (8.2)$$

Dicha ecuación representa los cambios observados en una propiedad escalar ψ a lo largo de las superficies isobáricas como la suma de dos

contribuciones independientes: cambios a lo largo de superficies neutrales (Jackett and McDougall, 1997) y cambios debidos al movimiento vertical de las isoneutras. $dp/dt|_{\gamma_n}$ denota el desplazamiento de las isoneutras y $\partial\psi/\partial p$ el gradiente vertical de la propiedad, el cual se asume ser constante en el tiempo. Esta descomposición puede ser comprobada comparando la suma de ambas componentes con el cambio isobárico observado.

Con el objeto de aplicar la metodología exlicada anteriormente, la temperatura y la salinidad fueron interpoladas desde la superficie a 3000 db en un grid con un intervalo de 50 db y 0.01 kg m^{-3} para la presión y la densidad neutral, respectivamente. Los intervalos de confianza del 95% para la media de las diferencias se calcularon en base al test de Student teniendo en cuenta la pérdida de grados de libertad en cada superficie de isobárica/isoneutra debida a la autocorrelación en el campo de remolinos.

RESULTADOS

Las diferencias de temperatura y salinidad en isóbaras, así como su promedio zonal, muestran un patrón similar para ambas propiedades. Éste se caracteriza por un descenso estadísticamente significativo en la capa más superficial (0-100 db) con una homogeneidad muy marcada en todo el transecto. Este descenso tan brusco se puede atribuir a la influencia de la atmósfera inmediatamente superior, la cual profundizó la capa de mezcla 30 m más en 2006 que en 1997, enfriando la superficie a 18°C aproximadamente. Debajo de la capa de mezcla, el Agua Noratlántica Central se extiende hasta los 600 db, definiendo la termoclina principal. Dentro de esta masa de agua los cambios más notables son: (i) un pronunciado incremento de la temperatura y la salinidad (solamente significativo para la última) entre 100 y 350 db, donde se encuentran valores de hasta 1.92°C y 0.46 en tres parches a lo largo de la sección, y (ii) un descenso de la salinidad entre 350 y 600 db sin variaciones en la temperatura, lo que implica que han habido cambios que no han conservado las propiedades θ/S . Desde 600 hasta 1500 db, correspondiente a capas intermedias, se distinguen dos masas de agua: el Agua Antártica Intermedia identificada por un mínimo relativo en salinidad, y el Agua Mediterránea caracterizada por un máximo en salinidad (Machín et al., 2006a). En estos niveles se alternan diferencias positivas y negativas que resultan en una media zonal no significativa. En capas profundas (>1500 db), ocupadas por el Agua Noratlántica Profunda, se observa que el agua es más cálida y salada a lo largo de la cuenca. Este incremento es estadísticamente significativo desde 1500 a 2300 db, alcanzando las tasas máximas de 0.29°C and 0.047 por década para la temperatura y salinidad, respectivamente, sobre los 1600 db.

La representación de las dos componentes en que se dividen los cambios isobáricos y la suma de ambas mostró una gran concordancia, indicando que la descomposición se realizó con éxito (Figuras 4.2a and 4.2b). Las aguas de la termoclina presentaron una capa de aumento en la temperatura y la salinidad en superficies isoneutras que produjo una salinificación en el campo isobárico. Sin embargo, la parte más profunda del Agua Noratlántica Central se enfrió y disminuyó la salinidad en las isoneutras a una tasa máxima de -0.26°C y -0.07 por década; de ahí que el diagrama θ/S obtenido a partir de los perfiles de temperatura y salinidad promediados zonalmente (Figura 4.3a) revele una curva para el Agua Noratlántica Central más fría y menos salada en 2006. Por otro lado, el hecho de que las líneas que unen puntos de igual presión no se mantengan paralelas a las isopicas, nos indica que ha tenido lugar un desplazamiento de las superficies neutrales tal y como se ven en la Figura 4.2c. En consecuencia, el hundimiento de las superficies neutrales compensó los cambios a lo largo de las isoneutras resultando en cambios en cambios no significativos a lo largo de las isóbaras en estos niveles. En aguas intermedias, ni los cambios isobáricos ni los cambios en las masas de agua son estadísticamente significativos (Figuras 4.2a and 4.2b). No obstante, las diferencias de temperatura y salinidad muestran valores negativos para el Agua Antártica Intermedia y valores positivos para el Agua Mediterránea, así como también cambios en su relación θ/S (Figura 4.3b). Aunque estos cambios no son significativos, las líneas que unen puntos de igual presión en el diagrama θ/S nos indican que estos cambios están influenciados por el desplazamiento de las isoneutras. El graficado del desplazamiento de la isoneutra (Figura 4.2c) muestra un hundimiento promedio de 30 db para la capa 1200-3000 db, el cual representa la principal causa del aumento de temperatura y salinidad en este rango de presiones.

Bindoff and McDougall (1994) propusieron tres procesos por los que pueden ser interpretados los cambios observados: calentamiento puro, endulzamiento puro y desplazamiento puro; cada uno de ellos haciendo referencia al cambio respectivo en el forzamiento atmosférico en la zona de formación de la masa de agua. Los dos primeros están relacionados con los flujos de calor y agua dulce, cambiando por tanto las características de la masa de agua, y el tercero está relacionado con el rotacional del estrés del viento, tasas de renovación de las masas de agua u ondas internas. La fuerza relativa de cada proceso, en términos de porcentaje de varianza explicada (A^w , A^f and A^h , donde w , f and h denota calentamiento, endulzamiento y desplazamiento, respectivamente), pueden ser estimados resolviendo las siguientes ecuaciones:

$$\frac{\rho^{-1} \rho'|_z}{R_\rho - 1} \begin{pmatrix} -(R_\rho - 1) & 0 & -R_\rho \\ 1 & R_\rho & 0 \\ R_\rho & R_\rho & R_\rho \\ 0 & (R_\rho - 1) & -1 \\ 1 & R_\rho & 0 \\ 1 & 1 & 1 \end{pmatrix} \times \begin{pmatrix} A^w \\ A^f \\ A^h \end{pmatrix} = \begin{pmatrix} \alpha\theta'|_z \\ \alpha\theta'|_n \\ N'\alpha\theta_z \\ \beta S'|_z \\ \beta S'|_n \\ N'\beta S_z \end{pmatrix} \quad (8.3)$$

donde $\rho^{-1} \rho'|_z$ es la anomalía de densidad a un nivel de presión fijo, N' es el cambio en presión de una superficie de densidad neutral, $|_z$ denota los cambios sobre las isóbaras, $|_n$ denota los cambios a lo largo de las isoneutras, y R_ρ ($R_\rho = \alpha\theta_z/\beta S_z$) es el ratio de estabilidad definido a partir de los coeficientes de expansión térmica y contracción salina, α y β , respectivamente, y los gradientes verticales de temperatura y salinidad, θ_z y S_z . Aunque se trata de un sistema de ecuaciones mal determinado, la proporción de la varianza explicada por cada uno de los procesos puede ser estimada haciendo la suposición de que solamente un proceso está actuando y aplicando un método inverso. Realizando esto distinguimos cuatro regímenes de presión en los cuales un único proceso tiende a dominar. En el Régimen I (350-600 db), correspondiente a los niveles inferiores del Agua Noratlántica Central, el endulzamiento puro explica más del 95% de la varianza, sugiriendo una modificación de la masa de agua en la zona de formación de la misma. En los Regímenes II (600-900 db) y III (900 y 1200 db), los cambios observados se pueden explicar por desplazamiento puro y endulzamiento puro, respectivamente, ambos estadísticamente significativos al 90%. En capas más profundas el nivel de varianza explicada desciende, aunque el desplazamiento puro explica el 60-90% de la señal en los niveles más profundos de las aguas intermedias y el Agua Noratlántica Profunda.

8.2.4 Nueve años de datos del transporte de masa en el límite oriental del giro subtropical del Atlántico Norte (Capítulo 5)

OBJETIVO

El objetivo en este capítulo es doble. Por un lado, se determina la variabilidad dinámica, a escalas estacionales e interanuales, de la corriente de frontera este del giro subtropical del Noratlántico; y por otro, se demuestra que las estimas en el transporte de la corriente de frontera este son necesarias para entender la variabilidad climática de la circulación meridional.

MATERIAL Y MÉTODOS

Entre enero de 1997 y enero de 1999 se instalaron 19 correntímetros distribuidos en 4 fondeos en el pasaje entre la isla de Lanzarote y la costa africana, conocido como el Pasaje de Lanzarote (PL) (Figura 5.1). Cada fondeo distribuye los correntímetros de manera que las tres masas de agua presentes en el PL sean muestreadas. El fondeo EBC-4 es el único que se sigue manteniendo hasta la actualidad; sin embargo, sólo se muestran los datos hasta febrero de 2006 debido a la falta de datos entre marzo de 2006 y febrero de 2008. Por tanto, en este trabajo se analizan las series de velocidad, temperatura, salinidad y presión de 9 años de duración obtenidas del fondeo EBC-4 entre febrero de 1997 y febrero de 2006. El fondeo EBC-4 está localizado en 28°44'N, 13°28'W, a una profundidad de 1280 m (Figure 5.1). Dicho fondeo está equipado con 5 correntímetros mecánicos Aanderaa instalados aproximadamente a 150, 300, 520, 870 y 1230 m. Durante estos 9 años el fondeo ha sido recuperado en 11 ocasiones para su mantenimiento.

El intervalo de muestreo se fijó en 2 horas para todos los correntímetros. En general, todos los correntímetros recogieron datos buenos durante los 9 años, excepto el más superficial en el que la falta de datos era substancial y se decidió, por tanto, excluir del análisis harmónico y de la variabilidad del transporte de masa.

Las series temporales se filtraron con un filtro de paso bajo de 40 horas para eliminar la marea y las señales iniciales. Las velocidades se rotaron al ángulo principal, a lo largo del cual la suma de los cuadrados de la distancia normal a los puntos de datos es mínima (Emery and Thomson, 1998), tal y como se realizó previamente en el PL por Hernández-Guerra et al. (2003).

También se utilizan los datos hidrográficos de las 12 ocupaciones (enero y octubre de 1997, marzo y julio de 1998, enero y mayo de 1999, abril de 2000, febrero de 2001, febrero y septiembre de 2003, febrero de 2005 y 2006) realizadas entre febrero de 1997 y febrero de 20006 en el PL. Las estaciones se realizaron con un SeaBird 911+ desde superficie hasta el fondo (Figura 5.1). Se calculó el transporte geostrófico para cada una de las ocupaciones considerando dos niveles de no movimiento, uno a la densidad neutral de 27.3 kg m^{-3} que marca el límite entre el Agua Noratlántica central que fluye hacia el sur y el Agua Antártica Intermedia que fluye hacia el norte (Hernández-Guerra et al., 2003), y el otro en el fondo. Dichos transportes serán comparados con la serie temporal de transportes del EBC-4 en la sección 5.6.

RESULTADOS

En la Tabla 5.1 se muestra la información de cada correntímetro y los parámetros estadísticos del flujo medido en EBC-4 en cuanto a velocidad, velocidad proyectada al ángulo principal y su media cuadrática, temperatura, salinidad, energía cinética y estabilidad direccional. Se observan valores similares a los documentados por (Hernández-Guerra et al., 2003) para los primeros cuatro años de la serie temporal, aunque con algunas diferencias menores. El correntímetro más superficial ahora muestra un aumento de la energía cinética y de la estabilidad de la corriente. El correntímetro instalado a 500 m muestra un descenso de la energía cinética comparado con los primeros cuatro años de la serie temporal.

Para la serie temporal de 9 años, las velocidades hacia el sur en el rango de $5\text{-}10 \text{ cm s}^{-1}$ se encuentran en los primeros correntímetros (instalados a 150 y 300 m, respectivamente), pareciendo más intensas durante la primavera y más débiles durante el verano y el otoño (Figura 5.2). El correntímetro instalado a 500 m tiene una velocidad media inferior a 5 cm s^{-1} con una estacionalidad similar a los correntímetros superficiales. Sin embargo, el patrón de velocidad correspondiente al correntímetro instalado en el Agua Antártica Intermedia (aproximadamente 870 m) cambia drásticamente. Se encuentran velocidades cercanas a cero con una pequeña tendencia hacia el norte entre los meses de febrero y junio, mientras que desde julio a noviembre tiene lugar una intensificación de la velocidad hacia el norte, alcanzando valores de hasta $4\text{-}5 \text{ cm s}^{-1}$. Desde noviembre hasta finales de diciembre se encuentra un cambio hacia el sur en la dirección de la velocidad, con valores cercanos a $5\text{-}6 \text{ cm s}^{-1}$. Finalmente, la señal encontrada en el correntímetro más profundo (1230 m), es muy variable y prácticamente nula, aunque se distingue una tendencia hacia el sur durante noviembre y diciembre.

Se aplicó un análisis principal de componentes para determinar, primero, si la corriente en el Pasaje de Lanzarote puede ser descrita como un dominio de dos o tres capas, y segundo, la influencia del afloramiento del noroeste de África en la dinámica del Pasaje de Lanzarote.

Primero se realizó un análisis principal de componentes temporal para las 19 series disponibles en el pasaje desde 1997 hasta 1999, con el fin de encontrar patrones de oscilación similares en todos los correntímetros y poder describir y cuantificar los procesos que fuerzan la variabilidad en las series temporales (Figura 5.3a). La significancia de los modos de oscilación fue estimada aplicando el método de Monte Carlo (Hammersley and Handscomb, 1964). El análisis principal de componentes

se realizó 100 veces para 19 series temporales aleatorias de las mismas dimensiones que las series temporales originales de velocidad. Para cada análisis se guardaron los diferentes valores propios obtenidos de la señal de ruido, de manera que los valores propios son considerados significativos cuando están por encima del 95% de los valores propios generados a partir de la señal de ruido. En la figura 5.3b se muestran los valores propios obtenidos de las series originales y de las aleatorias. Se puede observar que hay cuatro valores propios que caen por encima de los límites que resultan del análisis de Monte Carlo y que explican de forma acumulativa el 86.4% de la varianza total.

La figura Figure 5.3c muestra el primer modo significativo del análisis principal de componentes, el cual explica un 56.9% de la varianza de los datos. Dicho modo contiene valores positivos en todo el canal, con valores propios más altos entre 400-600 m y en el centro del pasaje, donde se localiza el EBC-4. Este patrón parece ser la combinación del modo barotrópico con el primer modo barocílico de la dinámica cuasi-geoestática (Müller and Siedler, 1992). El segundo modo significativo explica el 13.2% de la varianza y muestra una estructura de circulación de doble célula donde las capas superficiales fluyen en dirección contraria a las aguas intermedias (Figure 5.3d). La interfase entre ambas aproximadamente coincide con la parte baja del Agua Noratlántica Central en el pasaje (Hernández-Guerra et al., 2003). La profundidad de la interfase es más somera en la parte este del pasaje, donde tiene lugar el afloramiento del noroeste de África. El tercer modo explica el 11.2% de la varianza de los datos y marca la diferencia entre las aguas cercanas al talud continental y aquellas cercanas a las Islas Canarias (Figure 5.3e). Este modo parece estar relacionado con las diferentes dinámicas presentadas por el sistema de afloramiento del noroeste africano y la Corriente de Canarias. Debe ser mencionado que los valores máximos son encontrados en la capa superficial del afloramiento. El cuarto modo significativo, el cual explica sólo un 5.1% de la varianza de los datos, presenta un patrón complejo compuesto de tres regiones verticales, una cerca de las islas, otra en el centro del pasaje y otra cerca de la plataforma continental (Figure 5.3f).

Las amplitudes correspondientes a cada uno de estos modos se muestran en la Figura 5.4, en la que se puede observar que las mayores amplitudes coinciden con los primeros dos modos, indicando la importancia de los mismos.

En segundo lugar se realizó el mismo análisis con la serie temporal de velocidades recogidas en el EBC-4. La Figura 5.5a muestra el test de significancia de la serie temporal de 9 años. En este caso, solamente

dos modos son significativos. La Figure 5.5b muestra la distribución vertical de los valores propios significativos. Estos dos primeros modos de oscilación tienen la misma interpretación que para el análisis realizado en todo el pasaje. Es decir, que el primer modo parece ser la combinación del modo barotrópico y el primer modo barocílico de la dinámica cuasi-geostrófica y el segundo modo, que marca la estructura de circulación de doble célula, con el Agua Noratlántica Central fluyendo hacia el sur y el Agua Antártica Intermedia fluyendo hacia el norte. Las amplitudes temporales correspondientes a los modos mostrados en la Figura 5.4 indican una amplia variabilidad temporal, similar a la descrita en el conjunto de datos original.

Anteriormente se mostró que el tercer modo significativo estaba relacionado con la dinámica de afloramiento y no está presente en este análisis temporal de componentes principales. Este hecho sugiere que la dinámica de afloramiento no introduce una variabilidad relevante en el fondeo EBC-4.

Por tanto, si combinamos los análisis de componentes principales, espacial y temporal, la circulación en el pasaje puede ser descrita como una doble célula de circulación, con la capa superior ocupada por el agua Noratlántica Central y una pequeña influencia del afloramiento, y una segunda capa de aguas intermedias ocupada por el Agua Antártica Intermedia y el Agua Mediterránea. La mayor parte de la variabilidad (56%) está relacionada con el modo barotrópico y primer modo barocílico, mientras que la doble célula de circulación y el efecto del afloramiento tienen una menor influencia (aproximadamente 11-12%).

Por otro lado, se ha realizado un análisis harmónico, que ha sido completado con un análisis wavelet, para detectar señales periódicas en el pasaje. Puesto que la serie temporal de 9 años tiene algunos huecos, la Transformada de Fourier no se puede utilizar para extraer los harmónicos en el EBC-4. En su lugar hemos usado una técnica desarrollada por Lomb (1976) con el objetivo de detectar señales periódicas y estimar su significancia en datos recogidos de un modo heterogéneo. La justificación del uso de esta técnica es que provee una buena aproximación del espectro obtenido por el ajuste de ondas sinusoidales aplicando mínimos cuadrados a los datos y graficando la reducción de la suma de los residuos frente a la frecuencia. Este espectro de mínimos cuadrados provee la mejor medida de la energía con la que contribuyen las diferentes frecuencias a la varianza total de los datos y puede considerarse como una extensión natural de los métodos de Fourier para datos no uniformes. Dicho método ya ha sido aplicado a los primeros cuatro años de la serie temporal (Hernández-Guerra et al.,

2003), y ahora lo extendemos a los nueve años de registro para detectar señales con períodos mayores. El único inconveniente de este método es que está sujeto a fugas espectrales, es decir, el pico dominante aparece en la frecuencia más alta y también a otras frecuencias. Por ello se debe extraer de los datos originales una función harmónica con un período igual a la frecuencia más alta. Luego los residuos son utilizados para calcular el periodograma nuevamente y obtener la siguiente frecuencia de los datos (Lomb, 1976; Scargle, 1982; Hernández-Guerra et al., 2003).

La Tabla 5.2 muestra los resultados de estos cálculos junto con la amplitud, fase y varianza total explicada por cada frecuencia contenida en cada una de las series temporales. Recordemos que el correntímetro más superficial no ha sido considerado en este cálculo por el alto número de huecos presentes en la serie temporal. El nivel de significancia de cada frecuencia mostrada en Tabla 5.2 es del 99.9%. La señal más fuerte en las series temporales correspondientes a las profundidades de 300, 520 y 870 metros es el período anual. Aunque el período anual también aparece en la serie temporal de 1230 m, la varianza total explicada por ese período es menor que la de la señal semianual, la cual parece ser dominante en las partes intermedia y profunda del pasaje. En cada serie temporal aparece una señal significativa con un período de 3 meses. La varianza total explicada por este período es diferente en la termoclina y en capas intermedias y profundas. La diferencia varía de un 10-13% en aguas de la termoclina a un 5.4-5.6% en capas intermedias y profundas. Este hecho muestra que la señal estacional es muy importante en toda la columna de agua, especialmente dentro de la termoclina. Una señal significativa con un período de 2 meses se presenta en las aguas de la termoclina con una baja contribución a la varianza total explicada. Finalmente, hay dos señales más presentes en la serie temporal; la más larga con un período de 18 meses a una profundidad de 300 m y un 7.3% de varianza total explicada, y una señal con un período de 9 meses que aparece a 520 y 870 m. La contribución de este último período a la varianza total explicada es bastante pequeña, 1.8% y 2.3%, respectivamente, aunque significativa.

Una vez examinadas las periodicidades en el dominio de la frecuencia en el que implícitamente se asume que los procesos subyacentes son estacionales, aplicamos un análisis wavelet para transformar la serie temporal en el espacio de tiempo-frecuencia, de modo que podamos encontrar periodicidades intermitentes (Torrence and Compo, 1998; Torrence and Webster, 1999; Grinsted et al., 2004).

Muchos tests estadísticos asumen que la función de densidad de probabilidad es cercana a normal. Diferentes autores señalan que las series

que están lejos de una distribución normal producen resultados poco fidelígnos y menos significativos. Ocasionalmente puede ser, por tanto, buena idea transformar la función de densidad de probabilidad de la serie temporal. Sin embargo, hay que tener cuidado de no cambiarla imprudentemente. La transformada wavelet continua se aplicó a cada correntímetro de EBC-4 instalado en las diferentes masas de agua encontradas en el PL.

Las Figuras 5.7a y 5.7b muestran el espectro de energía de la transformada wavelet continua para cada correntímetro inmerso en el Agua Noratlántica Central. Claramente existen características comunes en la energía de las dos series temporales; por ejemplo, existe una banda de alta energía para el período de ~ 1 año (371 días) para todo el intervalo de tiempo, aunque éste prácticamente desaparece en 2002. Hay dos picos significativos en esa banda centrados alrededor de 2000-2002 y 2003-2005 en ambos correntímetros. Las dos series también muestran alta energía en la banda de ~ 9 meses (278 días) para el intervalo 2000-2002, aunque para las series temporales más profundas esta energía no está por encima del 5% del nivel de significancia. Se localizan dos picos significativos en la banda de ~ 6 meses (165-196 días) aproximadamente en 2001-2002 para el correntímetro más somero y 2002-2003 para la serie temporal más profunda en el Agua Noratlántica Central. Finalmente, se encuentran patrones similares en la banda de ~ 3 meses (90 días) alrededor de 2000 en ambos correntímetros y un pico significativo en 2005 para el correntímetro más superficial.

En la Figura 5.7c muestra tres bandas significativas bien marcadas para transformada wavelet continua de las serie temporal del Agua Antártica Intermedia. La primera está localizada en el período de ~ 1 año desde 1999 a 2005, excepto alrededor de 2002 en el que no está por encima del 5% del nivel de significancia. El segundo está localizado en el período de ~ 6 meses (185 días) para 2000-2004 y, finalmente, el tercer pico significativo ocurre en la banda de ~ 3 meses (90 días) en los años 2000, 2001 y 2002.

En la Figura 5.7d se muestra la transformada wavelet continua para la serie temporal del correntímetro instalado en el Agua Mediterránea. El patrón de energía wavelet para este correntímetro es bastante diferente de los correspondientes a los correntímetros más superficiales. La banda de ~ 1 año (352 días) es significativa y aparece justo al final de la serie temporal, alrededor de 2003-2005. Hay un pico significativo evidente en la banda de ~ 6 meses (188 días) en 2000-2001. Existe un pico significativo en el patrón de energía wavelet centrado en la banda de ~ 135 días alrededor de 2003 que no aparecía en el análisis harmónico.

Finalmente, hay dos picos significativos en la banda de ~ 3 meses (94 días) en 2004 y 2005.

Los resultados obtenidos a partir de este análisis están de acuerdo con las periodicidades mostradas para todos los correntímetros en la Tabla 5.2. Sin embargo, los resultados del análisis wavelet añaden información completamente nueva acerca de la localización de las periodicidades previamente obtenidas en el análisis harmónico.

En este trabajo también se describe la variabilidad en el transporte de masa de acuerdo a la estructura vertical en el PL obtenida mediante el análisis de componentes principales y con las periodicidades significativas presentadas anteriormente. Los transportes de masa se estiman para todo el PL usando la función polinomial obtenida por Hernández-Guerra et al. (2003) en las tres masas de agua presentes en el área de estudio.

La Figura 5.8 muestra la variabilidad temporal del transporte de masa para el Agua Nortatlántica Central, Agua Antártica Intermedia y Agua Mediterránea, respectivamente. La Figura 5.8a muestra el transporte de masa en el tiempo para las aguas de la termoclinia desde enero de 1997 hasta febrero de 2006. El transporte de masa medio es -0.81 ± 1.48 Sv, el cual está de acuerdo con el obtenido por Hernández-Guerra et al. (2003) para los primeros cuatro años de datos (-0.80 ± 1.1 Sv). Este hecho demuestra que el transporte de masa promedio para las aguas de la termoclinia no ha cambiado de forma significativa en últimos 5 años en comparación con los cuatro primeros. La serie de transporte de masa muestra fluctuaciones grandes en cortas escalas de tiempo, con un rango máximo entre -6.65 Sv hacia el sur y +6.45 Sv hacia el norte.

La Figura 5.8b muestra la variabilidad en los 9 años del transporte de masa del Agua Antártica Intermedia en el PL con un valor medio de $+0.09 \pm 0.57$ Sv. Este valor también está de acuerdo con el obtenido por Hernández-Guerra et al. (2003), indicando que el transporte de masa medio para el Agua Antártica Intermedia en el PL no ha cambiado de forma significativa en los últimos 5 años en comparación con los cuatro primeros. El rango para el Agua Antártica Intermedia es desde 2.0 a -2.0 Sv.

El transporte de masa para el Agua Mediterránea se muestra en la Figura 5.8c con un valor medio de -0.05 ± 0.17 Sv. Este valor, al igual que para el Agua Nortatlántica Central y el Agua Antártica Intermedia, coincide con el obtenido por Hernández-Guerra et al. (2003). Hay dos huecos significativos en la serie, el primero desde enero de 1997 hasta junio de 1998 y el segundo desde febrero de 2001 hasta marzo

de 2002. Por ello, el principio de esta serie se considera desde el final del primer hueco (junio 1998), mientras que el segundo hueco fue interpolado haciendo uso de los tres períodos significativos obtenidos en la sección 5.5. El rango para el Agua Mediterránea va desde -0.6 hasta 0.6 Sv.

En la Figura 5.8 también se muestran los trasportes de masa geostróficos obtenidos a partir de las estaciones hidrográficas en el PL. Los transportes de Ekman obtenidos para el PL fueron estimados en intervalos semanales según los datos de ERS-2 (enero 1997-junio 1999) y datos de QuikScat (julio 1999-febrero 2006). El transporte de Ekman se añadió a la primera capa para tener en cuenta el efecto del viento en el transporte geostrófico de masa. Los transportes de masa geostróficos obtenidos usando un nivel de no movimiento en la densidad neutral localizada entre el Agua Noratlántica Central y el Agua Antártica Intermedia coinciden mejor con los 9 años de transportes de masa en el EBC-4 que aquellos calculados usando el fondo como nivel de no movimiento.

Hernández-Guerra et al. (2002) estimó el transporte de masa en la capa de la termoclinia con datos de XBT en el PL. Estos autores evaluaron el transporte de masa cada dos meses durante dos años utilizando una relación θ/S de datos de CTD históricos. La Figura 5.9 muestra que los transportes de masa estimados con los datos de XBT y del fondeo EBC4 presentan una forma similar, indicando que el transporte de masa obtenido con el EBC-4 está de acuerdo con resultados previamente alcanzados con otros tipos de datos.

En cuanto a la variabilidad estacional, se generó un año canónico promediando los valores medios diarios sobre los nueve años de datos y así obtener la varibilidad mensual y estacional medias para el Agua Noratlántica Central, Agua Antártica Intermedia y Agua Mediterránea (Figura 5.10). La cuantificación del transporte de masa estacional para cada masa de agua durante los últimos nueve años se presentan en las Tablas 5.3, 5.4 and 5.5, respectivamente.

La Figura 5.10a muestra que las medias mensuales del transporte de masa para el Agua Noratlántica Central son hacia el sur a lo largo del año, excepto desde finales de octubre hasta principios de noviembre, cuando es aproximadamente nulo. Tal y como se muestra en la Tabla 5.3, el transporte de masa estacional es máximo en invierno (-1.30 ± 1.29 Sv), descendiendo en primavera (-0.99 ± 1.59 Sv) y verano (-0.57 ± 1.13 Sv), y alcanzando su valor mínimo en otoño (-0.44 ± 1.50 Sv).

Los transportes de masa mensuales para el Agua Antártica Intermedia

mostrados en la Figura 5.10b presentan un patrón diferente del encontrado para el Agua Nortatlántica Central. Se observa un transporte hacia el norte a lo largo del año excepto desde noviembre a enero. Diciembre es el mes en el que se observa el máximo transporte hacia el sur de -0.65 Sv . En agosto y septiembre se alcanzan los máximos transportes hacia el norte, $+0.53\text{ Sv}$ y $+0.50\text{ Sv}$, respectivamente. En la escala estacional, la Tabla 5.4 muestra un transporte de masa prácticamente nulo de $+0.02 \pm 0.47\text{ Sv}$ en el invierno. Durante la primavera y el verano, el transporte de masa del Agua Antártica Intermedia es hacia el norte con un valor medio de $+0.12 \pm 0.48\text{ Sv}$ and $+0.44 \pm 0.37\text{ Sv}$, respectivamente. Por el contrario, en invierno tiene un transporte hacia el sur de $-0.23 \pm 0.57\text{ Sv}$.

La Figura 5.10c muestra el transporte de masa mensual para el Agua Mediterránea. El transporte es muy bajo con un transporte máximo hacia el sur en diciembre ($-0.19 \pm 0.15\text{ Sv}$). El transporte estacional medio es siempre hacia el sur (Tabla 5.5), oscilando entre $-0.01 \pm 0.10\text{ Sv}$ en verano y $-0.04 \pm 0.11\text{ Sv}$ en primavera. Sin embargo, el transporte de masa hacia el sur que tiene lugar en otoño es tres veces mayor que el observado en primavera ($-0.12 \pm 0.12\text{ Sv}$).

La variabilidad interanual de los transportes de masa, mostrada en la Figura 5.11, se calculó como la suma acumulativa de los transportes medios mensuales para cada masa de agua. La serie temporal de 9 años se ha dividido en 5 períodos de tiempo diferentes: P1, desde enero de 1997 a septiembre de 1998, P2, desde septiembre de 1998 a julio de 2000, P3, desde julio de 2000 a marzo de 2003, P4, desde marzo de 2003 a noviembre de 2003 y P5, desde noviembre de 2003 a febrero de 2006. Estos diferentes períodos corresponden a cambios en las tendencias del transporte de masa acumulado respecto al transporte de masa medio de cada masa de agua durante los 9 años de datos.

La Figura 5.11a muestra un transporte de masa acumulado prácticamente nulo para el Agua Noratlántica Central durante el periodo P1. Durante P2, hay un incremento monótono claro del transporte de masa acumulado. La media anual en este periodo, -1.50 Sv , es el doble que la media para los 9 años. Durante P3, la pendiente del transporte acumulado para el Agua Noratlántica Central decrece y la media anual, -0.83 Sv , es cercana a la media de los 9 años. P4 tiene un transporte de masa acumulado nulo, similar a P1. Durante P5, la media anual del transporte de masa es semejante a la media del transporte de masa para los 9 años.

La Figura 5.11b muestra una tendencia en el transporte de masa del Agua Antártica Intermedia del triple durante P1, con un valor medio alrededor de $+0.28\text{ Sv}$. Durante P2, se observa un cambio de signo en

la tendencia del Agua Antártica Intermedia con un valor medio de -0.09 Sv. A este cambio de signo en la tendencia le sigue un nuevo cambio de signo durante P3, durante el cual se recupera la tendencia para los 9 años. P4 se caracteriza por una tendencia que cuadriplica la tendencia media, con un valor alrededor de +0.39 Sv. Finalmente, durante P5 el transporte de masa acumulado sigue incrementando su valor siguiendo la tendencia media para los 9 años. El transporte de masa acumulado para el Agua Antártica Intermedia muestra claramente valores máximos durante noviembre en toda la serie temporal, así como mínimos valores en enero.

La Figura 5.11c muestra el transporte de masa acumulado del Agua Mediterránea, el cual sigue el mismo patrón que el transporte de masa acumulado del Agua Noratlántica Central. Debido al hueco existente al inicio de la serie temporal de velocidades, el transporte de masa no se obtuvo para P1. Durante P2, la tendencia media casi duplica la media del transporte de masa del Agua Mediterránea para los 9 años, -0.08 Sv. P3 y P5 siguen la media del transporte para los 9 años, con un valor medio de -0.05 Sv. Durante P4 se observa un transporte de masa medio prácticamente nulo.

8.2.5 Circulación tridimensional en la zona de transición costera del noroeste de África (Capítulo 6)

OBJETIVO

En el capítulo 6 se investiga la circulación tridimensional en la zona de transición costera del noroeste africano con especial atención en dos aspectos: primero, se examinan las características de los diferentes regímenes dinámicos que nos encontramos a medida que nos movemos hacia océano abierto; y segundo, se cuantifican las diferentes contribuciones al movimiento vertical, es decir, las velocidades verticales inducidas por el viento, en estructuras mesoscalares y por transferencia diapicna debida al afloramiento.

MATERIAL Y MÉTODOS

Para llevar a cabo estos objetivos hemos utilizado los datos recogidos en 81 estaciones de CTD realizadas durante la campaña CONAFRICA (22 de marzo - 7 de abril de 2006), abordo del buque oceanográfico Hespérides, en un dominio de $200 \times 100 \text{ km}^2$ localizado al sur de las Islas Canarias más orientales (Figura 6.1). Las estaciones se distribuyeron en transectos paralelos a la costa africana con un es-

paciado meridional y zonal de unos 20 km. Los perfiles, obtenidos con un SeaBird 911Plus equipado con un fluorímetro, fueron interpolados cada 2 db y restringidos a los primeros 500 db de la columna de agua.

Para un mejor entendimiento de los procesos físicos observados en la región de estudio, se usaron datos de viento del escáterómetro Seawind a bordo del satélite QuikSCAT (<http://www.ifremer.fr/cersat/>) e imágenes de satélite de temperatura superficial del mar y clorofila. Ambas fuentes de datos mostraron la dominancia de condiciones favorables al afloramiento (ver Figuras 6.2 y 6.3). Vientos favorables al hundimiento ocurrieron de forma esporádica al principio y final de febrero y justo antes del muestreo.

Con el fin de calcular derivadas espaciales de las variables observadas y poder diagnosticar la velocidad vertical del campo mesoscalar, las variables hidrográficas se interpolaron a un grid tridimensional regular utilizando el método de análisis espacial objetivo (Bretherton et al., 1976). El grid de salida consistió en 21×44 puntos separados aproximadamente 5 km en las direcciones zonal y meridional. Dicho espaciado es un compendio entre la resolución espacial y la precisión de la interpolación. Por un lado, la resolución espacial del grid de salida está obligada por la separación entre estaciones pero debe ser capaz de resolver las escalas en las que estamos interesados. Por otro lado, los errores de la interpolación se incrementan con la densidad del grid y determinan la precisión de las derivadas espaciales. En la vertical hemos usado 34 niveles equiespaciados a 15 db desde 5 hasta 500 db. El campo medio de todas las variables se obtuvo ajustando a las observaciones un polinomio de segundo orden. Se establecieron los valores de 20 km y 0.01 para la escala característica horizontal (que se relaciona con las estructuras predominantes) y el ratio de la señal de ruido, respectivamente. Además, aquellas escalas que no pueden ser resueltas por el muestreo son filtradas realizando la convolución de un filtro adicional con longitud de onda de corte de 40 km (el doble de la distancia media entre estaciones).

Este esquema de interpolación se puede aplicar directamente a la temperatura T o la salinidad S , a partir de las cuales se pueden calcular otras variables como la temperatura potencial θ , la densidad potencial (referida a la superficie) ρ_θ y la densidad neutral γ_n (Jackett and McDougall, 1997). Para calcular la altura dinámica fijamos como nivel de referencia 500 db, el cual se corresponde con el nivel más profundo muestreado. Dicho nivel no está muy lejos del límite inferior del Agua Noratlántica Central, aproximadamente a unos 600-700 m, y es cercano a los niveles de referencia sugeridos por otros autores para el área del

sur de las Islas Canarias (Olbers et al., 1985; Pelegrí et al., 2006; Pastor et al., 2008). Puesto que el área muestreada incluyó estaciones costeras, decidimos usar el espesor de la capa (es decir, la altura dinámica referida al nivel inmediatamente inferior) como la variable a ser interpolada en los puntos del grid. Siguiendo este procedimiento se permite tomar el fondo como nivel de referencia en las estaciones más costeras, como en Csanady (1979). La altura dinámica se determinó posteriormente integrando hasta el nivel de referencia, y el resto de variables dinámicas se calcularon a partir de los campos de densidad y altura dinámica por diferencias finitas. Se presentan las distribuciones de θ y γ_n en lugar de T y $\rho\theta$ ya que la temperatura potencial es la variable apropiada cuando se consideran movimientos adiabáticos y la densidad neutral es más exacta para examinar los balances de masas de agua y otras propiedades.

Las velocidades verticales se pueden expresar como la suma de tres componentes: el movimiento asociado con la elevación/hundimiento de las isoneutras, el movimiento epipicno (a lo largo de las isoneutras) y el movimiento diapicno (a través de las isoneutras). Las dos primeras componentes no implican transferencia de masa entre las capas isoneutras. Nosotros aquí empleamos la aproximación más sencilla para evaluar estas componentes: asumimos que la elevación/hundimiento de las isoneutras y el movimiento epipicno resultan de movimientos ageostróficos que tienden a restaurar las desviaciones del balance geostrófico, y pueden ser diagnosticados a partir de la teoría quasigeostrófica (QG), y la convergencia-divergencia de Ekman en la capa de mezcla, la cual surge íntegramente del forzamiento inducido por el viento. Las velocidades diapicnas, por otro lado, fueron estimadas ajustando el balance de agua en las capas isoneutras, de modo que cualquier desbalance debe ser satisfecho a través de la transferencia de una capa a otra.

Las velocidades cuasigeostróficas asociadas a estructuras mesoscalares fueron inferidas resolviendo la ecuación omega según la formulación del vector Q (Hoskins et al., 1978, , ver Ecuación 6.8) con condiciones de contorno tipo Dirichlet ($w=0$) en las seis caras. Cerca de la superficie w_{qg} no tiene por qué ser exactamente igual a cero, sino que debe estar dada por una condición impuesta externamente, como por ejemplo la que deriva de la convergencia/divergencia en la capa de mezcla superficial. Sin embargo, como veremos posteriormente, esta variable alcanza valores mucho más bajos que w_{qg} a niveles más profundos y, por tanto, podemos realizar esta aproximación. En cuanto a la elección de $w_{qg} = 0$ en la frontera inferior implica que los movimientos mesoscalares son muy reducidos y, como veremos a continuación, los desplazamientos cerca de 500 db son pequeños, de modo que apoyan esta suposición. Las condiciones de frontera laterales son establecidas de una manera

más arbitraria; aquí hemos usado condiciones de Dirichlet en todas las fronteras. Se puede demostrar que, si la escala de las estructuras es menor que el tamaño del dominio, la elipticidad del dominio hace que las soluciones para w_{gg} en el interior del dominio no sean sensibles a las condiciones impuestas (ver por ejemplo Gomis and Pedder, 2005). En nuestro caso, las estructuras mesoscales son efectivamente más pequeñas que el dominio estudiado y hemos verificado que esta afirmación se cumple cuando dichas estructuras se localizan al menos unos puntos de la malla hacia el interior.

Por otro lado, los movimientos verticales dirigidos por el viento pueden ser inducidos por dos procesos que dependen del vector del estrés del viento horizontal a la superficie del mar: el bombeo de Ekman y el transporte de Ekman normal a la costa (p.e. Pickett and Paduan, 2003). El vector del estrés del viento horizontal a la superficie del mar se define como $\vec{\tau} = (\tau_x, \tau_y, 0)$, denotando τ_x y τ_y las componentes este-oeste y norte-sur, respectivamente. Este vector se puede calcular a partir del campo de vientos de Quikscat usando el logaritmo de Liu et al. (1996). En océano abierto la contribución más importante es el bombeo de Ekman, el cual resulta de la convergencia/divergencia generada en la capa de mezcla por el rotacional del estrés del viento. Las velocidades del bombeo de Ekman lineal, w_{ek} , son calculadas como $w_{ek} = (1/\rho f) \vec{k} \cdot (\nabla \times \vec{\tau})$, donde $\nabla \times \vec{\tau}$ es el rotacional del estrés del viento promediado durante el periodo de campaña y puede obtenerse aplicando diferencias finitas al estrés del viento dado por Quikscat. El bombeo de Ekman no lineal se desprecia ya que la vorticidad geostrófica relativa $\zeta_g = (\partial v_g / \partial x - \partial u_g / \partial y)$ permanece significativamente menor que f .

Cerca de la línea de costa, sin embargo, la contribución relevante en el movimiento vertical es la divergencia del transporte de Ekman. Para estimar las velocidades verticales asociadas al mismo, se calculó el transporte de Ekman normal a la línea de costa a partir de los datos de estrés del viento más cercanos a costa (aproximadamente a 30 km). El transporte de Ekman (por unidad de longitud) normal a la costa viene dado por $U = \tau_p / (\rho f)$, donde τ_p es la componente del estrés del viento paralela a la costa. Para obtener la velocidad vertical de afloramiento w_{up} necesitamos conocer el ancho del área donde tiene lugar el mismo, L_x , de modo que $w_{up} = U / L_x$. Se puede obtener una estima de la extensión de la obligación costera a partir del radio interno de deformación de Rossby para un sistema de afloramiento idealizado de dos capas, dado por $(gh)^{1/2} / f$, donde h es el espesor de la capa superior y $g = g(\rho_2 - \rho_1) / \rho_1$, con ρ_1 y ρ_2 siendo las densidades de las capas superior e inferior. Usando $\rho_2 - \rho_1 = 0.3 \text{ kg m}^{-3}$ y $h = 150 \text{ m}$ como valores típicos para la región (ver Sección 6.4.3) obtenemos un valor

para el radio de Rossby cercano a 100 km, el cual es similar al ancho del área de afloramiento observada. Por tanto, establecemos L_x igual al ancho del área de afloramiento, calculada como la distancia media entre la isóbata de 200 m y la zona frontal (según la definición utilizada en base a los contornos de altura dinámica a 20 db, ver Sección 6.4.2).

Finalmente, las velocidades verticales también pueden resultar por mezcla turbulenta. En un fluido estratificado la presencia de velocidades verticales positivas implica la transformación de energía cinética en energía potencial. Esto es posible en regiones críticamente estables, con cizallas de velocidad suficientemente grandes, las cuales ocurren frecuentemente en los sistemas frontales de zonas de afloramiento (Pelegrí and Richman, 1993; Kundu and Beardsley, 1991). Estas velocidades verticales normalmente se parametrizan en función del número de Richardson con un alto grado de incertidumbre. Aquí hemos usado una aproximación más simple basada en varios trabajos que muestran que los 500 db es un buen nivel de referencia para determinar las principales características de las corrientes a lo largo de la costa desde la región de afloramiento al sur de las Islas Canarias hasta Cabo Blanco (Olbers et al., 1985; Machín et al., 2006a; Pelegrí et al., 2006; Pastor et al., 2008). Entonces, cualquier desbalance en una de las capas se considera como el resultado de la convergencia/divergencia horizontal que debe ser compensado por las capas adyacentes a través de velocidades verticales diapicinas w_{dia} . Este concepto es útil en la valoración de intercambio de agua entre capas adyacentes en modelos tipo caja, como el que se discute a continuación.

RESULTADOS

La Figura 6.3 muestra los campos de temperatura superficial del mar y de clorofila-a el 29 de marzo y el 7 de abril, respectivamente. Los recuadros muestran cómo el océano abierto se caracteriza por aguas más cálidas y menos productivas, en contraste con las aguas frías y productivas de la zona de transición costera que ocupan una banda de unos 100 km a lo largo de la línea de costa. Las imágenes principales ilustran nuestra región de interés, al sur de las islas más orientales. Esta imagen del campo mesoscalar es muy similar a la encontrada por Barton et al. (2004) aproximadamente en la misma región en agosto de 1999. Ésta se caracteriza por la existencia de filamentos que se extienden desde la región costera y por una notable actividad mesoscalar, evidente tanto en la imagen de temperatura superficial del mar como en la de clorofila-a. Hay dos filamentos (F1 y F2) que aparecen como extensiones de agua fría y productiva que se desprenden de los cabos Bojador y Juby. Barton et al. (2004) señaló la relación que existe entre F1 y el

remolino ciclónico quasi-permanente atrapado en el canal de las islas más interiores, así como el F2 y un remolino anticiclónico intermitente que aparece al sureste de la isla de Fuerteventura, para formar sistemas que favorecen el intercambio entre las aguas de la plataforma continental y las de océano abierto. Entre ambos remolinos se identifica un dipolo A1-C1 que produce un flujo hacia costa.

La Figura 6.4 muestra la circulación y distribución de las propiedades hidrográficas a 20 db. La señal dominante es la corriente baroclina costera del afloramiento entrando a través del margen noreste (Figura 6.4a) y serpenteando hacia el suroeste hasta el margen sur del dominio, donde pierde fuerza y gira hacia el sureste. Las velocidades geostróficas más elevadas ($> 18 \text{ cm s}^{-1}$) están asociadas a los gradientes horizontales más bruscos en la altura dinámica a 20 db referenciada a 500 db, $D_{20/500}$. En la Figura 6.4a se observa que están acotadas por las isolíneas de 0.625 and 0.64 metros dinámicos, localizadas aproximadamente a 100 km de la costa africana. Estos valores de velocidad son consistentes con observaciones realizadas durante el invierno y resultados de la aplicación de modelos inversos en el pasaje al este de la isla de Lanzarote (Machín et al., 2006a).

Las distribuciones de propiedades concuerdan con la clásica celda vertical de afloramiento bidimensional (e.g. Gill and Clarke, 1974). Se puede distinguir un frente de plataforma que aproximadamente sigue la isóbata de 200 m y separa las aguas relativamente densas (frías y poco salinas) y enriquecidas en pigmentos que están adyacentes a las costa africana de la región de océano abierto (Figuras 6.4b,c). Además se puede observar una corriente hacia el sur a lo largo de la pendiente costera que trae aguas relativamente frías y poco salinas desde el norte, aparentemente asociado este frente. Los mayores gradientes horizontales a través del frente se encuentran al norte, donde la θ y la S decrecen alrededor de $1.4 \text{ }^{\circ}\text{C}$ y 0.12 en una distancia de 50 km.

En la Figura 6.5 (paneles superiores e intermedios) se presentan los campos de altura dinámica y la correspondiente velocidad geostrófica a 50, 110, 245 y 410 db (referida a 500 db), junto con los campos de θ y fluorescencia. Los campos de S no se muestran por su semejanza con los campos de θ , tal y como cabe esperar por la estrecha relación $\theta\text{-}S$ en aguas de superficie y centrales (Figura 6.6, ver siguiente subsección). Se observa una lengua de agua más fría y menos salina que se extiende al oeste de Cabo Juby, a lo largo de 27.8°N hasta la punta suroeste de la isla de Fuerteventura (14.5°O) donde se dirige hacia el sur (Figuras 6.3a and 6.4c). Se trata de un filamento somero, puesto que desaparece a los 50 db (paneles intermedios en la Figura 6.5). Los altos gradientes de θ a

través de la corriente se mantuvieron con la profundidad representando un sistema frontal que alcanzó los 245 db y que marca la frontera real entre las aguas afloradas en la costa y las de océano abierto.

El patrón de circulación geostrófica sigue la posición de la corriente superficial (20 db), la cual permanece invariante hasta los 245 db (paneles superiores en la Figura 6.5). La corriente aparece ligada al sistema frontal, como se puede ver en los campos de θ a 110 y 245 db, fluyendo paralela a la pendiente costera. La corriente y todos los remolinos tienen velocidades similares hasta los 110 db. A 245 db aún podemos encontrar corrientes intensas a lo largo del eje de la corriente principal y en los remolinos ciclónicos y anticiclónicos localizados entre Fuerteventura y Gran Canaria, mientras que aquellos remolinos al este de la corriente principal se vuelven débiles. A 410 db la corriente principal se debilita pero se pueden seguir apreciando flujos en los remolinos de Fuerteventura y Gran Canaria.

La distribución de fluorescencia *in situ* a 20 db (Figura 6.4b) muestra valores máximos sobre la plataforma continental, en concordancia con las aguas frías y enriquecidas en pigmentos que aparecían sobre la plataforma en las imágenes de satélite (Figura 6.3). La Figura 6.5 (paneles intermedios) revela diferencias significativas entre las distribuciones de fluorescencia *in situ* a 50, 110, 245 and 410 db y la correspondiente a 20 db. A 50 db los valores máximos (> 1.2 V) no se corresponden con las aguas de la plataforma (< 0.8 V) sino que presenta una distribución parcheada en una banda a lo largo del frente de afloramiento costero, el se encuentra inmediatamente después de la isoterma de 17.4°C . A 110 db los valores máximos se encuentran hacia océano abierto aunque la distribución permanece parcheada, apuntando a la posibilidad de hundimiento localizado ligado a algunas fases de remolinos y meandros en la región. Este punto será examinado en más profundidad en la Sección 6.5.3. En niveles inferiores, 245 y 410 db, los valores de fluorescencia son muy pequeños, probablemente no significativos.

La Figura 6.5 (paneles inferiores) ilustra los campos de ζ_g superpuestos en la imagen de temperatura superficial del mar del 29 de marzo. Los máximos y mínimos relativos de ζ_g se asocian a estructuras ciclónicas y anticiclónicas, con escalas similares al radio de deformación de Rossby (sobre 20 km, Pelegrí et al., 2005b). La isolínea de cero ζ_g define aproximadamente la línea del flujo del núcleo de la corriente principal, así como los márgenes de los remolinos mesoscales. El número de Rossby geostrófico, definido como $Ro = \zeta_g/f$, oscila desde -0.3 a 0.3 en superficie y decrece lentamente con la profundidad. Aunque la teoría QG debe ser usada estrictamente cuando $Ro \ll 1$, varios estudios

acerca de la aplicabilidad de esta teoría han mostrado que los errores asociados al calcular directamente variables tales como \vec{v}_g and ζ_g son del mismo orden que Ro (Shearman et al., 1999; Gomis et al., 2001). De ahí que, para nuestro estudio esperamos que estos errores no excedan el 30%, normalmente menos si nos alejamos del centro de los remolinos. Sin embargo, como el campo de velocidad vertical de las estructuras mesoscales w_{qg} depende de combinaciones no lineales de la derivada segunda de la densidad y la velocidad geostrófica, es difícil determinar cuál es el error asociado. Estos errores son probablemente del mismo orden que los valores máximos de Ro , importantes pero posiblemente no mucho mayores que los errores inherentes a la resolución horizontal del grid o la falta de sinopticidad del muestreo (Gomis and Pedder, 2005). Por ello concluimos que podemos confiar en los campos de w_{qg} pero con precaución, aceptando únicamente los patrones espaciales y los valores más elevados.

El diagrama θ -S muestra la presencia de Agua Noratlántica Central como la masa de agua principal en el rango de profundidades muestreado (Figura 6.6). El Agua Noratlántica Central se identifica por una relación θ -S lineal desde las aguas cercanas a la superficie hasta la isoneutra de $\gamma_n \approx 27.38 \text{ kg m}^{-3}$ (aproximadamente 700 m, Hernández-Guerra et al., 2005), por tanto cubriendo los primeros 500 m del océano como se muestra en la Figura 6.6. Puesto que el muestreo fue llevado a cabo a finales de invierno, cuando los flujos de calor océano-atmósfera empiezan a incrementarse (e.g. Hsiung, 1986), las aguas de océano abierto apenas muestran termoclina estacional. No obstante, la dispersión de θ -S en las capas superiores refleja las diferencias entre las aguas afloradas cerca de la pendiente continental y las aguas de océano abierto que han estado en la superficie el tiempo suficiente para ser modificadas por la interacción aire-agua.

Con el objetivo de clasificar los tipos de agua, hemos superpuesto tres curvas de θ -S medias que se obtuvieron uniendo las estaciones en función de su valor de $D_{20/500}$ (ver Figura 6.4a). Se han elegido los rangos $D_{20/500} \leq 0.625$, $0.625 \leq D_{20/500} \leq 0.64$ y $D_{20/500} \geq 0.64$ para representar las aguas afloradas, frontales y de océano abierto, respectivamente. Con esta división las tres curvas se diferencian bien y los tres dominios de las curvas, definidos por los datos dentro de una desviación estándar de las curvas medias, no se solapan. Debajo de esta capa superficial no se distinguen las tres curvas y se corresponde con el Agua Noratlántica Central del este. Esta relación única entre θ y S es la que, para la termoclina permanente superior, permite inferir los valores de S a partir de datos de θ (por ejemplo, permite inferir la distribución de S en los paneles intermedios de la Figura 6.5).

La Figura 6.7 muestra las secciones verticales de γ_n , la velocidad geostrófica meridional, v_g , θ y la fluorescencia a lo largo de 27.95°N, 27.55°N and 27.25°N. Las velocidades geostróficas, referidas a 500 db, revelan la estrecha relación entre el frente y la corriente principal. La corriente baroclina fluye separada de la costa, sobre una región de afloramiento de isoneutras. Las máximas velocidades de la corriente, aproximadamente 0.18 m s^{-1} , se observan en la superficie y decrecen a 0.05 m s^{-1} a 300 db. Esto confirma que la mayor parte de la señal baroclina de la corriente se encuentra confinada a las capas superiores, es decir que las velocidades no varían demasiado si elegimos el nivel de referencia a 400 db. Al este del frente las isoneutras se inclinan de nuevo contra la pendiente continental induciendo una corriente hacia el polo subsuperficial con el núcleo localizado a $\gamma_n=26.8 \text{ kg m}^{-3}$. En la sección sur (27.25°N), la corriente hacia el sur parece dividirse alrededor de la corriente hacia el polo (ver también el campo de \vec{v}_g a 245 db en la Figura 6.4a). Las corrientes geostróficas zonales son en general pequeñas, del orden de $\pm 0.1 \text{ m s}^{-1}$.

La elevación de las isotermas, isohalinas e isoneutras es notable hasta 100 km desde la costa e influye sobre los primeros 300 db de la columna de agua (Figura 6.7). Por ejemplo, la isoterma de 17 °C se eleva unos 150 db sobre 100 km en 27.55 y 27.95°N (paneles superiores e intermedios de la Figura 6.7) dando lugar a una pendiente media de 1.5×10^{-3} . La correspondencia entre la isoterma de 17.4 °C y el máximo profundo de fluorescencia, localizado en la parte superior de la nutriclina (Tett et al., 2002), es remarcable (Figura 6.7).

Además hemos calculado los transportes de masa que entran y salen del dominio simplemente integrando la velocidad a través de cada sección externa de la malla, desde superficie hasta 500 db, o el fondo si es más somero. Siguiendo el método propuesto por Kara et al. (2000), se obtiene una capa de mezcla que oscila entre 12 y 76 m. Por tanto, la columna de agua la dividimos en tres partes según las isoneutras 26.65, 26.85 y 27.162 kg m^{-3} . Estas capas son idénticas a las sugeridas por Ganachaud (2003) para el océano Noratlántico excepto la primera de ellas, la cual se ha elegido un poco más profunda para que se corresponda con la máxima capa de mezcla observada (76 m) y, por consiguiente, incluya todos los transportes de Ekman inducidos por el viento. La capa intermedia alcanza hasta los 15 °C, aproximadamente a 300 db en océano abierto, de modo que incluye la mayor parte de la columna de agua que aflora. La capa profunda va hasta unos 11.5 °C, cerca del nivel de 500 db. Esta capa está prácticamente inalterada por los movimientos verticales, lejos de la influencia directa del viento y tiene corrientes relativamente

débiles, por lo que no debería sufrir una mezcla substancial con la capa intermedia. La Figura 6.7 es útil para visualizar la estructura de densidad (paneles de la izquierda) y térmica (paneles de la derecha) de la columna de agua hasta los 500 db.

Los transportes de Ekman se calcularon a partir de las relaciones $T_{Ex} = \tau_y / (\rho f)$ y $T_{Ey} = -\tau_x / (\rho f)$, donde τ_x y τ_y corresponden al estrés del viento zonal y meridional promediados para el periodo de campaña. T_E toma los valores de 0.07, 0.12 and -0.11 Sv para las secciones norte, oeste y sur, respectivamente ($1 \text{ Sv} = 10^6 \text{ m}^3 \text{ s}^{-1} \sim 10^9 \text{ kg s}^{-1}$). Estos transportes se asumen que tienen lugar exclusivamente en la capa más superficial. Además se ha impuesto que el transporte de agua en la capa más profunda esté en balance asumiendo una velocidad barotrópica de $-2.3 \times 10^{-3} \text{ m s}^{-1}$ en la sección norte. Esta pequeña velocidad negativa está de acuerdo con los resultados del modelo inverso aplicado por Machín et al. (2006a) al pasaje al este de la isla de Lanzarote. Estos autores encontraron una velocidad de referencia media anual cercana a -0.01 m s^{-1} en 800 db, aunque con una variabilidad temporal importante.

En la Figura 6.8a se muestran los transportes de masa integrados por capas para cada sección. Sumando los transportes en las tres capas (0.34, 0.57 y 0.27 Sv a través de la superior, intermedia y profunda, respectivamente) da un total de 1.18 Sv fluyendo por la sección norte, con 1 Sv correspondiendo al transporte de Agua Noratlántica Central que realiza la Corriente de Afloramiento de Canarias entre las islas y la costa africana. Este resultado concuerda con el transporte medio determinado con datos de XBT y CTD en este pasaje (Hernández-Guerra et al., 2001, 2002; Knoll et al., 2002). También está de acuerdo con el transporte en los primeros 600 m estimado a partir de un anclaje localizado en el centro del canal que forman las islas con la costa africana (Hernández-Guerra et al., 2003). Una estimación reciente basada en nueve años de datos de dichos correntímetros muestran un valor medio similar al que hemos obtenido, $-0.81 \pm 1.48 \text{ Sv}$, aunque con una gran variabilidad (Fraile-Nuez et al., 2010).

Fuera de la costa del noroeste de África, la corriente de frontera es la Corriente de Canarias; abarca todo el archipiélago y más allá (aproximadamente 1000 km), con un transporte del orden de 5 Sv en los 700 m de Agua Noratlántica Central (Käse et al., 1985, 1986; Stramma and Siedler, 1988). Una fracción importante de este transporte ocurre en la pendiente continental, ligado al sistema frontal del afloramiento costero como la Corriente de Afloramiento de Canarias (Pelegrí et al., 2005a; Pelegrí et al., 2005b; Machín et al., 2006a). La Figura 6.8b revela un transporte máximo a través de 27.7°N , con un incremento máximo sobre

la zona frontal. Esta figura ilustra la presencia de un transporte hacia el sur significativo, tanto en la región de afloramiento (alrededor de 0.4 Sv de contribución barotrópica) como en el sistema frontal (alrededor de 1 Sv de contribución baroclina). Hacia océano abierto el transporte se incrementa lentamente a medida que la Corriente de Afloramiento de Canarias se une con la Corriente Canarias.

Los 1.18 Sv que entran por la sección norte se equilibran aproximadamente con 1.36 Sv que dejan la caja por la sección oeste y, en menor medida, por la sección sur (Figura 6.8a). El desbalance total, 0.18 Sv, refleja principalmente la convergencia del flujo en la capa intermedia y la divergencia en la capa más superficial. Este resultado implica una transferencia diapicna desde la capa intermedia a la capa superficial, como se espera que ocurra en las regiones de afloramiento (Pelegrí and Richman, 1993). Si asumimos que la mayoría de esta transferencia ocurre en la región frontal, cerca de 30 km de ancho y 100 km de largo, esto implica una velocidad diapicna de $w_{dia} = 6 \times 10^{-5} \text{ m s}^{-1}$ [5.2 m day $^{-1}$]. Los máximos valores son ciertamente más altos que este valor medio, probablemente respondiendo a estados subcríticos de la corriente baroclina de afloramiento (Kundu and Beardsley, 1991; Pelegrí and Richman, 1993).

Añadiendo el transporte de Ekman a todos los transectos que acotan nuestro dominio obtenemos un balance medio de Ekman de 0.08 Sv, que dividido por el área de afloramiento da una velocidad de afloramiento de $w_{up} = 0.8 \times 10^{-5} \text{ m s}^{-1}$ [0.7 m day $^{-1}$]. Como primera aproximación podemos decir que esta velocidad afectaría a toda la región de afloramiento hasta la isoterma de 15 °C.

La velocidad de bombeo de Ekman calculada para cada punto del dominio tiene una media negativa w_{ek} de $-0.3 \times 10^{-5} \text{ m s}^{-1}$ [-0.26 m day $^{-1}$]. Aunque es pequeño, este valor es consistente con el bombeo de Ekman negativo que ocurre en el giro subtropical (e.g. Leetma and Bunker, 1978). Si integramos sobre todo el dominio, éste corresponde a un transporte de -0.05 Sv, que es del orden del transporte de Ekman costero pero de signo contrario.

Los campos de \vec{v}_g y ζ_g fields (Figuras 6.9 y 6.10) ilustran cómo el serpenteo de la corriente da lugar a remolinos baroclinos a ambos flancos, con valores de ζ_g positivos hacia la costa y negativos hacia el océano abierto. El núcleo de la corriente, el cual debería tener vorticidad cero, realmente corresponde a una banda ancha de valores moderadamente bajos de ζ_g en la Figura 6.10. El campo de w_{qg} cambia lentamente con la profundidad dentro de la región frontal, con las máximas velocidades

(del orden de 10 m day^{-1}) ocurriendo entre 100 y 150 db. Además, tiene escalas más pequeñas que el campo de ζ_g , estando ligado a ciertas fases de los meandros y remolinos. Sin embargo, el campo de w_{qg} es muy parcheado dando lugar a un transporte neto de 0.01 Sv a cualquier profundidad.

Las velocidades verticales dentro de la región de afloramiento están controladas por la constricción costera, la cual induce la celda vertical bidimensional a lo largo de la sección normal a la costa. Esta celda vertical resulta en la transferencia de aguas subsuperficiales de 100-300 db a la superficie. Habíamos determinado una velocidad de afloramiento de 2 m day^{-1} a la cual se superponen velocidades verticales QG w_{gq} de valores moderados y estructura parcheada (Figuras 6.9 y 6.10).

En resumen, la w_{dia} es relativamente alta (sobre 5 m day^{-1}) pero ocurre en una región frontal estrecha contribuyendo, por tanto, con un transporte moderado de 0.18 Sv. El bombeo de Ekman es de -0.05 Sv y, como tiene lugar en todo el dominio, produce velocidades verticales pequeñas w_{ek} de 0.3 m day^{-1} . La divergencia costera de Ekman es 0.08 Sv y produce velocidades verticales w_{up} de 1 m day^{-1} sobre la región de afloramiento. En nuestra región, el transporte debido tanto a la divergencia costera de Ekman como al bombeo de Ekman es pequeño y su efecto conjunto aún menor. Finalmente, los valores máximos de w_{qg} (Figuras 6.9 y 6.10) son mucho más altos que w_{up} o w_{ek} e incluso w_{dia} , pero su distribución parcheada da lugar a un transporte pequeño.

Además hemos investigado el origen de las estructuras mesoscales. Tradicionalmente la actividad mesoscalar al sur de las Islas Canarias se atribuye al bloqueo que presentan las mismas a la Corriente de Canarias que fluye hacia el sur (Arístegui et al., 1994, 1997; Barton et al., 1998, 2004; Sangrà et al., 2005; Sangrà et al., 2007, 2009). Jiménez et al. (2008) encontró que este mecanismo topográfico se puede mantener a través del bombeo de Ekman en los flancos de las islas. Sin embargo, la presencia del sistema frontal ofrece la posibilidad de que algunos remolinos puedan ser generados a partir de instabilidades de la corriente baroclina. Con el objetivo de dilucidar el origen de los remolinos observados, hemos examinado las distribuciones verticales de θ a través de dos transectos diferentes que cruzan dipolos, uno localizado en la región de océano abierto (Dipolo 1) y el otro en la de afloramiento (Dipolo 2) (Figuras 6.11a,b). Seleccionamos estos dos dipolos como representativos de dos tipos diferentes de remolinos, barotrópico y profundo (Dipolo 1) frente a baroclino y somero (Dipolo 2). Ambos muestran un patrón térmico muy diferente, más evidente en las diferencias de θ entre los núcleos de los remolinos adyacentes tal y como se

muestra en la parte derecha de estas figuras. Las isotermas en el Dipolo 1 tienen una pendiente casi constante hasta los 400 db, sugiriendo una dominancia de la componente barotrópica y, por tanto, siendo indicativo de ser generado por las islas. Al contrario, el Dipolo 2 exhibe un aplanamiento de las isotermas a partir de los 250 db, de modo que su generación está aparentemente asociado a inestabilidades baroclinas del frente de afloramiento. Si estuviéramos examinando el dipolo formado por C1 y A1 Figure (Figura 6.3) encontraríamos que se trata de un tipo mixto, ya que A1 tiene también isotermas con pendientes significativas hasta llegar al fondo de la columna de agua muestreada (ver los paneles inferiores en las Figuras 6.7 y 6.9). Estas diferencias también son claras en la distribución de velocidad en ambos dipolos (Figuras 6.11a,c,d). El Dipolo 1 exhibe un campo de \vec{v}_g con una magnitud bastante constante con la profundidad, solamente cambiando cerca de los 500 db (paneles izquierdos de las Figuras 6.11c,d). Sin embargo, el Dipolo 2 presenta una estructura baroclinica clara, con una magnitud de \vec{v}_g que decrece rápidamente entre los 200 y 300 db (paneles derechos en las Figuras 6.11c,d). También se observan diferencias de su carácter diferente en el campo de w_{qg} ; el dipolo de océano abierto tiene mayores velocidades que el cercano a costa. Por tanto, los campos de θ y velocidad apuntan a un origen diferente, con el Dipolo 1 probablemente originado a través del bloqueo que presentan las islas al flujo de la Corriente de Canarias y el Dipolo 2 como resultado de la inestabilidad de la corriente frontal baroclinica. Recientemente, Sangrà et al. (2009) documentó que la región al sur de las Islas Canarias es una fuente importante de remolinos de larga vida que se propagan hacia el oeste, los cuales emplean seis meses para viajar distancias de 2000 km. Se observó que el 40% de los remolinos de larga vida observados en el Atlántico noreste subtropical procedían de la región al sur de Canarias, con una tasa media de fromación de 3-4 remolinos al año. Estos autores utilizaron técnicas de teledetección para identificar la fuente de los remolinos pero las imágenes carecían de la resolución suficiente cerca de costa. Entonces, ellos enfatizaron la importancia del efecto isla pero apuntaron a la posibilidad de que parte de la actividad mesoscalar estuviera generada en la zona de transición costera. Nuestros resultados respaldan la idea de la inestabilidad de una zona baroclinica costera como un mecanismo potencialmente importante de generación de remolinos.

Finalmente examinamos la distribución de fluorescencia. Los estudios previos indican que las zonas frontales, como las zonas de transición entre diferentes masas de agua con alta actividad mesoscalar, son lugares de producción primaria aumentada (Holligan, 1981; Jones and Halpern, 1981; Falkowski et al., 1991). Efectivamente, las imágenes de satélite (Pacheco and Hernández-Guerra, 1999) y los datos de campo de la

región canaria (Arístegui et al., 1997; Barton et al., 1998, 2004) han mostrado que la clorofila puede aumentar si está asociada a estructuras mesoscales específicas. Los principales factores que influencian el crecimiento del fitoplancton son la disponibilidad de radiación solar y nutrientes inorgánicos, el último siendo suministrado por los movimientos verticales y el transporte horizontal desde la zona de afloramiento (p.e. filamentos en la Figura 6.3). En cuanto al primer factor, la profundidad de la zona eufótica se ha observado que toma un valor bastante constante en 100 m para zona de estudio (Neuer et al., 2007), por lo que no parece un factor clave en la distribución espacial de la producción primaria. Puesto que no disponemos de datos de nutrientes, no podemos justificar este segundo factor, es decir el aporte de nutrientes. Sin embargo, basándonos en la distribución de fluorescencia podemos hacer algunas consideraciones en el papel potencial de las estructuras mesoscales en el modulado de la producción primaria. Los procesos físicos en las estructuras mesoscales tienden a acumular/retener la biomasa existente o estimular el crecimiento *in situ* del fitoplancton. Los remolinos ciclónicos elevan las isopicnas y, por tanto, tienden a aflorar nutrientes subsuperficiales en la zona eufótica; inversamente, los remolinos anticiclónicos hunden las isopicnas haciendo más compleja la conexión entre la luz y los nutrientes (Arístegui et al., 1997). No obstante, el papel de la elevación o hundimiento de las isopicnas en el aporte de nutrientes puede ser efectivo solamente durante cortos periodos después de la generación del remolino. Después de algún tiempo, normalmente del orden de unas pocas revoluciones del remolino o 10-20 días (Sangrà et al., 2005; Sangrà et al., 2007), el remolino está completamente formado y se han alcanzado los desplazamientos máximos de las isopicnas. Más allá de este tiempo el remolino empieza a decaer y los desplazamientos decrecen. En estos últimos estadíos el flujo tangencial medio se aproxima al balance geostrófico de modo que los movimientos advectivos verticales y radiales pueden surgir solamente como resultado de procesos difusivos. Ésta es posiblemente la razón de las diferencias en comportamiento entre remolinos ciclónicos y anticiclónicos: la proximidad de los nutrientes subsuperficiales en los remolinos anticiclónicos probablemente favorece la transferencia diapicna, al contrario de lo que ocurre en los remolinos anticiclónicos. Estas ideas son apoyadas con nuestros datos. Nosotros encontramos una correlación substancial entre los perfiles verticales de fluorescencia y w_{qg} hasta 110 db en aquellas regiones con alta actividad mesoscalar ($r \geq |\pm 0.6|$, $p \leq 0.1$). Este resultado apunta fundamentalmente al movimiento de las isopicnas (y el máximo de fluorescencia profundo) causado por velocidades verticales w_{qg} asociadas a estructuras mesoscales. Como se indicó anteriormente (Section 6.4.2), la profundidad de la isoterma de 17.4 °C sigue aproximadamente la base de la capa de mezcla. Puesto que

la profundidad de la capa de mezcla disminuye hacia la costa, esperamos que exista una correlación entre la profundidad de la isoterma de 17.4 °C y la profundidad del máximo profundo de fluorescencia; y efectivamente encontramos una alta correlación, $r = 0.68$, $p \leq 0.01$. Sin embargo, la intensidad del máximo profundo de fluorescencia no permanece constante. Existe una correlación negativa ($r = -0.37$, $p \leq 0.01$) entre la profundidad de la isoterma de 17.4 °C y la intensidad del máximo profundo de fluorescencia, indicando que cuanto más somero es el máximo profundo de fluorescencia es más intenso, p.e. los remolinos ciclónicos aparecen con altos niveles de fluorescencia.

8.3 Conclusiones y futuras líneas de investigación

Las conclusiones más importantes que han resultado de esta tesis son:

1. El análisis de secciones hidrográficas en el océano Atlántico tropical y subtropical sugiere que las aguas entre 600 y 1800 db se han estado calentando y salinificando desde 1957, aunque hay evidencias claras de una variabilidad interdecadal considerable impuesta sobre la tendencia a larga escala.
 - (a) El calentamiento documentado para el periodo 1957-1993 de las aguas intermedias y profundas superiores a lo largo de 7.5°N ha continuado hasta 2010; sin embargo, el enfriamiento de aguas más profundas se ha detenido o invertido parcialmente.
 - (b) La tendencia de calentamiento en el océano superior (600-1800 db) observada a lo largo de 24.5°N entre 1957 y 1998 se invirtió entre 1998 y 2004. Se observó un cambio similar en salinidad. Las aguas superiores se calentaron 0.27°C desde 1957 to 1998, el año más caliente y salino desde 1957. Posteriormente tuvo lugar un enfriamiento de -0.15°C entre 1998 y 2004.
 - (c) Las aguas de la región canaria presentan un aumento significativo en temperatura y salinidad en isóbaras entre 1500 y 2300 db. El máximo incremento (a 1600 db) está ocurriendo a una tasa de 0.29°C y 0.047 por década, las cuales son mucho más altas que los promedios zonales a lo largo de la cuenca este de la sección 24.5°N.

2. La descomposición de los cambios isobáricos en cambios a lo largo de las superficies neutrales y cambios debido al desplazamiento vertical de las isoneutras revelaron al primero de los mecanismos como el principal contribuyente de los cambios observados. No obstante, algunas masas de agua están cambiando. El Agua Noratlántica Central llegó en 2006 a la región Canaria en una forma más fría y menos salina que en 1997. Contrariamente, el Agua Antártica Intermedia y el agua Circumpolar superior en la sección 7.5°N fueron más cálidas y salinas en 2010 que en 1993.
3. Los datos Argo han corroborado los últimos patrones de cambio en 24.5°N, por tanto demostrando el valor de este tipo de datos para observar la variabilidad oceánica. Además su uso ofrece las ventajas de i) disponibilidad en casi tiempo real, ii) alta cobertura espacial, iii) menor ruido mesoscalar en comparación con las secciones hidrográficas y iv) permiten la inspección de los cambios a escalas temporales relativamente pequeñas.
4. El análisis de una serie temporal de 9 años de correntímetros instalados en el Pasaje de Lanzarote ha revelado un transporte medio anual de -0.81 ± 1.48 Sv para el Agua Noratlántica Central, $+0.09 \pm 0.57$ Sv para el Agua Antártica Intermedia and -0.05 ± 0.17 Sv para el Agua Mediterránea.
 - (a) La variabilidad estacional de estas masas de agua se caracteriza por un transporte máximo hacia el sur del Agua Noratlántica Central en invierno y primavera, seguido de un mínimo en verano y otoño. Se encuentran valores cercanos a cero para el Agua Antártica Intermedia durante invierno y primavera, con un transporte máximo en verano y negativo en otoño, cuando esta masa de agua invierte su flujo. El Agua Mediterránea tiene un patrón estacional similar al del Agua Noratlántica Central.
5. El análisis de datos de alta resolución recogidos al sureste de las Islas Canarias a finales de invierno de 2006 mostraron que la zona de transición costera del noroeste de África estaba dividida en tres regiones diferentes en base a sus características físicas y dinámicas: la región de afloramiento, frontal y de océano abierto.
 - (a) La región de afloramiento se caracterizó por aguas frías y débilmente estratificadas fluyendo hacia el ecuador, con una corriente subsuperficial hacia el polo sobre la pendiente continental de aproximadamente 5 cm s^{-1} .

- (b) La región frontal se caracterizó por una corriente baroclina fluyendo hacia el soroeste asociada con una elevación de las isoneutras; el transporte de la corriente es cercano a 1 Sv, con velocidades máximas de 18 cm s^{-1} en la superficie decreciendo a 5 cm s^{-1} a 300 db.
- (c) La zona frontal mostró la presencia de remolinos profundos probablemente generados por el bloqueo topográfico de las islas a la Corriente de Canarias, así como también remolinos más someros que probablemente surgieron como inestabilidades baroclinas de la corriente principal.
- (d) Las velocidades verticales cuasi-geostróficas, las cuales oscilaron entre -18 to 12 m dia^{-1} , fueron mayores que las velocidades verticales diapicnas asociadas a la región frontal (valor medio de 5 m dia^{-1}), las velocidades verticales generadas por el viento en la región de océano abierto como resultado de la divergencia horizontal del estrés del viento (una fracción de metro por día), y en la región de afloramiento debido a la obligación de la costa (sobre 2 m day^{-1}). Sin embargo, el parcheado de la velocidad vertical cuasi-geostrófica produjo un transporte vertical (0.01 Sv) de un orden más pequeño que el transporte de Ekman costero (0.07 Sv), el bombeo de Ekman integrado (-0.05 Sv) o la transferencia diaclina (0.18 Sv).

Los resultados documentados en esta tesis apuntan a diferentes direcciones con el objetivo de mejorar nuestro entendimiento de las variaciones a larga escala de las propiedades de las masas de agua en el océano Noratlántico. El análisis tiene que basarse ampliamente en nuestras habilidades avanzadas para reunir grandes cantidades de datos, tanto a través de las campañas convencionales o de sistemas innovadores como los perfiladores Argo, y la capacidad computacional que hemos adquirido para analizarlos. Particularmente, los datos oceanográficos deben ser vistos en conjunto con datos meteorológicos para trazar en el tiempo el origen las anomalías termohalinas observadas, y también con modelos numéricos, de manera que podamos predecir el camino futuro de dichos cambios.

A continuación se presenta un breve resumen de estas futuras líneas de investigación:

1. Utilizar la sección 24.5°N, recientemente realizada, para distinguir si los cambios observados son oscilaciones interanuales/interdecadales o representan una tendencia actual de larga escala;
2. Estudiar en mayor profundidad la variabilidad oceánica a escalas de tiempo más cortas, particularmente la presencia de oscilaciones termohalinas que están presentes en las secciones transatlánticas;
3. Eliminar las oscilaciones que perturban los campos termohalinos en las aguas centrales e intermedias a lo largo de 7.5°N y repetir el análisis de cambios de temperatura y salinidad;
4. Explorar la relación entre los cambios hidrográficos y las variaciones a larga escala en los patrones atmosféricos.
5. Estudiar la covariación a larga escala de los patrones de circulación y las propiedades físicas en la región Canaria a partir de datos de CTD y/o correntímetros;
6. Finalmente, investigar la evolución temporal del afloramiento del noroeste africano en términos de extensión y propiedades de las aguas afloradas, a través de datos observacionales y de modelos, para estimar el posible rango de variación y su papel potencial como termorregulador regional y global.

Bibliography

- Allen, J., Smeed, D., 1996. Potential Vorticity and Vertical Velocity at the Iceland-Færöes Front. *Journal of Physical Oceanography* 26, 2611–2634. 91
- Arbic, B., Owens, W., 2001. Climatic Warming of Atlantic Intermediate Waters. *Journal of Climate* 14, 4091–4108. 14, 35, 49, 56, 135
- Arhan, M., De Verdiére, A., Mémery, L., 1994. The Eastern Boundary of the Subtropical North Atlantic. *Journal of Physical Oceanography* 24, 1295–1316. 60, 90
- Arhan, M., Mercier, H., Bourles, B., Gouriou, Y., 1998. Hydrographic sections across the Atlantic at 7°30N and 4°30S. *Deep Sea Research* 45, 829–872. 14, 21, 22, 24, 136, 139, 140
- Arístegui, J., Sangrà, P., Hernández-León, S., Cantón, M., Hernández-Guerra, A., Kerling, J., 1994. Island-induced eddies in the Canary Islands. *Deep Sea Research* 41, 1509–1525. 90, 111, 115, 169
- Arístegui, J., Tett, P., Hernández-Guerra, A., Basterretxea, G., Montero, M., Wild, K., Sangrà, P., Hernández-León, S., Cantón, M., García-Braun, J., et al., 1997. The influence of island-generated eddies on chlorophyll distribution: a study of mesoscale variation around Gran Canaria. *Deep Sea Research* 44, 71–96. 115, 117, 118, 169, 171
- Baringer, M., Molinari, R., 1999. Atlantic Ocean baroclinic heat flux at 24° to 26°N. *Geophysical Research Letters* 26, 353–356. 31
- Barton, E., Arístegui, J., Tett, P., Cantón, M., García-Braun, J., Hernández-León, S., Nykjaer, L., Almeida, C., Almunia, J., Balsteros, S., Basterretxea, G., Escánez, J., García-Weill, L., Hernández-Guerra, A., López-Laatzén, F., Molina, R., Montero, M., Navarro-Pérez, E., Rodríguez, J., van Lenning, K., Vélez, H., Wild, K., 1998. The transition zone of the Canary Current upwelling region. *Progress in Oceanography* 41, 455–504. 90, 115, 117, 169, 171
- Barton, E., Arístegui, J., Tett, P., Navarro-Pérez, E., 2004. Variability in the Canary Islands area of filament-eddy exchanges. *Progress in Oceanography* 62, 71–94. 91, 99, 115, 117, 162, 169, 171
- Bindoff, N., McDougall, T., 1994. Diagnosing Climate Change and Ocean Ventilation Using Hydrographic Data. *Journal of Physical Oceanography* 24, 1137–1152. 15, 22, 34, 49, 52, 53, 137, 138, 142, 145, 147

- Bindoff, N., Willebrand, J., Artale, V., Cazenave, A., Gregory, J., Gulev, S., Hanawa, K., Le Quéré, C., Levitus, S., Nojiri, Y., Shum, C., Talley, L., Unnikrishnan, A., 2007. Observations: Oceanic Climate Change and Sea Level. In: Climate Change 2007: The Physical Science Basis. Contribution of Working Group I to the Fourth Assessment Report of the Intergovernmental Panel on Climate Change [Solomon, S., D. Qin, M. Manning, Z. Chen, M. Marquis, K.B. Averyt, M. Tignor and H.L. Miller (eds.)]. Cambridge University Press, Cambridge, United Kingdom and New York, NY, USA. 13, 31, 49, 135, 141
- Bower, A., 1989. Potential vorticity balances and horizontal divergence along particle trajectories in Gulf Stream meanders east of Cape Hatteras. *Journal of Physical Oceanography* 19, 1669–1681. 115
- Bowman, M., Iverson, R., 1978. Estuarine and plume fronts. Oceanic fronts in coastal processes, 87–104. 90
- Bretherton, F., Davis, R., Fandry, C., 1976. A technique for objective analysis and design of oceanographic experiments applied to MODE-73. *Deep Sea Research* 23, 559–582. 95, 159
- Brockman, C., Hughes, P., Tomczak, M., 1977. Currents, winds and stratification in the NW African upwelling region during early 1975. Data Report 32, Institut für Meereskunde an der Christian-Albrechts-Universität, Kiel, Germany, 45 pp. 90
- Bryden, H., Griffiths, M., Lavín, A., Millard, R., Parrilla, G., Smethie, W., 1996. Decadal changes in water mass characteristics at 24°N in the Subtropical North Atlantic Ocean. *Journal of Climate* 9, 3162–3186. 14, 31, 49, 135
- Bryden, H., McDonagh, E., King, B., 2003. Changes in ocean water mass properties: oscillations or trends? *Science* 300, 2086–2088. 44
- Chidichimo, M., Kanzow, T., Cunningham, S., Marotzke, J., 2010. The contribution of eastern-boundary density variations to the Atlantic meridional overturning circulation at 26.5°N. *Ocean Science Discussions* 6, 475–490. 84
- Csanady, G., 1979. The pressure field along the western margin of the North Atlantic. *Journal of Geophysical Research* 84, 4905–4915. 95, 160
- Cunningham, S., Alderson, S., 2007. Transatlantic temperature and salinity changes at 24.5°N from 1957 to 2004. *Geophysical Research Letters* 34, L14606. 13, 31, 49, 55, 84, 135

- Czaja, A., Marshall, J., 2000. On the interpretation of AGCMs response to prescribed time-varying SST anomalies. *Geophysical Research Letters* 27, 1927–1930. 83
- Ekman, V., 1905. On the influence of the earth's rotation on ocean currents. *Ark. f. Mat. Ast. och Fysik.*, Stockholm 6 (2), 11. 9, 131
- Emery, W., Thomson, R., 1998. Data analysis methods in physical oceanography. 664 pp., Elsevier, New York. 62, 149
- Falkowski, P., Zieman, D., Kolber, Z., Bienfang, P., 1991. Role of eddy pumping in enhancing primary production in the ocean. *Nature* 352, 55–58. 117, 170
- Fiekas, V., Elken, J., Müller, T., Aitsam, A., Zenk, W., 1992. A view of the Canary Basin thermocline circulation in winter. *Journal of Geophysical Research* 97, 12495–12510. 90
- Fraile-Nuez, E., Hernández-Guerra, A., 2006. Wind-driven circulation for the eastern North Atlantic Subtropical Gyre from Argo data. *Geophysical Research Letters* 33, L03601. 33, 60, 141
- Fraile-Nuez, E., Machín, F., Vélez-Belchí, P., López-Laatzen, F., Borges, R., Benítez-Barrios, V., Hernández-Guerra, A., 2010. Nine years of mass transport data in the eastern boundary of the North Atlantic Subtropical Gyre. *Journal of Geophysical Research* 115, C09009, doi:10.1029/2010JC006161. 108, 167
- Fuglister, F., 1960. Atlantic ocean atlas of temperature and salinity profiles and data from the International Geophysical Year of 1957–1958. Woods Hole Oceanography Institution, San Diego, Atlas Series 1, 209. 21, 31, 138
- Ganachaud, A., 2003. Large-scale mass transports, water mass formation, and diffusivities estimated from World Ocean Circulation Experiment (WOCE) hydrographic data. *Journal of Geophysical Research* 108, 3213, doi:10.1029/2002JC001565. 106, 166
- Ganachaud, A., Wunsch, C., 2000. Improved estimates of global ocean circulation, heat transport and mixing from hydrographic data. *Nature* 408, 453–457. 10, 133
- Gandin, L., 1965. Objective Analysis of Meteorological Fields. Israel Program for Scientific Translations. 95
- García-Muñoz, M., Arístegui, J., Pelegrí, J., Antoranz, A., Ojeda, A., Torres, M., 2005. Exchange of carbon by an upwelling filament off Cape Ghir (NW Africa). *Journal of Marine Systems* 54, 83–95. 90

- Gill, A., Clarke, A., 1974. Wind-induced upwelling, coastal currents and sea-level changes. Deep Sea Research 21, 325–345. 99, 163
- Gomis, D., García, M., López, O., Pascual, A., 2002. Quasi-geostrophic 3D circulation and mass transport in the western Bransfield Strait during Austral summer 1995/96. Deep Sea Research 49, 603–621. 91
- Gomis, D., Pedder, M., 2005. Errors in dynamical fields inferred from oceanographic cruise data Part I. The impact of observation errors and the sampling distribution. Journal of Marine Systems 56, 317–333. 34, 97, 104, 161, 165
- Gomis, D., Ruiz, S., Pedder, M., 2001. Diagnostic analysis of the 3D ageostrophic circulation from a multivariate spatial interpolation of CTD and ADCP data. Deep Sea Research 48, 269–295. 95, 104, 115, 165
- Grinsted, A., Moore, J., Jevrejeva, S., 2004. Application of the cross wavelet transform and wavelet coherence to geophysical time series. Nonlinear Processes in Geophysics 11, 561–566. 72, 153
- Hagen, E., Zülicke, C., Feistel, R., 1996. Near-surface structures in the Cape Ghir filament off Morocco. Oceanologica acta 19, 577–598. 90
- Hall, M., McCartney, M., Whitehead, J., 1997. Antarctic bottom water flux in the equatorial western atlantic*. Journal of Physical Oceanography 27, 1903. 27
- Hammersley, J., Handscomb, D., 1964. Monte carlo methods. 178 pp., Wiley, London. 65, 150
- Hernández-Guerra, A., Fraile-Nuez, E., Borges, R., López-Laatzén, F., Vélez-Belchí, P., Parrilla, G., Müller, T., 2003. Transport variability in the Lanzarote passage (eastern boundary current of the North Atlantic subtropical Gyre). Deep Sea Research 50, 189–200. xix, 60, 61, 62, 64, 66, 71, 74, 75, 77, 82, 90, 91, 108, 149, 150, 151, 152, 153, 155, 167
- Hernández-Guerra, A., Fraile-Nuez, E., López-Laatzén, F., Martínez, A., Parrilla, G., Vélez-Belchí, P., 2005. Canary Current and North Equatorial Current from an inverse box model. Journal of Geophysical Research 110, C12019, doi:10.1029/2005JC003032. 60, 91, 104, 165
- Hernández-Guerra, A., Joyce, T., Fraile-Nuez, E., Velez-Belchí, P., 2009. Using Argo data to investigate the meridional overturning circulation in the North Atlantic. Deep Sea Research, doi:10.1016/j.dsr.2009.10.003. 34

- Hernández-Guerra, A., López-Laatzen, F., Machín, F., de Armas, D., Pelegri, J., 2001. Water masses, circulation and transport in the eastern boundary current of the North Atlantic subtropical gyre. *Scientia Marina* 65, 177–186. 60, 61, 90, 91, 108, 167
- Hernández-Guerra, A., Machín, F., Antoranz, A., Cisneros-Aguirre, J., Gordo, C., Marrero-Díaz, A., Martínez, A., Ratsimandresy, A., Rodríguez-Santana, A., Sangrà, P., López-Laatzen, F., Parrilla, G., Pelegri, J., 2002. Temporal variability of mass transport in the Canary Current. *Deep Sea Research* 49, 3415–3426. 60, 61, 77, 108, 156, 167
- Hernández-Guerra, A., Nykjaer, L., 1997. Sea surface temperature variability off north-west Africa: 1981–1989. *International Journal of Remote Sensing* 18, 2539–2558. 65, 90
- Holligan, P., 1981. Biological implications of fronts on the northwest European continental shelf. *Philosophical Transactions of the Royal Society of London. Series A, Mathematical and Physical Sciences*, 547–562. 117, 170
- Hoskins, B., Draghici, I., Davies, H., 1978. A new look at the omega-equation. *Quarterly Journal of the Royal Meteorological Society* 104, 31–38. 91, 97, 160
- Hsiung, J., 1986. Mean surface energy fluxes over the global ocean. *Journal of Geophysical Research* 91, 10585–10606. 104, 165
- Hughes, P., Barton, E., 1974. Stratification and water mass structure in the upwelling area off northwest Africa in April/May 1969. *Deep Sea Research* 21, 1–628. 90
- Huyer, A., Barth, J., Kosro, P., Shearman, R., Smith, R., 1998. Upper-ocean water mass characteristics of the California Current, summer 1993. *Deep Sea Research* 45, 1411–1442. 90
- Iselin, C., 1939. The influence of vertical and lateral turbulence on the characteristics of the waters at mid-depths. *Trans. Amer. Geophys. Union* 20, 414–417. 9, 132
- Jackett, D., McDougall, T., 1997. A Neutral Density Variable for the Worlds Oceans. *Journal of Physical Oceanography* 27, 237–263. 22, 35, 50, 60, 95, 138, 142, 146, 159
- Jiménez, B., Sangrà, P., Mason, E., 2008. A numerical study of the relative importance of wind and topographic forcing on oceanic eddy shedding by tall, deep water islands. *Ocean Modelling* 22, 146–157. 115, 169

- Jones, B., Halpern, D., 1981. Biological and physical aspects of a coastal upwelling event observed during March–April 1974 off northwest Africa. Deep Sea Research 28, 71–81. 117, 170
- Joyce, T., Pickart, R., Millard, R., 1999. Long-term hydrographic changes at 52° and 66°W in the North Atlantic Subtropical Gyre and Caribbean. Deep Sea Research 46, 245–278. 14, 135
- Joyce, T., Robbins, P., 1996. The long-term hydrographic record at Bermuda. Journal of Climate 9, 3121–3131. 14, 135
- Kanzow, T., Cunningham, S., Rayner, D., Hirschi, J., Johns, W., Baringer, M., Bryden, H., Beal, L., Meinen, C., Marotzke, J., 2007. Observed flow compensation associated with the MOC at 26.5 N in the Atlantic. Science 317, 938–941. 84
- Kara, A., Rochford, P., Hurlburt, H., 2000. An optimal definition for ocean mixed layer depth. Journal of Geophysical Research 105, 16. 106, 166
- Käse, R., Price, J., Richardson, P., Zenk, W., 1986. A quasi-synoptic survey of the thermocline circulation and water mass distribution within the Canary Basin. Journal of Geophysical Research 91, 9739–9748. 90, 108, 167
- Käse, R., Zenk, W., Sanford, T., Hiller, W., 1985. Currents, fronts and eddy fluxes in the Canary Basin. Progress in Oceanography 14, 231–257. 108, 167
- Kawase, M., Sarmiento, J., 1985. Nutrients in the Atlantic thermocline. Journal of Geophysical Research 90, 8961–8979. 60
- Keenlyside, N., Latif, M., Jungclaus, J., Kornblueh, L., Roeckner, E., 2008. Advancing decadal-scale climate prediction in the North Atlantic sector. Nature 453, 84–88, doi:10.1038/nature06921. 44
- Kerr, R., 2008. Global warming: Mother nature cools the greenhouse, but hotter times still lie ahead. Science 320, 595, doi: 10.1126/science.320.5876.595. 44
- Keyser, D., Shapiro, M., 1986. A review of the structure and dynamics of upper-level frontal zones. Monthly Weather Review 114, 452–499. 91
- Kiehl, J., Trenberth, K., 1997. Earth's annual global mean energy budget. Bulletin of the American Meteorological Society 78, 197–208. xiii, 6
- Knoll, M., Hernández-Guerra, A., Lenz, B., López-Laatzén, F., Machín, F., Müller, T., Siedler, G., 2002. The Eastern Boundary Current system between the Canary Islands and the African Coast. Deep Sea Research 49, 3427–3440. 60, 61, 90, 91, 108, 167

- Krauss, W., 1986. The North Atlantic current. *Journal of Geophysical Research* 91, 5061–5074. 90
- Kuhlbrodt, T., Griesel, A., Montoya, M., Levermann, A., Hofmann, M., Rahmstorf, S., 2007. On the driving processes of the Atlantic meridional overturning circulation. *Reviews of Geophysics* 45, RG2001. xiii, 11
- Kundu, P., Beardsley, R., 1991. Evidence of a critical Richardson number in moored measurements during the upwelling season off Northern California. *Journal of Geophysical Research* 96, 4855–4868. 91, 98, 108, 162, 168
- Láiz, I., Sangrà, P., Pelegrí, J., Marrero-Díaz, A., 2001. Sensitivity of an idealized subtropical gyre to the eastern boundary conditions. *Scientia Marina* 65, 187–194. 60
- Lavín, A., Bryden, H., Parrilla, G., 2003. Mechanisms of heat, freshwater, oxygen and nutrient transports and budgets at 24.5 N in the subtropical North Atlantic. *Deep Sea Research* 50, 1099–1128. 31, 141
- Le Treut, H., Somerville, R., Cubasch, U., Ding, Y., Mauritzen, C., Mokssit, A., Peterson, T., Prather, M., 2007. Historical Overview of Climate Change. In: *Climate Change 2007: The Physical Science Basis. Contribution of Working Group I to the Fourth Assessment Report of the Intergovernmental Panel on Climate Change* [Solomon, S., D. Qin, M. Manning, Z. Chen, M. Marquis, K.B. Averyt, M. Tignor and H.L. Miller (eds.)]. Cambridge University Press, Cambridge, United Kingdom and New York, NY, USA. xiii, 4, 6
- Leetma, A., Bunker, A., 1978. Updated charts of the mean annual wind stress, convergences in the Ekman layer, and Sverdrups transports in the North Atlantic. *Journal of Marine Research* 36, 311–322. 110, 168
- Levitus, S., Antonov, J., Boyer, T., 2005. Warming of the world ocean, 1955–2003. *Geophysical Research Letters* 32, L02604. 13, 135
- Levitus, S., Boyer, T., 1994b. World Ocean Atlas 1994, Volume 4: Temperature, NOAA Atlas NESDIS 4. U.S. Department of Commerce, Washington, D.C., 117 pp. 34
- Levitus, S., Burgett, R., Boyer, T., 1994a. World Ocean Atlas 1994, Volume 3, Salinity, NOAA Atlas NESDIS 3. U.S. Department of Commerce, Washington, D.C., 99 pp. 34
- Levitus, S. E., 2006. World Ocean Atlas 2005, Volumes 1-4, Salinity, NOAA Atlas NESDIS Volumens 61-64. NOAA, Silver Spring, Md. 34

- Liu, W., Tang, W., Labor, J. P., 1996. Equivalent neutral wind. National Aeronautics and Space Administration, Jet Propulsion Laboratory, California Institute of Technology. 98, 161
- Lomb, N., 1976. Least-squares frequency analysis of unequally spaced data. *Astrophysics and space science* 39, 447–462. 69, 71, 152, 153
- López-Jurado, J., González-Pola, C., Vélez-Belchí, P., 2005. Observation of an abrupt disruption of the long-term warming trend at the Balearic Sea, western Mediterranean Sea, in summer 2005. *Geophysical Research Letters* 32, L24606, doi:10.1029/2005GL024430. 44
- Lozier, M., Owens, W., Curry, R., 1995. The climatology of the North Atlantic. *Progress in Oceanography* 36, 1–44. 60
- Lumpkin, R., Speer, K., 2007. Global ocean meridional overturning. *Journal of Physical Oceanography* 37, 2550–2562. 11, 133
- Luyten, J., Pedlosky, J., Stommel, H., 1983. The Ventilated Thermocline. *Journal of Physical Oceanography* 13, 292–309. 9
- Machín, F., Hernández-Guerra, A., Pelegrí, J., 2006a. Mass fluxes in the Canary Basin. *Progress in Oceanography* 70, 416–447. 49, 50, 60, 90, 91, 98, 99, 106, 108, 145, 146, 162, 163, 167
- Machín, F., Pelegrí, J., 2006b. Effect of the Canary Islands in the blockage and mixing of the North Atlantic eastern water masses. *Geophysical Research Letters* 33, L04605, doi:10.1029/2005GL025048. 111
- Machín, F., Pelegrí, J., 2009. Northward Penetration of Antarctic Intermediate Water off Northwest Africa. *Journal of Physical Oceanography* 39, 512–535. 60, 83
- Machín, F., Pelegrí, J., Fraile-Nuez, E., Vélez-Belchí, P., López-Laatzen, F., Hernández-Guerra, A., 2010. Seasonal flow reversals of Intermediate Waters in the Canary Current System east of the Canary Islands. *Journal of Physical Oceanography*, doi: 10.1175/2010JPO4320.1. 83
- Manríquez, M., Fraga, F., 1982. The distribution of water masses in the upwelling region off Northwest Africa in November. *Rapports et Proces-verbeaux des Reunions Conseil International pour l'Exploration de la Mer* 180, 39–47. 90
- Mason, E., 2009. High resolution modelling of the Canary Basin oceanic circulation. Ph.D. thesis, Ph. D. Thesis, Universidad de Las Palmas de Gran Canaria, Las Palmas, Spain. 83

- Millot, C., Candela, J., Fuda, J., Tber, Y., 2006. Large warming and salinification of the Mediterranean outflow due to changes in its composition. Deep Sea Research 53, 656–666. 56
- Mittelstaedt, E., 1983. The upwelling area off northwest Africa. A description of phenomena related to coastal upwelling. Progress in Oceanography 12, 307–331. 90
- Mittelstaedt, E., Pillsbury, D., Smith, R., 1975. Flow patterns in the Northwest African upwelling area. Ocean Dynamics 28, 145–167. 90
- Mouriño, B., Fernández, E., Alves, M., 2004. Thermohaline structure, ageostrophic vertical velocity fields and phytoplankton distribution and production in the North East Atlantic subtropical front. Journal of Geophysical Research 109, C04020, doi:10.1029/2003JC001990. 91
- Müller, T., Siedler, G., 1992. Multi-year current time series in the eastern North Atlantic Ocean. Journal of Marine Research 50, 63–98. 65, 66, 90, 151
- Navarro-Pérez, E., Barton, E., 2001. Seasonal and interannual variability of the Canary Current. Scientia Marina 65. 82
- Neuer, S., Cianca, A., Helmke, P., Freudenthal, T., Davenport, R., Meggers, H., Knoll, M., Santana-Casiano, J., González-Dávila, M., Rueda, M., Llinás, O., 2007. Biogeochemistry and hydrography in the eastern subtropical North Atlantic gyre. Results from European time-series station ESTOC. Progress in Oceanography 72, 1–29. 118, 171
- Nykjaer, L., van Camp, L., 1994. Seasonal and interannual variability of coastal upwelling along northwest Africa and Portugal from 1981 to 1991. Journal of Geophysical Research 99, 14197–14208. 90
- Olbers, D., Wenzel, M., Willebrand, J., 1985. The interference of North Atlantic circulation patterns from climatological hydrographic data. Reviews of Geophysics 23, 313–356. 95, 98, 160, 162
- Pacheco, M., Hernández-Guerra, A., 1999. Seasonal variability of recurrent phytoplankton pigment patterns in the Canary Islands area. International Journal of Remote Sensing 20, 1405–1418. 90, 117, 170
- Paillet, J., Mercier, H., 1997. An inverse model of the eastern North Atlantic general circulation and thermocline ventilation. Deep Sea Research 44 (8), 1293–1328. 60
- Parrilla, G., Lavín, A., Bryden, H., García, M., Millard, R., 1994. Rising temperatures in the subtropical North Atlantic Ocean over the past 35 years. Nature 369, 48–51. 13, 31, 35, 43, 49, 56, 135, 142

- Parrilla, G., Neuer, S., Le Traon, P., Fernández-Suárez, E., 2002. Topical studies in oceanography: Canary Islands Azores Gibraltar Observations (CANIGO)-Volume 1: Studies in the northern Canary Islands basin. Deep Sea Research 49, 3409–3413. 60, 90
- Pastor, M., Pelegrí, J., Hernández-Guerra, A., Font, J., Salat, J., Emelianov, M., 2008. Water and nutrient fluxes off Northwest Africa. Continental Shelf Research 28, 915–936. 95, 98, 111, 160, 162
- Pedder, M., 1993. Interpolation and filtering of spatial observations using successive corrections and gaussian filters. Monthly Weather Review 121, 2889–2902. 34
- Pelegrí, J., Arístegui, J., Cana, L., González-Dávila, M., Hernández-Guerra, A., Hernández-León, S., Marrero-Díaz, A., Montero, M., Sangrà, P., Santana-Casiano, M., 2005a. Coupling between the open ocean and the coastal upwelling region off northwest Africa: water recirculation and offshore pumping of organic matter. Journal of Marine Systems 54, 3–37. 82, 90, 108, 111, 167
- Pelegrí, J., Marrero-Díaz, A., Ratsimandresy, A., 2006. Nutrient irrigation of the North Atlantic. Progress in Oceanography 70, 366–406. 90, 95, 98, 160, 162
- Pelegrí, J., Marrero-Díaz, A., Ratsimandresy, A., Antoranz, A., Cisneros-Aguirre, J., Gordo, C., Grisolía, D., Hernández-Guerra, A., Laiz, I., Martínez, A., Parrilla, G., Pérez-Rodríguez, P., Rodríguez-Santana, A., Sangrà, P., 2005b. Hydrographic cruises off northwest Africa: the Canary Current and the Cape Ghir region. Journal of Marine Systems 54, 39–63. 90, 104, 108, 111, 164, 167
- Pelegrí, J., Richman, J., 1993. On the role of shear mixing during transient coastal upwelling. Continental Shelf Research 13, 1363–1400. 98, 108, 111, 162, 168
- Pérez, F., Ríos, A., King, B., Pollard, R., 1995. Decadal changes of the θ -S relationship of the Eastern North Atlantic Central Water. Deep Sea Research 42, 1849–1864. 56
- Pickett, M., Paduan, J., 2003. Ekman transport and pumping in the California Current based on the US Navy's high-resolution atmospheric model (COAMPS). Journal of Geophysical Research 108, 3327, doi:10.1029/2003JC001902. 98, 161
- Pollard, R., Regier, L., 1992. Vorticity and Vertical Circulation at an Ocean Front. Journal of Physical Oceanography 22, 609–625. 91

- Potter, R., Lozier, M., 2004. On the warming and salinification of the Mediterranean outflow waters in the North Atlantic. *Geophysical Research Letters* 31. 56
- Reid, J., 1994. On the total geostrophic circulation of the North Atlantic Ocean: flow patterns, tracers, and transports. *Progress in Oceanography* 33, 1–92. 60
- Roemmich, D., Wunsch, C., 1984. Apparent changes in the climatic state of the deep North Atlantic Ocean. *Nature* 307, 447–450. 13, 49, 56, 135
- Roemmich, D., Wunsch, C., 1985. Two transatlantic sections: Meridional circulation and heat flux in the subtropical North Atlantic Ocean. *Deep Sea Research* 32, 619–664. 31
- Rudnick, D., 1996. Intensive surveys of the Azores front. 2. Inferring the geostrophic and vertical velocity fields. *Journal of Geophysical Research* 101, 16291–16304. 91
- Sangrà, P., Auladell, M., Marrero-Díaz, A., Pelegrí, J., Fraile-Nuez, E., Rodríguez-Santana, A., Martín, J., Mason, E., Hernández-Guerra, A., 2007. On the nature of oceanic eddies shed by the Island of Gran Canaria. *Deep Sea Research* 54, 687–709. 90, 91, 115, 118, 169, 171
- Sangrà, P., Pascual, A., Rodríguez-Santana, A., Machín, F., Mason, E., McWilliams, J., Pelegrí, J., Dong, C., Rubio, A., Arístegui, J., et al., 2009. The Canary Eddy Corridor: A major pathway for long-lived eddies in the subtropical North Atlantic. *Deep Sea Research* 56, 2100–2114. 90, 91, 115, 117, 169, 170
- Sangrà, P., Pelegrí, J., Hernández-Guerra, A., Arregui, I., Martín, J., Marrero-Díaz, A., Martínez, A., Ratsimandresy, A., Rodríguez-Santana, A., 2005. Life history of an anticyclonic eddy. *Journal of Geophysical Research* 110, C03021, doi:10.1029/2004JC002526. 90, 91, 115, 118, 169, 171
- Sarafanov, A., Sokov, A., Demidov, A., 2007. Water mass characteristics in the equatorial North Atlantic: A section nominally along 6.5°N, July 2000. *Journal of Geophysical Research* 112, C12023. 14, 136
- Scargle, J., 1982. Studies in astronomical time series analysis. II- Statistical aspects of spectral analysis of unevenly spaced data. *The Astrophysical Journal* 263, 835–853. 69, 71, 153
- Shearman, R., Barth, J., Kosro, P., 1999. Diagnosis of the three-dimensional circulation associated with mesoscale motion in the California Current. *Journal of Physical Oceanography* 29, 651–670. 91, 104, 165

- Siedler, G., Onken, R., 1996. Eastern recirculation. The warmwater-sphere of the North Atlantic Ocean, edited by W. Krauss, 339–364, Gebrüder Borntraeger, Berlin. 60
- Smith, W., Sandwell, D., 1997. Global Sea Floor Topography from Satellite Altimetry and Ship Depth Soundings. *Science* 277, 1956. xv, 63
- Stewart, R., 2005. Introduction to physical oceanography. Texas A & M University. xiii, 8
- Stommel, H., 1979. Determination of water mass properties of water pumped down from the ekman layer to the geostrophic flow below. *Proceedings of the National Academy of Sciences* 76, 3051–3055. 9, 132
- Stramma, L., Siedler, G., 1988. Seasonal changes in the North Atlantic subtropical gyre. *Journal of Geophysical Research* 93, 8111–8118. 108, 167
- Team, A. D. M., 2002. Argo Data Management Handbook. 32 pp. 32, 33
- Team, A. S., 1998. On the design and implementation of Argo: an initial plan for a global array of profiling floats. International CLIVAR Project Office Report 21, GODAE Report 5, GODAE International Project Office, Melbourne, Australia, 32 pp. 31
- Tejera, A., García-Weil, L., Heywood, K., Cantón-Garbín, M., 2002. Observations of oceanic mesoscale features and variability in the Canary Islands area from ERS-1 altimeter data, satellite infrared imagery and hydrographic measurements. *International Journal of Remote Sensing* 23, 4897–4916. 90
- Tett, P., Arístegui, J., Barton, D., Basterretxea, G., De Armas, J., Escánez, J., León, S., Lorenzo, L., Montero, N., 2002. Steady-state DCM dynamics in Canaries waters. *Deep Sea Research* 49 (17), 3543–3559. 106, 166
- Tintoré, J., Gomis, D., Alonso, S., Parrilla, G., 1991. Mesoscale dynamics and vertical motion in the Alborán Sea. *Journal of Physical Oceanography* 21, 811–823. 91
- Tomczak, M., 1978. Distribution of water masses in surface-layers of Northwest African upwelling area. *Geophysical Journal of the Royal Astronomical Society* 53, 183. 90
- Tomczak, M., 1981. An analysis of mixing in the frontal zone of South and North Atlantic Central Water off North-West Africa. *Progress in Oceanography* 10, 173–192. 60

- Torrence, C., Compo, G., 1998. A practical guide to wavelet analysis. *Bulletin of the American Meteorological Society* 79, 61–78. 72, 153
- Torrence, C., Webster, P., 1999. Interdecadal changes in the ENSO–monsoon system. *Journal of Climate* 12, 2679–2690. 72, 153
- van Aken, H., 2000. The hydrography of the mid-latitude Northeast Atlantic Ocean: The intermediate water masses. *Deep Sea Research* 47, 789–824. 60
- Van Camp, L., Nykjaer, L., Mittelstaedt, E., Schlittenhardt, P., 1991. Upwelling and boundary circulation off Northwest Africa as depicted by infrared and visible satellite observations. *Progress in Oceanography* 26, 357–402. 90
- Vargas-Yáñez, M., Parrilla, G., Lavín, A., Vélez-Belchí, P., González-Pola, C., 2004. Temperature and salinity increase in the eastern North Atlantic along the 24.5°N in the last ten years. *Geophysical Research Letters* 31. 13, 31, 49, 55, 135
- Vélez-Belchí, P., Hernández-Guerra, A., Fraile-Nuez, E., Benítez-Barrios, V., 2010. Changes in temperature and salinity tendencies of the upper subtropical north atlantic ocean at 24.5°n. *Journal of Physical Oceanography* 40, 2546–2555. 27
- Wright, W., Worthington, L., 1970. The water masses of the North Atlantic Ocean: a volumetric census of temperature and salinity. *American Geographical Society*, New York. 60